UNIVERSIDAD DE GRANADA
DEPARTAMENTO DE FÍSICA TEÓRICA Y DEL COSMOS
PROGRAMA DE DOCTORADO EN FÍSICA Y CIENCIAS DEL ESPACIO

PHYSICAL AND CHEMICAL PROPERTIES OF GALAXIES WITH STAR FORMATION IN DIFFERENT ENVIRONMENTS

Memoria presentada por

Salvador Duarte Puertas

INSTITUTO DE ASTROFÍSICA DE ANDALUCÍA
CONSEJO SUPERIOR DE INVESTIGACIONES CIENTÍFICAS

bajo la dirección de:

Dr. José Manuel Vilchez Medina y **Dr. Jorge Iglesias Páramo**

para optar al grado de DOCTOR INTERNACIONAL

November 29, 2019

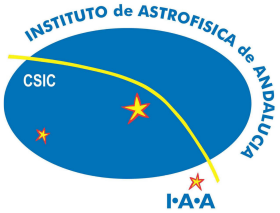

EXCELENCIA
SEVERO
OCHOA

Editor: Universidad de Granada. Tesis Doctorales
Autor: Salvador Duarte Puertas
ISBN: 978-84-1117-159-5
URI: http://hdl.handle.net/10481/71855

Contents

Agradecimientos

Ahora viene la parte más difícil aunque a priori debiera ser la más sencilla. Tengo tantísimo que agradecer a tanta gente que temo no acordarme de alguien. Si ese fuese el caso, posiblemente sepas de mi mala memoria. Me he imaginado escribiendo esta parte miles de veces, es muy importante para mi pues es vuestra parte, la de las personas que más quiero y a las que deseo reconocer en estas líneas. Sois mi aliento y mi gasolina.

Creo que es de justicia empezar agradeciendo a mis padres todo el apoyo incondicional que me han dado durante estos años, mucho antes de empezar este proyecto. Otros habrían tirado la toalla hace mucho mucho tiempo, pero vosotros siempre vais a contracorriente. Soy como soy gracias a vosotros (para lo bueno y para lo malo) y me servís de inspiración para querer mejorar día a día como persona. Por eso quiero daros las gracias y deciros que os quiero mucho (aunque no os lo diga lo suficiente). Un importante lugar ocupa el resto de mi familia, encabezada por mi hermana (Carmina, soy como tú -pero más feo-, eres super luchadora y todo un referente para mi), mi cuñaaaaooo (mi amigo y hermano, gracias por estar en mi vida, eres de las mejores personas que conozco), mi sobrino (que es un maquinón y estoy súper orgulloso de él y de como es como persona) y mi tito (mi pepito grillo particular que siempre ha velado para que dé lo mejor de mi). Prometo veros más ahora que he terminado (esto es extensible a muchísima más gente, así que daros por aludidos).

A Gema, mi pilar. Eres la persona que más me ha soportado (con lo cabezón que soy, tienes una paciencia casi infinita), comprendido (como buena casi portuguesa) y querido durante este tiempo y más allá. Siempre me has empujado para que persiga mis sueños con más fuerza de la que creía tener y me has dado aliento cuando ya no me quedaba más. Gracias por arrancarme una buena sonrisa cuando más falta me hacía y por compartir tus planes (presentes y futuros) conmigo (pues eso). Por supuesto muchas gracias a toda la familia de Gema y en especial a Bella, que siempre me ha acogido con todo el cariño del mundo.

Pepe y Jorge, que os voy a decir. Sois mi espejo y los valores en los que quiero reflejarme (mucho más allá de los científicos). Gracias por la oportunidad que me habéis dado y por la paciencia (infinita) que habéis mostrado siempre conmigo. Jorge, siempre has mirado por mi bien (salvo en la subida a la Alcazaba), me ofreciste uno de los regalos más especiales que podrías haberme dado: SITELLE (el que espero que sea mi futuro profesional) del que siempre te estaré agradecido. Pepe, gracias por sacar horas de donde no había para formarme (no olvido tu etapa de director, madre mía, hemos compartido muchísimas horas). Gracias por mirar siempre por mi bien y encauzarme. Se me va a hacer muy raro no compartir un buen café (o té) para hablar largo

y tendido de ciencia (u otros temas más alejados de la ciencia).

A mis compañeros del IAA. A Carol, una de las personas más especiales que he tenido la suerte de conocer en el IAA, que sepas que tienes un amigo para siempre. A Enrique (y Roco) muchas gracias por ayudarme tanto, eres el ejemplo de que con voluntad y sacrificio no hay barreras, gracias por enseñármelo. Al tridente de sabios armoniosos (A. F, A. L y Paco), sois de lo mejor que he conocido por el IAA: A Antonio (A. Fuentes), eres una de las personas más maravillosas que existe (y que he tenido el placer de conocer) además de ser un maquinón (te aguantas, ya queda por escrito), voy a extrañarte muchísimo felón (no sabes cuanto). A Antonio (A. Lorenzo), ha llovido desde que empezamos con los papeleos de la tesis (y del momento escalera ni te cuento)...al final era cierto eso de que en un momento estábamos en la puerta del salón de actos para defender (eres otro maquinón, que raro se me va a hacer no compartir contigo tantas charlas mañaneras). A Paco (F. Nogueras, el del catálogo de GALACTICNUCLEUS que es famoso), eres incluso mejor que los dos Antonios (no Paco no harmony, cántate algo Paco), que no me entere yo que en Alemania no te tratan bien! (eres de los mejores investigadores que conozco). A Naím, a Estefanía (aka La Niña de las Conchas) y a Pablo, muchas gracias por todo, me acogisteis en vuestro zulo y conseguisteis que me sintiera como en casa (también sois unos máquinas), hemos compartido un montón de anécdotas y sufrimientos!! A Laura, aunque llegaste la última eres añeja, gracias por soportarnos y animarnos a A.F. y a mi (sinciencia XL te hará fuerte), vas a dejar huella en el IAA (tomad nota que fui de los primeros en decirlo). A Laly, eres una inspiración, me alegro que estés trabajando con gente tan magnífica como son los trabajadores/compañeros de CAHA. También quiero dar las gracias a Sergio, Jesús Escobar, Javi Blasco, Clara, Pique, César, Ancor (trol, a ver si nos vemos más!!), al entrepreneur (todo un desafío a las leyes de la naturaleza, eres una de las personas que más me alegras el día cuando te veo, gracias por existir y está ahí o allí, de ida o vuelta, con paso firme hacia algún lugar), Pablo Santos, Teresa, Guille, Feli, Antonio Arroyo (te he pasado el testigo tío), Sara, Martín, Jackeline, Fran, Manu Lampón, Antxón, Rainer, Adrián, Alejandro, Igor, Chony, Jaime, Pepa, Isabel, Emilio, Rubén, Mike, Toño, Jonathan, Cristina (Torrededía), Rosa, Juanjo, María Ángeles, Miguel, José Luís, Eva, Antonio, Rafa, Tapia, Alonso y muchos más, en definitiva a todo el personal del IAA (personal investigador, de portería, de limpieza, de mantenimiento, de informática, de gestión...). Gracias por conseguir que eche de menos tanto un sitio (y su gente) tan especial como es el IAA, ha sido un orgullo pertenecer a esta familia.

Para mis compañeros (y amigos) de la Universidad también quiero dedicarles un trocito de texto. Muchas gracias a Simon y Mamen, con vosotros pude empezar a soñar con ser astrofísico, sois los culpables de que estas líneas existan. En especial quiero destacar (y agradecer) a Simon por ese don que tiene de detectar cuando alguien necesita ayuda y, de una forma desinteresada, estar siempre disponible para quien lo necesite y cuando lo necesite, que pena que sólo exista un Simon. También quiero agradecer por todo a Almudena, Isa, Eduardo, Mónica, Ute, Estrella, Jorge, Ana, Tomás, Laura, David, Migue, Lluís, Juan Carlos, Antonio, Ángel Delgado, Carmen Recio, Francisco (el tío que más sabe de Blender en toda España), Carlos e Inma. Los futboleros Alberto, Paloma, Ignacio (Nacho el 30 meter), Razvan, Irene (también conocida como Irina), Nico...

A todos los trabajadores de CAHA, en especial a Pablo (tengo ganas de verte tiaco), Alba,

Jesús, Gilles, Ana (again, eres tan grande que tenías que aparecer dos veces). Se que puede sonar a tópico, pero sois unas grandísimas personas. Viva Calar Alto!

A todos los miembros de ESTALLIDOS (todos sin excepción!!)!! de la Complu (Armando, África, Cristina), de la Universidad Autónoma de Madrid (Marina, Ángeles), del CIEMAT (Iker y Mercedes), del CAB (Vital), del IAC (Jairo, Adriana, Alejandro, David, Casiana, Amanda...).

Por supuesto quiero dedicar unas líneas a mis queridos compañeros (y amigos) de la Université Laval. Muchas gracias por acogerme tan lejos de casa y hacerme sentir tan bien (incluso con -31 grados de temperatura...). Muchas gracias por la paciencia que habéis tenido conmigo y por hacerme sentir tan bien valorado y especial. Quiero agradecer muchísimo a Laurent y Thomas toda la ayuda que me habéis dado, espero poder trabajar con vosotros pronto y durante mucho tiempo. También quiero agradecer a Carmelle, Laurie, Maxime, Ismael...

También quiero dedicar unas líneas a mis amigos de toda la vida (me habéis aguantado muchísimos años), a Antonio Muela (hemos estudiado unas cuantas horas juntos, gracias por tener siempre un hueco para verme en tus incursiones por Granada, aunque pasen mil años sin verte parece que sólo ha pasado un día), Chema, Nico, Blas, los Javis, Adri (una de las personas más especiales que conozco), Maria José (la tía más fiestera, responsable y maquinona que conozco, te debo muchísimos cafés!!) y en definitiva a todos los compañeros del barrio y de Física. Y muchas gracias a Charlotte, que paciencia has tenido conmigo!

Espero no haberme olvidado de mucha gente. Sin duda aquí tendrían que aparecer muchas más personas. GRACIAS A TODOS! Espero seguir caminando con vosotros.

Abstract

This thesis focusses on the study of the properties of galaxies with massive star formation from the perspective of their environments and the possible associated effects; for this, we study on the one hand general relations of properties like Star Formation Rate (SFR), stellar mass, and metallicity for a large sample of galaxies containing mostly field galaxies (from Sloan Digital Sky Survey, SDSS) and on the other hand, the properties of star formation regions in the compact group of galaxies Stephan's Quintet (SQ), as inferred from their emission line fluxes.

The main objectives of this thesis are:

- to state the main basic relations of galaxies with star formation in the local Universe. For this, we have selected a large sample (209 276) galaxies from SDSS, and we have studied their main properties relations (SFR, metallicity, stellar mass) taking into account appropriate aperture corrections due to the limited size of the fiber. We have make use of empirical aperture corrections obtained from two-dimensional spectroscopy from the CALIFA project sample of galaxies (Iglesias-Páramo et al. 2013, 2016), to determine the total value of the emission line fluxes (e.g. [OII]λ3727, Hβ, [OIII]λ5007, Hα, and [NII]λ6584) of the star-forming galaxies from SDSS.
- to make a complete study of the star formation regions detected in the field of view of SQ by means of the wide field IFTS (imaging Fourier transform spectrometer) SITELLE. Given that galaxy-galaxy interactions are ubiquitous in this group of galaxies, the spatial distribution of the star formation regions is not closely associated with the galaxy discs as in the case of normal spiral galaxies; a non negligible fraction of them are found along tidal tails or other structures resulting from interactions. The combination of the wide field of view of SITELLE and the ability to detect regions with emission lines makes this project unique for a complete study of the main properties of star formation regions in this highly disrupted system of galaxies.

Resumen

Esta tesis se centra en el estudio de las propiedades de las galaxias con formación estelar masiva desde el punto de vista de sus entornos y los posibles efectos asociados; para ello hemos estudiado por un lado las relaciones generales de algunas propiedades como la tasa de formación estelar (SFR), la masa estelar y la metalicidad para una gran muestra representativa de galaxias que contienen principalmente galaxias de campo (de Sloan Digital Sky Survey, SDSS) y, por otro lado, las propiedades de las regiones con formación estelar en el grupo compacto de galaxias conocido como el Quinteto de Stephan (SQ).

Los objetivos principales de la tesis son:

- establecer las principales relaciones básicas de las galaxias con formación estelar en el Universo local. Para ello, hemos seleccionado una gran muestra de galaxias con formación estelar (209 276) de SDSS y hemos estudiado las principales relaciones de sus propiedades (SFR, metalicidad, masa estelar) teniendo en cuenta las correcciones de apertura apropiadas debido al tamaño limitado de las fibras de SDSS. Hemos utilizado correcciones de apertura empíricas obtenidas a partir de la espectroscopía bidimensinal de la muestra de galaxias del proyecto CALIFA (Iglesias-Páramo et al. 2013, 2016) para determinar el valor total de los flujos de las líneas de emisión (e.g. [OII]λ3727, Hβ, [OIII]λ5007, Hα y [NII]λ6584) de las galaxias con formación estelar de SDSS.
- hacer un estudio completo de las regiones con formación estelar detectadas en el campo de visión de SQ mediante el espectrógrafo de amplio campo de transformada de Fourier SITELLE. Dado que las interacciones galaxia-galaxia predominan en este grupo compacto de galaxias, la distribución espacial de las regiones con formación estelar no están estrechamente asociadas con los discos de las galaxias como en el caso de las galaxias espirales normales; una fracción no despreciable de ellas se encuentra a lo largo de las colas de marea así como de otras estructuras resultantes de las distintas interacciones. La combinación del amplio campo de visión que tiene SITELLE y la capacidad para detectar regiones con líneas de emisión hace que este proyecto sea único para realizar un estudio completo de las principales propiedades de las regiones con formación estelar en este sistema de galaxias altamente perturbado.

Structure of this thesis

This thesis is divided into seven chapters. It consists of a first introductory chapter, four chapters corresponding to the different researches made during these four years of my PhD thesis, the conclusions, and a final chapter of future work. The introductory chapter is intended to make a general framework of the main topic of this thesis - the star forming properties of galaxies from global (chapters 2 and 3) and local (chapters 4 and 5) points of view -. Concerning the remaining four chapters at the core of the thesis, two of them have been published in the scientific journal Astronomy and Astrophysics (A&A): Duarte Puertas, S., Vilchez, J. M., Iglesias-Páramo, J., Kehrig, C., Perez-Montero, E., and Rosales-Ortega, F. F., 2017, A&A, Vol. 599, id.A71, 13 pp.; and Duarte Puertas, S., Iglesias-Páramo, J., Vilchez, J. M., Drissen, L., Kehrig, C., and Martin, T., 2019, A&A, Vol. 629, id.A102, 20 pp. (Figure 4.6 is the Cover Letter of this issue), and the other two have been submitted to the same journal. Each of these four chapters starts with a short introduction where the particular details of the subject are explained. The main conclusions of this thesis, as well as the guidelines of my future work can be found in the last two chapters.

Chapter 1

Introduction

Contents

1.1 The realm of galaxies

The concept of *galaxy* is established in today's scientific background, but there was a time (not so long ago as we might think) when even astrophysicists were not clear about what a galaxy was or if there were more than one. Until 100 years ago, the majority of astrophysicists thought that the entire Universe was contained in a single galaxy, the Milky Way. The observations carried out by Keeler until the year 1900 helped them to increase understanding about nebulae thanks to the detection of spiral nebulae. Years later, through spectrographic studies of spiral nebulae, Slipher (1917) found that these spiral nebulae had high radial velocities (~570 km s^{-1}) very different from those found in the stars from the same sample (~20 km s^{-1}). In April 1920 what is known nowadays as the "Great Debate" took place. In this debate, the nature of "spiral nebulae" [1] and their distance from us were discussed. In this debate, the figures of two scientists called Shapley and Curtis stood out, although there were many more scientists who participated and who had an impact on this debate. For more information about the "Great debate" I recommend Trimble (1995) and the references therein. Shapley defended the idea that the Milky Way contained the entire Universe and, therefore, nebulae were in fact galactic objects. Instead, Curtis believed that the spiral nebulae were objects similar to the Milky Way, maintaining the idea, based on observations of novae in M31, that they were actually extragalactic objects. The debate remained open until 1926 thanks to Hubble's discovery by estimating the distance to NGC 6822 at 214 kpc, when he evidenced that NGC 6822 was outside the Milky Way. This fundamental discovery made it possible for the discipline of extragalactic physics to begin. In a descriptive way, we define *galaxy* as the set of gravitationally-bound stars, which contain gas, dust and dark matter.

1.1.1 Hubble sequence

There are a large number of galaxies in the Universe, each of them different from the others. We aim to characterise a large number of them using their morphology, colour, size, star formation, environment, the amount of metals they contain, etc. The characterisation of galaxies is necessary to be able to study their fundamental properties and the relationships that may exist between them.

Galaxies have diverse forms, presenting substantial morphological differences from each other. The classification of galaxies based on their morphology is relevant since different types of galaxies correspond to different mechanisms of galactic formation and dependence on the environment. The first scheme to classify the morphology of galaxies was proposed by Hubble (1936) considering optical range (see Fig. 1.1) published in his work entitled *Realm of the Nebulae*. Hubble (1936) divided the galaxies into three categories:

- Spiral galaxies (S). They are divided into two classes: barred galaxies (SBa, SBb and SBc) and non-barred galaxies (Sa, Sb and Sc). They have a nucleus in the centre of the galaxy (bulge) and a flat disk around it. The bulge is more prominent in the Sa-type galaxies than in the Sc. The name refers to the spiral structure showed in its arms where the stars' movements are orderly. Although they can have stars with a wide range of ages, the spiral

[1] Today we know the spiral nebulae as spiral galaxies.

arms are mainly composed of young stars, giving them the typical blue colour that this kind of galaxies have. In addition, these galaxies can have large amounts of gas and dust and their star formation is usually active.

- Elliptical galaxies (E). They are divided into types E0 through to E7, depending on their ellipticity. They are composed of old stars that have randomly-distributed velocities, with a very small (or zero) amount of gas and dust and a low star formation. They have a soft light distribution and they tend to be more massive than spirals, since they typically have stellar masses of about 10^{11} $M_{\odot}$.
- Lenticular galaxies (S0). They have characteristics of both spiral and elliptical galaxies. In addition, they have a central bulge and a flat disk without the spiral character. Their interstellar medium is poor, so like in elliptical galaxies, they do not have large amounts of gas and dust.

Hubble distinguised the galaxies into two evolutionary types: early-type and late-type galaxies. Early-type galaxies encompass elliptical and lenticular galaxies, while late-type galaxies are spirals (now irregular galaxies are also added to this category). Hubble incorrectly thought that galaxies evolved from elliptical to spiral but today it is thought that galactic evolution happens in the other direction. For historical reasons, this denomination is still in use.

An alternative and improved classification was proposed by de Vaucouleurs (1959), providing a three-dimensional representation of the morphological classification of galaxies (see Fig. 1.2). In this diagram, intermediate morphological types were introduced to those proposed by Hubble, with the galaxies divided into subtypes of spiral galaxies (Sa, Sab, Sb, Sbc, Sc, Scd, Sd, and their corresponding barred types), with or without inner ring, or irregular galaxies. The latter are rich in gas and dust and do not have a well-defined structure.

From all of the above, we can see that some of the properties of galaxies (e.g. amount of gas, dust, star formation) correlate with their morphology.

1.1.2 HII regions and star-forming galaxies

Studying HII regions and star-forming galaxies will help us to understand how galaxies evolve chemically and what was their history of star formation. From these objects, we will determine the physical conditions of the ionised gas and the chemical composition of the interstellar medium (ISM), as well as some physical properties (e.g. star formation rate -SFR-, oxygen abundance -O/H-, nitrogen to oxygen abundance -N/O-, dust extinction, and the kinematics of the region) as well as the possible relationships that might exist between them.

An HII region (e.g. Orion, see Fig. 1.3) is the volume of gas ionised by at least one hot young star (types OB), with an effective temperature $T_{\rm eff} \geq 25\,000$ K. These stars are massive (>8 $M_{\odot}$) and emit in the ultraviolet (UV) large amounts of Lyman continuum photons. The most abundant element in HII regions is hydrogen,[2] therefore, the main energetic mechanism in HII regions is photoionisation. There are also other elements in HII regions, for example oxygen, nitrogen, etc.

[2]It should be noted that the main element of which the stars are composed is hydrogen (Payne 1925).

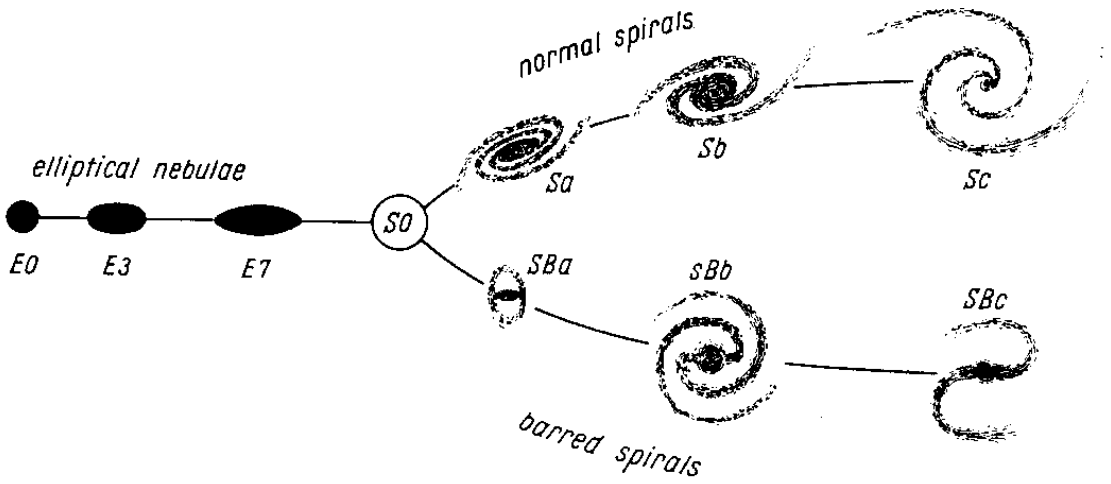

Figure 1.1: Original morphological diagram by Hubble (1936). On the left side, we can see the elliptical galaxies, ranging from type E0 to type E7 depending on their ellipticity. On the right, we can see the spiral galaxies, which are divided into barred galaxies (bottom) and normal, or non-barred, galaxies (top). The lenticular galaxies are in the place where the spiral and elliptical galaxies cross.

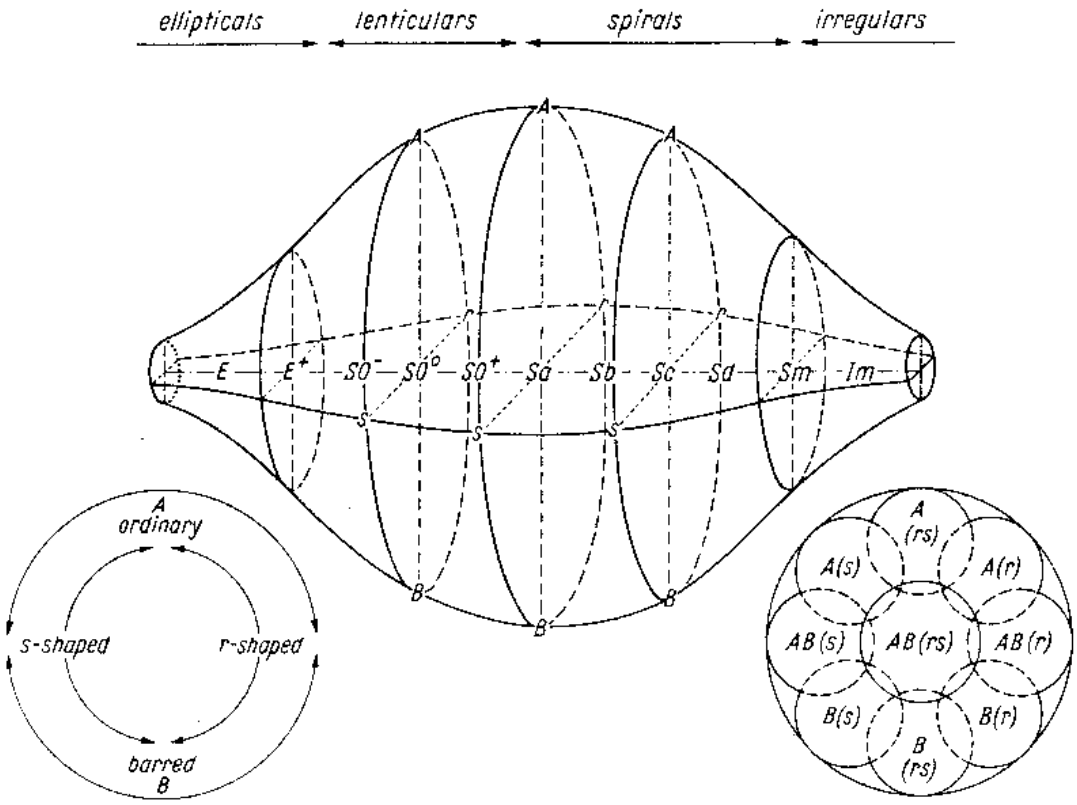

Figure 1.2: Original morphological classification by de Vaucouleurs (1959).

The UV photons emitted by massive stars collide with the electrons from hydrogen atoms. If the incident photon has enough energy, it will eject the electron from the nucleus. This free electron

will have a kinetic energy equal to the difference between the energy of the incident photon and the ionisation potential. Also, it can be absorbed by a cation (the proton from the hydrogen atom) emitting one photon with a certain amount of energy. We will have diffuse radiation if these photons escape from the region without being re-absorbed (case A) or, conversely, interact with another atom by ionising or exciting it (case B). To form an HII region, the number of ionised hydrogen atoms must be at least equal to or greater than the recombined electrons. The size of the HII regions is determined by the radius of Strömgren (with a typical size of dozens of parsecs) which is deduced from the radius of the HII region of gas ionised by a massive hot star, taking into account the balance between the number of photoionisations and recombinations. Their size will depend on the rate of ionising photons emitted and the density of the region (Strömgren 1939). When the number of young and massive stars in the region is in the hundreds, we will be talking about giant HII regions. These regions are extended, bright, and usually have typical diameter sizes of kpc (e.g. Firpo 2012).

As we noted in the previous section, the position of star-forming galaxies on the BPT diagram is well-known. Below the demarcation of Kauffmann et al. (2003a), star-forming galaxies are dominated by the spectrum of the HII regions in the star-forming areas of the galaxy, which implies that AGN's contribution is less than 1% (Brinchmann et al. 2004b). The SFR range of normal galaxies varies from ~0 (gas-poor elliptical galaxies, lenticular galaxies, and some dwarf galaxies) to ~20 $M_\odot$ yr^{-1} (gas-rich spiral galaxies), although it can reach up to ~ 100 $M_\odot$ yr^{-1} for selected starburst galaxies (Kennicutt 1998a). The metallicity of star forming galaxies ranges from from slightly higher solar values to close almost 40 times less than the solar values (e.g. IZw18, Kehrig et al. 2016).

The main properties of galaxies are not independent from each other; instead observations have shown that some of them are related One of the most widely used is the SFR – stellar mass relation (see Fig. 1.4). Noeske et al. (2007) reported that the SFR and the stellar mass of star forming galaxies follow an increasing sequence (the main sequence); quenched galaxies (i.e. those that do not form stars) are out of this sequece. The SFR – stellar mass relation is produced both in the local Universe and at higher redshifts (e.g. Madau et al. 1996; Brinchmann et al. 2004b; Iglesias-Páramo et al. 2006; Elbaz et al. 2007; Salim et al. 2007; Kennicutt et al. 2008; Peng et al. 2010; Whitaker et al. 2012; Drake et al. 2013, 2015). Note that the most massive galaxies contain more gas and could therefore have higher SFR values (Richards et al. 2016). Upon reaching a stellar mass of $\sim 10^{10.5} M_\odot$, galaxies experience a drop in their SFR and leave this sequence. When we divide the SFR by the stellar mass of the galaxy, we obtain the specific SFR (sSFR). The sSFR can be interpreted as the current efficiency of new star formation in a galaxy if we compare it with its average star formation activity in the past (Karim et al. 2011). Less massive galaxies will be more efficient compared to more massive ones.

One of the most studied relationships and key to understanding the formation and evolution of galaxies is the relation between metallicity and stellar mass of the galaxy (MZR).[3] It was initially proposed by Lequeux et al. (1979), and later it was studied by a huge number of authors (e.g.

[3] Although this relationship can be studied both in its gaseous form and in its stellar form, during this work we will always refer to the metallicity of gas.

Figure 1.3: Example of HII region: Orion Nebula (M 42), the closest to us. Credits: NASA, ESA, M. Robberto (Space Telescope Science Institute/ESA) and the Hubble Space Telescope Orion Treasury Project Team.

Vila-Costas & Edmunds 1992; Garnett 2002; Pilyugin et al. 2004; Tremonti et al. 2004; Lee et al. 2006; Zahid et al. 2014). The MZR has a strong correlation between mass and metallicity where metallicity increases with stellar mass. This relationship extends from masses of 10^7 $M_\odot$ to 10^{12} $M_\odot$. The most massive galaxies are the most chemically evolved. The shape of the MZR depends strongly on the calibrations used to derive the metallicity (Maiolino & Mannucci 2019). In the MZR, there are many empirical and bayesian metallicity calibrators that do not fit the positions of the galaxies in the local Universe derived with direct metallicity measurements. Thus, it will be necessary to use empirical calibrators that reproduce the positions of these nearby galaxies with well-defined metallicity values. Tremonti et al. (2004) studied the MZR for a sample of SDSS galaxies, finding a scatter of $\sim$ 0.1 dex (see Fig. 1.5). This scatter correlates with other

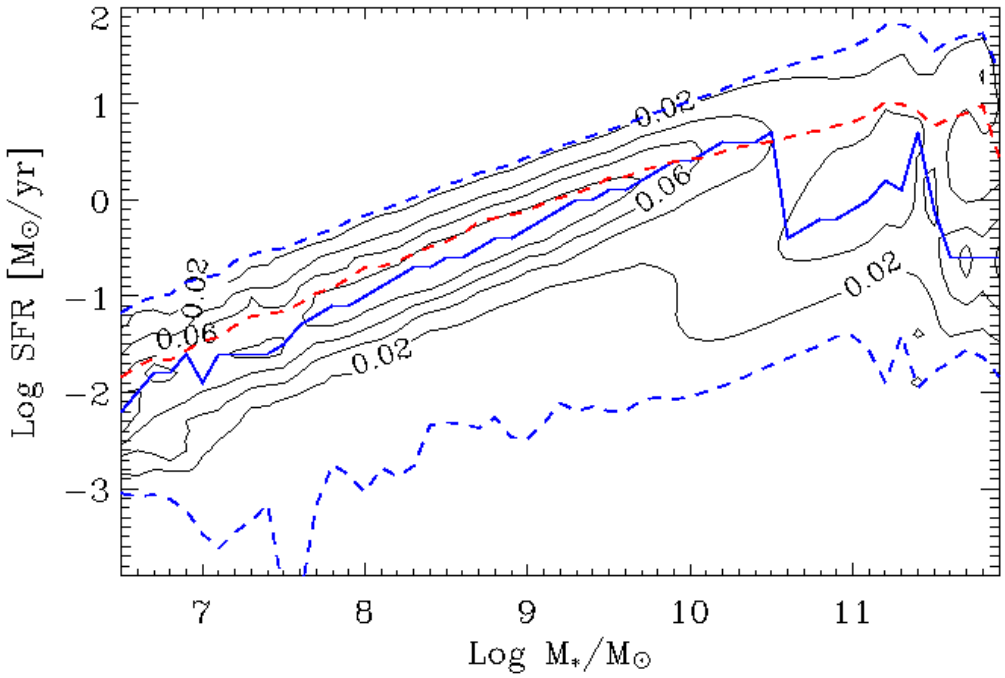

Figure 1.4: The SFR – stellar mass relation for all galaxies without AGN contribution in Brinchmann et al. (2004b, their figure 17). The black contours and the red line show the conditional likelihood of SFR and the average SFR at a given stellar mass.

properties of galaxies and has been studied thoroughly. The SFR was proposed as a secondary parameter of the MZR by Ellison et al. (2008) with the aim of minimising the scatter. They found that at a given stellar mass, galaxies with greater metallicity values had lower SFR than galaxies with lower metallicity values, which had a higher SFR. Therefore, galaxies with lower metallicity values have a more active star formation. Mannucci et al. (2010) and Lara-López et al. (2010b) studied the fundamental metallicity relation (FMR). Lara-López et al. (2010b) proposed the existence of a well-defined fundamental plane between these three properties (i.e. metallicity, stellar mass, and SFR). There is some controversy about the existence of this fundamental plane (Maiolino & Mannucci 2019). From the observations of galaxies with bidimensional integral field spectroscopy (IFU) such as CALIFA (Sánchez et al. 2012) and MANGA (Bundy et al. 2015), the existence of the relation between the MZR and the SFR has been questioned (e.g. Sánchez et al. 2013, 2017; Barrera-Ballesteros et al. 2017). These articles indicate that the relationship is produced by aperture effects existing in the SDSS observations. Salim et al. (2014) repeated the study using this same data and found that the relationship actually exists. Therefore, a study that minimises all the effects, correcting the SFR for aperture, with an accurate calculation of metallicity, as we have discussed in this paragraph, is necessary for a better understanding of the relation between the MZR and the SFR.

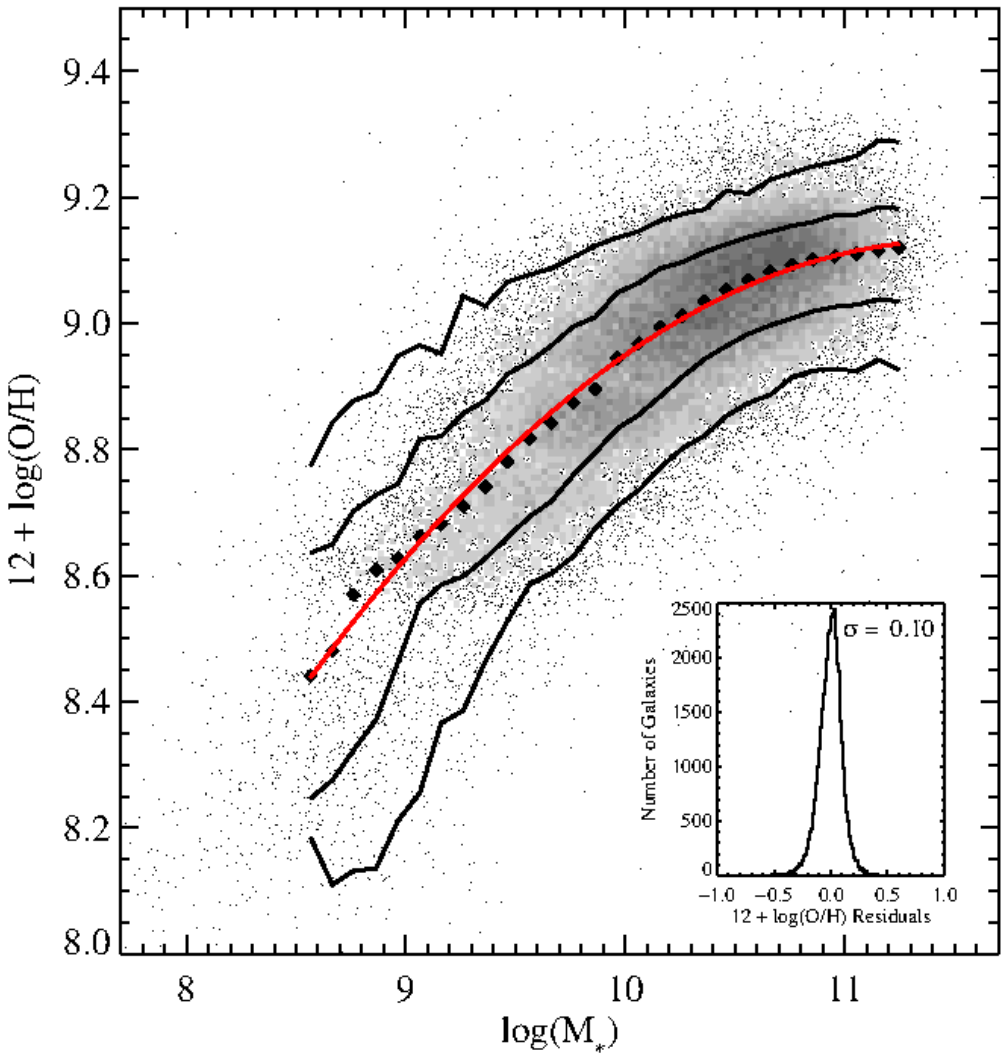

Figure 1.5: MZR for a sample of ~ 53 000 galaxies with star formation in SDSS. The red line represents the best fit to the data. The black solid lines represent the contours at 68% and 95%. This figure has been extracted from the article Tremonti et al. (2004, their figure 6).

1.1.3 Spectroscopic classification

With the advent of spectroscopic observations, a wide range of possibilities was opened up in the study and understanding of objects which form part of the vast Universe (e.g. stars, HII regions, galaxies). This new field of study allowed us to characterise astrophysical objects using new methodologies from their spectrum.

There are several methods for classifying the different spectral profiles of objects that have emission lines depending on their excitation mechanism. These methods will be used by us, for example to select HII regions and star-forming galaxies. One of the most used is the BPT diagram, initially proposed by Baldwin, Phillips, & Terlevich (1981), although subsequently revised by Veilleux & Osterbrock (1987). These diagnostic diagrams are based on the intensity ratios of

a series of emission lines that are close in wavelength on the spectrum[4] and this ratio provides us information on different ISM parameters that are linked to excitation, temperature, etc. The line ratios considered in these diagrams are [OI]/Hα, [SII]/Hα, [NII]/Hα, and [OIII]/Hβ. Throughout this work we will refer to log([OIII]/Hβ) versus log([NII]/Hα) as the BPT diagram. Figure 1.6 shows a clear example of this diagram, where the relation between log([OIII]/Hβ) and log([NII]/Hα) proposed by Veilleux & Osterbrock (1987) is displayed. In the BPT diagram, the positions of the HII regions as well as the star-forming galaxies (or active galactic nucleus -AGN- galaxies) are well determined (see Sect. 1.1.2) since these diagrams take into account the diversal excitation mechanisms that dominate each object. Note that both HII regions and star-forming galaxies are objects ionized by massive stars, however, non-thermal processes (e.g. shocks) dominate in AGN galaxies. In this BPT diagram, star-forming galaxies and HII regions show a clear correlation where the higher the log([OIII]/Hβ) value, the lower the log([NII]/Hα) value and vice versa.

The increasing number of spectroscopic galaxy surveys (e.g. Sloan Digital Sky Survey (SDSS), York et al. 2000; 2dFGRS, Colless et al. 2001) have resulted in very large numbers of galaxies ($\sim 10^6$ galaxies), allowed a clearer definition of the curves used to differentiate star-forming from AGN galaxies were improved (see Fig. 2.1). Kewley et al. (2001) set a limit to distinguish star-forming galaxies from AGNs by combining synthesis of stellar populations and photoionization models. Subsequently, Kauffmann et al. (2003a) proposed a more precise limit, which served to differentiate galaxies into three zones: star-forming galaxies and HII regions, AGN galaxies, and composite galaxies. The latter are located in between the demarcation of Kauffmann et al. (2003a) and Kewley et al. (2001). Composite galaxies have components of both star-forming and AGN objects. In the literature, there are other strict demarcations for regions with star formation (e.g. Stasińska et al. 2006). Other diagrams only considered the [NII]/Hα axis in order to differenciate HII from AGN galaxies. A clear example of this is the WHAM diagram (Cid Fernandes et al. 2011). This diagram only considered the [NII]/Hα ratio as well as the equivalent width of Hα, EW(Hα)[5], allowing us to differentiate passive from active galaxies.

1.2 The environment of galaxies

Galaxies are mostly found in pairs, small associations and groups, and also large clusters and super clusters, delineating the hierarchical structure of the Universe (e.g. Abell 1958; Zwicky et al. 1961; Karachentsev 1980; Kennicutt & Kent 1983; Karachentsev et al. 2004; Yang et al. 2007; Hao et al. 2010; Karachentsev et al. 2013), although they can also be isolated with no other galaxies close to them (e.g. Karachentseva 1973; Argudo-Fernández et al. 2015). The different size of the aforementioned galaxy aggregates show different properties (e.g. number of components, velocity dispersions, local densities) that, as we explain below, play an important role in the evolution of the galaxies.

Some of the most relevant observational evidences of the effect of the environment are:

Toomre & Toomre (1972) demonstrated that close interactions of disc galaxies could result

[4]Note that they will not have to be corrected for extinction since they will be equally affected.

[5]We defined the equivalent width of Hα as the ratio between the Hα flux and its continuum.

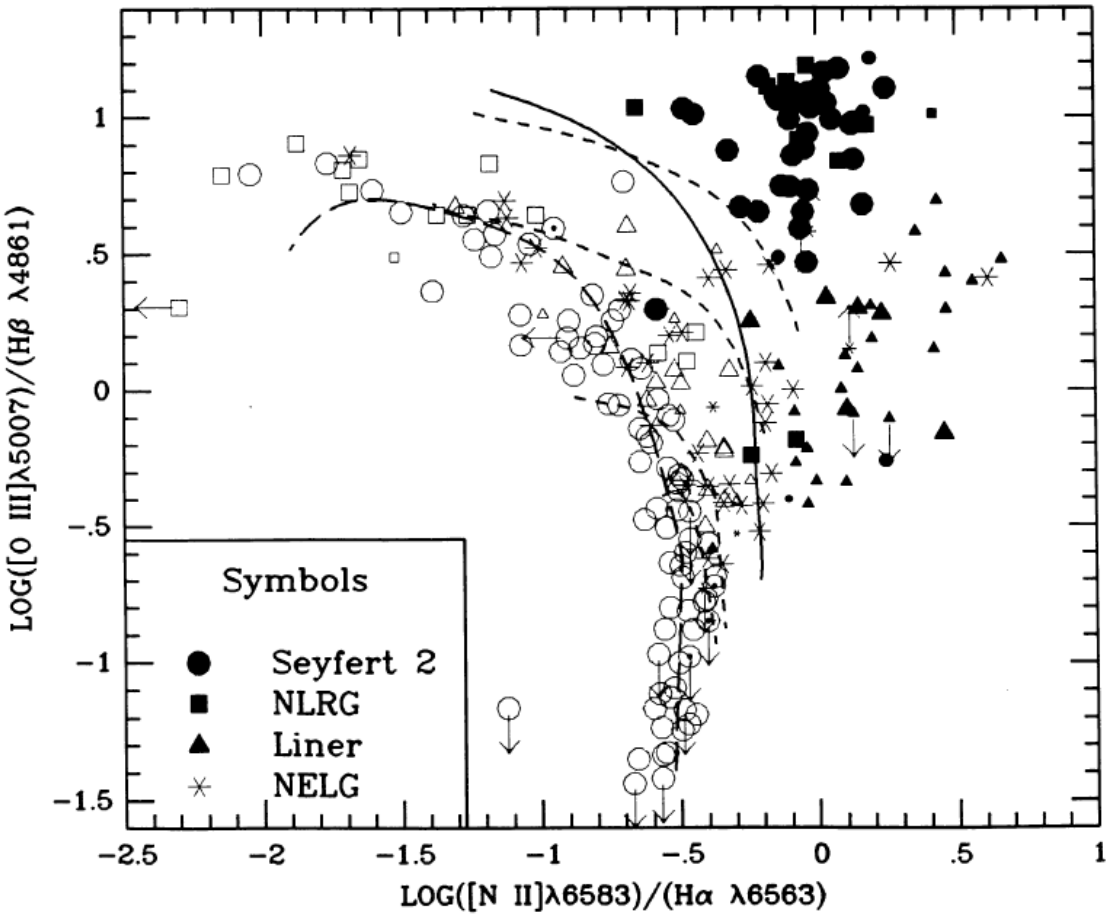

Figure 1.6: BPT diagram ([OIII]λ5007/Hβ versus [NII]λ6583/Hα) publisehd by Veilleux & Osterbrock (1987, their figure 1). The HII regions, seyfert 2, HII regions in the nucleus, starburst galaxies, LINER, HII galaxies, NLRG, NELG are shows with a empty circle, filled circle, $\odot$, empty triangle, fill triangle, empty square, fill square and a star, respectively. The short-dashed lines shows the curves for the HII regions models from Evans & Dopita (1985) for the temperatures $T_\star$=56 000, 45 000, 38 500, and 37 000 from up to bottom, respectively. The long-dashed curves show the HII region models according to McCall et al. (1985). The solid curve divides the HII regions and the AGNs.

in the disruption of discs and the formation of long tidal tails containing not only stars, but also interstellar gas, and possibly triggering starburst. In some cases, the final fate is the merging of the two galaxies into a bright elliptical galaxy (e.g. Larson 1975; White 1978).

Dressler (1980) found that the fraction of spiral galaxies in clusters decreases when the local density of galaxies increases (i.e. towards the centre of the clusters), which is known as the "morphology – density relation" (see Fig. 1.7). Similarly, the the fraction of galaxies with active star formation decreases at high local densities, which is the "star formation – density relation" (e.g. Balogh et al. 1998, 2004; Lewis et al. 2002; Gómez et al. 2003; Hwang et al. 2019). This relation seems to hold up to z~1 (Peng et al. 2010), although some authors claim a revearsal of this relation at high redshifts (e.g. Elbaz et al. 2007; Cooper et al. 2008; Hwang et al. 2019), see Fig. 1.8.

Several physical processes have been proposed to be at the origin of these observational relations:

Ram-pressure stripping: the gas is subtracted from the galaxy due to the pressure exerted by the intercluster medium on the gaseous component of the galaxy (Gunn & Gott 1972). This process is related to the additional pressure that a galaxy experiences when it moves through a hot, dense medium which is pushing it in the opposite direction to the movement of the galaxy (e.g. Singh et al. 2019).

Starvation: theoretically proposed by Larson et al. (1980) to explain the transformation of spiral to lenticular galaxies, and more widely developed by Bekki et al. (2002). The gas-rich galaxies are surrounded by a halo of hot gas which is cooled by falling on the cold gaseous component for subsequent star formation. The intergalactic medium removes the hot gas component in the cluster environment which prevents cooling and thus eliminates the future possibility of star formation processes.

Galaxy harassment: successive close encounters between galaxies at high velocities (especially if a spiral galaxy interacts with a massive galaxy) can govern galaxy evolution in the clusters, subtracting the gas and transforming the morphology of the galaxy (Moore et al. 1996).

Among the different types of galaxy aggregates, one of them stands out for its particular properties: the compact groups of galaxies. They are typically composed by 4-8 galaxies, and show local densities of galaxies of the order of the ones measured close the centers of rich clusters, but velocity dispersions similar to the ones measured for poor/loose groups, what suggest that they sould be highly unstable and eventually collapse after few crossing times. The seminal work by Hickson (1982) on the study of these structures, resulted in a catalog of 100 compact groups (HCGs), probably the most studied on this subject till nowadays. Although initially it was defined from the Palomar optical plates without any information on radial velocities, latter on Hickson et al. (1992) obtained spectra for most of the galaxies and discovered some background and foreground intruder galaxies in some of the groups. Among the 100 groups in Hickson's catalogue, it can be found Stephan's Quintet (SQ, HCG 92). This group, discovered by Stephan (1877) appears as a high concentration of galaxies in the sky with ubiquitous signs of interactions, although one of its components is a foregound galaxy (NGC7320), as pointed by a recession velocity much lower than the median of the group. SQ as been largely researched by many authors at different wavelengths: Radio (e.g. Williams et al. 2002; Lisenfeld et al. 2002, 2004; Guillard et al. 2012); Ultraviolet (e.g. Xu et al. 2005; Torres-Flores et al. 2009; de Mello et al. 2012); X-ray (e.g. Trinchieri et al. 2003, 2005; O'Sullivan et al. 2009; Heida et al. 2012); Infrared (e.g. Appleton et al. 2006, 2013, 2017; Cluver et al. 2010; Guillard et al. 2009, 2010), Visible (e.g. Moles et al. 1998; Iglesias-Páramo & Vílchez 2001; Sulentic et al. 2001; Mendes de Oliveira et al. 2001, 2004; Iglesias-Páramo et al. 2012; Trancho et al. 2012; Konstantopoulos et al. 2014; Rodríguez-Baras et al. 2014). An evolutionary study was proposed by Moles et al. (1997), suggesting that the collapse of this group could be prevented due to the continuous accretion of galaxies that enter the group injecting kinetic energy to the rest of the galaxies. The large number of interaction signatures as well as the HI distribution of SQ also support this explanation (Verdes-Montenegro et al. 2001). In our study we have focused on the complete population of star forming regions

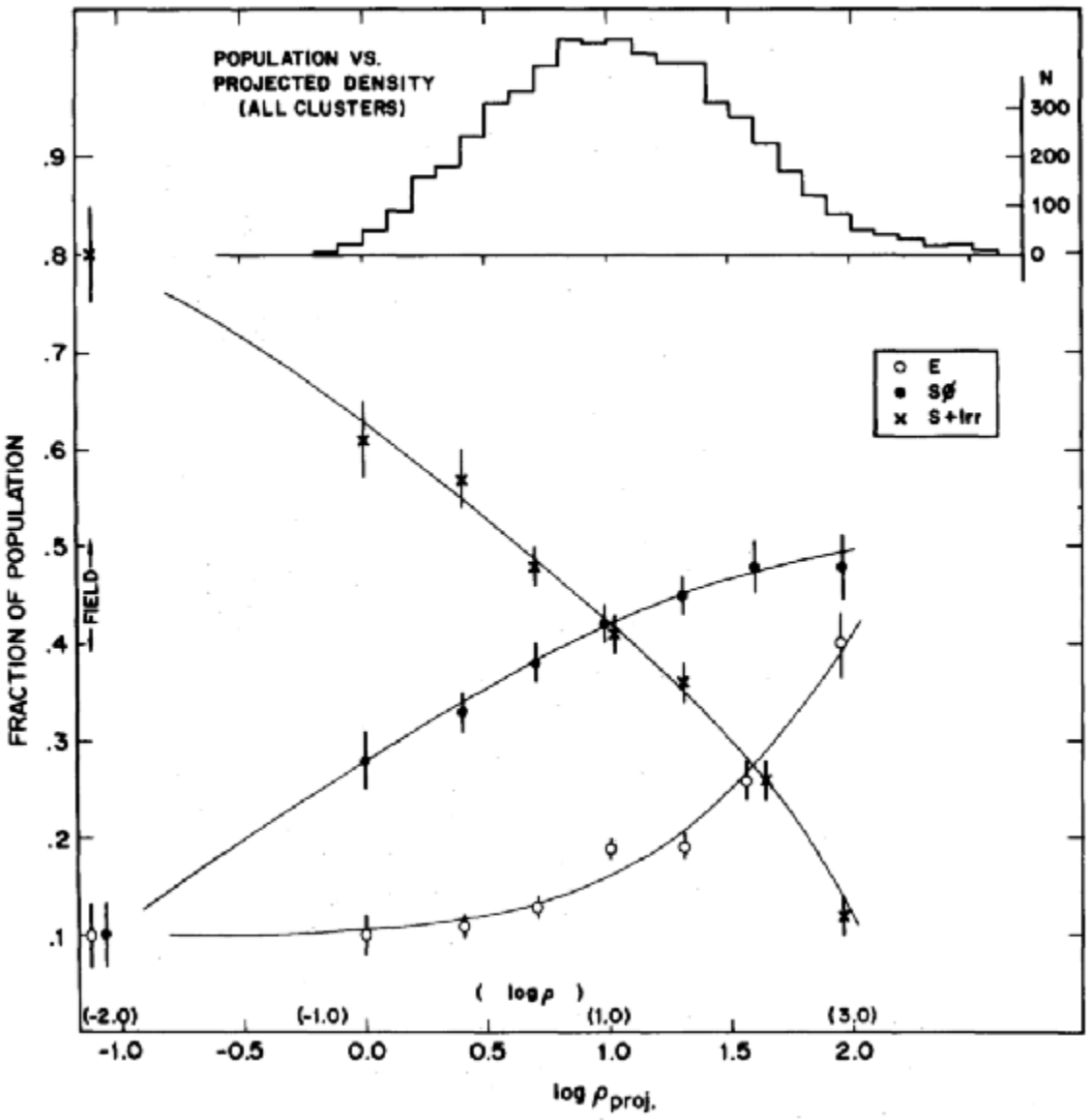

Figure 1.7: Fraction of E, S0, spiral and irregular galaxies as a function of the logarithm of the projected density, in galaxies per Mpc^{-2}. This figure has been extracted from the article Dressler (1980, their figure 4).

of SQ (many of which are found along the tidal features out of the main bodies of the galaxies) to infer the evolutionary history of SQ through the properties of its HII regions. In this study, we have taken an innovative approach to working with SQ and for this purpose we have used an unique instrument (SITELLE) that allows us to study its star formation regions thoroughly and in a spatially-resolved way.

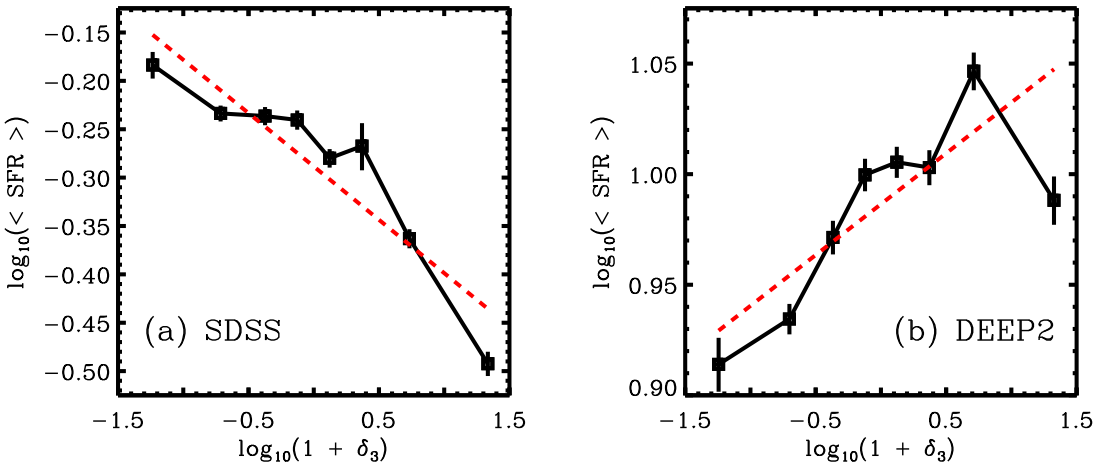

Figure 1.8: The dependence of mean SFR on environment at z ∼ 0.1 (left) and at z ∼ 1 (right). The logarithm of the mean SFR and of the error in the mean SFR in discrete bins of galaxy overdensity within the SDSS–A and DEEP2–A samples is show. The dashed red line in each plot shows a linear–regression fit to the data points. Figure 11 in Cooper et al. (2008).

1.3 Framework and scope of the thesis

This thesis intends a comprehensive study of star formation in galaxies at different scales: a) a global scale, where the whole star formation activity of galaxies is measured, irrespective of their local environment, and relations linking global properties are revisited; and b) a local scale, where a complete census of star formation regions in the compact group of galaxies SQ is performed.

Chapters 2 and 3 deal with a large sample of galaxies (209 276) with star formation from the SDSS, and from their spectra, the relations between global SFR, metallicity and stellar mass are discussed taking into account the importance of aperture corrections (Iglesias-Páramo et al. 2013, 2016); since this sample is largely dominated by field galaxies, no environmental effects are discussed.

Chapters 4 and 5 follow a different approach, and focus on a single group of galaxies, SQ, where interactions are ubiquitous. By using the imaging Fourier Transform Spectrograph (IFTs) SITELLE (Spectromètre Imageur à Transformée de Fourier pour l'Etude en Long et en Large de raies d'Emission), we perform for the first time a complete census of the star formation regions widespread around the galaxies of the group. A detailed analysis of their SFR, metallicity and kinematical properties is presented, intended to tackle on the origin and evolution of this fascinating structure.

Chapter 2

Aperture-free star formation rate of SDSS star-forming galaxies

Contents

This chapter is based on the publication:
"Aperture-free star formation rate of SDSS star-forming galaxies"
by S. Duarte Puertas, J. M. Vilchez, J. Iglesias-Páramo, C. Kehrig, E. Pérez-Montero, and F. F. Rosales-Ortega
Published in A&A, 599, A71 (2017)

A table of the aperture-corrected fluxes and SFR for ~210 000 SDSS star-forming galaxies and related relevant data is only available at the CDS via anonymous ftp to cdsarc.u-strasbg.fr (130.79.128.5) or via http://cdsarc.u-strasbg.fr/viz-bin/qcat?J/A+A/599/A71

2.1 Introduction

In the last two decades we have witnessed the revolutionary appearance of large area surveys with a huge number of galaxies observed (e.g. Sloan Digital Sky Survey (SDSS), York et al. 2000; 2dFGRS, Colless et al. 2001; VVDS, Le Fèvre et al. 2005; GAMA, Driver et al. 2011). These surveys have been very useful for performing a complete study of the non-uniform distribution of galaxies in the Universe (large-scale structure) and to understand galaxy formation and evolution. They also give us information about important properties of galaxies, such as morphology, stellar mass, star formation rate, metallicity, and dependence on the environment. These surveys used single-fibre spectroscopy with small apertures (e.g. 2" diameter for 2dFGRS and GAMA, and 3" diameter for SDSS) and therefore cover a limited region of the galaxy, thus providing partial information on the extensive properties of galaxies. For a more detailed analysis of the integrated properties of each galaxy, it is necessary to make use of integral field spectrographs (IFS, e.g. Kehrig et al. 2012, 2016). IFS surveys, such as SAURON (Bacon et al. 2001), PINGS (Rosales-Ortega et al. 2010), MASSIV (Contini et al. 2012), CALIFA (Sánchez et al. 2012; García-Benito et al. 2015), and MANGA (Bundy et al. 2015), are based on arrays of fibres and allow us to obtain information from the whole galaxy. However, the integration times necessary to observe each galaxy are long, hindering the acquisition of a large number of galaxies in comparison with that obtained from single-fibre surveys.

It is clear that to gain a better insight into the global properties of galaxies we need tools that allow us to link both single-fibre and IFS surveys. In this work we make use of one of these tools for the purpose of studying the total current star formation rate (hereafter SFR) of star-forming galaxies, using their total Hα fluxes emitted by the gas ionised by young massive stars (e.g. Kennicutt 1998b; Kennicutt et al. 2009). The SFR presents a well-known characteristic relation with the stellar mass (e.g. Brinchmann et al. 2004b). In the SFR–stellar mass plane (SFR–$M_\star$), active star-forming galaxies define a distinct sequence called main sequence (Noeske et al. 2007). In addition, less active star-forming galaxies (e.g. quenched and ageing star-forming galaxies) appear in this plane located at higher masses and lower SFR values (e.g. Renzini & Peng 2015; Casado et al. 2015; Leslie et al. 2016), as well as a family of outliers to this main sequence (MS) that are generally interpreted as starbursts driven by merging (e.g. Rodighiero et al. 2011). The MS of star formation has been parametrized by the following equation:

$$\log(\mathrm{SFR}) = \alpha \log(\mathrm{M}_\star) + \beta. \tag{2.1}$$

From a theoretical point of view, recent studies have obtained values for α (MS slope) near to unity (e.g. Dutton et al. 2010; Sparre et al. 2015; Tissera et al. 2016). Dutton et al. (2010) used a semi-analytic model of disc galaxies parametrizing several properties: for example, SFRs and metallicities were computed in a spatially resolved way as a function of galactic radius. For galaxies with stellar masses between 10^9 $M_\odot$ and 10^{11} $M_\odot$ the slope found in Dutton et al. (2010) is α = 0.96. In contrast, Sparre et al. (2015) used Illustris (state-of-the-art cosmological hydrodynamical simulation of galaxy formation; Nelson et al. 2015) to reproduce the observed star formation MS, finding a similar slope to Dutton et al. (2010) at low redshift. From observational studies quoting

Hα based SFR determinations, the MS slope varies preferentially between ~0.6 and ~1, and β between ~ -9 and ~ -3, depending on the precise methodology and data used (see e.g. Rodighiero et al. 2011; Speagle et al. 2014, and references therein). An important factor behind this spread in α and β values can be related to the aperture corrections applied to the Hα measurements.

In order to evaluate the SFR of a galaxy in single-fibre surveys, an aperture correction needs to be applied to account for the entire galaxy. This correction becomes essential in order to analyse the SFR dependence with redshift (z), especially for samples of star-forming galaxies at low z. Many such studies have dealt with the SFR of star-forming galaxies in the local Universe (e.g. Brinchmann et al. 2004b; Iglesias-Páramo et al. 2006; Salim et al. 2007; Kennicutt et al. 2008; Peng et al. 2010) and others extended to medium and large redshift (e.g. Madau et al. 1996; Elbaz et al. 2007; Peng et al. 2010; Whitaker et al. 2012; Drake et al. 2013, 2015). At lower redshift the effects produced by a fixed aperture size will be clearly more significant than for high redshifts. It is important to note that for galaxies about the size of the Milky Way, the 3-arcsec-diameter SDSS fibre never encompasses the complete galactic disc. For this reason, it is always necessary to use aperture corrections to derive the total SFR when using the SDSS Hα fluxes. An extra drawback produced by this limitation of the SDSS fibre is particularly relevant for "late-type" spiral galaxies (i.e. disc-dominated galaxies with Hubble type from Sb to Sdm, Dahlem 1997) since they present higher star formation in the outer parts of their discs. Therefore, the Hα flux measured by SDSS for these galaxies would lead to an underestimation of the total SFR.

Several studies have already emphasised the importance of quantifying the effect of aperture in the observational data (e.g. Kewley et al. 2005; Kennicutt et al. 2008; Mast et al. 2014) and also when comparing with the theoretical model predictions (Guidi et al. 2016). To our knowledge, a solid empirical aperture correction has not yet been implemented in a systematic way for the analysis of large samples of galaxies. Up to now, most studies quantifying the total SFR of galaxies from single-fibre surveys apply aperture corrections using model-based methods (e.g. Brinchmann et al. 2004b; Salim et al. 2007). Other works apply geometrical considerations in order to compensate for the unobserved Hα emission of the galaxy, scaling it according to its broad-band photometric map, or by using analytical recipes (e.g. Hopkins et al. 2003, 2013). For SDSS star-forming galaxies, Brinchmann et al. (2004b) originally corrected SDSS fibre SFRs from aperture effects using the resolved colour information available for each galaxy. In the Max-Planck-Institut für Astrophysik and Johns Hopkins University (MPA-JHU) database[1] (Kauffmann et al. 2003b; Brinchmann et al. 2004b; Tremonti et al. 2004; Salim et al. 2007) the Brinchmann et al. (2004b) methodology, improved following Salim et al. (2007), was used to derive SFRs. It is important to note that MPA-JHU galactic SFRs always include the nuclear emission. In addition, the median profiles of the growth curve corresponding to the Hα/Hβ aperture correction decreases when galaxy radius increases (Iglesias-Páramo et al. 2013). Thus, galaxies for which only the central zones are observed present overestimated extinction (Iglesias-Páramo et al. 2016, hereafter IP16): on average, some bias is expected in MPA-JHU SFRs since galaxies' extinction gradients were not accounted for (Richards et al. 2016).

A rigorous methodology to derive the total SFR of a galaxy should make use of its entire Hα

[1] Available at http://www.mpa-garching.mpg.de/SDSS/.

flux and Hα/Hβ ratio. For single-fibre surveys, the total Hα flux of a galaxy can be obtained using an empirical aperture correction for Hα derived from IFS of nearby galaxies. According to Iglesias-Páramo et al. (2013, 2016), the CALIFA project allows an accurate aperture correction for Hα to be derived empirically. IP16 provide the growth curve of Hα flux as a function of R_{50}, the Petrosian radius containing 50% of the total galaxy flux in the r-band, on the basis of a representative sample of 165 star-forming galaxies from the CALIFA survey (Sánchez et al. 2012; Husemann et al. 2013; Walcher et al. 2014). In this work we make use of the empirical aperture correction from IP16 in order to obtain the total Hα flux for a sample of ~210,000 star-forming galaxies from the SDSS. From this total Hα flux we derive aperture-corrected values of SFR in each galaxy, which will allow us to study the global relation between the SFR, stellar mass, and redshift.

To our knowledge this work represents the first attempt to analyse the behaviour of the present-day SFR for a large sample including all SDSS star-forming galaxies using the total Hα emission empirically corrected by Hα aperture coverage in a systematic manner. The structure of this chapter is organised as follows. In Sect. 2.2 we describe the data and provide a description of the methodology used to select the star-forming galaxies. We detail the methodology used to derive the entire Hα flux using the empirical aperture correction and the corresponding SFR in Sect. 2.3. Our main results are presented in Sect. 2.4 and the associated discussion in Sect. 2.6. Finally, a summary and the main conclusions of our work are given in Sect. 2.7.

Throughout the chapter, we assume a Friedman-Robertson-Walker cosmology with $\Omega_{\Lambda 0} = 0.7$, $\Omega_{m0} = 0.3$, and $H_0 = 70\,\mathrm{km\,s^{-1}\,Mpc^{-1}}$. We use the Kroupa (2001) universal initial mass function (IMF).[2]

2.2 Data and sample

2.2.1 Sample selection

Our study is based on the MPA-JHU public catalogue (Kauffmann et al. 2003b; Brinchmann et al. 2004b; Tremonti et al. 2004; Salim et al. 2007), which gives spectroscopic data of the galaxies in the Sloan Digital Sky Survey Data Release 7 (SDSS-DR7) (Abazajian et al. 2009). The SDSS spectroscopic primary sample of galaxies is complete in Petrosian r magnitude in the range $14.5 \leq r \leq 17.7$ (Strauss et al. 2002; Brinchmann et al. 2004a). We added the photometric data from the SDSS-DR12 (York et al. 2000; Alam et al. 2015) to the MPA-JHU catalogue. The MPA-JHU catalogue contains 1,477,411 objects, of which 933,310 are galaxies with spectroscopic properties. In this catalogue, the stellar masses are estimated using spectral energy distribution (SED) fitting to ugriz photometry as described in Kauffmann et al. (2003b). The line fluxes[3] are corrected for foreground Galactic reddening and extinction using the attenuation curve from O'Donnell (1994)

[2]It is necessary to multiply the Kroupa (2001) SFR estimation by 1.6 to transform from the Kroupa (2001) IMF to the Salpeter (1955) IMF and by 0.943 to transform from Kroupa (2001) to Chabrier (2003) IMF (Marchesini et al. 2009; Mannucci et al. 2010).

[3]MPA-JHU re-normalised its flux outputs to match the photometric fibre magnitude in the r-band. See the MPA-JHU website.

and the extinction from Schlegel et al. (1998). Finally, MPA-JHU provides the emission line fluxes measured using Gaussian fittings over the subtracted continuum and the signal-to-noise (S/N) in the whole spectrum. For those galaxies with multiple entries we selected only those with the largest S/N in the whole spectrum, reducing the total number of galaxies to 874,701.

We selected our primary sample according to the following criteria:

1. The galaxy stellar mass [$\log(M_\star/M_\odot)$] is selected in the range between 8.50 and 11.50. Galaxies without any estimation of the stellar mass are discarded in order to carry out a proper comparison between the SFR and the stellar mass.

2. We restricted our sample to the galaxies with small relative error of size measurements of R_{50} ($\Delta(R_{50})/R_{50} \leq 1/3$). In agreement with this consideration, we removed those galaxies with $\Delta(R_{50})/R_{50}$ greater than 1/3, which may be detrimental for our study when we use the growth curves from IP16 in order to derive the aperture corrected Hα flux (as will be explained in Sect. 2.3.1).

3. We considered galaxies with values for 1.5"/R_{50} higher than 0.3 (i.e. $R_{50} \leq$ 5"), where 1.5" is the radius of the SDSS fibre. Iglesias-Páramo et al. (2013) showed that the seeing may affect the Sérsic profile for values below this cut-off limit for the parameter 1.5"/R_{50}, according to the analytical study carried out by Trujillo et al. (2001). The full width at half maximum (FWHM) of the point spread function (PSF) has a median value of ~3.6" in the CALIFA observations (Husemann et al. 2013; Iglesias-Páramo et al. 2013).

4. We did not consider galaxies whose SDSS spectra were classified as quasi stellar objects (QSO). In the original catalogue we have found 14,476 QSO galaxies.

5. Spectroscopic redshift in the range $0.005 \leq z \leq 0.22$. The lower z-limit of 0.005 was adopted in order to: a) minimise the effect in the photometric measurements for the larger nearby galaxies; b) to include galaxies with the lowest luminosities (Brinchmann et al. 2004b). It is expected that a sizeable fraction of the low luminosity SDSS galaxies could remain unobserved for the redshift range considered (e.g. Blanton et al. 2005).

Our resulting primary sample contains 655,734 galaxies (74.97% of the original catalogue).

2.2.2 Selection of the star-forming galaxies

We selected a subset of 209,276 star-forming galaxies from our primary sample described in Sect. 2.2.1 (31.92% from our primary sample in Sect. 2.2.1) applying the following criteria:

1. The S/N is greater than three for the fluxes in the strong emission lines Hα, Hβ, [OIII], and [NII]. We have defined the S/N as the ratio of the flux and the statistical error flux, calculated with the pipeline described in Tremonti et al. (2004) (Kewley & Ellison 2008). Below this limit in S/N, an important fraction of galaxies present negative line fluxes (Brinchmann et al. 2004b).

Table 2.1: Values of relevant parameters corresponding to the median ($\pm1\sigma$ confidence interval) of the distribution for the star-forming galaxies in six redshift bins up to z=0.22 in the total sample.

(1) Δz	(2) $\log(M_\star/M_\odot)$	(3) S/N F(Hα)	(4) S/N (whole spec.)	(5) EW(Hα) [Å]	(6) R_{50} ["]	(7) # galaxies
0.005-0.05	$9.34^{+0.56}_{-0.46}$	$67.16^{+34.51}_{-29.24}$	$12.42^{+8.29}_{-5.20}$	$24.31^{+23.47}_{-11.56}$	$3.11^{+1.14}_{-1.14}$	41,883
0.05-0.08	$9.93^{+0.43}_{-0.40}$	$63.57^{+30.35}_{-23.68}$	$11.87^{+5.94}_{-4.18}$	$23.17^{+20.13}_{-10.42}$	$2.63^{+1.01}_{-0.86}$	62,616
0.08-0.11	$10.25^{+0.34}_{-0.36}$	$61.08^{+29.58}_{-22.86}$	$11.52^{+4.81}_{-3.54}$	$22.75^{+19.62}_{-10.07}$	$2.31^{+0.77}_{-0.67}$	48,178
0.11-0.14	$10.48^{+0.30}_{-0.36}$	$55.29^{+28.74}_{-21.32}$	$11.14^{+4.05}_{-3.25}$	$23.52^{+20.75}_{-10.43}$	$2.10^{+0.64}_{-0.58}$	31,084
0.14-0.18	$10.62^{+0.28}_{-0.44}$	$55.04^{+29.99}_{-22.13}$	$10.45^{+3.64}_{-3.28}$	$25.90^{+26.52}_{-11.96}$	$1.92^{+0.60}_{-0.59}$	17,465
0.18-0.22	$10.70^{+0.36}_{-0.50}$	$43.47^{+32.23}_{-20.98}$	$8.93^{+3.45}_{-3.55}$	$29.42^{+35.78}_{-14.69}$	$1.69^{+0.65}_{-0.59}$	8,050
0.005-0.22	$10.11^{+0.51}_{-0.66}$	$60.76^{+31.86}_{-24.1}$	$11.44^{+5.59}_{-3.89}$	$23.73^{+21.74}_{-10.8}$	$2.39^{+1.08}_{-0.76}$	209,276

The columns correspond to: (1) range of redshift considered; (2) median of the $\log(M_\star/M_\odot)$; (3) median of the S/N (Hα flux); (4) median of the S/N per whole spectrum range; (5) median of the EW(Hα) [Å]; (6) median of the petrosian R_{50} ["]; (7) number of galaxies.

2. We selected the pure star-forming galaxies according to the Kauffmann definition in the BPT diagnostic diagram (e.g. Baldwin et al. 1981; Veilleux & Osterbrock 1987; Kewley et al. 2001; Kauffmann et al. 2003a): [OIII]λ 5007/Hβ versus [NII]λ 6583/Hα (see Fig. 2.1):

$$\log([\mathrm{OIII}]/\mathrm{H}\beta) \leq \frac{0.61}{[\log([\mathrm{NII}]/\mathrm{H}\alpha) - 0.05]} + 1.3. \quad (2.2)$$

log([OIII]/Hβ) values below this curve imply a contribution to Hα from active galactic nuclei (AGN) less than 1%, (i.e. discarding composite or AGN galaxies; Kauffmann et al. 2003a; Brinchmann et al. 2004b).[4]

3. The Hα equivalent width (EW(Hα))[5] is greater than or equal to three. This condition is assumed to avoid passive galaxies as defined by Cid Fernandes et al. (2011).

In Table 2.1 we present the median ($\pm1\sigma$ confidence interval)[6] of several parameters split into six redshift bins within the range $0.005 \leq z \leq 0.22$. In column 1 the Δz is presented, column 2 shows the $\log(M_\star/M_\odot)$, columns 3 and 4 show the S/N for the Hα emission line flux and the S/N per whole spectrum range, respectively; the EW(Hα) is presented in column 5, column 6 displays the R_{50}, and the number of galaxies per redshift bin is quoted in column 7.

[4]Galaxies classified as AGN or composite using the SDSS fibre spectra and hosting star formation throughout their discs could be missed in the construction of the final sample.

[5]The EW(Hα) is defined as the ratio between the Hα flux and the continuum flux near to Hα. For the sake of simplicity in this work we assume |EW(Hα)|.

[6]The definition of $\pm1\sigma$ used in this work is: $+1\sigma$ = percentile 84 - median; -1σ = median - percentile 16.

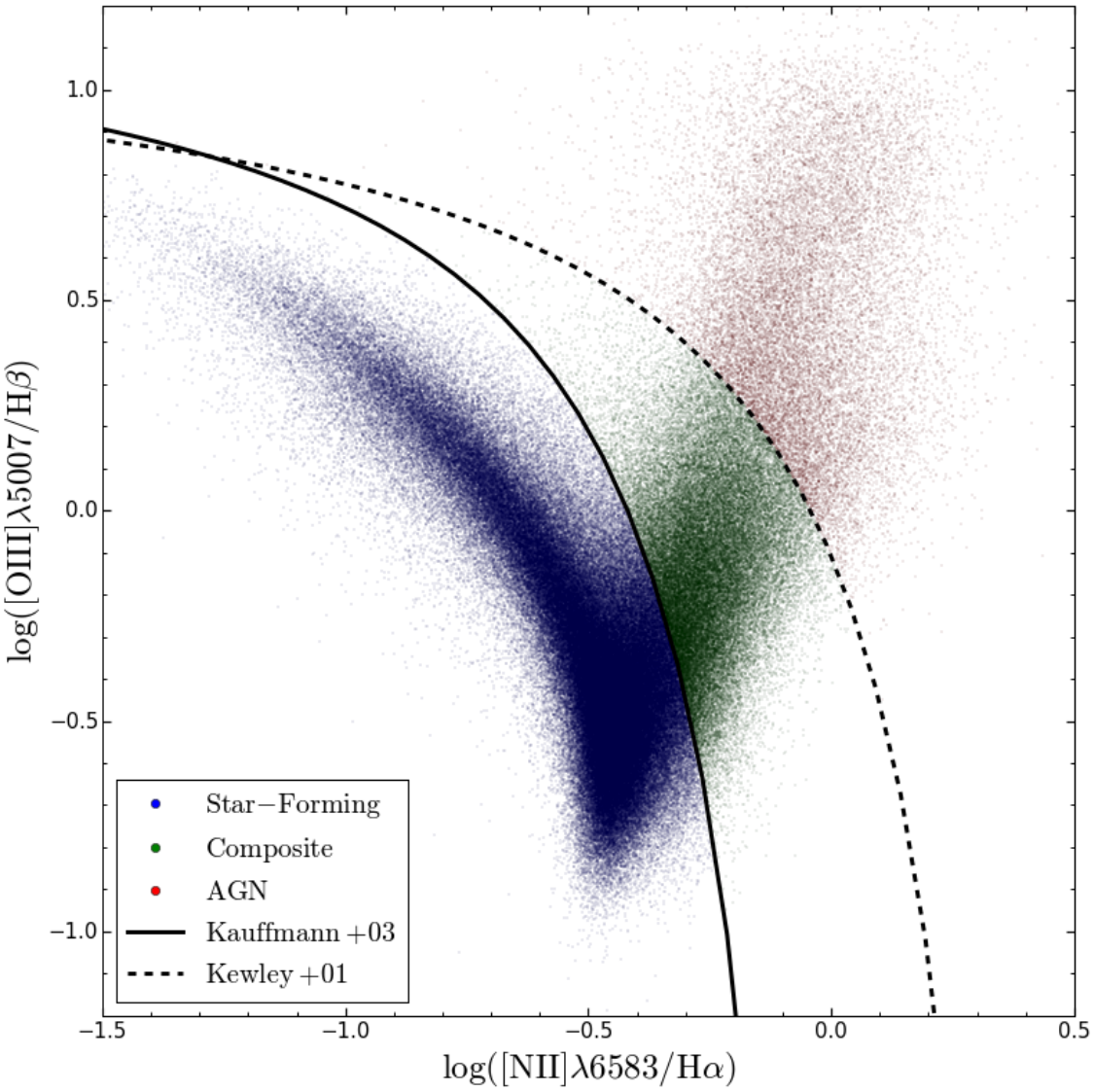

Figure 2.1: [OIII]λ 5007/Hβ versus [NII]λ 6583/Hα diagnostic diagram (BPT) for the SDSS galaxies. Blue, green, and red points represent star-forming galaxies in the present work (209,276), composite galaxies (57,926), and AGN galaxies (19,392), respectively. The dashed line shows the Kewley et al. (2001) demarcation and the continuous line shows the Kauffmann et al. (2003a) curve.

2.3 Empirical aperture correction and derivation of the SFR

2.3.1 Empirical aperture correction

The fact that SDSS fibres (3" diameter) cover only a limited region of a galaxy at low-redshift Universe ($z < 0.22$), implies that only a limited amount of Hα emission can be measured. In order to derive the total Hα flux of each galaxy in our final sample, we corrected the SDSS Hα fluxes for aperture using the empirical aperture corrections in IP16.[7] IP16 provide aperture corrections for emission lines and line ratios in a sample of spiral galaxies from the CALIFA database. Median growth curves of Hα and Hα/Hβ, up to $2.5R_{50}$, were computed to simulate the effect of observing galaxies through apertures of varying radii. The median growth curve of the Hα flux (the Hα/Hβ ratio) shows a monotonous increase (decrease) with radius, with no strong dependence on galaxy properties (i.e. inclination, morphological type, and stellar mass). The IP16 sample of CALIFA star-forming galaxies spans over the whole range in galaxy mass studied in this work (see IP16 for more details and Fig. 2.2).

To strengthen the relevance of the CALIFA star-forming galaxies sample used in this work for the analysis of SDSS star-forming galaxies, a series of tests have been performed. First, the similarity between the galaxy stellar mass distributions of both samples has been statistically confirmed applying a Kolmogorov-Smirnov (KS) test, from which the following results have been obtained: $D_{n1,n2} = 0.08$ and p-value = 0.36, indicating that we cannot reject the hypothesis that both samples are drawn from the same distribution (see Fig. 2.3). Second, the relations between SFR–$M_\star$ and galaxy size–$M_\star$ for star-forming galaxies from CALIFA and SDSS samples have been analysed (see Sect. 2.5); conclusive positive results have been achieved showing how the medians of the SFR of CALIFA galaxies are consistent with the results obtained in this work for SDSS galaxies over the whole range of galaxy mass (see Sect. 2.5). Likewise for the galaxy size–$M_\star$ relation, the plot of R_{50} vs. $M_\star$ (see Sect. 2.5) shows that the medians of CALIFA galaxies are clearly consistent with the SDSS galaxies distribution.

SDSS Hα fluxes were previously corrected for extinction using the Balmer decrement as measured by the Hα/Hβ ratio ($F_{H\alpha/H\beta}{}^{ap,\ corr}$). To do so, the median Hα/Hβ flux ratio growth curve normalised to the Hα/Hβ flux ratio at $2.5R_{50}$, $X(\alpha\beta_{50})$, was applied to each galaxy, and the Hα/Hβ ratio was computed according to its corresponding value of $1.5/R_{50}$ following IP16 (see Eq. 2.3):

$$F_{H\alpha/H\beta}{}^{ap,\ corr} = \frac{F_{H\alpha/H\beta}{}^{0}}{X(\alpha\beta_{50})} \tag{2.3}$$

being

$X(\alpha\beta_{50}) = 0.0143x^5 - 0.1091x^4 + 0.2959x^3 - 0.3125x^2 + 0.0274x + 1.1253$,

where $x = (1.5/R_{50})$ for each galaxy, $F_{H\alpha/H\beta}{}^{0}$ is the SDSS Hα/Hβ ratio.

Theoretical case B recombination was assumed (the theoretical Balmer decrement, $I_{H\alpha/H\beta} = 2.86$; $T = 10^4$ K, and low-density limit $n_e \sim 10^2$ cm^{-3}; Osterbrock 1989; Storey & Hummer 1995) together with the Cardelli et al. (1989) extinction curve with $R_v = A_v/E(B-V) = 3.1$ (O'Donnell 1994; Schlegel et al. 1998).

[7] For those galaxies in the final sample with $1.5/R_{50} \geq 2.5$ (172 objects) aperture correction of the Hα flux was applied according to Fig. 2 in IP16.

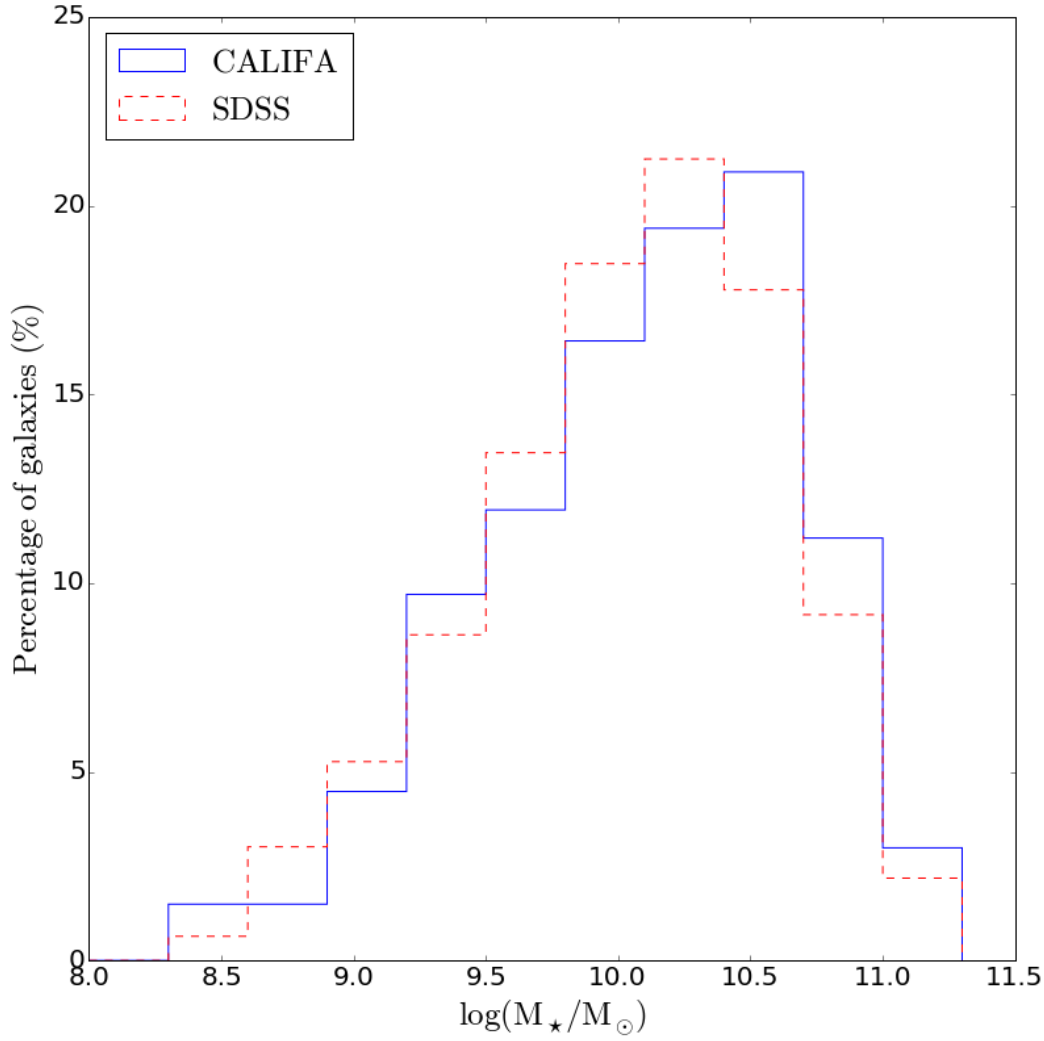

Figure 2.2: Distributions of the stellar mass, in percentage, of SDSS star-forming galaxies (red dashed line) and IP16 CALIFA star-forming galaxies (blue solid line).

Equation 2.4 presents the aperture-corrected Hα flux, $F_{H\alpha}^{ap,\ corr}$, as a function of the Hα flux in the SDSS fibre, $F_{H\alpha}^{0}$, and the X(α_{50}), the median Hα flux growth curve normalised to the Hα flux at 2.5R_{50}:

$$F_{H\alpha}^{ap,\ corr} = \frac{F_{H\alpha}^{0}}{X(\alpha_{50})} \tag{2.4}$$

being

$X(\alpha_{50}) = 0.0037x^5 + 0.0167x^4 - 0.2276x^3 + 0.5027x^2 + 0.1599x$

where $x = (1.5/R_{50})$ for each galaxy. According to IP16, for an aperture radius of 2.5R_{50} an average of $\sim$ 85% of the total Hα flux of (non-AGN) spiral galaxies is enclosed.

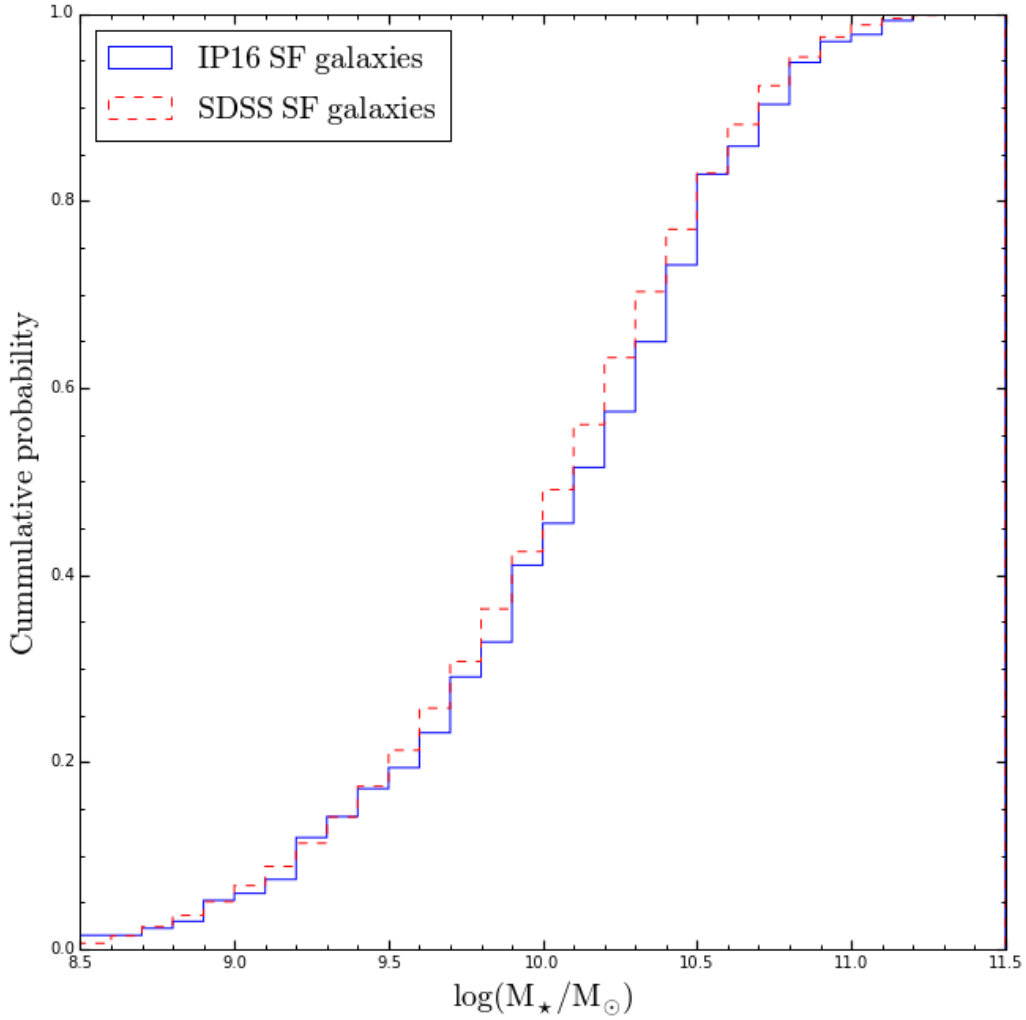

Figure 2.3: Cumulative distributions of $M_\star$ for the IP16 star-forming galaxies (blue solid line) and SDSS star-forming galaxies (red dashed line) used in the Kolmogorov-Smirnov two-sample test.

Equation 2.5 presents the total Hα flux, $F^{tot}_{H\alpha}$, corrected for aperture effects and extinction:

$$F^{tot}_{H\alpha} = \frac{F^{ap,\ corr}_{H\alpha}}{10^{-0.4\,A(H\alpha)}} \tag{2.5}$$

, where the extinction in Hα, $A(H\alpha) = 1.758\,c(H\beta)$. The reddening coefficient is $c(H\beta) = -\frac{1}{f(H\alpha)} \log\left(\frac{F_{H\alpha/H\beta}{}^{ap,\ corr}}{I_{H\alpha/H\beta}}\right)$, and $f(H\alpha)$ is the reddening curve.

2.3.2 Aperture-corrected star formation rate

The present day SFR is defined as the stellar mass formed per unit time traced by the young stars. The SFR can be derived from the Hα luminosity, and it is parametrized as $SFR = L(H\alpha)/\eta_{H\alpha}$,

the ratio of observed Hα luminosity[8] to the conversion factor $\eta_{H\alpha}$ (Brinchmann et al. 2004b). The parameter $\eta_{H\alpha}$ varies with the physical properties of the galaxy, total stellar mass, and metallicity (see Charlot et al. 2002; Hirashita et al. 2003; Brinchmann et al. 2004b).

Kennicutt et al. (2009) assumed $\eta_{H\alpha}$ is a constant value, $\eta_{H\alpha} = 10^{41.26}$ erg/s/$M_\odot$/yr, which resulted in a good typical conversion factor, though $\eta_{H\alpha}$ can in fact vary as much as ~0.4 dex going from the least to the most massive galaxies (Brinchmann et al. 2004b). In order to parametrize the variation of the $\eta_{H\alpha}$ as a function of stellar mass, we have used the median of the $\eta_{H\alpha}$ likelihood distribution for the five stellar mass ranges as shown in fig. 7 in Brinchmann et al. (2004b): $\log(M_\star/M_\odot) < 8$; $8 < \log(M_\star/M_\odot) < 9$; $9 < \log(M_\star/M_\odot) < 10$; $10 < \log(M_\star/M_\odot) < 11$; $\log(M_\star/M_\odot) > 11$. The relation between $\eta_{H\alpha}$ and galaxy stellar mass has been parametrized through a two-order polynomial fit as presented in Eq. 2.6:

$$\log(\eta_{H\alpha_{adj}}) = -0.011\,x^2 + 0.124\,x + 41.107, \tag{2.6}$$

where $x = \log(M_\star/M_\odot)$.

We used the values of $\eta_{H\alpha}$ from Eq. 2.6 to calculate the SFR = L(Hα)/$\eta_{H\alpha}$ for our galaxy sample. Hereafter, we refer to the aperture-corrected $\log(SFR) - \log(M_\star)$ relation as the SFR–$M_\star$ relation for our sample of galaxies. Also, from now on we refer to the SFR and the specific SFR (sSFR = SFR/$M_\star$) derived here as the empirical aperture-corrected SFR and sSFR for star-forming galaxies.

Notwithstanding the above, possible effects associated with, for example, diffuse ionised gaseous emission, geometry, or galaxy inclination should be considered (e.g. Relaño et al. 2006; Kennicutt et al. 2009; Kennicutt & Evans 2012; van der Wel et al. 2014). Although a comprehensive study of these effects could be hard to handle (e.g. Kennicutt & Evans 2012), recent work by Iglesias-Páramo et al. (2013, 2016) concluded that the Hα flux growth curve and the Hα/Hβ are insensitive to the galaxy inclination for a broad range of b/a (i.e. galaxy diameters ratio) including from edge-on to face-on galaxies. The effects of the geometry of the HII regions and the contribution of the diffuse ionised gas component are more difficult to quantify. We believe that these effects should be statistically minimised in this work, given the size of the sample and the large diversity of galaxy types used in IP16.

2.4 Results

2.4.1 Extinction of the star-forming galaxies in the SDSS sample

The extinction suffered by the Hα photons, A(Hα), derived in this work goes from 0 to 2 mag, with a median of A(Hα) = 0.85 mag[9] (in agreement with previous work: Buat et al. 2002; Hopkins et al. 2003; Brinchmann et al. 2004b; Nakamura et al. 2004; Momcheva et al. 2013). A(Hα) presents

[8] The Hα luminosity of a galaxy is $L(H\alpha) = 4\pi\, d^2\, F^{tot}_{H\alpha}$, d being its luminosity distance corresponding to the SDSS spectroscopic redshift.

[9] ~ 4% of galaxies in our sample present negative values of A(Hα), though consistent with A(Hα) = 0 mag within the errors. For these galaxies the value of A(Hα) has been set to zero.

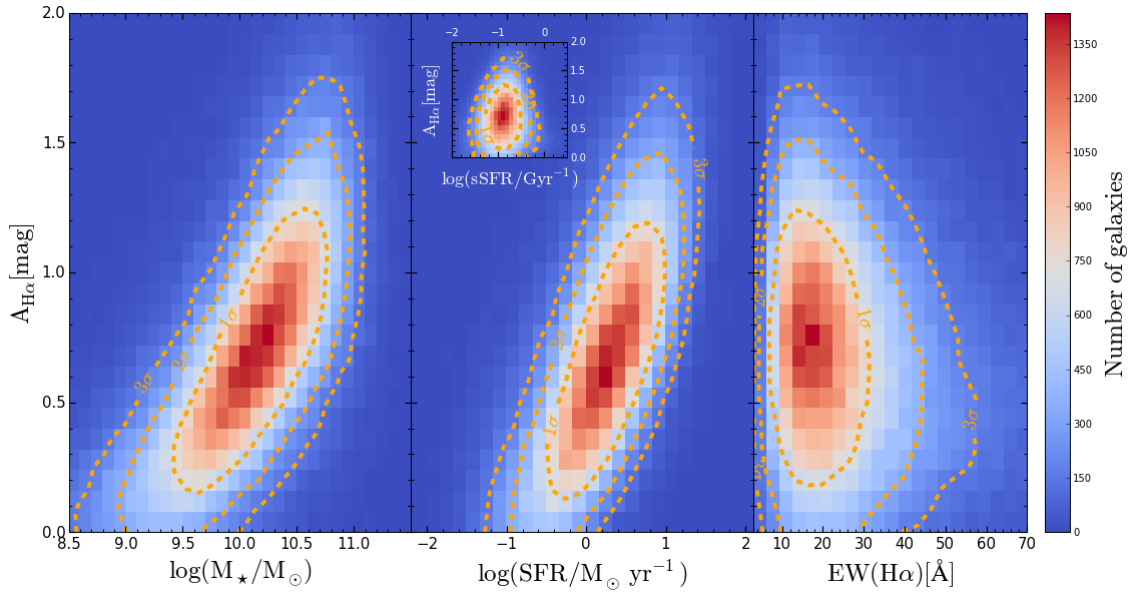

Figure 2.4: Density plots for the SDSS star-forming galaxies: i) Left panel: the relation between $\log(M_\star/M_\odot)$ and A(Hα); ii) Central panel: the relation between $\log(SFR/M_\odot\,yr^{-1})$ and A(Hα), the inset plot shows the A(Hα)-$\log(sSFR/Gyr^{-1})$ relation; iii) Right panel: the relation between EW(Hα) and A(Hα). The dashed lines represent the 1σ, 2σ, and 3σ contours.

a strong dependence with galaxy mass, as shown in Fig. 2.4 (left panel), being larger for more massive galaxies, (see Brinchmann et al. 2004b; Whitaker et al. 2012; Momcheva et al. 2013; Koyama et al. 2015). Moreover, A(Hα) shows a trend with the SFR, with A(Hα) $\leq$ 0.2 mag for those galaxies presenting the lowest SFR ($\log(SFR/M_\odot\,yr^{-1}) \approx -0.5$) whereas the highest values of A(Hα) are associated with the galaxies with the largest SFR (Fig. 2.4 central panel). Only a mild trend can be appreciated when A(Hα) is plotted versus the sSFR, confirming the strong weight that galaxy stellar mass has in the variation of A(Hα). The behaviour of A(Hα) as a function of EW(Hα) is shown in Fig. 2.4 (right panel). Galaxies showing the median value of A(Hα) cluster around EW(Hα) $\sim$ 15Å. For EW(Hα) $>$ 30Å, A(Hα) presents a strong decline, approximating to values near 0.2 mag and lower for EW(Hα) above 60Å. An upper envelope for the maximum of the A(Hα) can be seen, decreasing towards larger values of EW(Hα).

The results presented above tell us that the A(Hα) extinction correction can be substantial and therefore must be applied to all galaxy samples to be used in the study of the SFR. Moreover, these results also show that the behaviour of A(Hα) appears to be different depending on the EW(Hα) of star-forming galaxies, showing a strong relation with galaxy mass and total SFR (see e.g. Koyama et al. 2015).

2.4.2 Parametrizing the aperture-corrected SFR–$M_\star$ relation for star-forming galaxies

In Fig. 2.5 we present the aperture-corrected SFR–$M_\star$ relation for our sample of star-forming galaxies (see Sect. 2.2.2). The SDSS fibre flux for each galaxy was corrected for aperture and

extinction as explained in Sect. 2.3.1. The SFR was derived for each galaxy of the sample applying the methodology described in Sect. 2.3.2. The running median of the distribution of points plotted in Fig. 2.5 (red solid line) has been fitted with the following analytical expression:

$$\log(\mathrm{SFR}(\mathrm{H}\alpha)) = -0.03105\mathrm{x}^3 + 0.892\mathrm{x}^2 - 7.571\mathrm{x} + 17.71, \tag{2.7}$$

where $\mathrm{x} = \log(\mathrm{M}_\star/\mathrm{M}_\odot)$.

For the sake of comparison with previous work (see Sect. 2.6), a straight linear fit to the running median distribution in Fig. 2.5 has been obtained as follows:

$$\log(\mathrm{SFR}) = \alpha\mathrm{x} + \beta, \tag{2.8}$$

where slope $\alpha = 0.935(\pm0.001)$, $\beta = -9.208(\pm0.001)$, and $\mathrm{x} = \log(\mathrm{M}_\star/\mathrm{M}_\odot)$.

Figure 2.5 also shows the three-order polynomial fit to the running median of the values of SFR computed from the SDSS fibre flux without any correction by aperture (green dashed line). It is clear from Fig. 2.5 that the corrected SFR is, on average, more than 0.65 dex above the values corresponding to the SDSS fibre flux. The SFR–$\mathrm{M}_\star$ relation obtained is consistent with the relation shown by Catalán-Torrecilla et al. (2015) for their sample of star-forming galaxies of the CALIFA survey (see Fig. 2.8).

The inset plot shows the sSFR–$\mathrm{M}_\star$ relation for our sample, corrected for aperture and extinction. The fits to the running medians of the aperture-corrected sSFR–$\mathrm{M}_\star$ (red solid line) and the SDSS fibre fluxes (green dashed line) are also shown. From the sSFR–$\mathrm{M}_\star$ relation, we observe that the fit to the running median distribution is decreasing slightly for the entire stellar mass range selected, consistent with recent predictions (see e.g. Sparre et al. 2015, and references therein).

For the sake of completeness, in Table 2.2 we present median values ($\pm1\sigma$ confidence interval) of the derived log(SFR) for twelve stellar mass bins ($\Delta\log(\mathrm{M}_\star/\mathrm{M}_\odot) = 0.25$ dex each) within the range $8.5 \leq \log(\mathrm{M}_\star/\mathrm{M}_\odot) \leq 11.5$. In column 1 the range of $\log(\mathrm{M}_\star/\mathrm{M}_\odot)$ is presented, column 2 shows the $\log(\mathrm{SFR}/\mathrm{M}_\odot\,\mathrm{yr}^{-1})$, and the number of galaxies per stellar mass bin is quoted in column 3.

2.4.3 Aperture-corrected SFR as a function of the $M_\star$ and z interval

The aperture-corrected SFR as a function of the $\mathrm{M}_\star$ is studied in six redshift bins in the range $0.005 \leq \mathrm{z} \leq 0.22$. Figure 2.6 presents this evolution for the star-forming galaxy sample in the following redshift intervals: $0.005 \leq \mathrm{z} < 0.05$, $0.05 \leq \mathrm{z} < 0.08$, $0.08 \leq \mathrm{z} < 0.11$, $0.11 \leq \mathrm{z} < 0.14$, $0.14 \leq \mathrm{z} < 0.18$, and $0.18 \leq \mathrm{z} \leq 0.22$. In this figure, for each z range, the corresponding line is the fit to the running median of the differences between the aperture-corrected SFR and the SFR within the SDSS fibre as a function of the $\mathrm{M}_\star$.

This figure shows that: i) over the whole range of galaxy stellar masses studied, the average aperture correction goes from ~0.7 to ~0.8 for $0.005 \leq \mathrm{z} \leq 0.05$; ii) aperture corrections increase with galaxy mass for each redshift interval for $0.05 \leq \mathrm{z} \leq 0.22$; reaching from ~0.2 for $\log(\mathrm{M}_\star/\mathrm{M}_\odot) = 10$ to ~0.6 for $\log(\mathrm{M}_\star/\mathrm{M}_\odot) = 11$, for $0.18 \leq \mathrm{z} \leq 0.22$.

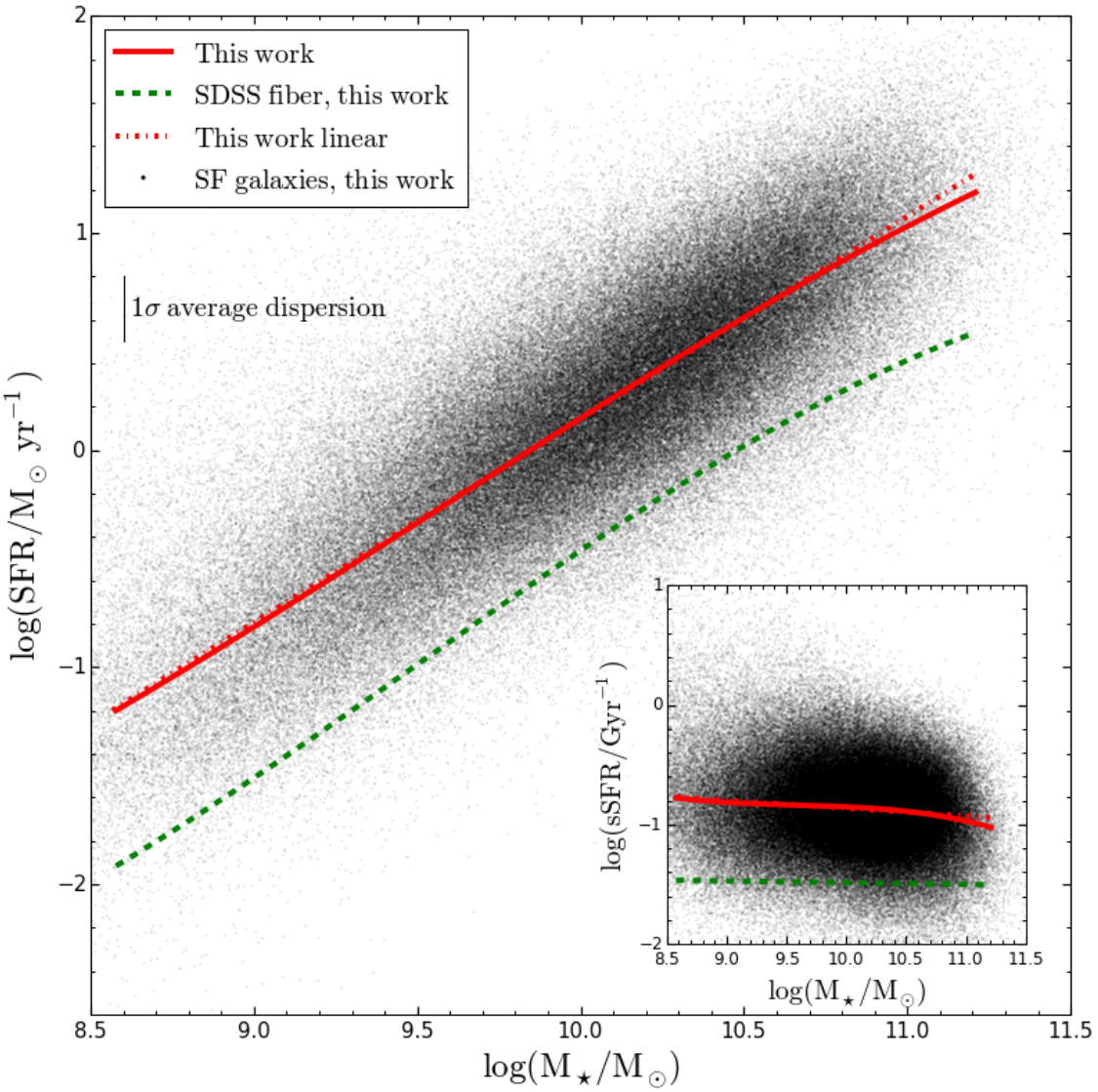

Figure 2.5: Relation between the SFR and $M_\star$ for star-forming galaxies. The red solid line and green dashed line represent the fit to the running median for bins of 2,000 objects in this work and in the SDSS fibre, respectively. The red dotted line represents the linear fit to the running median for bins of 2,000 objects in this work. The vertical black line shows the 1σ average dispersion (~ 0.3 dex). The inset plot shows the sSFR–$M_\star$ relation for our sample and the running median, for bins of 2,000 objects, for the sSFR corrected for aperture (red solid line) and inside the SDSS fibre (green dashed line).

Table 2.2: Values of aperture-corrected SFR corresponding to the median ($\pm 1\sigma$ confidence interval) of the distribution for the star-forming galaxies in twelve stellar mass bins in the total sample.

(1) $\Delta\log(M_\star/M_\odot)$	(2) $\log(SFR/M_\odot\,yr^{-1})$	(3) # galaxies
8.50-8.75	$-1.11^{+0.56}_{-0.42}$	3,926
8.75-9.00	$-0.94^{+0.49}_{-0.40}$	6,724
9.00-9.25	$-0.69^{+0.43}_{-0.40}$	10,397
9.25-9.50	$-0.45^{+0.41}_{-0.38}$	15,405
9.50-9.75	$-0.19^{+0.38}_{-0.36}$	22,512
9.75-10.00	$0.03^{+0.36}_{-0.34}$	29,989
10.00-10.25	$0.26^{+0.35}_{-0.34}$	35,854
10.25-10.50	$0.49^{+0.33}_{-0.35}$	36,230
10.50-10.75	$0.71^{+0.33}_{-0.35}$	28,016
10.75-11.00	$0.92^{+0.33}_{-0.37}$	14,986
11.00-11.25	$1.08^{+0.33}_{-0.37}$	4,563
11.25-11.50	$1.19^{+0.38}_{-0.40}$	674
8.50-11.50	$0.23^{+0.58}_{-0.69}$	209,276

The columns correspond to: (1) range of $\log(M_\star/M_\odot)$; (2) median value of $\log(SFR/M_\odot\,yr^{-1})$ and error value; (3) number of galaxies.

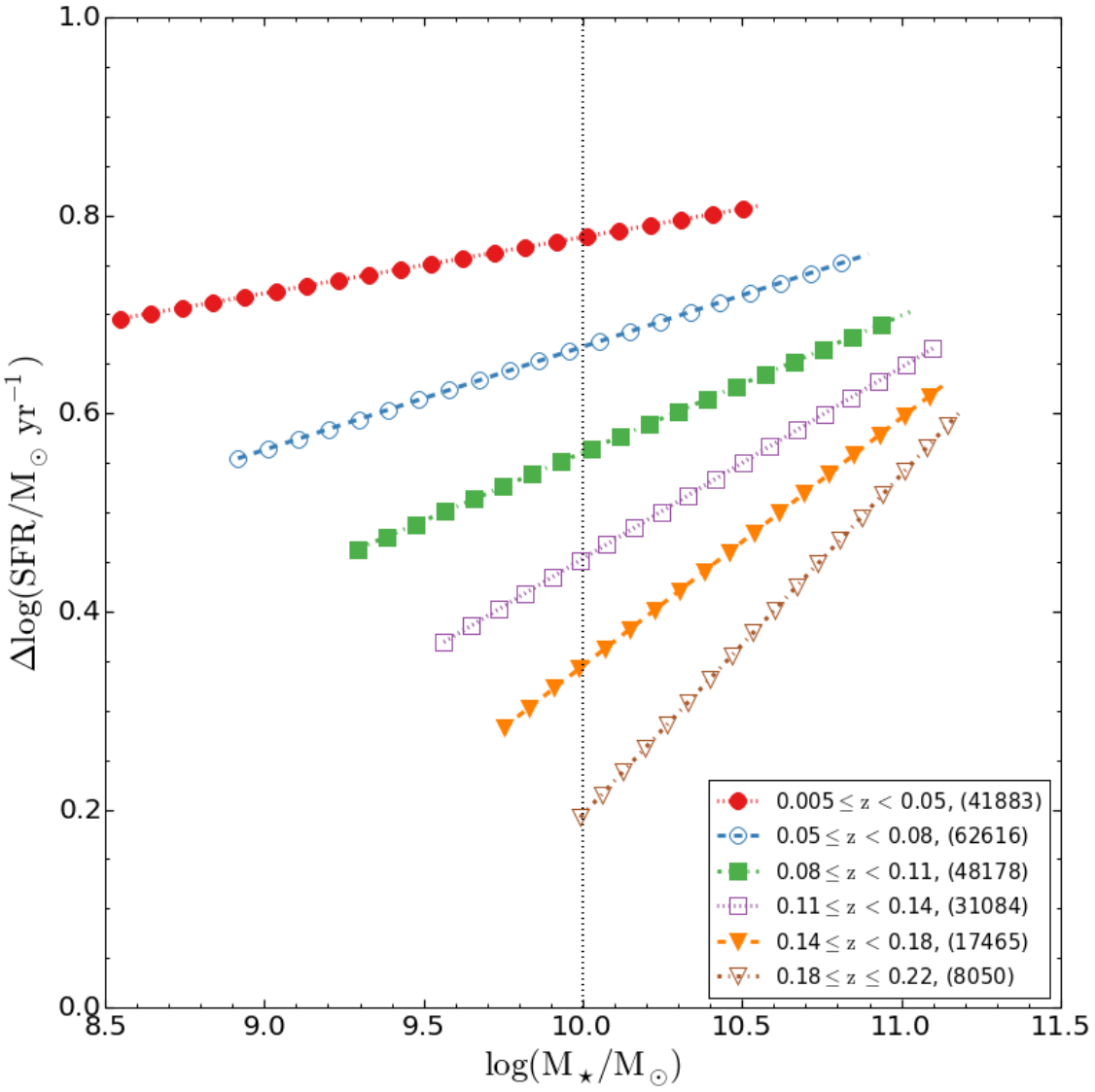

Figure 2.6: The empirical SFR corrections (total - SDSS fibre) vs. $M_\star$ relation. Red, blue, green, magenta, orange, and gold lines represent the fit to the running median for bins of 1,000 objects in six redshift bins up to z = 0.22 for a sample of star-forming galaxies. The numbers of star-forming galaxies in each redshift bin appear on the legend. The vertical black dotted line corresponds to the reference value at $\log(M_\star/M_\odot) = 10$.

In Table 2.3, for each z range, we present the median ($\pm 1\sigma$ confidence interval) of the derived $\log(SFR/M_\odot\,yr^{-1})$ and $\log(M_\star/M_\odot)$ along three stellar mass bins and for the whole mass range ($8.5 \leq \log(M_\star/M_\odot) \leq 11.5$) for six redshift bins in the range $0.005 \leq z \leq 0.22$. In column 1 the Δz is displayed, the $\Delta\log(M_\star/M_\odot)$ is presented in column 2, column 3 shows the $\log(SFR/M_\odot\,yr^{-1})$, column 4 shows the $\log(M_\star/M_\odot)$, and the number of galaxies per stellar mass bin is quoted in column 5. All this information is presented in Fig. 2.7 for the sample of galaxies in the range of redshift and stellar mass considered. In this figure we show the relation between total SFR and $M_\star$ for our sample of star-forming galaxies, along three stellar mass bins for the whole mass range ($8.5 \leq \log(M_\star/M_\odot) \leq 11.5$), and for six redshift bins in the range $0.005 \leq z \leq 0.22$.

2.5 The SFR–$M_\star$ and galaxy size–$M_\star$ relations of SDSS and CALIFA star-forming galaxies

In order to strengthen the relevance between CALIFA and SDSS galaxies, we have compared CALIFA star-forming galaxies in the SFR–$M_\star$ and size–$M_\star$ diagrams with the SDSS galaxies (Figs. 2.8 and 2.9, respectively). Figure 2.8 shows the SFR–$M_\star$ for SDSS and CALIFA star-forming galaxies. The SFRs values for the CALIFA galaxies were computed consistently following the methodology presented in Sect. 2.3.2 of this work, using the data for the star-forming galaxies in Catalán-Torrecilla et al. (2015, private communication). The linear fit to the running median of the aperture-corrected SFR–$M_\star$ distribution for the complete sample ($0.005 \leq z \leq 0.22$), and for the first redshift range considered ($0.005 \leq z < 0.05$) are shown, together with the median values of SFR and $M_\star$ along five stellar mass bins for CALIFA star-forming galaxies; equitable number of galaxies have been considered in each bin.

Figure 2.9 shows the size–$M_\star$ for SDSS and CALIFA star-forming galaxies. The linear fit to the running median of the size–$M_\star$ distribution for the complete sample ($0.005 \leq z \leq 0.22$) and the median values of size and $M_\star$ along five stellar mass bins for CALIFA star-forming galaxies are shown; equitable number of galaxies have been considered in each bin.

From the figures we can see that the median values of the SFR of CALIFA galaxies are representatives with the results obtained in this work for (nearby $0.005 \leq z < 0.05$) SDSS galaxies over the whole range of galaxy mass. Likewise, the median values of the galaxy size of CALIFA galaxies are visibly consistent with the SDSS galaxies distribution. Taking into account these results, we can consider CALIFA star-forming galaxies as representative of the SDSS star-forming galaxies sample used in this work.

2.6 Discussion

We start by comparing our SFR values (Sect. 2.3.2) with the ones provided by the MPA-JHU database.[10] The MPA-JHU database gives the SFR within the 3" fibre of the SDSS and the total SFR corrected for aperture (Brinchmann et al. 2004b; Salim et al. 2007) (hereafter SFR_{MPA}).

[10] A total of 4,566 star-forming galaxies from our final sample are not considered since the MPA-JHU database provided -9999 for their SFR values.

Table 2.3: Values of stellar mass and aperture-corrected SFR per stellar mass and redshift bins corresponding to the median ($\pm 1\sigma$ confidence interval) of the distribution for the star-forming galaxies in the total sample.

(1)	(2)	(3)	(4)	(5)
Δz	$\Delta \log(M_\star)$	log(SFR)	$\log(M_\star)$	# galaxies
	8.50-9.50	$-0.79^{+0.42}_{-0.45}$	$9.10^{+0.27}_{-0.33}$	25,872
0.005-0.05	9.50-10.50	$-0.14^{+0.44}_{-0.42}$	$9.82^{+0.34}_{-0.23}$	15,354
	10.50-11.50	$0.63^{+0.39}_{-0.47}$	$10.62^{+0.16}_{-0.10}$	657
	8.50-11.50	$-0.55^{+0.58}_{-0.54}$	$9.34^{+0.56}_{-0.46}$	41,883
	8.50-9.50	$-0.35^{+0.37}_{-0.39}$	$9.35^{+0.11}_{-0.22}$	8,775
0.05-0.08	9.50-10.50	$0.04^{+0.39}_{-0.37}$	$9.96^{+0.32}_{-0.29}$	48,229
	10.50-11.50	$0.64^{+0.37}_{-0.38}$	$10.64^{+0.18}_{-0.10}$	5,612
	8.50-11.50	$0.03^{+0.45}_{-0.42}$	$9.93^{+0.43}_{-0.40}$	62,616
	8.50-9.50	$-0.04^{+0.42}_{-0.57}$	$9.34^{+0.11}_{-0.22}$	1,265
0.08-0.11	9.50-10.50	$0.29^{+0.33}_{-0.34}$	$10.16^{+0.22}_{-0.29}$	35,641
	10.50-11.50	$0.67^{+0.36}_{-0.36}$	$10.66^{+0.20}_{-0.12}$	11,272
	8.50-11.50	$0.36^{+0.39}_{-0.37}$	$10.25^{+0.34}_{-0.36}$	48,178
	8.50-9.50	$0.22^{+0.45}_{-0.50}$	$9.38^{+0.09}_{-0.18}$	351
0.11-0.14	9.50-10.50	$0.53^{+0.29}_{-0.37}$	$10.28^{+0.16}_{-0.31}$	16,143
	10.50-11.50	$0.78^{+0.33}_{-0.33}$	$10.69^{+0.21}_{-0.14}$	14,590
	8.50-11.50	$0.64^{+0.34}_{-0.37}$	$10.48^{+0.30}_{-0.36}$	31,084
	8.50-9.50	$0.60^{+0.37}_{-0.55}$	$9.40^{+0.07}_{-0.15}$	136
0.14-0.18	9.50-10.50	$0.63^{+0.36}_{-0.45}$	$10.23^{+0.20}_{-0.30}$	6,292
	10.50-11.50	$0.95^{+0.31}_{-0.31}$	$10.77^{+0.21}_{-0.17}$	11,037
	8.50-11.50	$0.85^{+0.34}_{-0.41}$	$10.62^{+0.28}_{-0.44}$	17,465
	8.50-9.50	$1.06^{+0.24}_{-0.68}$	$9.42^{+0.07}_{-0.13}$	53
0.18-0.22	9.50-10.50	$0.69^{+0.39}_{-0.40}$	$10.25^{+0.17}_{-0.25}$	2,931
	10.50-11.50	$1.12^{+0.31}_{-0.34}$	$10.90^{+0.23}_{-0.25}$	5,066
	8.50-11.50	$0.99^{+0.36}_{-0.46}$	$10.70^{+0.36}_{-0.50}$	8,050

The columns correspond to: (1) range of z considered; (2) range of $\log(M_\star/M_\odot)$; (3) median value of the $\log(SFR/M_\odot\ yr^{-1})$ and error value; (4) median value of the $\log(M_\star/M_\odot)$ and error value; (5) number of galaxies.

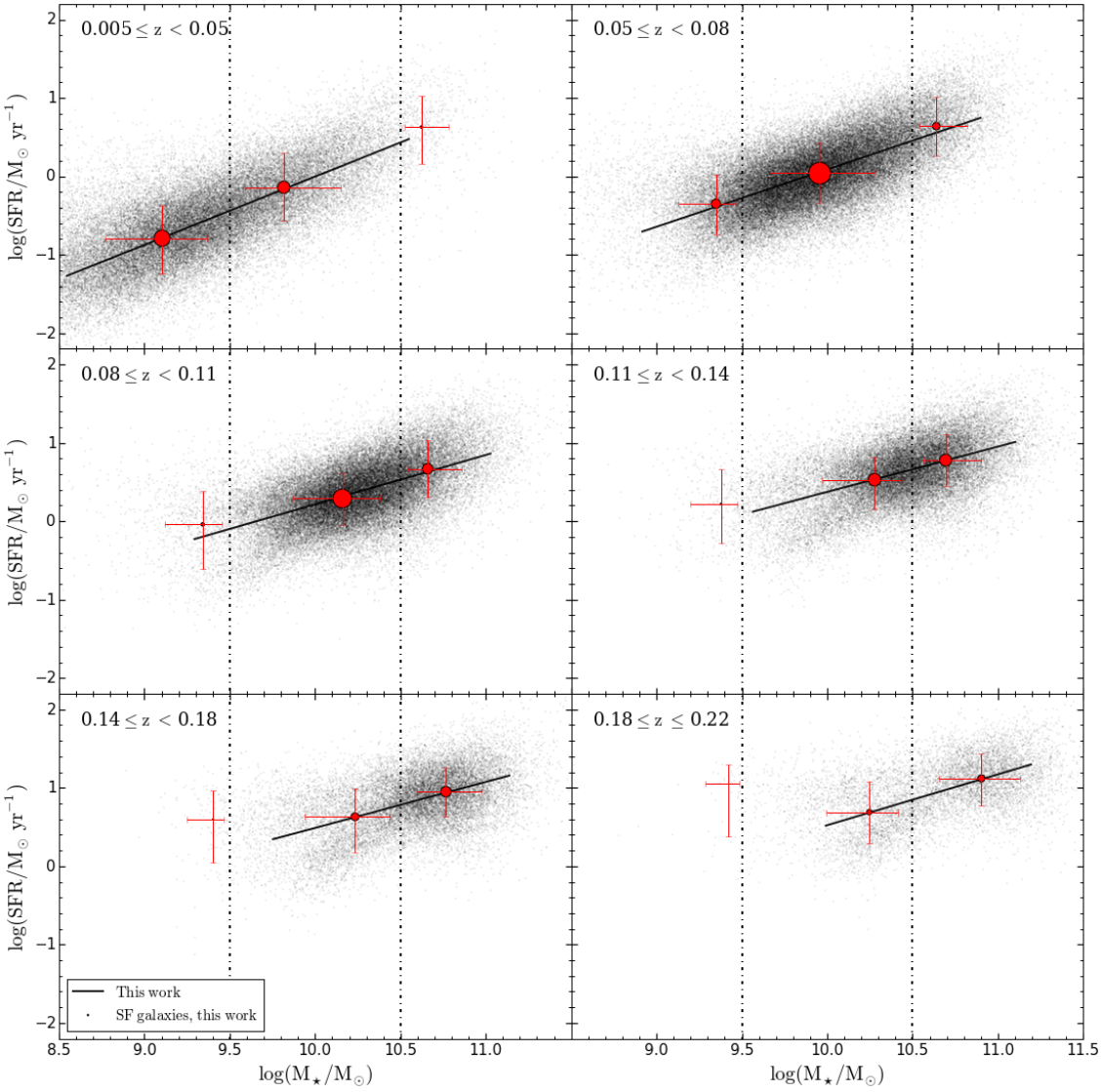

Figure 2.7: Relation between the SFR and $M_\star$ for SDSS star-forming galaxies, along three stellar mass bins for the whole mass range ($8.5 \leq \log(M_\star/M_\odot) \leq 11.5$) and for six redshift ranges in the range $0.005 \leq z \leq 0.22$. The black solid line represents the fit to the running median for bins of 1,000 objects in this work for each redshift range. Red dots represent the medians of SFR and $M_\star$ per stellar mass bin and redshift range. The error bars in x- and y-axis represent the $\pm 1\sigma$ confidence interval for stellar mass and SFR, respectively. The symbol sizes increase with the number of objects contained in each mass range.

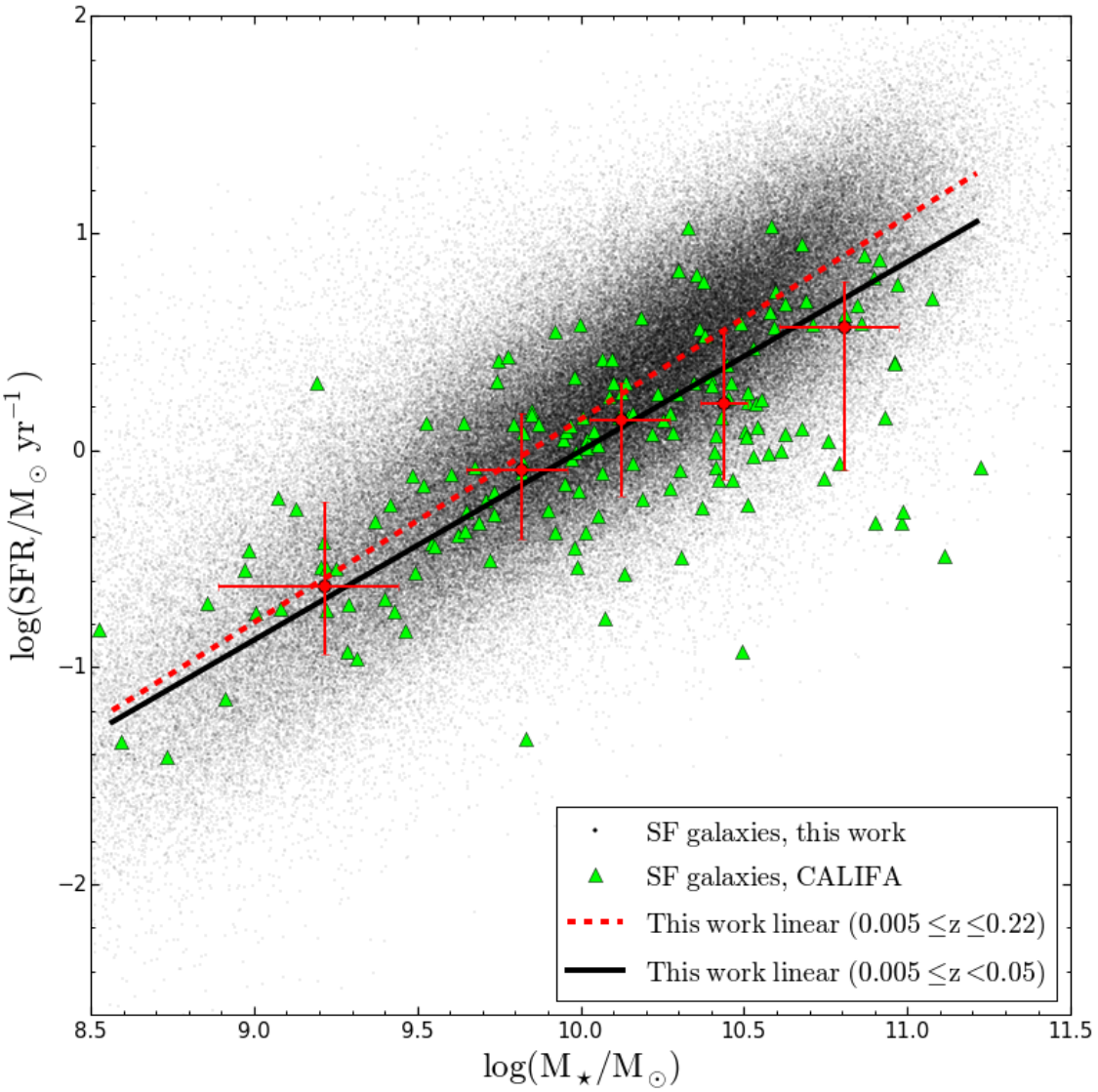

Figure 2.8: SFR–$M_\star$ relation for SDSS (this work) and CALIFA (Catalán-Torrecilla et al. 2015) star-forming galaxies. SFR–$M_\star$ fit to the running median for bins of 2,000 objects obtained in this work for the complete sample (red dashed line) and for bins of 1,000 objects in the range of z between $0.005 \leq z < 0.05$ (black solid line). Red dots represent the median values of SFR and $M_\star$ for CALIFA star-forming galaxies along five stellar mass bins for an equitable number of galaxies in each bin. The error bars in x- and y-axis represent the $\pm 1\sigma$ confidence interval for stellar mass and SFR, respectively.

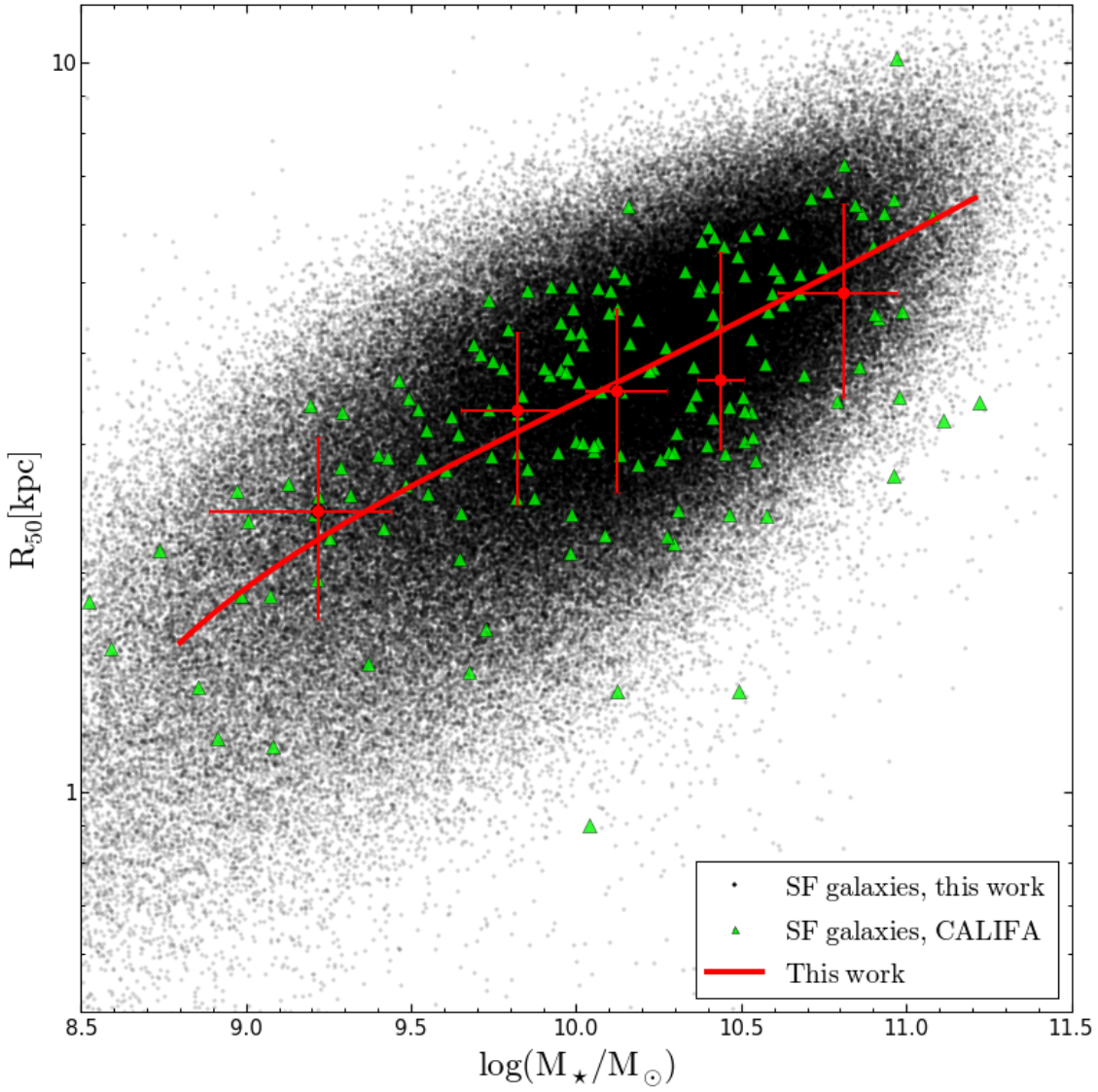

Figure 2.9: Size–$M_\star$ relation for SDSS (this work) and CALIFA (Catalán-Torrecilla et al. 2015) star-forming galaxies. Red solid line represents the linear fit to the running median for bins of 2,000 objects in the SDSS star-forming galaxies. Red dots represent the median values of size and $M_\star$ for CALIFA star-forming galaxies along five stellar mass bins for an equitable number of galaxies in each bin. The error bars in x- and y-axis represent the $\pm 1\sigma$ confidence interval for stellar mass and size, respectively.

Brinchmann et al. (2004b) originally corrected fibre SFRs from aperture effects using the resolved colour information available for each galaxy. Salim et al. (2007) noted an overestimation of these SFRs for galaxies with low levels of star formation, attributed to the larger contribution from dusty high-metallicity starbursts inside these galaxies.[11] Consequently, these authors improved the Brinchmann et al. (2004b) technique (see Salim et al. 2007, for a detailed description) and several studies have used these values of SFR reported by these authors (e.g. Zahid et al. 2012; Renzini & Peng 2015).

A different aperture correction was applied by Hopkins et al. (2003), assuming that the Hα emission-line flux can be traced across the whole galaxy by the r-band emission. Hopkins et al. (2003) derived the total Hα flux as a function of the difference between the total petrosian r-band magnitude (r_{petro}) and the corresponding magnitude inside the SDSS fibre (r_{fibre}) as: $F^{corr}_{H\alpha} = F^{0}_{H\alpha} \times 10^{-0.4(r_{petro}-r_{fibre})}$ (see also Pilyugin et al. 2013). For the sake of comparison, the total Hα flux and the corresponding L(Hα) and SFR for all the galaxies in our final sample was recalculated according to the aperture correction recipe from Hopkins et al. (2003) [equation B3, appendix B]. Here we have refined the Hopkins et al. (2003) recipe for Hα flux aperture correction following the methodology explained in Sect. 2.3.2. The only difference between our refined Hopkins et al. (2003) recipe and Hopkins et al. (2003) methodology is that the former is based on Eq. 2.6 which converts Hα into SFR, while the latter uses a constant conversion value of 41.26.

In Fig. 2.10 (left plot) we show the difference between SFR_{MPA} and the empirical SFR derived in this work ($SFR_{This\ work}$) as a function of $SFR_{This\ work}$. In the right plot we present the difference between the SFR derived applying the Hopkins et al. (2003) aperture correction and $SFR_{This\ work}$ as a function of $SFR_{This\ work}$. We discriminate between high- (EW(Hα) $\geq$ 40Å; blue points) and low-level (EW(Hα) $<$ 40Å; red points) Hα emitting galaxies. The left plot shows that: i) a significant scatter is present, especially for the low-level Hα emitters, being critical (over 1 dex) for low SFRs; and ii) those galaxies with large SFRs and high EW(Hα) show values of SFR_{MPA} somewhat closer to the ones derived in this work, though large systematic differences and big scatter remain. In the right plot, the average SFR values derived according to Hopkins et al. (2003) show a systematic difference with respect to $SFR_{This\ work}$ ones, and a significant scatter (up to ~1dex) is apparent. Galaxies with EW(Hα) $<$ 40Å present a larger scatter and a clear offset from those with EW(Hα) $\geq$ 40Å. The differences between the SFR values derived using Hopkins et al. (2003) recipe and the ones obtained in this work could be reduced when we refine the Hopkins et al. (2003) methodology, as explained above; however, a noticeable scatter and some systematics between red and blue points remain. In this regard, we should bear in mind that the r-band flux of star-forming galaxies includes a contribution from Hα and nearby emission lines and, in fact, should behave as a rough tracer of HII regions. On the other hand, we note in passing that those objects with prominent bulges (likely correlating with the lower level star-formation objects in this sample) should contribute to the emission in the r-band in a more significant manner (e.g. Richards et al. 2016).

In Fig. 2.11 we show the $SFR_{This\ work}$ versus $M_\star$ for each galaxy in our sample and compare the fit to the SFR–$M_\star$ relation derived with previous results from theoretical and observational

[11] http://wwwmpa.mpa-garching.mpg.de/SDSS/DR7/sfrs.html

works. We present (panel a) the linear fit to the running median to the SFR–$M_\star$ relation: i) using the empirical total SFR from this work; ii) based on the SFR_{MPA}; iii) SFR that we obtained applying the Hopkins et al. (2003) recipe and also our refined method of Hopkins et al. (2003) recipe; iv) SFR for the Hα SDSS fibre flux derived in this work. Finally, in this figure (panel c) we also show recent theoretical predictions for the SFR vs. $M_\star$ relation from i) Sparre et al. (2015) at z=0 using the Illustris simulation for star-forming galaxies with stellar masses between 10^9 $M_\odot$ and $10^{10.5}$ $M_\odot$ and ii) by Dutton et al. (2010) at z=0 using a semi-analytic model for star-forming galaxies with stellar masses between 10^9 $M_\odot$ and 10^{11} $M_\odot$. In Fig. 2.11 (panels b and d) we present the differences between the fit to the SFR–$M_\star$ relation of this work and those obtained for MPA-JHU, Hopkins et al. (2003), our refined method of Hopkins et al. (2003) recipe, Dutton et al. (2010), and Sparre et al. (2015). The difference between the aperture-corrected SFR in this work and the SFR corresponding to the SDSS fibre is also shown.

As we can see in Fig. 2.11, the overall difference between SFR_{MPA} and this work amounts to ~ 0.6 dex going from the less to the more massive galaxies. The fit to the SFR–$M_\star$ relation shows that SFR_{MPA} leads to systematically larger values of the SFR for masses $M_\star/M_\odot < 10^9$ ($\approx$0.35 dex) and conversely, under-predicts the SFR[12] by $\approx$0.3 dex for $M_\star/M_\odot > 10^{11}$. Recent studies have reached similar results (e.g. Richards et al. 2016).[13] In this respect, we should bear in mind that galaxies with $\log(M_\star/M_\odot) \gtrsim 10.5$ may host large bulges containing little star formation, and therefore for these objects aperture correction can be problematic (e.g. Brinchmann et al. 2004b; Momcheva et al. 2013; Richards et al. 2016). Conversely, for less massive galaxies, the aperture problems become considerably smaller. The empirical SFR–$M_\star$ fit of this work also shows a systematic difference with the relation derived using Hopkins et al. (2003). The fit to the points obtained with the refined method of the Hopkins et al. (2003) recipe presented here gives a much better result. Excellent agreement is found with the Sparre et al. (2015) and Dutton et al. (2010) predictions.

It is important to note that the MS slope obtained from SFR_{MPA} is ~0.71. As far as we know, those studies that used the SFR values from the MPA-JHU catalogue obtained similar slopes (e.g. Elbaz et al. 2007; Zahid et al. 2012; Renzini & Peng 2015, show slopes of 0.77, 0.71, 0.76, respectively). On the other hand, as mentioned in Sect. 2.4.2 (see Eq. 2.8), the MS slope obtained in this work is 0.935. The MS slope calculated in this work is in very good agreement with the predictions of semi-analytical models by Dutton et al. (2010), giving a zero point of the MS relation consistent with our result. Agreement is also found after the comparison of the MS slope with the predictions of the Illustris cosmological hydrodynamical simulations of galaxy formation by Sparre et al. (2015).

Finally, the SFR–$M_\star$ relation obtained in this work appears consistent with recent IFS observations of modest-size samples of galaxies (e.g. Catalán-Torrecilla et al. 2015; Richards et al. 2016). This concordance is relevant given the fact that total SFR values by Catalán-Torrecilla et al.

[12] We have checked that the difference between SFR_{MPA} and our SFR values is systematic along the range $0.005 \leq z \leq 0.22$. In the larger redshift interval ($0.11 \leq z \leq 0.22$) the SFR predictions by different methods converge as expected, since the geometrical region covered by the SDSS fibre increases.

[13] We note that in Richards et al. (2016) the sample of galaxies with $\log(SFR/M_\odot\,yr^{-1}) < -1.5$ seems to be under-populated.

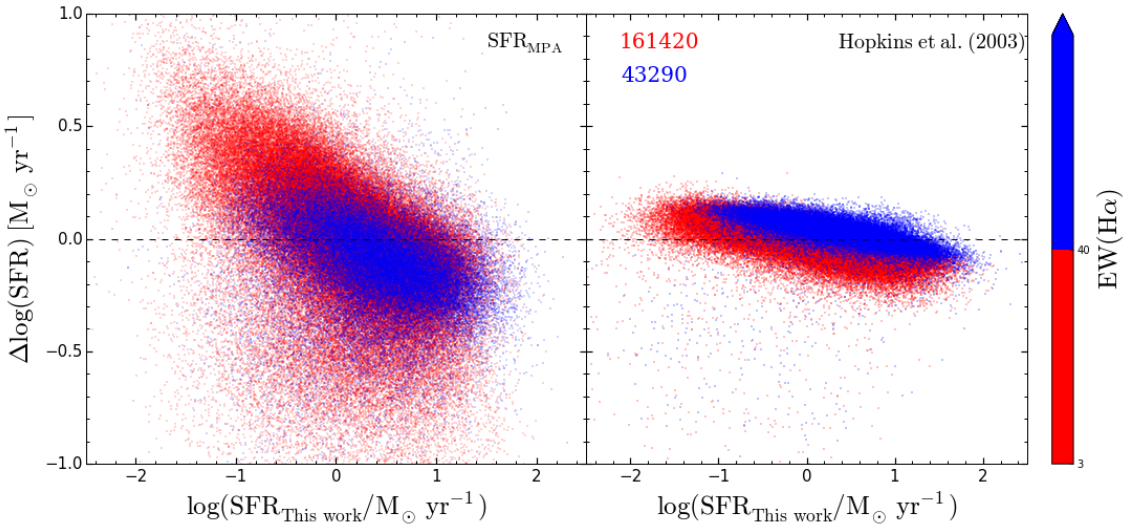

Figure 2.10: Left panel: difference of, $\Delta\log(\mathrm{SFR})$, total SFR provided by MPA-JHU (Brinchmann et al. 2004b; Salim et al. 2007) and our total empirical $\mathrm{SFR}_{\mathrm{This\ work}}$ as a function of $\mathrm{SFR}_{\mathrm{This\ work}}$; Right panel: difference of the total SFR derived using the Hopkins et al. (2003) aperture correction for the Hα flux and $\mathrm{SFR}_{\mathrm{This\ work}}$ as a function $\mathrm{SFR}_{\mathrm{This\ work}}$. Upper numbers represent the number of high- (red points) and low-level (blue points) Hα emitting galaxies. The black dashed line indicates $\Delta\log(\mathrm{SFR}) = 0$.

(2015) and Richards et al. (2016) are obtained integrating the Hα flux over the spatially resolved galaxies, whereas in this work total SFRs are derived from the SDSS fibre Hα flux corrected for aperture effects.

2.7 Summary and conclusions

This work provides a robust study of the total empirical SFR of galaxies and its dependence on stellar mass, extinction, and redshift. Here we present the first study that uses total Hα flux, corrected for aperture from empirical Hα growth curves, to analyse the behaviour of present-day SFR and sSFR of all SDSS star-forming galaxies. This empirical aperture correction is based on a sample of 165 spiral galaxies from the CALIFA project (IP16). Concurrently, we have derived the SFR–$\mathrm{M}_\star$ and the sSFR–$\mathrm{M}_\star$ relations applying our considerations. We have compared these relations, free from aperture effects, with other methods (e.g. Hopkins et al. 2003; Brinchmann et al. 2004b) and with predictions from recent theoretical models (e.g. Dutton et al. 2010; Sparre et al. 2015).

Our main conclusions are the following:

1. The mean empirical aperture-corrected SFR, averaged over galaxy stellar mass, for the entire sample of SDSS star-forming galaxies amounts to ~0.65 dex.

2. The average aperture-corrected SFR for nearby galaxies, $0.005 \leq z \leq 0.05$, is between ~0.7 and ~0.8. For larger z ($0.05 \leq z \leq 0.22$) aperture corrections increase with galaxy mass

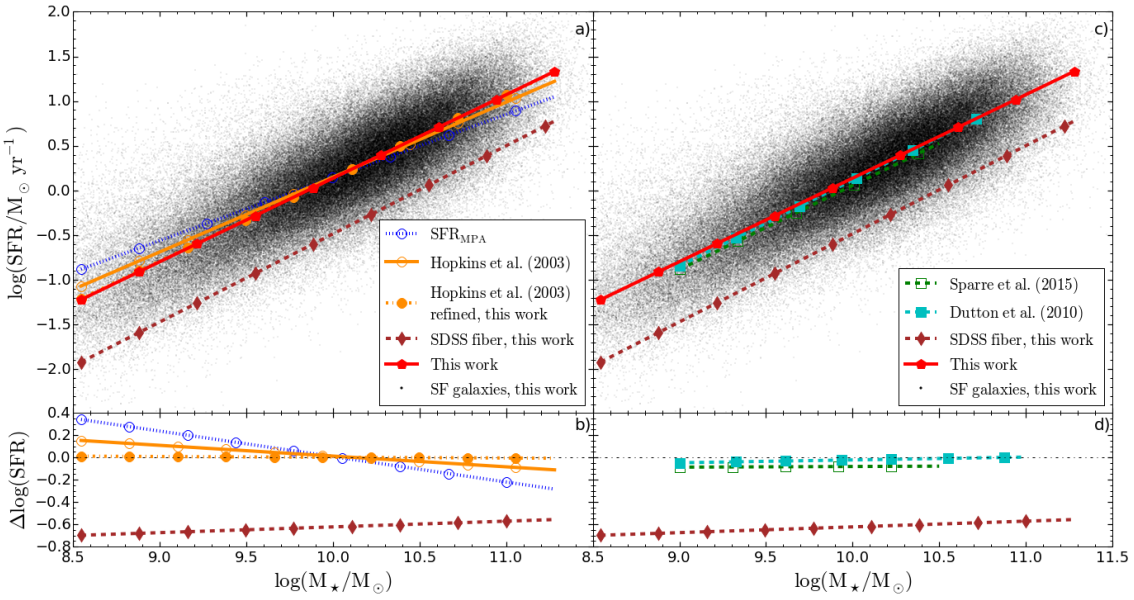

Figure 2.11: SFR$_{\text{This work}}$-M$_\star$ relation for star-forming galaxies compared with previous theoretical and observational works. Comparison with observational studies: Panel a) SFR–M$_\star$ fits to the running median for bins of 2,000 objects obtained in this work (red solid line) and from the SDSS fibre (brown dashed line), together with the values provided by MPA-JHU (blue dotted line), using the Hopkins et al. (2003) recipe (orange solid line), and from our refined method of Hopkins et al. (2003) recipe (orange dashed line). Panel b) Difference vs. M$_\star$ between SDSS fiber SFRs and SFR$_{\text{This work}}$ and between observational studies and SFR$_{\text{This work}}$ (colours as in upper left panel). Dotted line shows $\Delta\log(\text{SFR}) = 0$. Comparison with theoretical studies: Panel c) SFR–M$_\star$ fits to the running median for bins of 2,000 objects obtained in this work (red solid line) and from the SDSS fibre (brown dashed line), together with the predictions from Sparre et al. (2015) (green dashed line) and Dutton et al. (2010) (cyan dashed line). Panel d) Difference vs. M$_\star$ between SDSS fiber SFRs and SFR$_{\text{This work}}$ and between theoretical predictions and SFR$_{\text{This work}}$ (colours as in upper right panel). Dotted line shows $\Delta\log(\text{SFR}) = 0$.

along each redshift interval.

3. The aperture-free SFR–$M_\star$ relation obtained in this work is: $\log(SFR) = 0.935(\pm0.001)\log(M_\star/M_\odot) - 9.208(\pm0.001)$. When comparing total SFRs from previous works with ours, we find: a) the SFR–$M_\star$ relation by MPA-JHU (Brinchmann et al. 2004b; Salim et al. 2007) provides larger SFR values (by ~0.3 dex) for $\log(M_\star/M_\odot) \leq 9$; conversely, MPA-JHU SFR values for $\log(M_\star/M_\odot) \geq 11$ appear systematically lower (by up to 0.3 dex); b) overall consistency is found with selected observational studies based on integral field spectroscopy of individual galaxies (e.g. Catalán-Torrecilla et al. 2015; Richards et al. 2016); c) excellent agreement is obtained with theoretical predictions of recent semi-analytic models of disc galaxies (Dutton et al. 2010), and with Illustris hydrodynamical simulations (Sparre et al. 2015); d) the SFRs derived applying the Hopkins et al. (2003) recipe show a systematic difference along the range of galaxy stellar mass. When this derivation is refined following the methodology described in this work (see Sect. 2.3.2), together with the Hopkins et al. (2003) formula for Hα flux aperture correction, the SFRs obtained appear consistent with our results for high SFR objects, showing substantial scatter notably for the lowest SFR values.

4. A slope $d\log(SFR)/d\log(M_\star) = 0.935$ is derived for our SFR–$M_\star$ relation. This value is higher than those found with MPA-JHU data (e.g. Elbaz et al. 2007; Renzini & Peng 2015), which are ~0.76, with a significant spread. The slope found in this work perfectly agrees with recent theoretical predictions (Dutton et al. 2010; Sparre et al. 2015), giving further support to the empirical Hα aperture correction used. For the specific SFR (sSFR) a slightly decreasing trend is seen along the entire range of stellar mass explored.

5. The total SFR values of the entire sample present a clear correlation with extinction, in overall qualitative agreement with recent works (e.g. Whitaker et al. 2012; Koyama et al. 2015).

Chapter 3

Mass-Metallicity and Star Formation Rate in Galaxies: a complex relation tuned to stellar population age

Contents

This chapter is based on the paper:
"Mass-Metallicity and Star Formation Rate in Galaxies: a complex relation tuned to stellar population age"
by S. Duarte Puertas, J. M. Vilchez, J. Iglesias-Páramo, et al.
in preparation

3.1 Introduction

Since the pioneering work of Lequeux et al. (1979), a plethora of papers have studied the relation between metallicity and galaxy stellar mass, as well as with other fundamental parameters of galaxies (e.g. Vila-Costas & Edmunds 1992; Garnett 2002; Pilyugin et al. 2004; Tremonti et al. 2004; Lee et al. 2006; Zahid et al. 2014). In all of these works a strong correlation between total stellar mass ($M_\star$) and metallicity of galaxies was highlighted. The mass-metallicity relation (MZR) thus remains a key ingredient for our understanding of the formation and evolution of galaxies. Theoretical models predict a tight relation (e.g. Mouhcine et al. 2008; Sakstein et al. 2011; Davé et al. 2011; Romeo Velonà et al. 2013; Okamoto et al. 2017; De Rossi et al. 2017; Torrey et al. 2018) illustrating how galaxy evolution is driven by galaxy mass and gas accretion and outflows.

The overall shape of the MZR is believed to respond mainly to the action of galactic winds and enriched outflows in addition to metal astration driven by star formation and galaxy stellar mass. The MZR reaches a maximum near saturation at the high mass end ($\log(M_\star/M_\odot) \geq 10.5$), and then levels off to a metallicity asymptotically close to the oxygen yield (e.g. Pilyugin et al. 2007). The study of these processes in galaxies of different masses can shed light, in particular, to ascertain whether the MZR could be emerging from a local relationship within galaxies or rather represents a truly global scale relation, e.g. linked to galaxy mass. Other processes related to e.g. galaxy downsizing or massive gas accretion and star formation can be also involved (e.g. Finlator & Davé 2008).

SFR was introduced as a secondary parameter of the MZR aiming at reducing the scatter observed, and the so-called fundamental mass-metallicity SFR relation was defined (MZSFR; e.g. Ellison et al. 2008; Mannucci et al. 2010; Lara-López et al. 2010b). In this fundamental relation SFR anti-correlates with metallicity, at fixed galaxy stellar mass, and some models outline a possible secondary dependence of MZR with SFR (e.g. Dayal et al. 2013). An intense debate has developed within this new framework mainly devoted to understand the exact role played by the SFR (e.g. Sánchez et al. 2013), with particular focus on the detection of possible evolution of MZSFR with redshift. A good fraction of these studies have been performed using single aperture (e.g. SDSS) spectroscopy of galaxies to derive the oxygen abundance of the ionized gas, a proxy of galaxy metallicity, using measurements of bright emission lines; often, SFR estimations for these galaxies were derived from the same spectral information (e.g. SDSS fibre spectra), and present-day SFRs computed from the luminosity of Hα emission. Other estimates of the SFR of galaxies can be derived using multiparametric fitting of their spectral energy distribution using evolutionary population synthesis models and inverting population synthesis equations.

The study of possible evolution of the MZR zero point and slope with cosmic time and SFR can shed light on how galaxies formed, were assembled and evolve, an also on the infall and galactic wind phases of their chemical evolution. The MZR has been extensively studied as a general scaling relation of star-forming galaxies in the local Universe (e.g. Mannucci et al. 2010; Lara-López et al. 2010b; Kashino et al. 2016), as a function of galaxy environment (e.g. Ellison et al. 2009; Petropoulou et al. 2011, 2012; Peng & Maiolino 2014; Pilyugin et al. 2017), and in

medium and high redshift surveys (e.g. Brown et al. 2016; Hunt et al. 2016; Kojima et al. 2017). Some evolution is expected of the shape or the zero point of the MZR (e.g. Lara-López et al. 2010a; Møller et al. 2013; Pilyugin et al. 2013); though, other works find no significant evolution for the MZSFR (e.g. Mannucci et al. 2010; Cresci et al. 2012).

The existence of a possible dependence of MZR on SFR is presently under debate (e.g. Sánchez et al. 2013, 2017; Barrera-Ballesteros et al. 2017), especially after the recent observations of a large number of galaxies with IFS in CALIFA and MANGA surveys, or with integrated spectra by Hughes et al. (2013). In order to carry out an in depth study of the relation between MZR and SFR we must address the systematic effects involved, as discussed in Telford et al. (2016). Systematic effects associated to e.g. S/N, aperture effects, or the metallicity indicators used, among others, can affect the derivation of the MZR and any possible dependence of MZR with SFR.

The problem of metallicity derivation from spectroscopy of large data samples has been discussed elsewhere (e.g. Curti et al. 2017, and references therein), and since temperature sensitive lines fluxes are not available for the huge majority of these objects (e.g. in SDSS), abundance calibrations are applied to derive their metallicity. Not all abundance calibrations appear equally reliable when comparing to directly derived oxygen abundances. In fact, recent abundance calibrations empirically calibrated provide an abundance which, statistically, is typically within 0.2 dex uncertainty of the direct value. In this respect, some support can be gained using complementary versions of the MZR relation, e.g. using stellar metallicity derived either from integrated young stellar populations (e.g. Gallazzi et al. 2005) or for individual massive stars (e.g. Bresolin et al. 2016); or deriving oxygen abundance directly from stacked spectra of mass-grouped star-forming galaxies (e.g. Andrews & Martini 2013); also, replacing oxygen abundance by nitrogen abundance (N/O), an abundance ratio less dependent on electron temperature and a well known "chemical clock" (e.g. Edmunds & Pagel 1978; Pilyugin et al. 2003; Mollá et al. 2006) adding useful chemical evolution information. In this work, the caveats mentioned above have been taken into account for the metallicity derivation and analysis, and the corresponding sanity checks performed when appropriate.

Among the critical effects to be corrected for aperture effects, produced by incomplete or partial coverage of the observed galaxies (e.g. SDSS 3 arcsec fibre spectroscopy). IFS of a large sample of galaxies of CALIFA has provided the method to correct by aperture and spatial sampling effects (Mast et al. 2014; Gomes et al. 2016; Iglesias-Páramo et al. 2016). It has been shown that aperture effects translate in clear flux deficits which, in the case of e.g. SFR, imply corrections of up to ~0.6 dex (Iglesias-Páramo et al. 2013, and Chapter 2); whereas model-based aperture corrections do not solve this problem. In the case of spectroscopy the situation is not trivial; line fluxes and line ratios, and its corresponding extinction correction, must be aperture corrected before deriving oxygen and nitrogen abundances. In particular, differential extinction correction across the disks of galaxies can not be overlooked. In Iglesias-Páramo et al. (2016) empirically CALIFA based aperture correction are provided for the relevant lines.

In this work we benefit from the methodology and knowledge gained with the CALIFA survey and apply it here to minimise systematic effects. Hence we examine in detail the behaviour of the

relation between MZR and SFR for a large and complete sample of SDSS star-forming galaxies (see Chapter 2 for details)[1] using the total fluxes of their emission lines empirically corrected by extinction and aperture in a consistent manner. A robust MZR locus has been derived which is found fully consistent with the "anchoring" points of galaxies with a direct derivation of abundance. A strong relation between MZR and SFR across the whole range of galaxy mass has been unveiled, showing a complex pattern of slope changes of the MZR-SFR relation which appears tuned to the age of the stellar population of galaxies.

The chapter is organised as follows: in Sect. 3.2 we describe the data and we provide a description of the methodology used to select the sample. The methodology used to derive all the parameters used in this work is presented in Sect. 3.3. Main results, discussion and conclusions are given in Sect. 3.4. Finally, supplementary material has been added to Sect. 3.5. Throughout the chapter, we assume a Friedman-Robertson-Walker cosmology with $\Omega_{\Lambda 0} = 0.7$, $\Omega_{m0} = 0.3$, and $H_0 = 70\,km\,s^{-1}\,Mpc^{-1}$. We use the Kroupa (2001) universal IMF.

3.2 Data and sample

Our study is based on the catalogue of 209 276 star-forming galaxies extracted from SDSS-DR12 (Alam et al. 2015) and presented in Chapter 2. The galaxies span a redshift (z) and stellar mass ranges of $0.005 \leq z \leq 0.22$ and $8.5 \leq \log(M_\star/M_\odot) \leq 11.5$. We use aperture corrected SFR measurements from the database of Chapter 2. All the emission line fluxes (i.e. Hα, Hβ, [OII]$\lambda\lambda$3727, 3729, [NII]λ6584, and [OIII]λ5007 emission lines), $\log(M_\star/M_\odot)$, z, and $D_n(4000)$[2] used in this work have been provided by MPA-JHU public catalogue[3] (Kauffmann et al. 2003b; Brinchmann et al. 2004b; Tremonti et al. 2004; Salim et al. 2007). From this catalogue we have selected a subset of 194 353 SDSS star-forming galaxies according to the following criteria: i) $z \geq 0.02$. Due to the SDSS spectral range (3800-9200 Å), this is the minimum redshift required to include and measure [OII]$\lambda\lambda$3727, 3729; this emission line is necessary to derive the metallicity (see Sect. 3.3) in our spectra (Pilyugin et al. 2012; Pérez-Montero et al. 2013). ii) A S/N always greater than three is imposed for all the line fluxes used to derive SFR, oxygen abundance, and N/O.

3.3 Empirical aperture correction and chemical abundances

As it is well known, the SDSS fibres (3 arcsec diameter) cover only a limited region of a galaxy in the low-z Universe ($z < 0.22$). In order to obtain the total SFR for all the galaxies in our sample we have used the aperture corrected SFR values from Chapter 2, where a detailed description of aperture correction of SDSS Hα flux measurements is presented.

The aperture correction of the Hα flux and $\log([OIII]\lambda5007/H\beta)$, $\log([NII]\lambda6584/H\alpha)$, and

[1] Duarte Puertas et al. (2017).

[2] $D_n(4000)$ corresponds to the narrow definition of the 4000Å break strength from Balogh et al. 1999 that can be considered a proxy of stellar population age.

[3] Available at http://www.mpa-garching.mpg.de/SDSS/.

Hα/H$_\beta$ flux ratios of our sample was performed using the aperture correction formulae by Iglesias-Páramo et al. (2016). These corrections were derived for a sample of CALIFA disk galaxies representative of the different types and masses (see Table 20 in Iglesias-Páramo et al. 2016). The aperture correction recipe for [OII]$\lambda\lambda$ 3727, 3729 has been provided to us by Iglesias-Páramo et al. (private communication). Conversely, as shown in Belfiore et al. (2016), the D$_n$(4000) break strength index remains substantially constant across star-forming galaxies, given that their young stellar component appears well distributed through out all the galactic disk; hence no aperture correction was applied for it. In summary, for each galaxy of our sample the SDSS fibre line fluxes (i.e. Hα, Hβ, [OII]$\lambda\lambda$ 3727, 3729, [NII]λ 6584, and [OIII]λ 5007) were corrected for extinction following Sect. 2.3.1, and then they were aperture-corrected applying the equations in Table 20 of Iglesias-Páramo et al. (2016). These emission line fluxes are necessary for the derivation of oxygen and nitrogen abundances, as explained below.

In order to derive the metallicity of sample galaxies, given that the faint temperature sensitive lines are not available, we must rely on bright lines abundance calibrations (including from [OII], [OIII] to [NII]). It is well known that some calibrations produce different absolute values of O/H; especial care has been exercised in this work in the selection of the abundance calibrations applied. We first follow the study updated by Curti et al. (2017) for O/H derivation and have selected their calibration of O3N2 which presents the wider O/H prediction range with the smallest dispersion. In addition, to derive the nitrogen to oxygen ratio, we have also adopted the empirical calibrations by Pilyugin & Grebel (2016) for nitrogen (their eq. 13) and oxygen (their eqs. 4, 5) abundances. These calibrations selected are all empirical, i.e. they are calibrated against direct derivations of abundances calculated with electron temperature measurements. Finally, we have used the photoionization model HIIChemistry (Pérez-Montero 2014) which is able to reproduce chemical abundances consistent with their corresponding direct derivations[4]. Oxygen and nitrogen abundances for our sample galaxies have been derived with the three selected methods and free from aperture effects, given that the emission line fluxes used were all aperture corrected, corresponding to the entire galaxy. The abundances obtained for each object resulted consistent within the errors and overall, the three abundance outputs from the calibrations selected are statistically consistent to within ~0.15 dex; with the higher consistency and lowest errors being achieved especially for the nitrogen to oxygen abundance ratio. Taking this fact into account, in this work we adopt for each galaxy as representative abundances the O/H and N/O obtained applying Pilyugin & Grebel (2016).

In Fig. 3.1, we show the oxygen abundance, 12 + log(O/H), versus total stellar mass for the 194 353 galaxies in our sample clearly reproducing the MZR relation. A further quality check of our MZR derivation can be performed comparing with the oxygen abundance and total stellar mass[5] for the Milky Way and ten well known nearby galaxies for which precise abundance values of their HII regions are available from direct electron temperature measurements. These nearby

[4] A known feature is that most photoionization model abundances are typically overestimated; while HIIChemistry abundances appear consistent with direct derivations

[5] NGC 55, NGC 300, and M 33 stellar masses transformed from Chabrier (2003) to Kroupa (2001) IMF dividing by 0.943 (Mannucci et al. 2010).

galaxies show well defined spatially resolved radial abundance gradients, thus their representative abundance corresponding to the integrated galaxy flux can be easily derived following CALIFA survey. According to Sánchez et al. (2013), for galaxies presenting 12 + log(O/H) abundance at the effective radius, 12 + log(O/H)$_{\rm Reff}$ $\leq$ 8.6 dex, the mean difference between 12 + log(O/H) of the integrated galaxy flux and 12 + log(O/H)$_{\rm Reff}$ is ∼-0.03 dex; whereas for galaxies with 12 + log(O/H)$_{\rm Reff}$ above 8.6 dex, this difference amounts to ∼0.06 dex. We have applied this small conversion to calculate the representative 12 + log(O/H) abundances of our selected nearby galaxies; these objects are also shown in Fig. 3.1. It can be seen that the selected sample of nearby galaxies and our sample of SDSS star-forming galaxies show excellent agreement delineating the local universe MZR, free from aperture effects, derived in this work.

3.4 Discussion and conclusions

In Fig. 3.2 we show the MZR diagram, with the fits to the running medians for seven SFR intervals overplotted. The strong correlation between oxygen abundance and galaxy stellar mass, shown in the MZR plot, is evident for the seven SFR line fits shown. We can see also how these iso-SFR loci tend to saturate at higher abundances and level off near solar metallicity[6]. For fixed log(M$_\star$/M$_\odot$), galaxies with a higher metallicity present lower SFR than lower metallicity galaxies, confirming previous findings (e.g. Mannucci et al. 2010).

In Fig. 3.3 we show our aperture corrected 12 + log(O/H) (panel a) and log(N/O) (panel b) versus SFR for the galaxy sample (grey points) following the same statistical procedure as in the previous figure. In panel a, the values found in the running median and the fits to the running median of galaxy mass are shown for six log(M$_\star$/M$_\odot$) intervals of Δ log(M$_\star$/M$_\odot$) = 0.5 dex each (see also Figure SM 3.6), plotted by black-dotted lines. The total range in galaxy stellar mass covered being 8.5 $\leq$ log(M$_\star$/M$_\odot$) $\leq$ 11.5 in both panels. The overlaid colour dashed lines show the fits to the running median of the D$_{\rm n}$(4000) index of the sample galaxies, calculated for six intervals from D$_{\rm n}$(4000) $<$ 1.1 to D$_{\rm n}$(4000) $\sim$ 1.5, with ΔD$_{\rm n}$(4000) = 0.1 dex each, as indicated in the plot; in parenthesis the total number of points per interval is quoted. In panel b, we show the behaviour of log(N/O) against SFR of the sample (grey points); a strong correlation is present, -somewhat steeper than in panel a-, between these two properties. A wide range in log(N/O) is covered by our SDSS galaxy sample, going from over-solar (log(N/O)$_\odot$= -0.86) values to the typical level of low metallicity dwarf galaxies (log(N/O) ∼ -1.5). As in panel a, the corresponding fits to the running median of galaxy mass (black-dotted lines) and of D$_{\rm n}$(4000) (colour lines) are shown for the same ranges and intervals considered. Overall, the behaviours of sample galaxies observed in both plots show excellent agreement.

It is important to bear in mind that D$_{\rm n}$(4000) depends on stellar population age, presenting lowest values for the youngest stellar populations, while the older ones show higher values (Balogh et al. 1999). In panels a and b of Fig. 3.3 we can see how for fixed log(M$_\star$/M$_\odot$), galaxies with lower SFR present systematically higher values of D$_{\rm n}$(4000), suggesting that they host old stellar populations. For D$_{\rm n}$(4000) $>$ 1.2, we can see how the massive (log(M$_\star$/M$_\odot$) $>$ 10.5) galaxy

[6]Solar metallicity: 12 + log(O/H)$_\odot$ = 8.69 (Asplund et al. 2009).

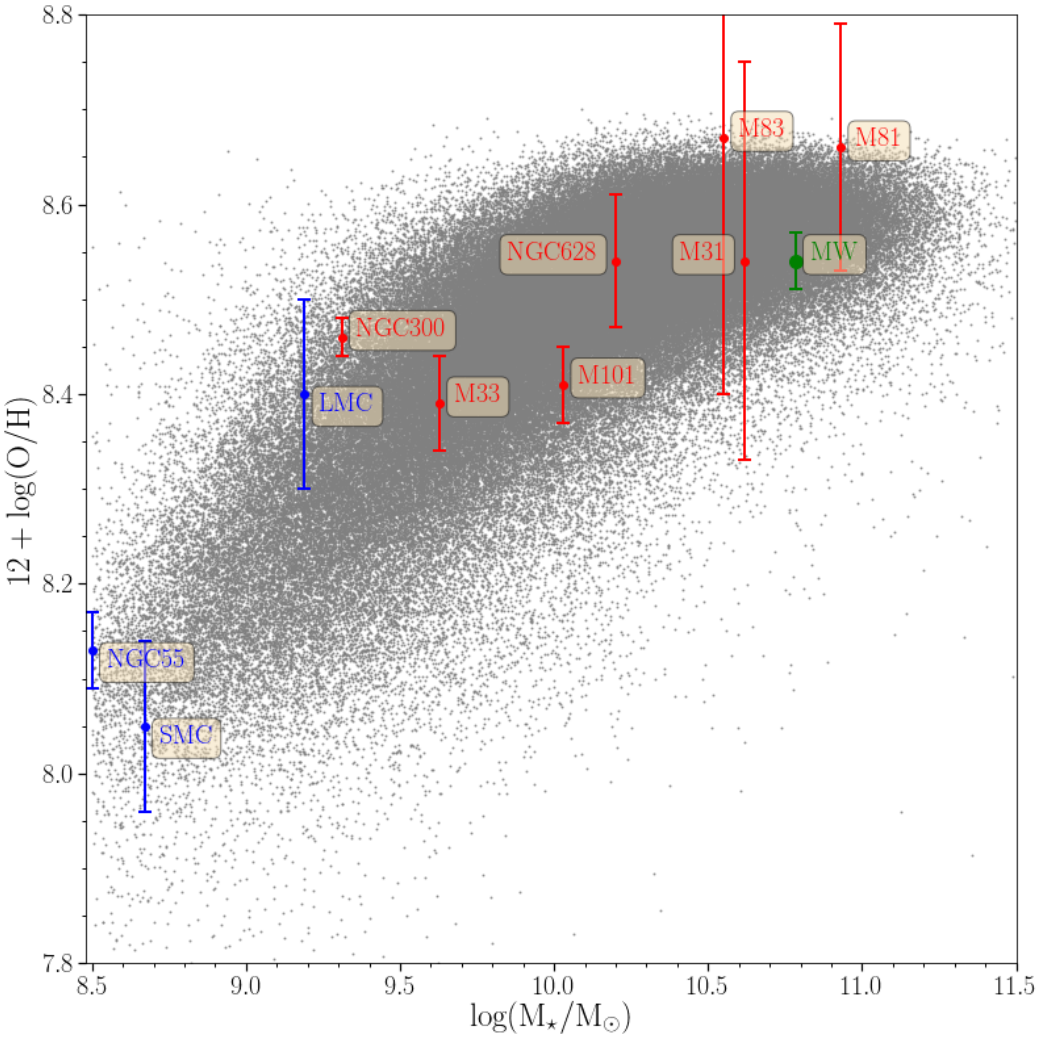

Figure 3.1: Aperture corrected MZR. Star-forming galaxies of our sample (grey dots), as well as the Milky Way (green mark) and other nearby galaxies (labelled; coloured points) with direct (from electron temperature) oxygen abundances are shown. Blue or red colour indicate galaxies with a flat or non-zero radial oxygen gradient, respectively. *References as follows: galaxy name, O/H reference, stellar mass reference; SMC, LMC, M81 Bresolin et al. (2016), Kudritzki et al. (2012); NGC 55, Magrini et al. (2017), Lee et al. (2006); MW (Orion), Simón-Díaz (2010), Licquia & Newman (2015); M83, M33, NGC 300 Bresolin et al. (2016); Kang et al. (2016); M 31, Zurita & Bresolin (2012), Fisher & Drory (2011); M 101, Croxall et al. (2016), Skibba et al. (2011); NGC 628, Berg et al. (2015), Cook et al. (2014).*

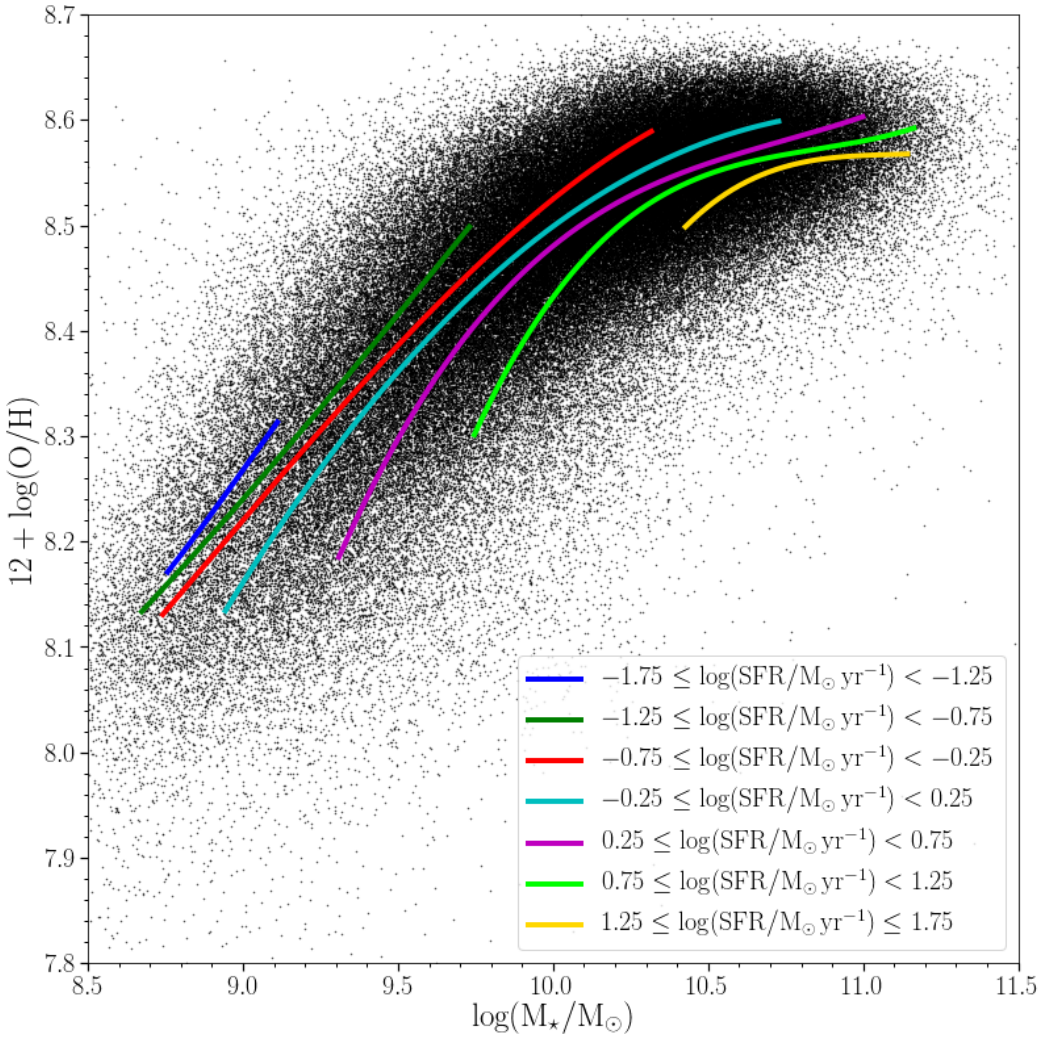

Figure 3.2: Relation between 12+log(O/H) and $M_\star$ for SDSS star-forming galaxies, grey points. Overplotted blue, green, red, cyan, magenta, lime, and yellow solid lines represent the fits to the running median of the SFR of the galaxies, calculated in bins of 1000 galaxy points, corresponding to seven SFR intervals as indicated.

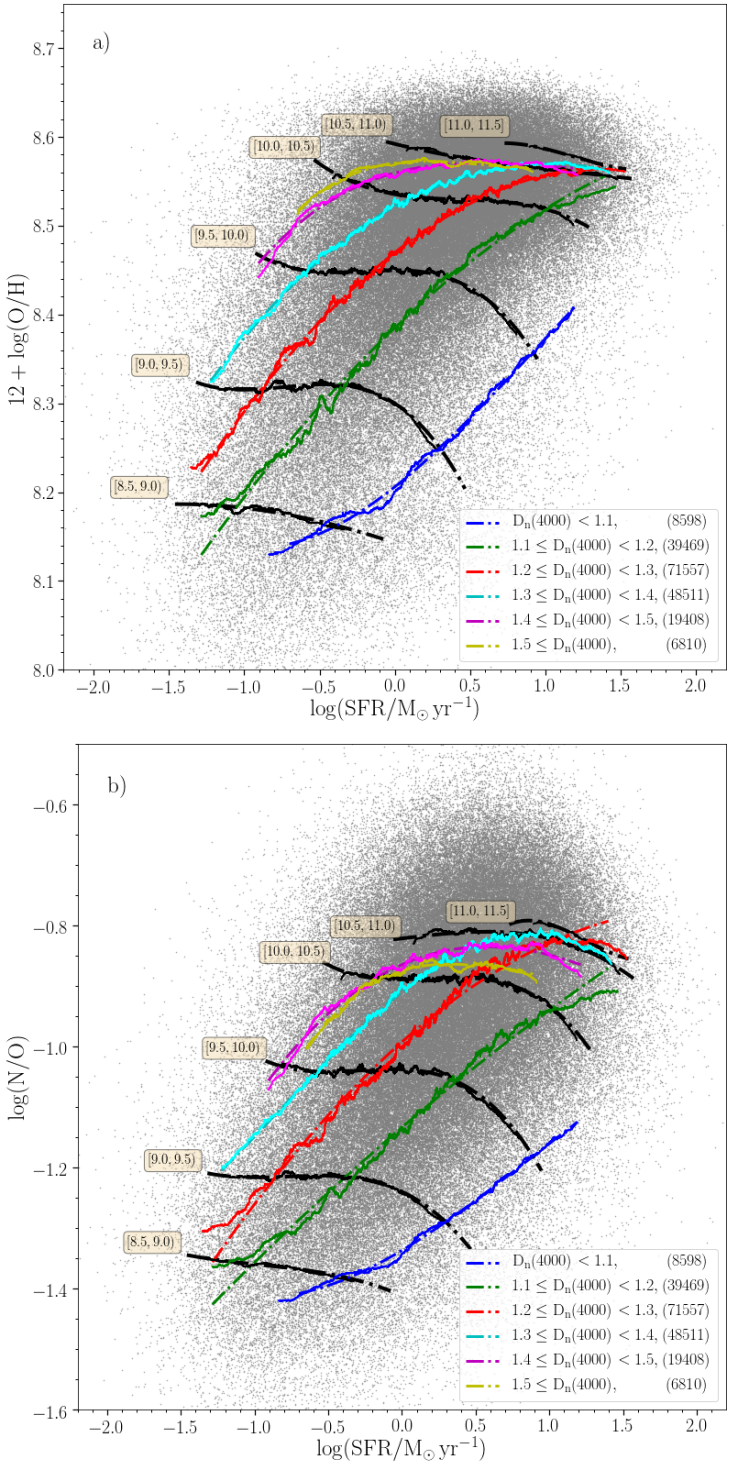

Figure 3.3: Panel a) Relation between the $12 + \log(O/H)$ and SFR for star-forming galaxies. Blue, green, red, cyan, magenta, and yellow solid and dashed lines represent the values found in the running median and the fit to the running median, respectively, for bins of 1000 objects in six $D_n(4000)$ bins. The number of star-forming galaxies in each $D_n(4000)$ bin appear on the legend. Black solid and dotted lines show the $12 + \log(O/H)$ vs. SFR values found in the running median and the fits to the running median, repectively, for bins of 1000 objects in six $\log(M_\star/M_\odot)$ bins (each box shows the $\log(M_\star/M_\odot)$ range considered). Panel b) Relation between the $\log(N/O)$ and SFR for star-forming galaxies (colours and numbers of star-forming galaxies in each $D_n(4000)$ bins as in panel a).

lines tend to saturate and flatten in both panels above 12 + log(O/H) ≥ 8.55 and log(N/O) ≥-0.9, irrespective of their SFR. In panel a of Fig. 3.3 it can be seen that, for nearly the entire mass range of the sample (log($M_\star/M_\odot$) ≤ 11), oxygen abundance, 12 + log(O/H), shows a nearly flat or very mild decrease with respect to SFR along the black-dotted lines until reaching the green line, corresponding to 1.1 ≤ $D_n(4000)$ < 1.2. After passing the green line towards higher SFR along each black-dotted line, 12 + log(O/H) drops suddenly with a negative slope against SFR (Δ log(O/H)/Δ logSFR∼-0.15), specially strong for the stellar mass bins [9, 9.5) and [9.5, 10), see Figure SM 3.6.

This behaviour appears to be common to all galaxies with stellar mass log($M_\star/M_\odot$) < 10.5; for this galaxy mass range the green iso-$D_n(4000)$ line defines, in fact, an effective "isochrone" for sample galaxies which marks also the sudden change in the derivative of oxygen abundance against SFR. This plot may illustrate why the case for a universal oxygen abundance versus SFR (negative) relation is still controversial for local samples of galaxies. It can be seen also that the region for which the metallicity-SFR relation may hold varies for each galaxy total stellar mass; therefore a negative dependence of metallicity on SFR could be seen but always in those galaxies hosting the youngest stellar population (i.e. $D_n(4000)$ ≤ 1.1). A similar behaviour can be observed in panel b of Fig. 3.3, now for log(N/O). Again for galaxies with (log($M_\star/M_\odot$) ≤11), the dependence shown by log(N/O) on SFR is very mild if any, except when the green iso-$D_n(4000)$ line is reached. Beyond this point, moving towards larger SFR for fixed stellar mass (i.e. black-dotted lines), a strong and negative dependence of Δ log(N/O)/Δ logSFR is evident. The log(N/O) values at which this changing slope occurs go from those typical of dwarf galaxies up to solar. The similar behaviours exhibited against SFR in panels a and b from oxygen abundance and nitrogen to oxygen abundance ratio, respectively, can give us some hints to understand the chemical evolution of our sample galaxies.

We have found a locus in the planes 12 + log(O/H)-SFR and log(N/O)-SFR delimiting two broad regions for the sample galaxies, with and without a clear dependence on SFR, along each galaxy stellar mass sequence. This locus appear well represented on each plot by the line corresponding to sample galaxies with $D_n(4000)$ < 1.2, for which according to Mateus et al. (2006), the mean stellar age expected is below ∼150 Myr. Along this locus, it seems that abundance and SFR for each total stellar mass (i.e. specific SFR) behave tuned, defining a sort of "effective isochrone", corresponding to the average stellar population of each galaxy. This applies only to galaxies with (log($M_\star/M_\odot$) < 10.5); for more massive galaxies we can not observe this behaviour in our sample. For these massive galaxies lines of the $D_n(4000)$ index converge at high metallicity (near solar to supersolar), and oxygen abundance and N/O do not show observable decrease, suggesting an evolution without metallicity loss and driven by galaxy mass.

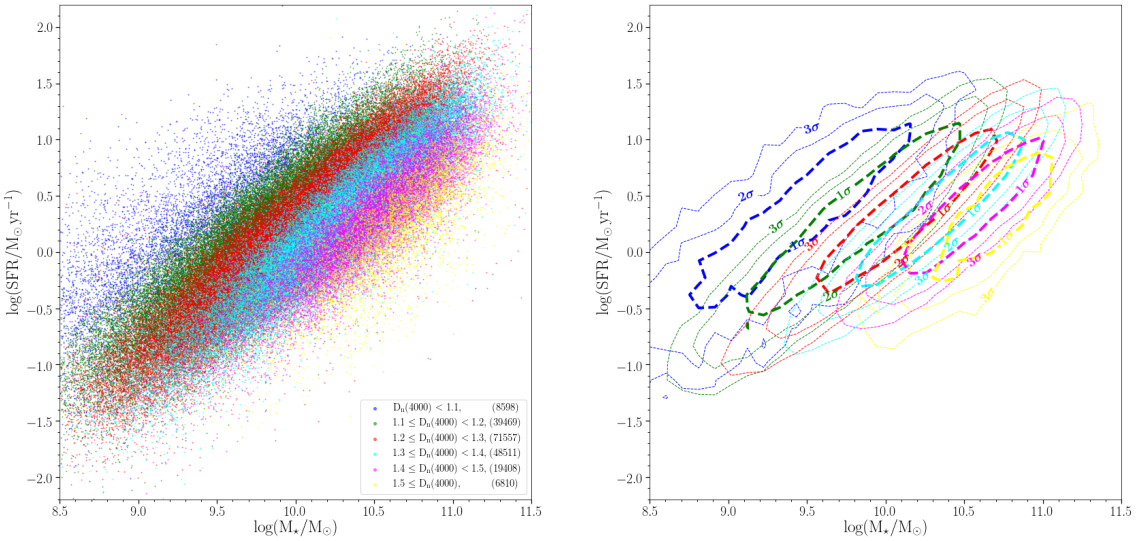

Figure 3.4: Relation between SFR and $M_\star$ for star-forming galaxies colour coded according to the $D_n(4000)$ parameter (left panel) and its corresponding confidence limits from 1 to 3σ (right panel).

Interestingly enough, a direct consequence of the above definition has been the selection of a sub-sample of galaxies which populate the youngest part of the two diagrams of Fig. 3.3. This group of (8598) galaxies are "outliers" from the negative correlation of the sample, and cluster around the iso-line $D_n(4000) < 1.1$, on average in panels a and b. It is for these group of very young galaxies for which the large changing slopes with SFR are observed. These outliers are not only dwarf galaxies, they sample a large range in galaxy stellar masses; and showing always the largest SFR measured for it mass class. This is easily appreciated in Fig. 3.4 where the relation between SFR and $M_\star$ for our sample of SDSS star-forming galaxies is presented; galaxies are colour coded according to the $D_n(4000)$ parameter. For each fixed stellar mass, a range in SFR is observed where the largest SFR corresponding to the youngest objects. In order to ascertain the nature of these 8598 galaxies we have performed a sanity check and confirmed their metallicity and SFR (see Figures SM 3.7, 3.8, and 3.9 to gain more insight into the nature of this sub-sample of galaxies). We have checked the SFR derived for these galaxies, confirming that these values were not produced by aperture corrections since outliers were corrected below the average. We have searched the fluxes of the measured SDSS spectra of the outliers and have verified for all these galaxies with electron temperature (i.e. with S/N([OIII]λ4363) > 5) that their direct (electron temperature based) abundances agree with our oxygen abundance values to within ~-0.025 dex on average (see Fig. 3.5).

The apparent metallicity-SFR anticorrelation still appears to be controversial; this relation has been interpreted as the consequence of a possible selection effect, and also possibly resulting from the existence of massive infall of mainly metal poor gas on the galaxies, which would produce a strong enhancement of the SFR and, at the same time, should dilute the metallicity of the interstellar medium (ISM) (Ellison et al. 2008; Mannucci et al. 2010) giving rise to an expected anticorrelation between 12 + log(O/H) and SFR. This picture seems to be supported by some

theoretical work (e.g. Sakstein et al. 2011; Dayal et al. 2013). Though recent observational work has questioned this. We have shown in this work a deep and complex relation between the MZR and SFR tuned to the mean age of the galaxy stellar population. Anticorrelation between oxygen abundance and SFR appear to be significant only for galaxies hosting the youngest stellar populations. The massive infall scenario, could be invoked to explain these high SFR objects; however for these galaxies log(N/O)-SFR also anticorrelate, unexpectedly for the standard infall scenario where N/O should not be much affected. Further deep spectroscopic observations of the extreme SFR "outliers" subsample could provide valuable information to solve this issue.

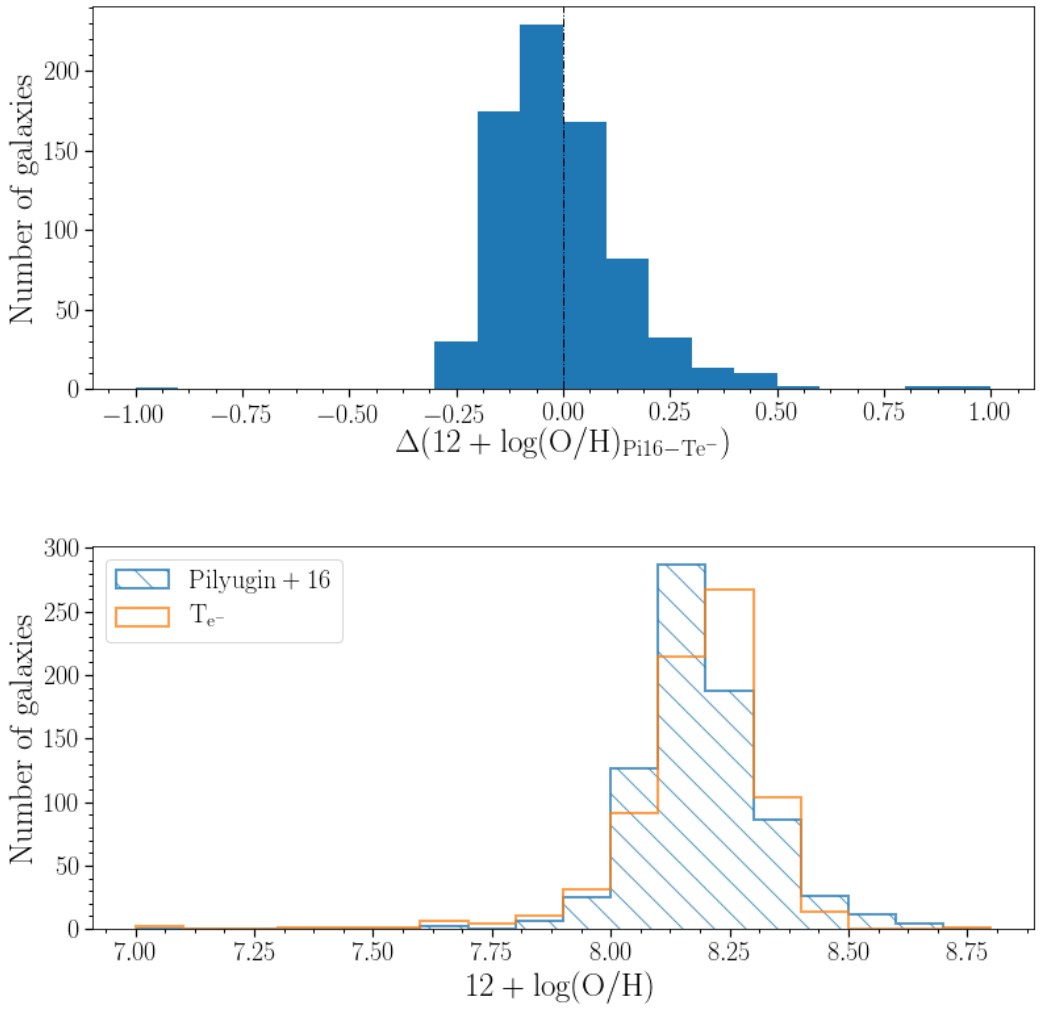

Figure 3.5: Upper panel) Distribution of difference between aperture corrected and direct (electron temperature based) oxygen abundances for SDSS star-forming outliers galaxies with S/N([OIII]λ4363) > 5, Δ12+log(O/H)$_{Pi16-Te^-}$. Lower panel) Distribution of oxygen abundance for SDSS star-forming outliers galaxies using Pi16 methodology (blue dashed histogram) and using direct methodology (orange open histogram).

3.5 Supplementary material

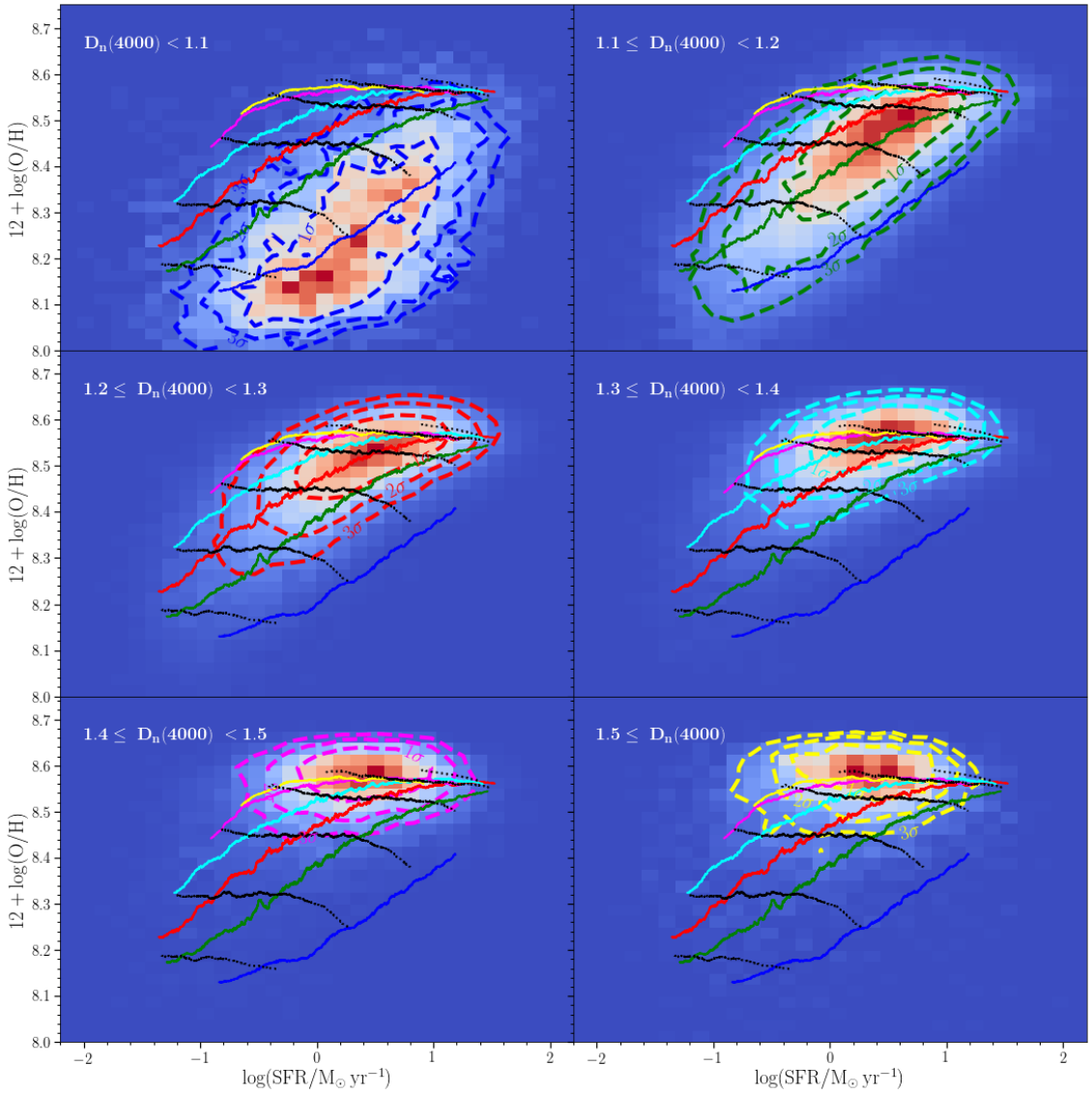

Figure SM 3.6: **Detailed analysis of the 12+log(O/H)–SFR density plot presenting confidence limits for each $D_n(4000)$ bin.** Density plots for the relation between the 12+log(O/H) and SFR for star-forming galaxies for six $D_n(4000)$ ranges. All the lines have the same colours as Fig. 3.3. The dashed lines represent the 1σ, 2σ, and 3σ contours in each $D_n(4000)$ bin.

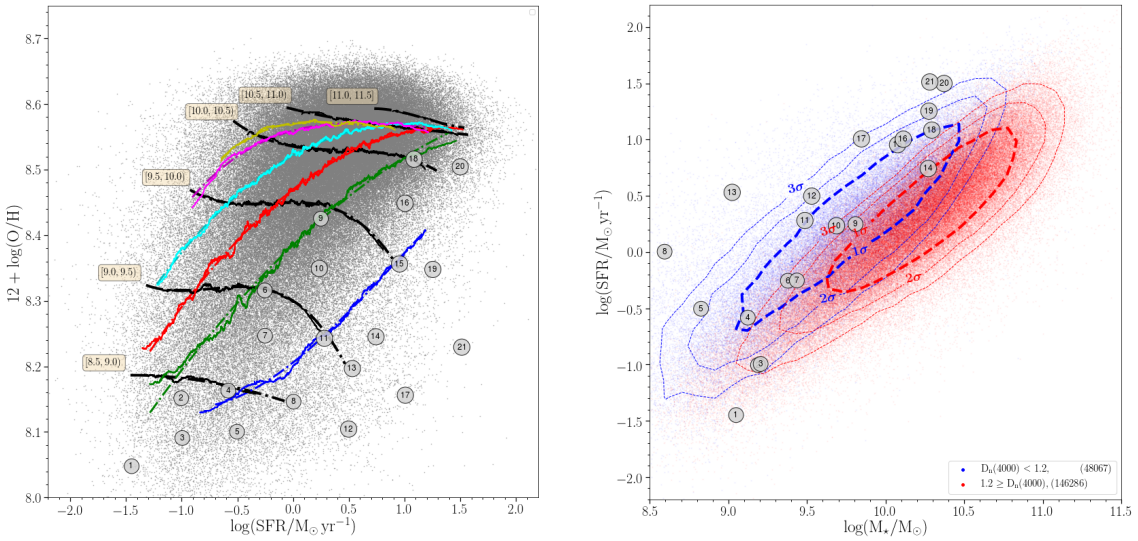

Figure SM 3.7: **Selection of 21 galaxies from the 12+log(O/H) vs. SFR diagram.** Left panel) Relation between 12+log(O/H) and SFR for star-forming galaxies. All the lines have the same colours as Fig. 3.3. A sample of 21 galaxies has been selected (as an example) in this diagram, the positions are represented with grey circles and have been labelled from 1 to 21 according to their SFR. Right panel) Relation between SFR and $M_\star$ for star-forming galaxies. The points have been colour coded according to their $D_n(4000)$, blue if $D_n(4000) < 1.2$ and red if $D_n(4000) \geq 1.2$. The dashed lines represent the 1σ, 2σ, and 3σ contours in each $D_n(4000)$ sub-sample. Grey circles shows the position in the SFR-$M_\star$ diagram of the 21 galaxies.

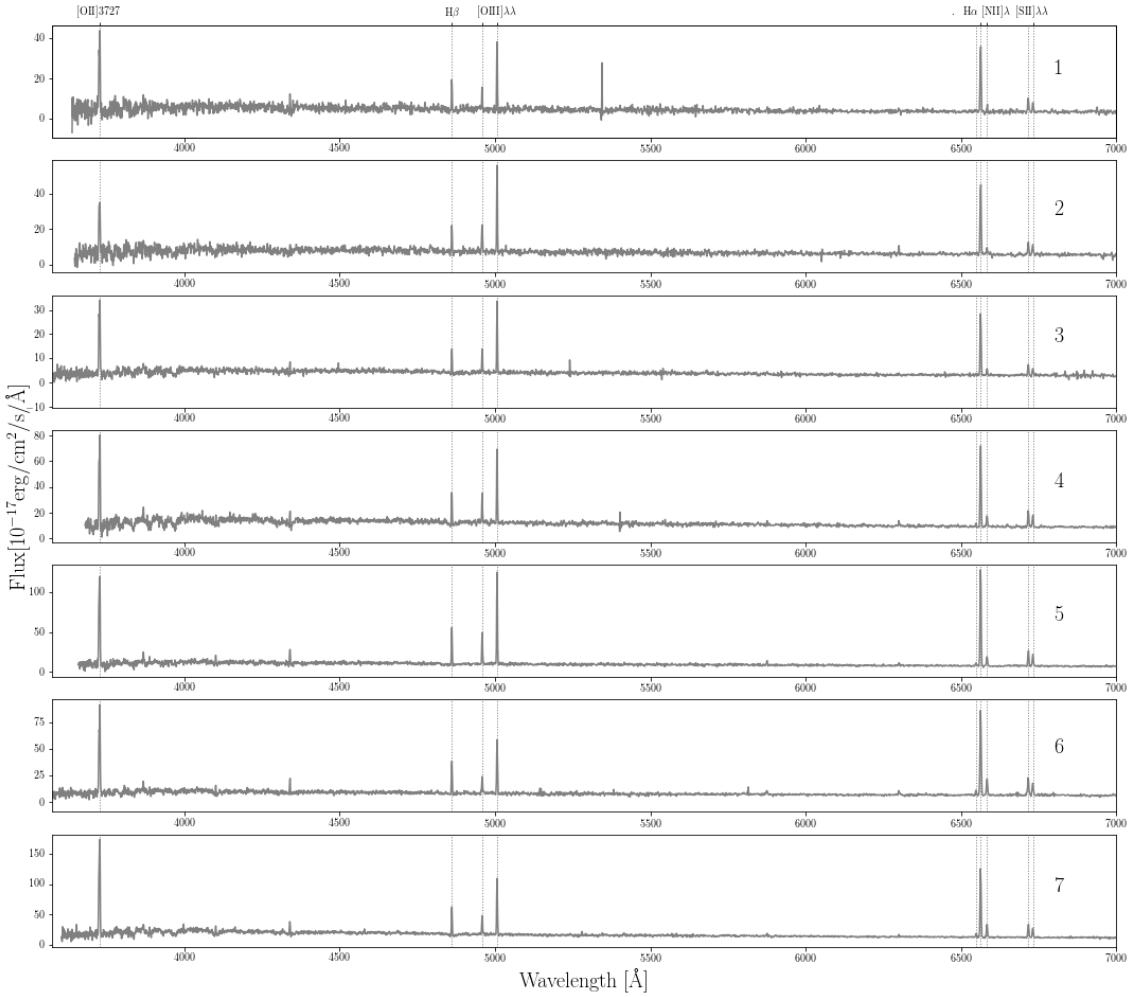

Figure SM 3.8: Spectra of the 21 galaxies defined in Fig. 3.7. Grey dotted lines show the location of the emission lines studied in this chapter. The galaxy label is indicated in each panel (right part).

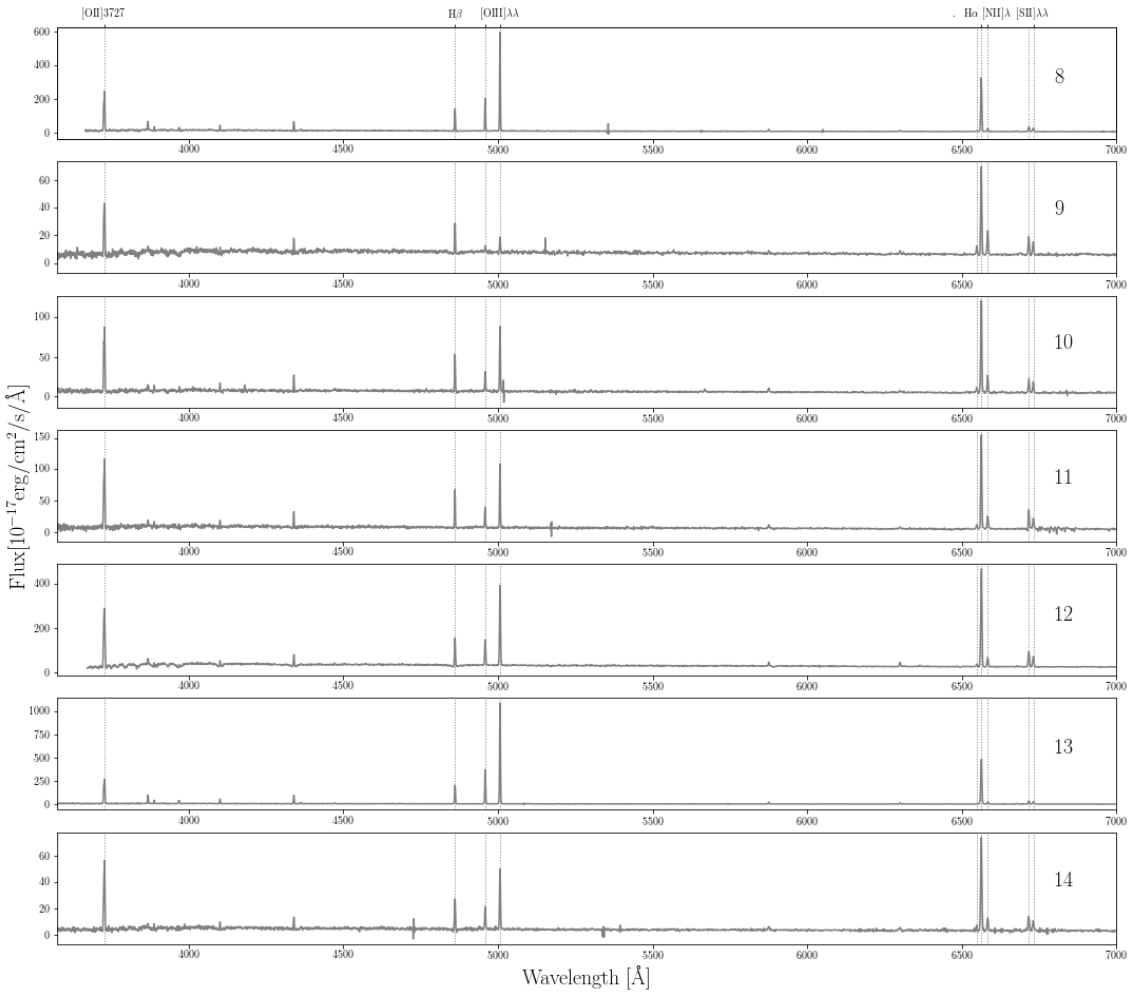

Figure SM 3.8: continued.

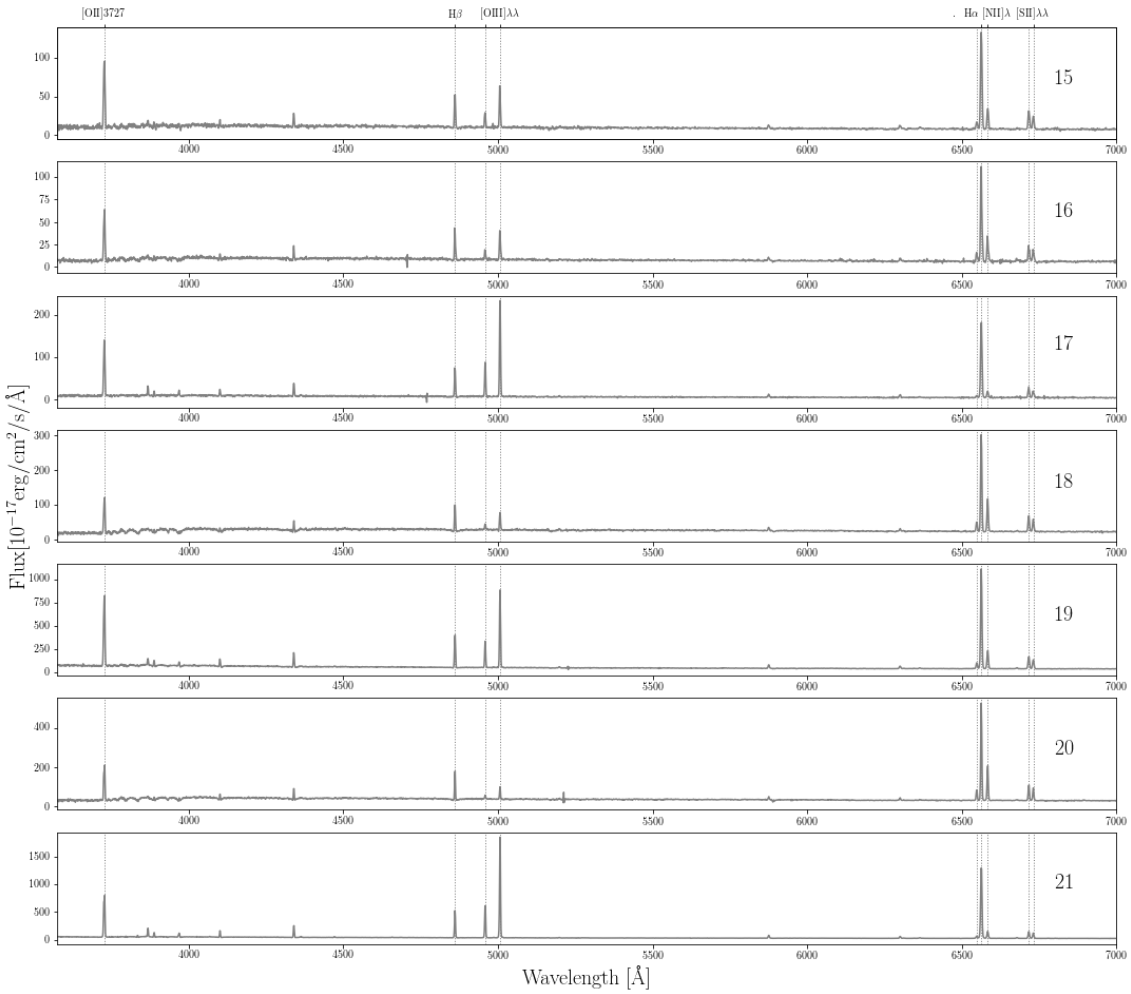

Figure SM 3.8: continued.

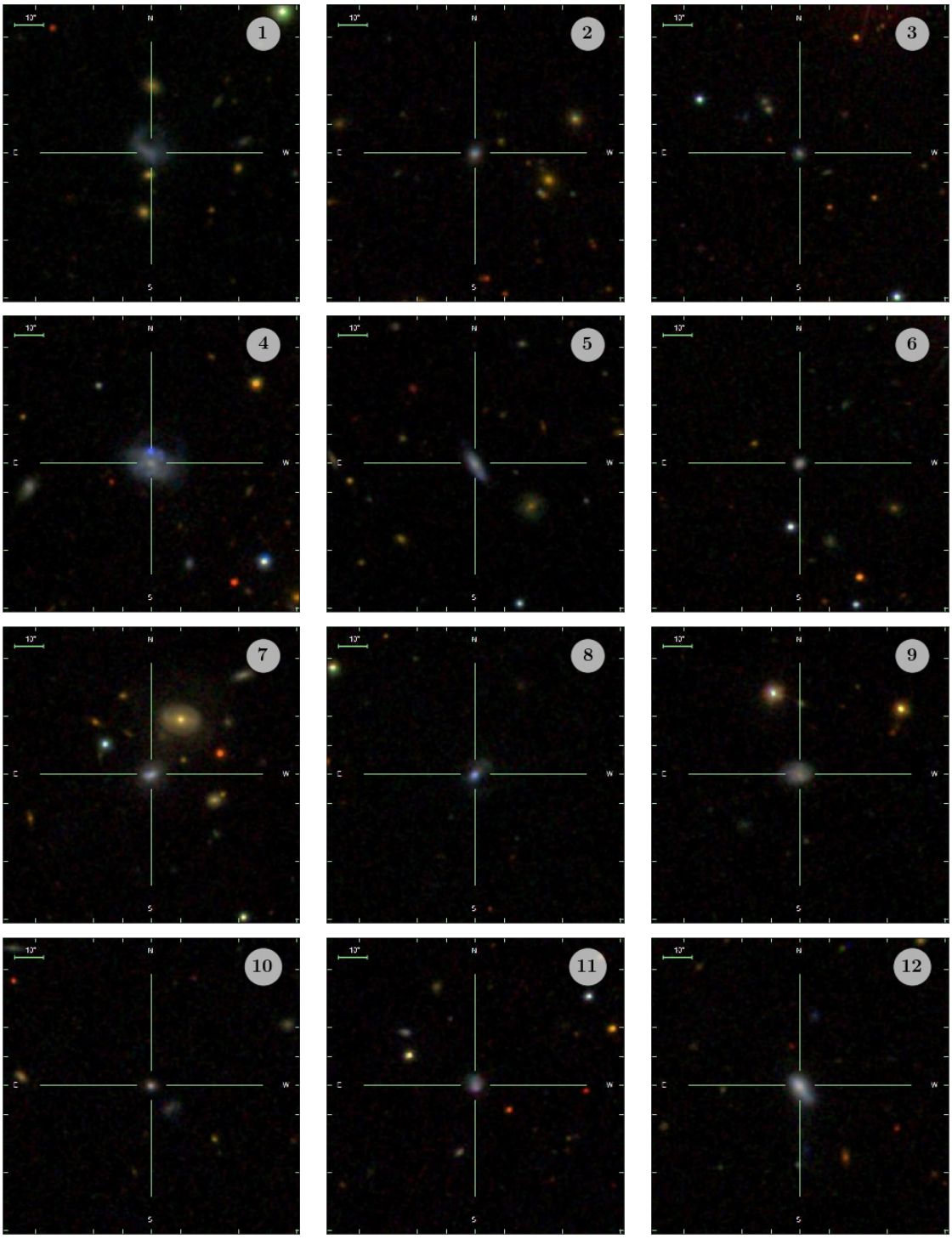

Figure SM 3.9: SDSS three-colour images of 21 galaxies defined in Fig. 3.7 in the SDSS-DR12 footprint. North is up and East is left. The galaxy label is indicated in each panel (upper right).

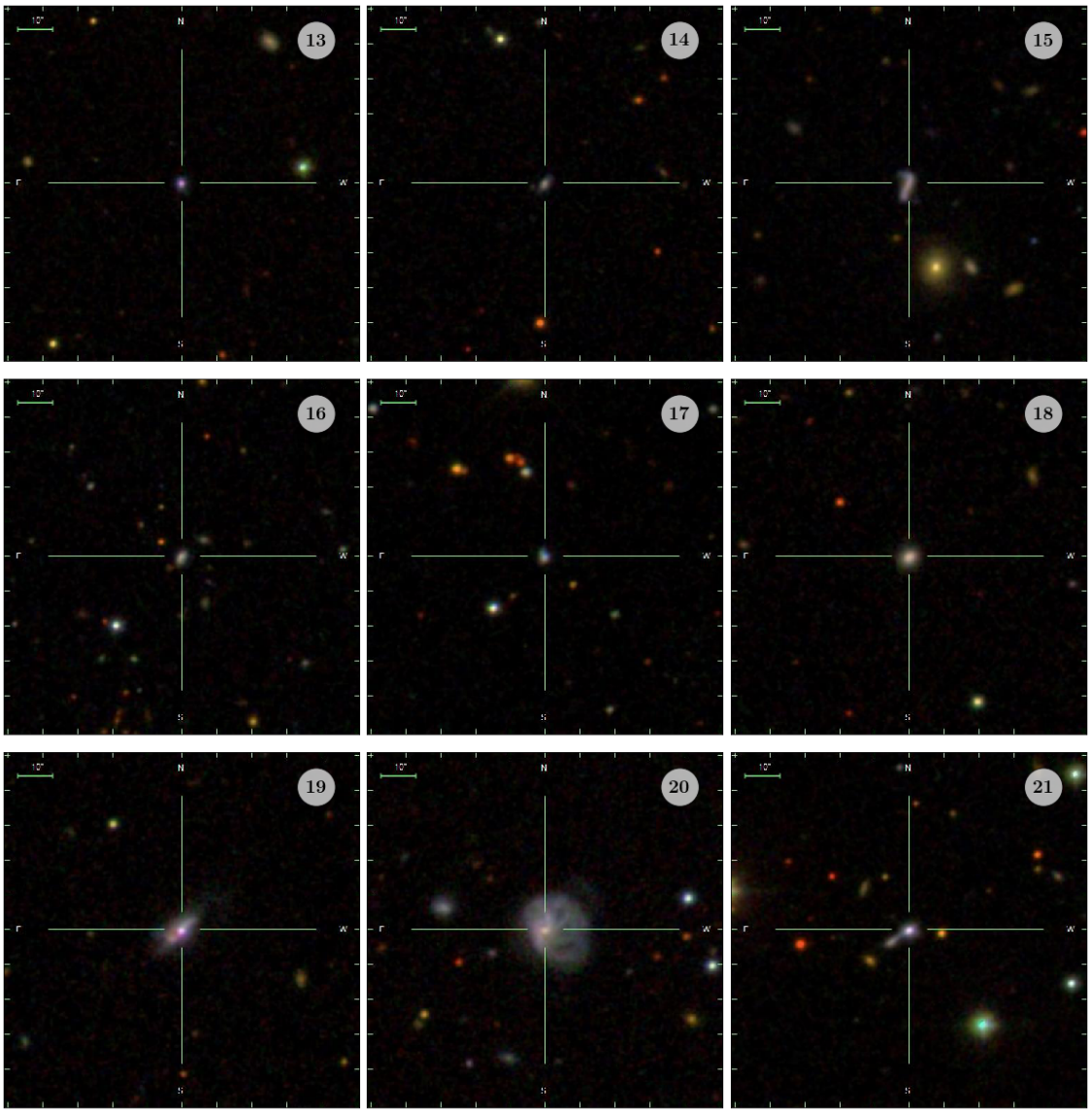

Figure SM 3.9: continued.

Chapter 4

Searching for intergalactic star forming regions in Stephan's Quintet with SITELLE. I. Ionised gas structures and kinematics

Contents

This chapter is based on the publication:
"Searching for intergalactic star forming regions in Stephan's Quintet with SITELLE. I. Ionised gas structures and kinematics"
by S. Duarte Puertas, J. Iglesias-Páramo, J. M. Vilchez, L. Drissen, C. Kehrig, and T. Martin
Published in A&A, 629, A102 (2019)

The data of the radial velocity and the Hα flux fitting are available at the CDS via anonymous ftp to cdsarc.u-strasbg.fr (130.79.128.5)
or via http://cdsarc.u-strasbg.fr/viz-bin/cat/J/A+A/629/A102

4.1 Introduction

Stephan's Quintet (SQ, Stephan 1877) is one of the most studied galaxy aggregates and it represents a unique laboratory for understanding how a compact group evolves. SQ is composed of elliptical (NGC7317 and NGC7318A) and spiral galaxies (NGC7319, NGC7320c, and NGC7318B). NGC7318B is a gas-rich galaxy that has experienced several interactions throughout its evolution (e.g. Moles et al. 1997; Sulentic et al. 2001). One foreground spiral galaxy (NGC7320) with a discordant redshift (Burbidge & Burbidge 1961) can also be seen in the field of view (FoV) of SQ.

Moles et al. (1997) and Sulentic et al. (2001) suggested that compact groups of galaxies are formed by acquiring intruder galaxies associated with a large-scale structure. All the galaxies of SQ, except NGC7318B, have evolved dynamically, losing their ISM. Moles et al. (1997) proposed an evolutionary model for SQ based on two intruders, an old intruder (OI, NGC7320c) and a new intruder (NI, NGC7318B). SQ is at an advanced state of interaction, evidenced by the existence of, for example, at least young and old tidal tails with ages of 150-200 Myr and 400-500 Myr, respectively (Fedotov et al. 2011); a large-scale shock region (LSSR, e.g. Allen & Hartsuiker 1972; Ohyama et al. 1998; Iglesias-Páramo et al. 2012) produced by an ongoing interaction between NGC7318B and both NGC7319 and debris material from previous interactions; a diffuse gas halo close to NGC7317 composed by old stars that indicates that the formation of SQ took place several Gyr ago (Duc et al. 2018).

From the kinematical point of view, SQ covers a large radial velocity range (~5500 – ~6600 $km\ s^{-1}$). The core of SQ (i.e. NGC7317, NGC7318A, and NGC7319) and NGC7320c show a mild radial velocity dispersion, whereas NGC7318B has an unusually high radial velocity dispersion compared to the others (ΔV ~1000 $km\ s^{-1}$), indicating that it is not bound to the SQ (Trinchieri et al. 2005). Classically, two radial velocity structures were detected by Sulentic et al. (2001): the gas associated with the SQ and the gas associated with NI, where most of the emission detected in the ISM comes from the NI. Iglesias-Páramo et al. (2012) observed three radial velocity components but could only focus on the lower part of the shock. The LSSR spans a wide range of redshift (e.g. Konstantopoulos et al. 2014). Its structure and gas distribution have not been entirely examined until now due to the inability to fully study the system (from NGC7320c to NGC7317).

SQ has been widely researched with different wavelengths by many authors: with radio (e.g. Williams et al. 2002; Lisenfeld et al. 2004; Guillard et al. 2012); ultraviolet (e.g. Xu et al. 2005; de Mello et al. 2012); X-ray (e.g. Trinchieri et al. 2003; Heida et al. 2012); infrared (e.g. Appleton et al. 2006, 2017; Cluver et al. 2010; Guillard et al. 2009); and visible (e.g. Moles et al. 1998; Iglesias-Páramo & Vílchez 2001; Sulentic et al. 2001; Mendes de Oliveira et al. 2004; Iglesias-Páramo et al. 2012; Trancho et al. 2012; Konstantopoulos et al. 2014; Rodríguez-Baras et al. 2014). There are also photometric studies (e.g. Gallagher et al. 2001; Fedotov et al. 2011; Duc et al. 2018) and simulations (e.g. Renaud et al. 2010; Hwang et al. 2012). Finally, several previous interferometric Fabry-Perot studies of the SQ (e.g. Sulentic et al. 2001; Mendes de Oliveira et al. 2001) have been done with diverse spatial coverages in wavelength-velocity resolution, though sometimes making difficult the discrimination between the emission of nearby lines at different velocities.

This work is based on the spectroscopic data from SITELLE (Grandmont et al. 2012), an imaging Fourier transform spectrometer (IFTS), attached to the Canada-France-Hawaii Telescope (CFHT). SITELLE allows us to study, for the first time, a large FoV considering the optical spectrum ranging from the UV atmosphere limit to the red, in order to study the physical, chemical, and kinematical properties of the entire SQ area. Our study presents an extensive spectral mapping that covers from the inner SQ 'core' to the large gas halo surrounding the SQ. SITELLE observations offer us a great opportunity to perform an unbiased search for the star forming and tidal emission regions (e.g. tidal dwarf galaxies, TDG) present in the SQ in order to study their origin and properties. These data also provide a detailed spectroscopic mapping of the extended shock zone and its associated emission, with a seeing limited spatial resolution (~0.8″). This is relevant to obtain a more complete view of the ionisation structure of the shock and its environment, discriminating in velocity space the shock ionised gas from other intervening gaseous material (e.g. HII regions from the arms of the central spiral galaxies, gas associated with the AGN main galaxy).

The structure of this chapter is organised as follows: in Sect. 4.2 we describe the data and the methodology used to select the Hα emission regions from the SQ. We detail our main results in Sect. 4.3. Finally, the discussion and main conclusions of our work are presented in Sect. 4.4. Line fluxes within the SN1, SN2, and SN3 data cubes, and the study of the physical properties and excitation conditions of the gas, will be presented in Chapter 5. Throughout the chapter, we assume a Friedman-Robertson-Walker cosmology with $\Omega_{\Lambda 0} = 0.7$, $\Omega_{m0} = 0.3$, and $H_0 = 70\,\mathrm{km\,s^{-1}\,Mpc^{-1}}$.

4.2 Observations and data analysis

4.2.1 Observations

SITELLE is an IFTS that aims to study the spatially-resolved spectra of extended sources. It has a FoV of 11′x11′ (0.32″ per pixel, Drissen et al. 2019), suitable for investigating complex and extensive systems of galaxies such as SQ. The observations were carried out in August 2015 and July 2016 (P.I. Drissen) under an average seeing of ~0.8″. The three filters SN1, SN2, and SN3 were used to capture the emission lines of our interest: [OII]λ3727, [OIII]$\lambda\lambda$4959,5007, Hβ, [NII]$\lambda\lambda$6548,6583, [SII]$\lambda\lambda$6716,6731, and Hα. Table 4.1 shows the observing parameters (right ascension or RA, declination or DEC, observing date, spectral range, number of steps, mean resolution, and the total exposure time) considered for each filter. Figure 4.1 shows a SITELLE deep-colour image of the SQ field composed using the integrated emission on the SN1, SN2, and SN3 data cubes (see Drissen et al. 2019, Sect. 5.4). We worked the data cubes in wavenumbers (cm^{-1}), which is SITELLE's natural units.

4.2.2 Reduction, calibration, and measurements

The data were fitted using the Python-based software ORCS (Martin et al. 2015). Data were recalibrated in wavelength using the OH sky lines that are visible in most parts of the FoV. We fitted the OH sky lines using the function SpectralCube.map_sky_velocity and the resulting corrections

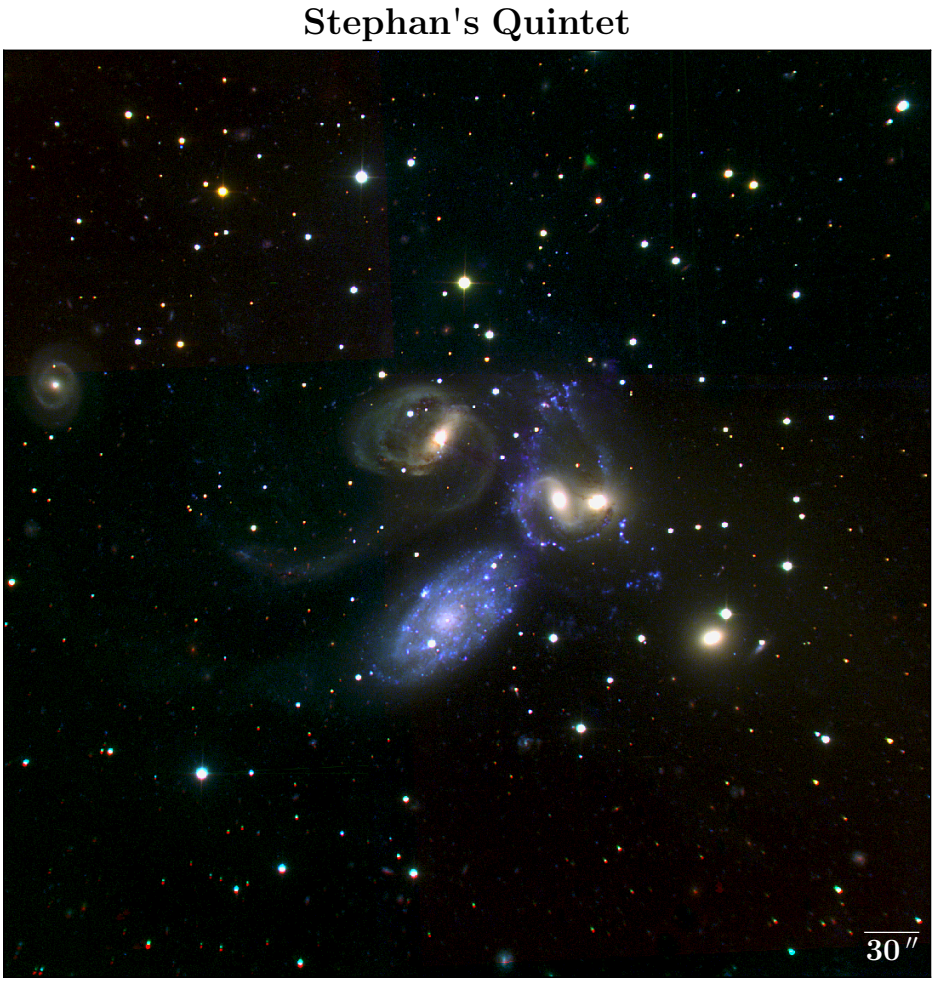

Figure 4.1: SITELLE deep-colour image of SQ composed using SN1, SN2, and SN3 data cubes. North is top and east is left. The distance considered for SQ in this chapter is d = 88.6 Mpc (from the NASA/IPAC Extragalactic Database known as NED). At the distance of SQ, 30″ corresponds to ~13.04 kpc.

Table 4.1: Observing parameters.

(1) Filter	(2) SN1	(3) SN2	(4) SN3
RA (h m s)	22:36:05.30	22:36:05.30	22:36:05.84
DEC (^{o} $'$ $''$)	33:58:59.9	33:58:59.9	33:59:09.6
Observing date	2016-07-09	2016-07-10	2015-08-07
			2015-08-08
Spectral range T > 90% (nm)	363-386	482-513	648-685
Number of steps	85	169	342
Exp. time/step (s)	75	65	25
Total exp. time (h)	1.77	3.05	2.37
Mean resolution, R	500	760	1560

The columns correspond to: (1) Filter properties; (2) SN1; (3) SN2; (4) SN3. See the text for detail.

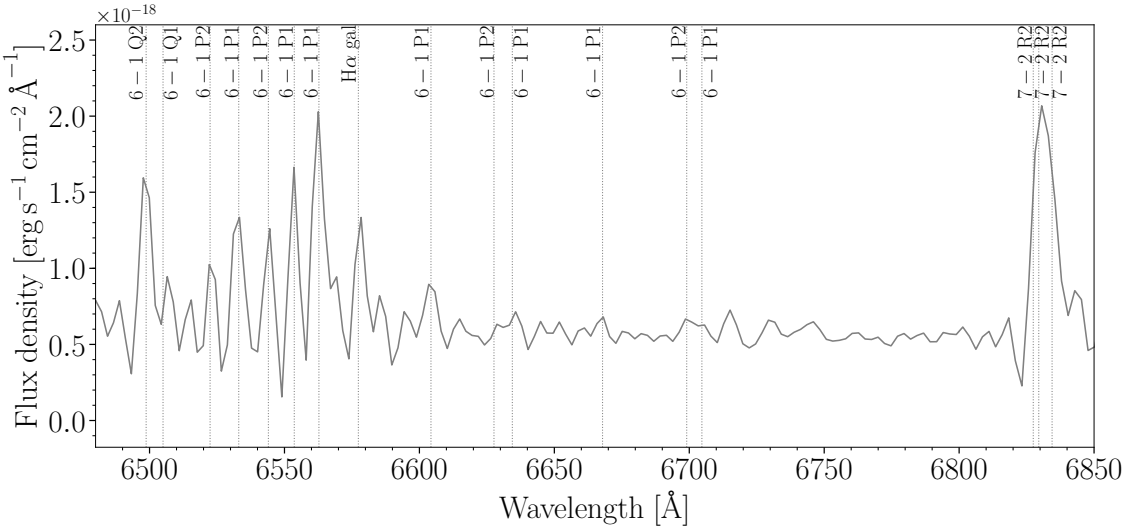

Figure 4.2: Median sky spectrum in SN3 data cube (2700 pixels have been combined). The dashed vertical lines show multiple known OH sky lines.

were implemented to the cube using SpectralCube.correct_wavelength (Martin et al. 2018). For each data cube, we subtracted the sky using the median sky spectrum from three dark regions (2700 pixels were used). For illustrative purposes, we show the median sky spectrum in the SN3 data cube in Fig. 4.2. In order to obtain a more precise radial velocity correction we used the function get_radial_velocity_correction. Through this function, we found a shift of 15 $km\,s^{-1}$ that was added to the measured velocity. The flux calibration was performed using the data cube of the standard star GD71. The Galactic extinction is very small, E(B - V) = 0.07, according to the NASA/IPAC Extragalactic Database known as NED[1], and we did not correct for it. The methodology used to analyse the data involved several steps that we describe below.

Searching for Hα emission

We considered a binning 3x3 to amplify the signal-to-noise ratio (~450 000 pixels). In addition a study was done only in Hα for a binning 6x6 (see Sect. 4.3.3)[2] in order to unveil the lowest surface brightness gaseous emission in SQ. Subsequently, we searched for the wavenumber position (k_{max}) where the maximum intensity peak of the Hα emission line (A_{max}) is found in the typical wavenumber range of SQ ($\Delta K_{SQ} = [14820, 15021]\,cm^{-1}$) and NGC7320 ($\Delta K_{NGC7320} = [15147, 15239]\,cm^{-1}$), selecting the largest A_{max} between them. Once we found the position of the maximum intensity, we derived the standard deviation when the transmission curve is higher than 90% for the SN3 filter (std_{90}). To compute std_{90}, the typical wavenumber range for the emission lines Hα, [NII]$\lambda\lambda$6548,6583, and [SII]$\lambda\lambda$6716,6731 of each pixel have not been considered. We selected those pixels with $\frac{A_{max}}{std_{90}} \geq 2.5$ (~25 800 pixels). We assumed that the maximum value corresponds to the Hα position. We know that the maximum in the AGN galaxy nucleus corresponds to [NII]λ6583 and this effect will be corrected later. We used the k_{max} value to derive the possible initial velocity for Hα ($v_{ini}(H\alpha)$) according to the following equation: $v_{ini}(H\alpha) = \left[\left(\left(\frac{1e7}{k_{max}\cdot\lambda(H\alpha)\cdot 0.1}\right) - 1\right)\cdot c\right]$, where $\lambda(H\alpha) = 6562.8$ nm and $c = 299792\,km\,s^{-1}$.

Identifying Hα emission regions

We fitted the spectrum for every selected pixel using the $v_{ini}(H\alpha)$ derived above. Initially, we fitted each spectrum to a sincgauss function (the convolution of a Gaussian with a sinc function) for Hα and [NII]$\lambda\lambda$6548,6583 simultaneously. The theoretical relation [NII]λ6548/6583=0.333 is considered. When the broadening of the Hα line was lower than 70 $km\,s^{-1}$, we adjusted the spectrum using a sinc function (the instrumental line shape, Martin et al. 2016). When no emission was detected in [NII]λ6583, we refitted the spectrum only for the Hα emission line. The output parameters are the radial velocity, broadening, intensity peak, flux, and the corresponding uncertainties, as well as the standard deviation of each spectrum. After fitting the Hα line, we selected the pixels with $contrast(H\alpha) = \frac{A_{fit}}{std_{90}} \geq 5$, where A_{fit} is the intensity peak of the Hα emission line obtained from the fitting, and $v_{ini}(H\alpha) \geq 5000\,km\,s^{-1}$ (~950 pixels). Figure 4.3 shows the Hα flux

[1] http://ned.ipac.caltech.edu/

[2] Binning 6x6 was chosen after an iterative process to maximise the the signal-to-noise ratio while minimising the contribution of the background sky.

(upper panel) and Hα radial velocity (lower panel) maps for the ~2100 pixels (binning 3x3) with contrast(Hα) $\geq$ 5 and without velocity restrictions. We detect Hα emission in several galaxies: NGC7319, NGC7320c, NGC7320 (the foreground galaxy with an average radial velocity of 786 $km\ s^{-1}$, see inset plot in the lower panel for more details), and the new dwarf galaxy in SQ (NG, see Sect.4.3.4 and ID. 176 in Table 4.2). Also, we detect Hα emission from the starbursts A and B (SQA and SQB, e.g. Xu et al. 1999). Additionally, this figure shows emission from the young tidal tail (YTT, e.g. Lisenfeld et al. 2002), LSSR, and the NI (e.g. Moles et al. 1997). We also detect emission to the left of NGC7317; this region is discussed in depth in Sect. 4.3.4. From the sample of pixels selected above, we searched for all the Hα emission region candidates associated with the SQ. To do so, we first grouped the spatially associated emitting pixels. Then, the individual Hα regions associated with each group of pixels are defined searching for the local emission peaks in the Hα map using the Python-package ASTRODENDRO[3]; The membership of each group of pixels to a given individual Hα region has been defined from the segmentation method using the Python packages SCIPY.NDIMAGE and SKIMAGE.MORPHOLOGY.WATERSHED. This method allows us to define a population of 209 SQ Hα region candidates.

One velocity component analysis for each SQ Hα emission region

For each Hα emission region we obtained the integrated spectrum adding the flux of its pixels; then all integrated spectra were fitted using the ORCS function ORCS.FIT_LINES_IN_INTEGRATED_REGION. The spectral lines Hα and [NII]$\lambda\lambda$6548,6583 are fitted to a sincgauss function simultaneously, and when broadening of the Hα line is smaller than 70 $km\ s^{-1}$, a sinc function was used, as detailed above. As the beginning of the SN3 transmission curve coincides with the emission lines [SII]$\lambda\lambda$6716,6731 at SQ's redshift, we only take into account in the fit the spectral line [SII]λ6716 for those Hα emission regions with radial velocities lower than 6260 $km\ s^{-1}$, and [SII]λ6731 for those Hα emission regions with velocities lower than 5760 $km\ s^{-1}$. The output parameters are the radial velocity, broadening, intensity peak, total flux, and the corresponding uncertainties, as well as the standard deviation of each spectrum. The emission lines from the SN1 and SN2 data cubes were fitted using the velocity found in the previous step for Hα as a reference. It is important to note that we assumed the Hα radial velocity as the representative velocity for every Hα emission region. We followed the same methodology as previously described. For SN1 we fitted the spectral line [OII]λ3727. For SN2 we fitted the lines Hβ and [OIII]$\lambda\lambda$4959,5007 in the wavenumber range [19493, 20746]cm^{-1} (assuming the theoretical relation [OIII]λ4959/5007=0.333). The standard deviation for the SN1 and SN2 filters (std_{90}) was derived as above. Figure 4.4 illustrates examples of the line fits for the SN1, SN2, and SN3 filters. All the line fluxes fitted in the SN1, SN2, and SN3 data cubes will be presented in Chapter 5.

[3]This tool estimates the background in our images and we searched the regions that have FWHM ~9 pixels and have peaks ~ 3σ above the background, from our sample of selected pixels.

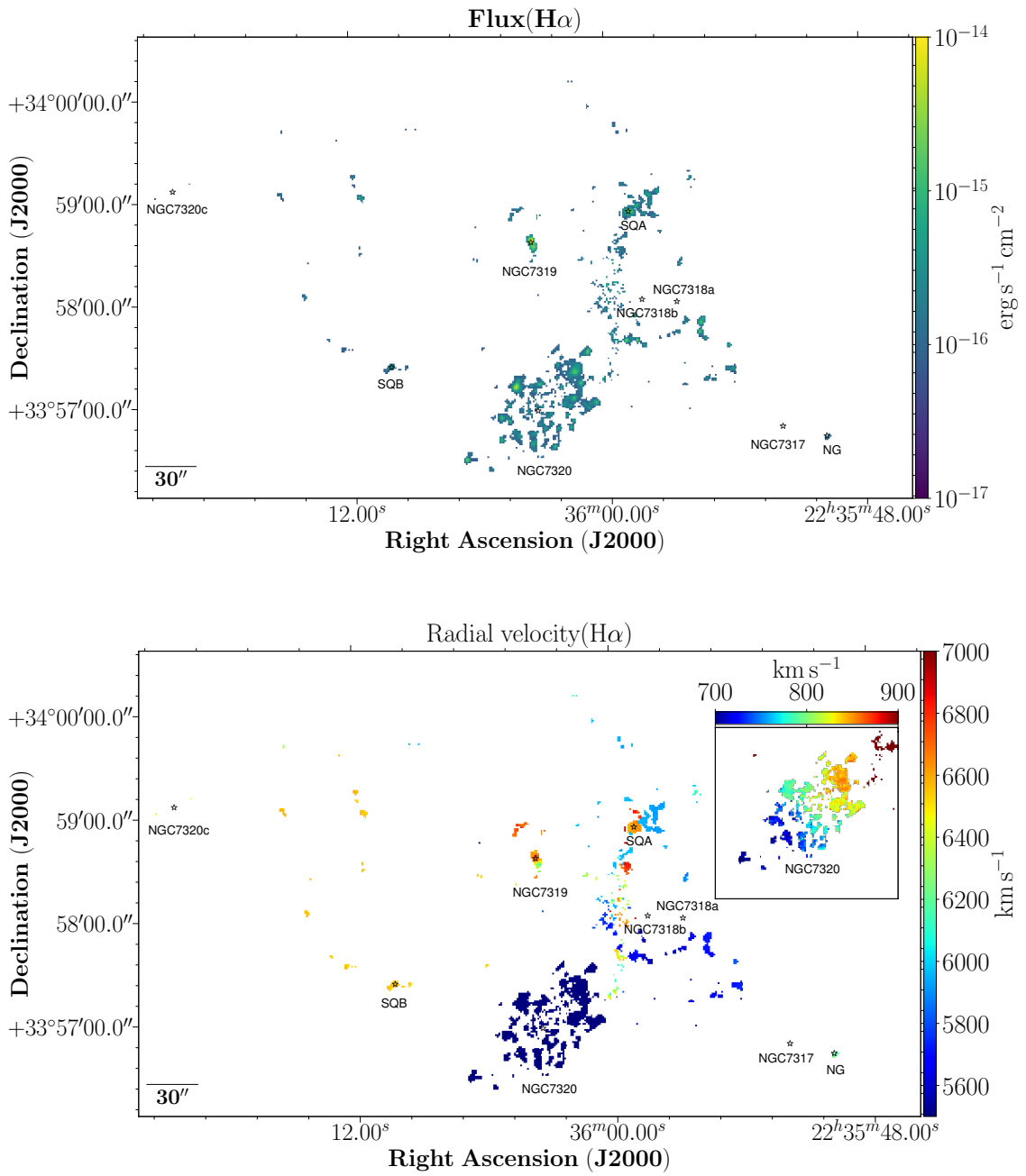

Figure 4.3: (Top panel) Hα flux map of SQ considering pixels with Hα contrast ≥ 5. (Bottom panel) Hα radial velocity map of SQ considering pixels with contrast(Hα) ≥ 5. The inset plot in the right panel indicates the radial velocity map of NGC7320, the foreground galaxy, with contrast(Hα) ≥ 5 (see the text for details). NG (new dwarf galaxy) indicates the position of the new dwarf galaxy in SQ (see Sect.4.3.4).

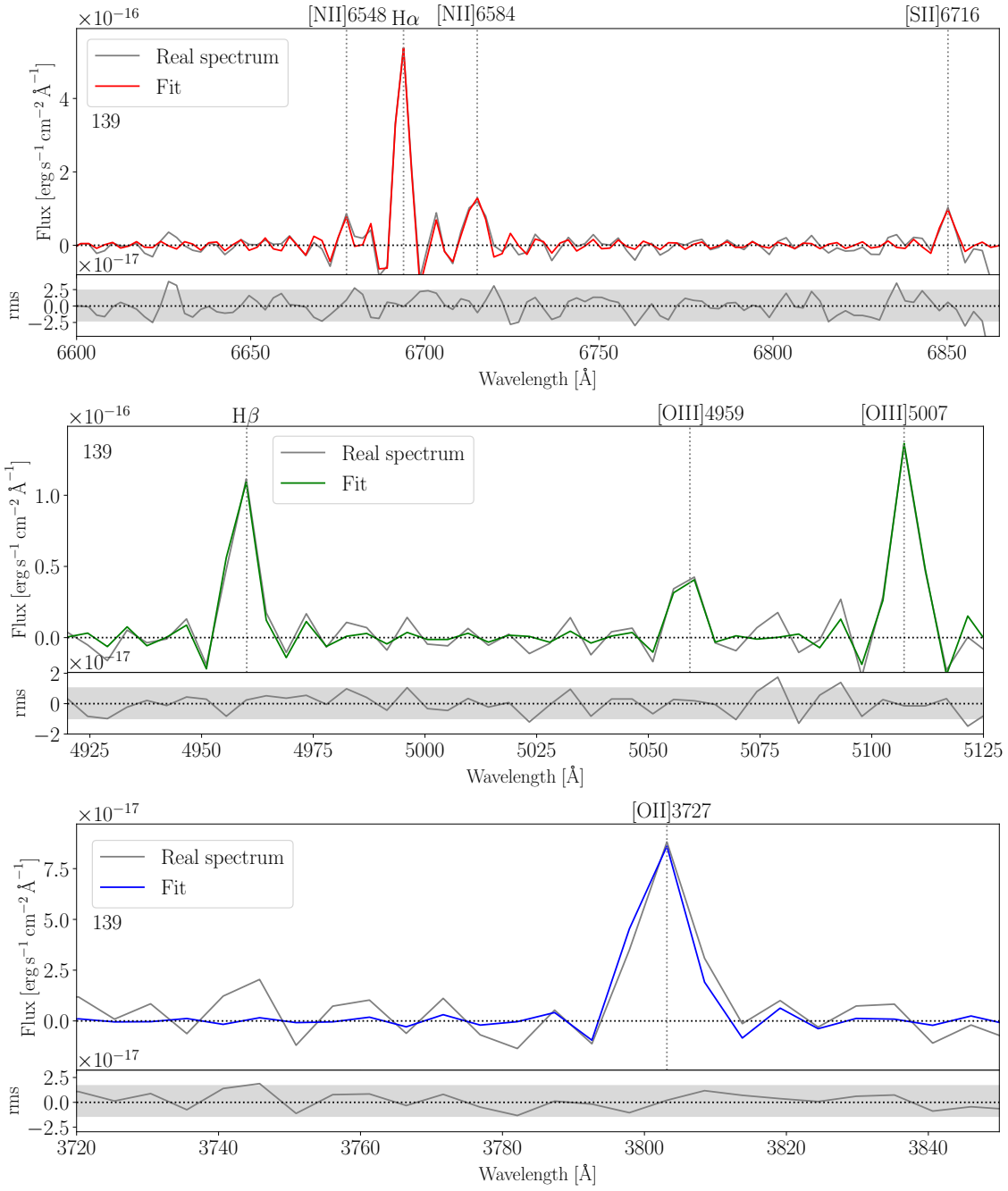

Figure 4.4: Fitting example: Spectra from region 139. In each upper panel, the grey line shows the real spectrum and the red, green, and blue coloured lines show the fit obtained with ORCS in the SN3, SN2, and SN1 filters, respectively. In the upper panels, the grey dotted lines show the location of the emission lines studied for this region. In the lower panels, the grey line shows the residual after the fit. The horizontal grey band indicates the 3σ scatter.

Complex kinematics spectral fitting of emission regions

The one-velocity-component spectral fitting procedure produced unsatisfactory results for a selection of emission regions. A close visual inspection of these fits showed complex kinematics, with large velocity dispersion for the emission regions associated with the AGN galactic nucleus of NGC7319 and the shock region (see Fig. 4.3 lower panel). Taking into account our spectral resolution and the signal-to-noise ratio, we studied only two velocity components for those emission regions with the velocity components resolved, as follows:

The Hα, [NII]$\lambda\lambda$6548,6583, and [SII]$\lambda\lambda$6716,6731 emission lines of the spectrum of the SQ shock region were fitted simultaneously in the wavenumber range [14820, 15021]cm^{-1} and with a sincgauss function. When one or both velocity components presented contrast in the Hα line lower than three, we assumed that they fit the criterion to be considered as one velocity components. Finally, for the rest of the emission lines ([OII]λ3727, Hβ, and [OIII]$\lambda\lambda$4959,5007), we performed a two-component fit using the velocities and line widths derived from the Hα fit as input. We found 22 SQ Hα emission regions with line profiles that can be fit with two velocity components.

4.2.3 Sample of SQ Hα emission regions

Following the methodology described above, we found 209 candidate emission regions in the SQ field. However, in this work we only focus on those regions that belong to SQ (hereafter, 'SQ Hα emission regions') according to the following criteria: i) the radial velocity of the region is within the radial velocity range of SQ (between ~5600 and ~7000 $km\ s^{-1}$); and ii) at least one additional emission line besides Hα has been detected in the data cubes. According to this criteria, 175 SQ Hα emission regions were found. From these regions, 22 present broad Hα profiles that have been fit using two velocity components. There may be more than two velocity components, but for our spectral resolution, the residuals of the fit produced are found to be within a band of width 3 sigma rms of the defined continuum window. We selected the minimum number of components obtained, considering the resolution and the signal-to-noise ratio of our data cubes.

In Figs. 4.6 and 4.7 we show the sample of 175 SQ Hα emission regions found in this work. The location of the 15 extra Hα emitter regions presented in Table 4.3. are also shown. In Table 4.2 we present the catalogue of these SQ Hα emission regions. In Column 1 the region name is presented, Column 2 shows the RA and Dec coordinates, Columns 3 and 4 show the radial velocity and the area, Column 5 indicates the corresponding subzone. We add the information for NGC7320c which is discussed in Sect. 4.3.4 (ID 1 in Table 4.2). We have compared our results with the recent works by Konstantopoulos et al. (2014) and Iglesias-Páramo et al. (2012). From the 40 Hα emitting regions presented in Konstantopoulos et al. (2014), 34 have the same α, δ as our regions. Twenty-five of these regions can be directly compared since they present a single value of radial velocity. When compared with Iglesias-Páramo et al. (2012), which has lower spatial resolution, only six regions were identified (pointings M and S). Fig. 4.5 shows the distribution of the difference between our Hα radial velocity and previous works, Δv. The mean of the differences between our Hα radial velocities and the ones in these previous works, Δv, is $\Delta v = 1.1 \pm 14.9\ kms^{-1}$, which is consistent to within the errors.

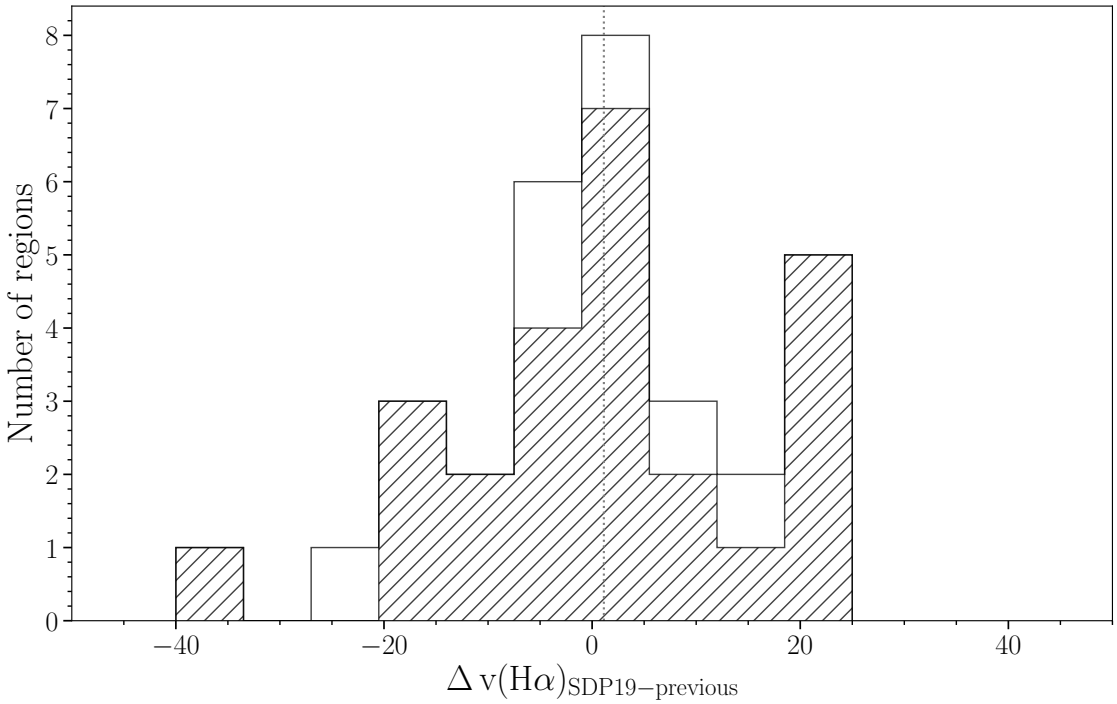

Figure 4.5: Distribution of difference between Hα radial velocity from this work, v(H$\alpha_{This\ work}$), and previous work (Iglesias-Páramo et al. 2012; Konstantopoulos et al. 2014). Grey vertical dashed line shows the position of the average found for Δv. The dashed histogram represents the sample of SQ HII regions when we compare the Hα radial velocity from this work and Konstantopoulos et al. (2014).

For the sake of the analysis of the sample, in the following we separate the SQ emission regions in two sub-samples: lower radial velocity sub-sample (LV) composed of those regions where the radial velocity $\leq 6160\ km\ s^{-1}$ (for the two velocity components fit, the lowest radial velocity was considered); conversely, the higher radial velocity sub-sample (HV) is defined including all the regions with radial velocity $> 6160\ km\ s^{-1}$ (for the two velocity components fit, the greatest radial velocity was considered). The nominal radial velocity of $6160\ km\ s^{-1}$ was chosen as a limit value to highlight the discrete emission features associated with NI (NGC7318B).

Figure 4.8 presents the different zones and subzones defined by the 175 SQ Hα emission regions (see below). In Fig. 4.9 we show the radial velocity versus RA diagram in the upper right panel; Dec versus radial velocity diagram in the upper right panel; and a three-dimensional view (i.e. RA – Dec – radial velocity diagram) of SQ Hα emission regions in the lower panel. From the three-dimensional information obtained considering Figs. 4.8 and 4.9, we have defined 12 zones and 28 subzones in SQ. We have divided the zones (and thus the subzones) in the following way: i) YTT (e.g. Lisenfeld et al. 2002), so that North and South strands are respectively YTTN and YTTS, and NGC7320c is the old intruder (OI); ii) NGC7319 (NGC7319 nucleus, NGC7319 'arm', North lobe); iii) Hα 'bridge'; iv) high radial velocity strands, Hs (H1 and H2); v) SQA (e.g. Xu et al. 1999); vi) low radial velocity strands, Ls (L1, L2, L3, and L4); vii) shock strands, Shs (Sh1, Sh2, Sh3, and Sh4); viii) North and South of SQA (NSQA and SSQA, respectively); ix) tidal tail at North of NSQA (NW, e.g. Renaud et al. 2010); x) NI (e.g. Moles et al. 1997) strands, NIs (NI1, NI2, NI3, NI4, and NI5); xi) southern debris region (SDR, e.g. Fedotov et al. 2011); and xii) NG (see Sect. 4.3.4). Also, the 15 extra Hα emitter regions from Sect. 4.3.5 are shown. Section 4.3.3 explains in more detail the connections between each zone and subzone. For each zone a detailed study was made to understand better the kinematic and chemical processes acting on SQ (see Sect. 4.3 and Chapter 5.

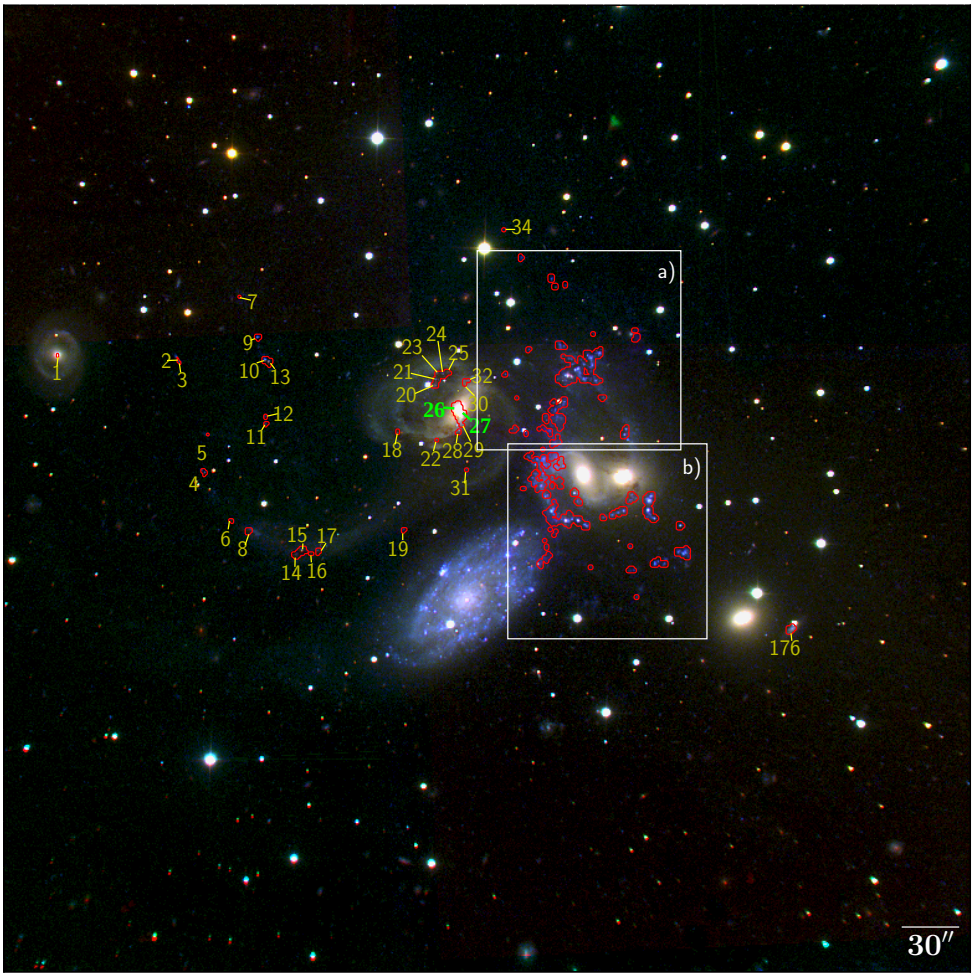

Figure 4.6: SITELLE composite image from deep SN1, SN2 and SN3 data cubes of SQ. The red lines represent the Hα contours corresponding to all 175 SQ Hα emission regions defined in Sect. 4.2.3. The Hα regions from YTT, NGC7319, NGC7320c, and NG are labelled according to the nomenclature from Table 4.2. Green and yellow labels identify the SQ Hα regions showing a broad and narrow line profile, respectively. A zoomed-in view of the areas marked with the white rectangles are shown in Fig. 4.7.[a]

[a]Front page cover in the scientific journal Astronomy and Astrophysics in September 2019.

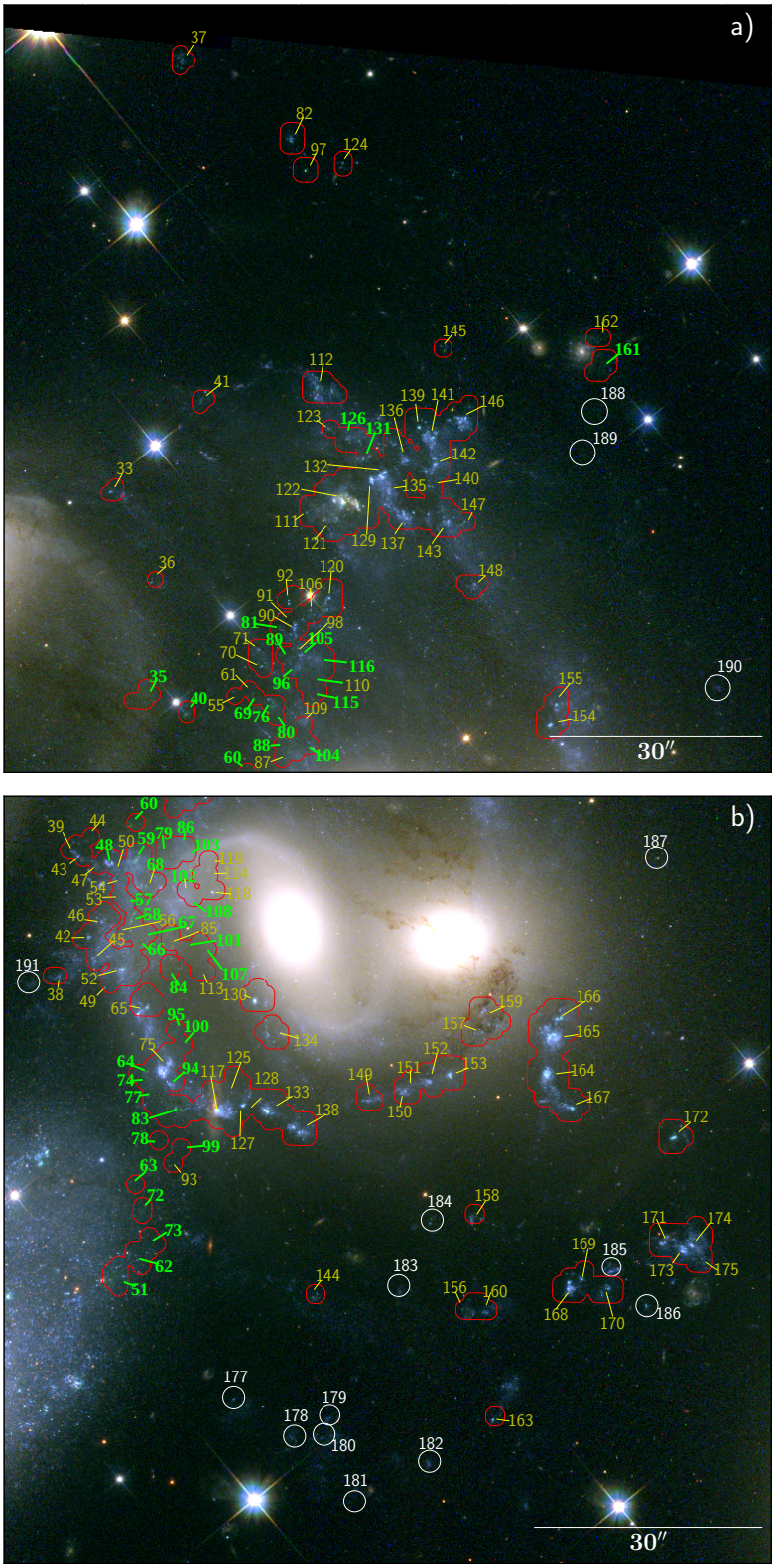

Figure 4.7: Zoomed-in view of image from Hubble Space Telescope Wide Field Camera 3, also known as HST/WFC3 (PID 11502, PI Keith S. Noll) showing regions a) and b) from Fig. 4.6. The red circles and labels are defined as in Fig. 4.6. White circles show the location of the 15 extra Hα emitter regions presented in Table 4.3. Green and yellow labels identify the SQ Hα regions showing a broad and narrow line profile, respectively.

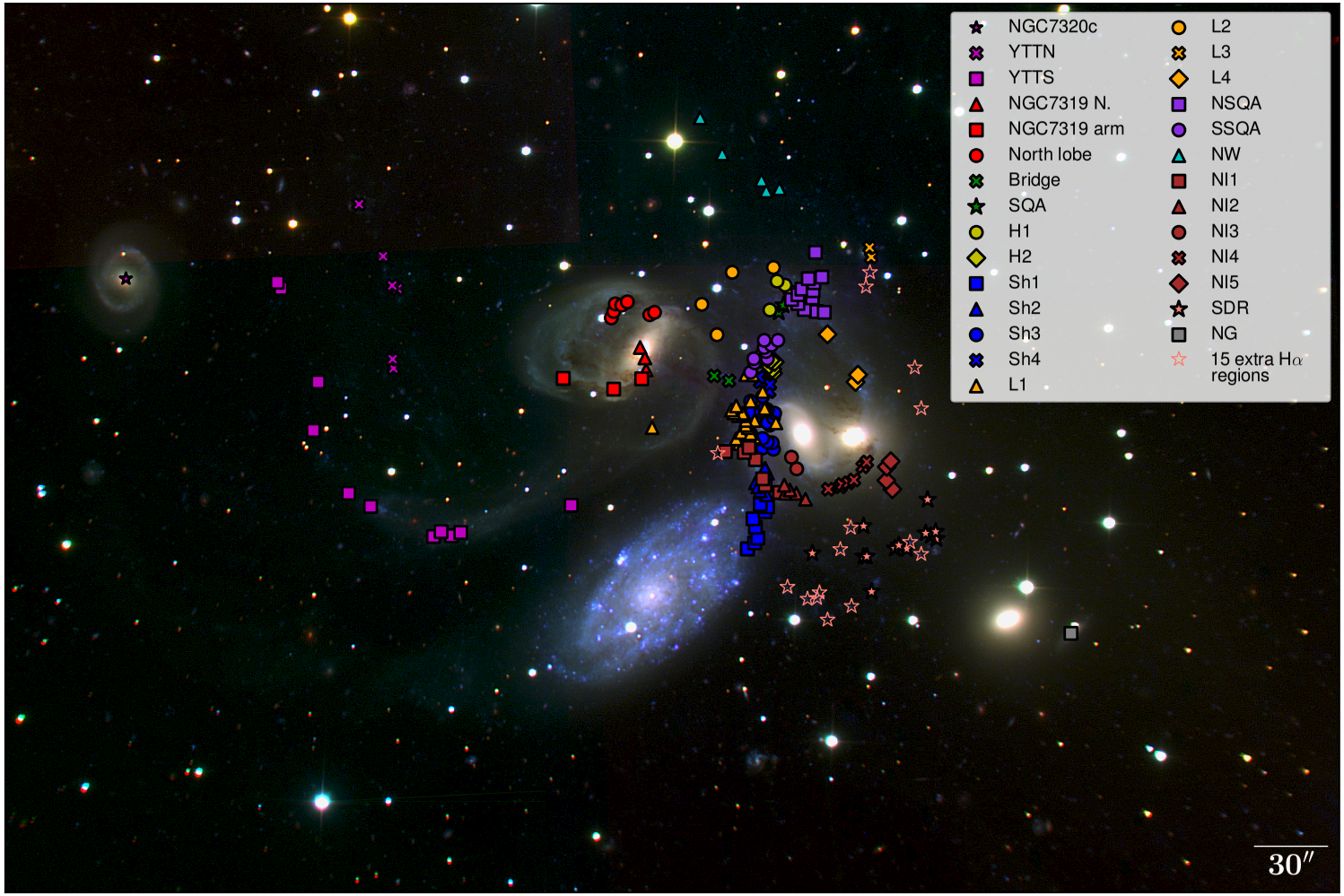

Figure 4.8: Different systems of emission line objects defined here and indicated on SITELLE deep-colour image of SQ. Shown are the positions of YTTN and YTTS (magenta crosses and squares, respectively); NGC7319 nucleus, 'arm', and North lobe (red triangles, squares, and circles, respectively); bridge (green crosses); SQA (green stars); Hs (H1: yellow circles; H2: yellow diamonds); Shs (Sh1: blue squares; Sh2: blue triangles; Sh3: blue circles; Sh4: blue crosses); Ls (L1: orange triangles; L2: orange circles; L3: orange crosses; L4: orange diamonds); NSQA and SSQA (violet squares and circles); NW (cyan triangles); NIs (NI1: brown squares; NI2: brown triangles; NI3: brown circles; NI4: brown crosses; NI5: brown diamonds); SDR (salmon stars); and NG (grey squares). In addition, the salmon unfilled stars show the position of the 15 extra Hα emitter regions in Sect. 4.3.5 from Table 4.3.

4.3 Results

4.3.1 Kinematical properties of SQ Hα emission regions

Figure 4.10 shows the radial velocity maps for the 175 SQ Hα regions. The SQ Hα regions have been catalogued in two velocity sets, LV and HV, according to the definitions given in Sect. 4.2.2. Traditionally, two velocity ranges were observed in the shock zone. However, Iglesias-Páramo et al. (2012) showed an additional velocity range in the shock region. As can be seen in Fig. 4.3, at least five different velocity ranges are clearly distinguished, therefore, we can see two more velocity components. For low radial velocity components, two radial velocity ranges are shown: i) v=[5600-5900] $km\ s^{-1}$, associated with the NIs and the SDR; ii) v=[5900-6100] $km\ s^{-1}$, associated with the North of NSQA, SSQA, NW, and the Ls. For high radial velocity components, three radial velocity ranges are shown: i) v=[6100-6600] $km\ s^{-1}$, associated with the Shs, connecting the part of SQ with high radial velocities with the lower radial velocities; ii) v=[6600-6800] $km\ s^{-1}$, associated with the YTT, SQA, and AGN North lobe; iii) v=[6800-7000] $km\ s^{-1}$, associated with the Hs, the strands that connect Shs with SQA, and those regions of strands Sh3 and Sh4 (e.g. ID 56, 80b, 85, 89b, and 113) that are closest to the Hs strands.

The upper panel of Figure 4.10 shows a radial velocity gradient that was found in the SQ Hα emission regions from NI2 to SSQA, NI2 to NI3, and NI2 to NI5, increasing northwards up to 6100 $km\ s^{-1}$ (the minimum radial velocity is in region 149, radial velocity ~5610 $km\ s^{-1}$). Located North of NSQA we can see the tidal tail NW with radial velocity ~6000 $km\ s^{-1}$. According to the simulations from Renaud et al. (2010), NW could have been formed by the merger between NGC7318B and NGC7318A. We have no clear evidence of this, but we believe that NSQA and SSQA have participated in this formation. This possible large-scale structure, which could be linked with the region 145 (v=5994 $km\ s^{-1}$), is revealed. NI strands and SDR have lower radial velocities than ~5900 $km\ s^{-1}$. Moreover, regions with radial velocities higher than 6160 $km\ s^{-1}$ are presented in Fig. 4.10 (lower panel). We detected several strands (Shs) that connect HV with LV parts covering a range of radial velocities from ~6100 to ~6600 $km\ s^{-1}$. SQA has radial velocity ~6670 $km\ s^{-1}$. Additionally, the North lobe has radial velocities from 6750 to 6870 $km\ s^{-1}$. We found two SQ regions in the Hα 'bridge' (radial velocity ~6400 $km\ s^{-1}$, see Sect.4.3.3 for more information). The strands H1 and H2 connect Shs with SQA. The radial velocity and the Dec increase in H1 up to region 111 (radial velocity ~7000 $km\ s^{-1}$). From region 111 to SQA (in H2) the radial velocity decreases. The NGC7319 nucleus (regions 26, 27, and 29) shows radial velocities between ~6350 and 6760 $km\ s^{-1}$ as a result of the outflow from the nucleus (Rodríguez-Baras et al. 2014). It is noteworthy that the NGC7319 'arm' has regions with radial velocities from ~6710 (in region 28) to ~6600 $km\ s^{-1}$ (in region 18). We do not discard the possibility that it is produced by the interaction between NGC7319 and another galaxy and it will remain as a conatus of tidal tail. The YTT has an average radial velocity of ~6620 $km\ s^{-1}$. YTT increases its radial

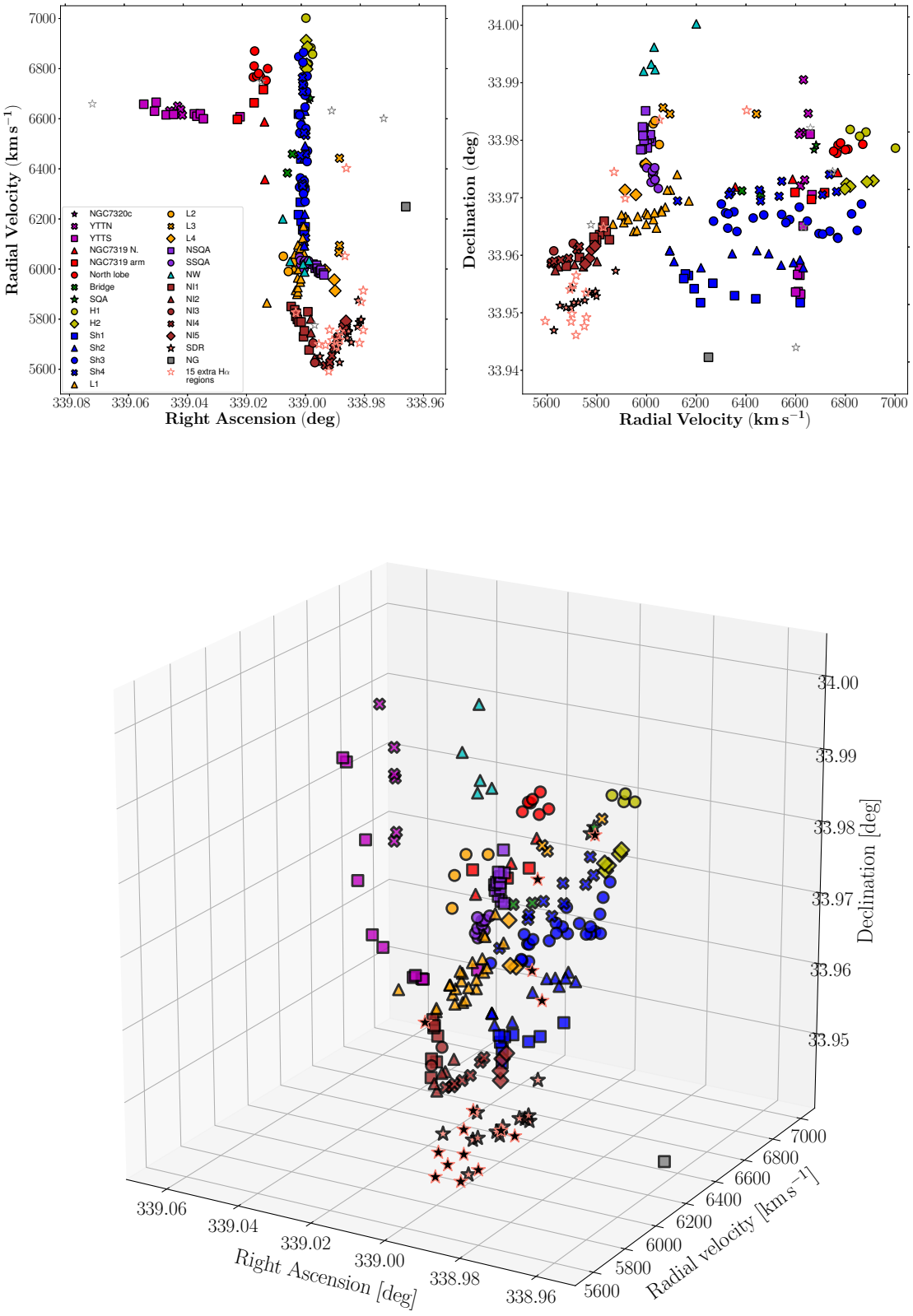

Figure 4.9: Shown in the upper left panel is the radial velocity versus RA diagram; in the upper right panel: Dec versus radial velocity diagram; in the lower panel: three-dimensional view of SQ Hα emission regions (RA, Dec, and radial velocity diagram). All the points in the figures have the same colours and markers as Fig. 4.8. In both upper panels, the nuclei of NGC7320c, NGC7319, NGC7318B, NGC7318A, and NGC7317 are marked with an unfilled grey star.

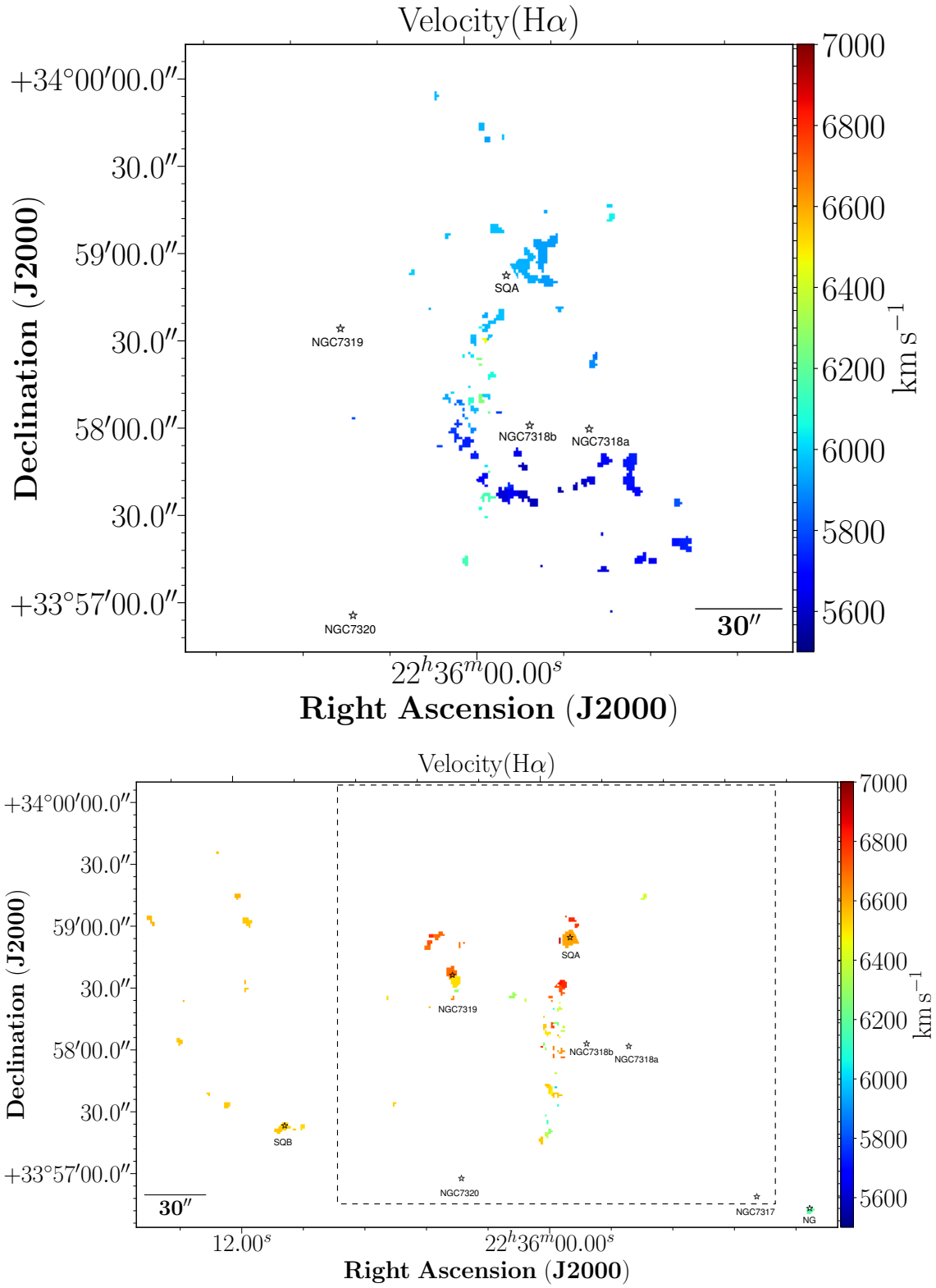

Figure 4.10: SQ spatial map, colour-coded according to radial velocity of Hα for LV sample (upper panel) and HV sample (lower panel). The box in the lower panel indicates the zoomed zone shown in the upper panel.

velocity as we move away from NGC7319. Another interesting finding is the NG (see Sect. 4.3.4).

4.3.2 Regions with broad line profile

As we can see in Sect. 4.2.3, SQ presents regions with broad and narrow line profiles. The regions showing a broad line profile are located in the LSSR, the AGN nucleus of NGC7319, and the L1 and L4 zones. In Fig. 4.11 we show several examples of these individual regions (noted as ID 58, 59, 60, 68, 83 in Table 4.2) across the LSSR, and their corresponding fits using two sincgaussian functions, as explained in Sect. 4.2.3. A close visual inspection has also been carefully performed of all the fits of the broad line profile.

In Fig. 4.12 we present the broad Hα profile we found for region 161 located in the L4 area, a somewhat outlying zone (see Fig. 4.8), and its two velocity component fits. As far as we know, this broad profile is presented here for the first time for region 161. It is tempting to associate this broad profile region with a nearby secondary maximum apparent in the X-Ray maps of Trinchieri et al. (2005). However, the precise nature and the excitation of this gas still has not been ascertained.

In order to show the wide range of velocities encompassed within LSSR, its integrated emission is presented in Fig. 4.13 in the SN1, SN2, and SN3 filter windows. To obtain these spectra, we considered all the Hα emission detected (binning 6x6 and contrast ≥ 2) with Hα radial velocities $\geq$ 5000 $km\ s^{-1}$ within a rectangle centred on the coordinate RA=339 deg and Dec=33.966 deg, with a width of ΔRA= 27.786 arcsec and a height of ΔDec=99.512 arcsec (defined according to the definition of the flux, as determined in the next section). As expected, the integrated spectra from LSSR show broad lines and several predominant peaks (e.g. Hα and [NII]λ6584). For illustrative purposes, these can be compared with a typical narrow-lined Hα emission region (i.e. ID 164; Fig. 4.14).

4.3.3 Unveiling low surface brightness Hα emission

In order to detect the low surface brightness Hα emission regions, we produced a deep overview of all the Hα emission of the SQ system in Fig. 4.15. This was produced using a binning 6x6, contrast(Hα)$\geq$2, and radial velocities in the range of the SQ, in order to increase the detectability of the low surface brightness emission, as explained in Sect. 4.2.2. From a statistical analysis of our Hα flux measurements, we find that below a value of Hα flux per pixel of 6×10^{-18} erg/s/cm^2 we can distinguish a very low surface brightness Hα component besides the SQ Hα emission regions measured, see Fig. 4.16. The upper right panel of Fig. 4.15 shows a zoomed-in view of the LSSR, whereas the lower panels, as in Fig. 4.9, shows an overlapped view of the symbols corresponding to the very low surface brightness regions detected with the SQ Hα emission regions found in Sect.4.2.3. This low surface brightness gas emission represents different components spread throughout the whole system. This gives us important information about the connections between the different SQ zones (see Sect. 4.2.3) and helps us to better understand the complexity of SQ.

At lower radial velocities, v$\leq$6160 $km\ s^{-1}$ (see lower panels in Fig. 4.15), we observe at least

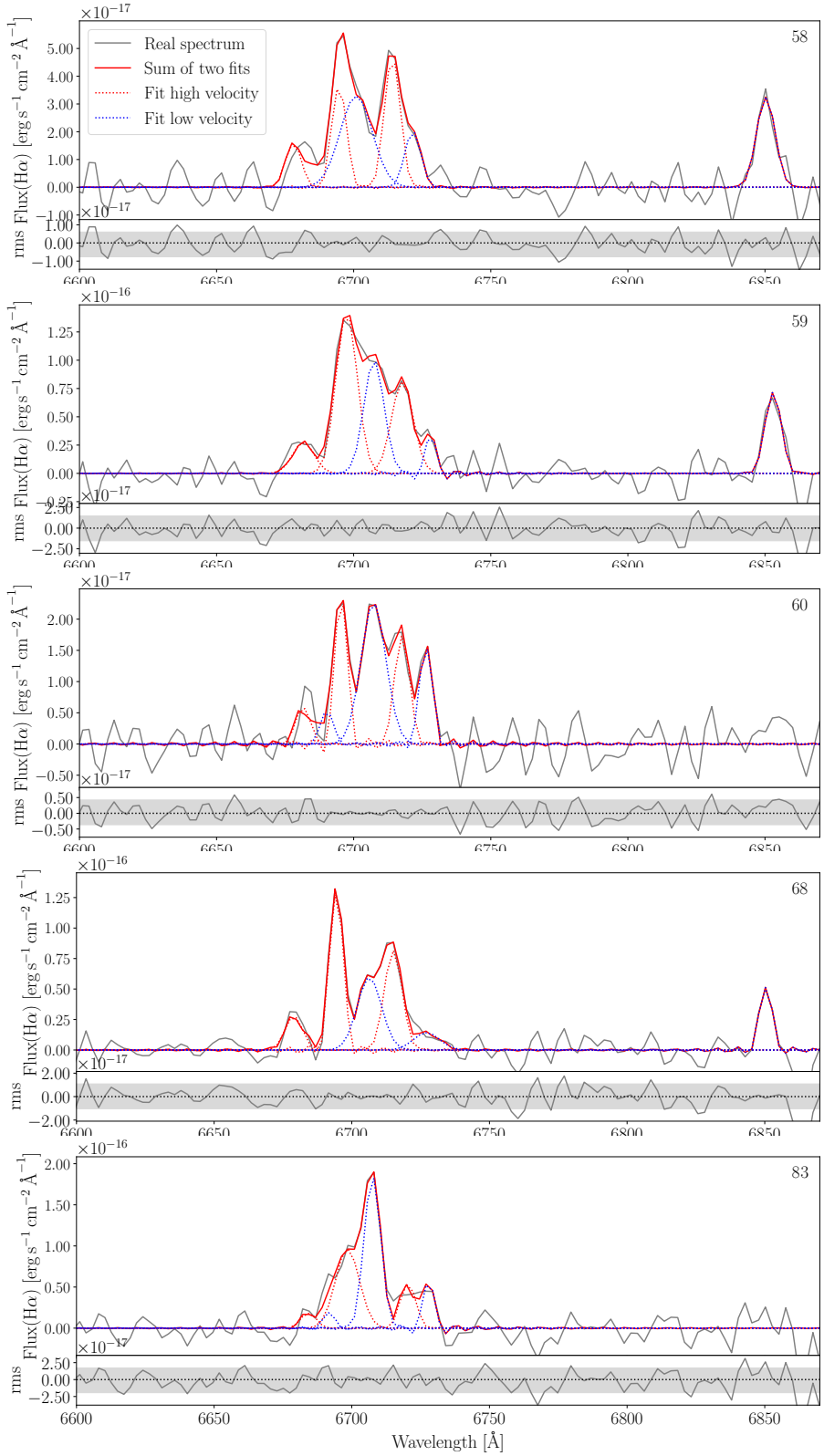

Figure 4.11: From top to bottom: examples of the line fits from regions 58, 59, 60, 68, and 83 with a broad line profile. In each upper panel, the grey line shows the real spectrum, and the red and blue dotted lines correspond to the fit of the low and high velocity components. The red solid line shows the sum of the two velocity component fits. The name of the region is indicated in each upper panel (top right). In the lower panels, the grey line shows the residual after the fit. The horizontal grey band indicates the 3σ scatter.

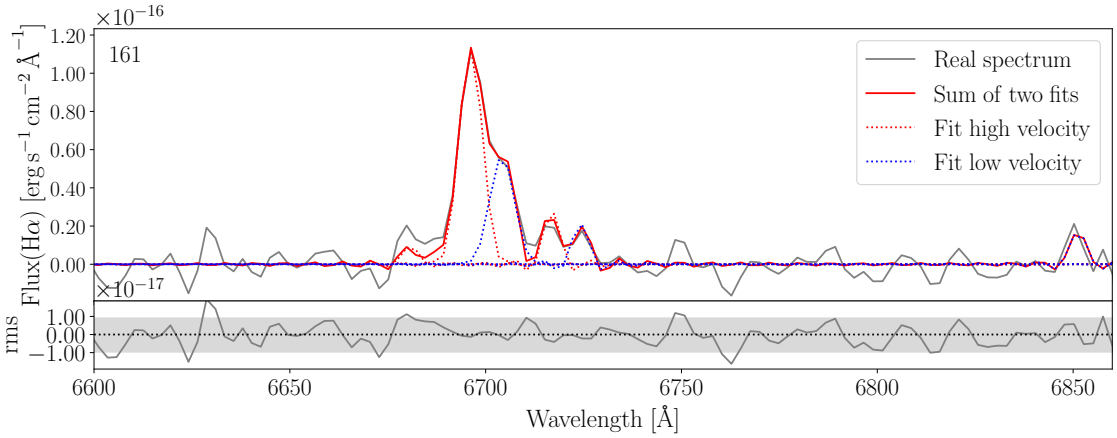

Figure 4.12: Same as Fig.4.11 but for region 161.

two subsystems that were probably in collision. On one hand, NI (brown symbols)[4] colliding with the debris field in the shock path at L1 strand (orange triangles), on the other hand, the interaction between NSQA and SSQA (violet squares and circles, respectively). While the collision between NI and the debris field in the LSSR appears to be ongoing at this moment (e.g. Iglesias-Páramo et al. 2012), our observations indicate that the interaction between NSQA and SSQA has had at least one previous collision. Several strands of ionised gas emerging from NSQA are found here: to the North of NSQA a tidal tail, NW (cyan triangles) is indicated, while on the right we see the strand L3 (which increases towards higher radial velocities, ~6470 $km\ s^{-1}$, orange crosses) and the strand L4 (that goes southwards and could link with NI, orange diamonds). The strand L2 (orange circles) connects NSQA with SSQA, which reinforces the idea that NSQA and SSQA have had at least one previous interaction. The strand L1 joins the system formed by NSQA and SSQA with NI1. We must bear in mind that the majority of the regions from the strand L1 are compatible with fast shocks without precursor for solar metallicity and low density, with velocities between 175 $km\ s^{-1}$ and 300 $km\ s^{-1}$ from Allen et al. (2008) models (see Chapter 5).

At intermediate radial velocities (i.e. from v~6160 to ~6660 $km\ s^{-1}$), several strands can be seen connecting Hs with Ls through the Shs strands (namely Sh1, Sh2, Sh3, and Sh4 represented by blue squares, triangles, circles, and crosses, respectively; see Figs. 4.9, upper right panel, and 4.15). It seems clear that this gas is a product of the interaction processes that occurred in SQ between NI and the debris field in the shock, although understanding these processes becomes complex. We also see at radial velocities ~6360 $km\ s^{-1}$ Hα flux that connects the shock (Sh4 strand) with NGC7319, into an Hα 'bridge' (green crosses). This bridge has also been observed at other wavelength ranges (e.g. molecular hydrogen bridge detected: Cluver et al. 2010; Guillard et al. 2010; Appleton et al. 2013, 2017). In Fig. 4.15 (lower left panel) we can appreciate that this connection extends several hundred $km\ s^{-1}$.

At higher radial velocities, v>6660 $km\ s^{-1}$ we distinguish several gas strands. On one hand, from the NGC7319 nucleus (red triangles) an outflow emerges, from radial velocities ~6760 $km\ s^{-1}$ to ~6350 $km\ s^{-1}$, in agreement with Rodríguez-Baras et al. (2014). On the other hand,

[4]All symbols referenced in this subsection come from Fig. 4.8.

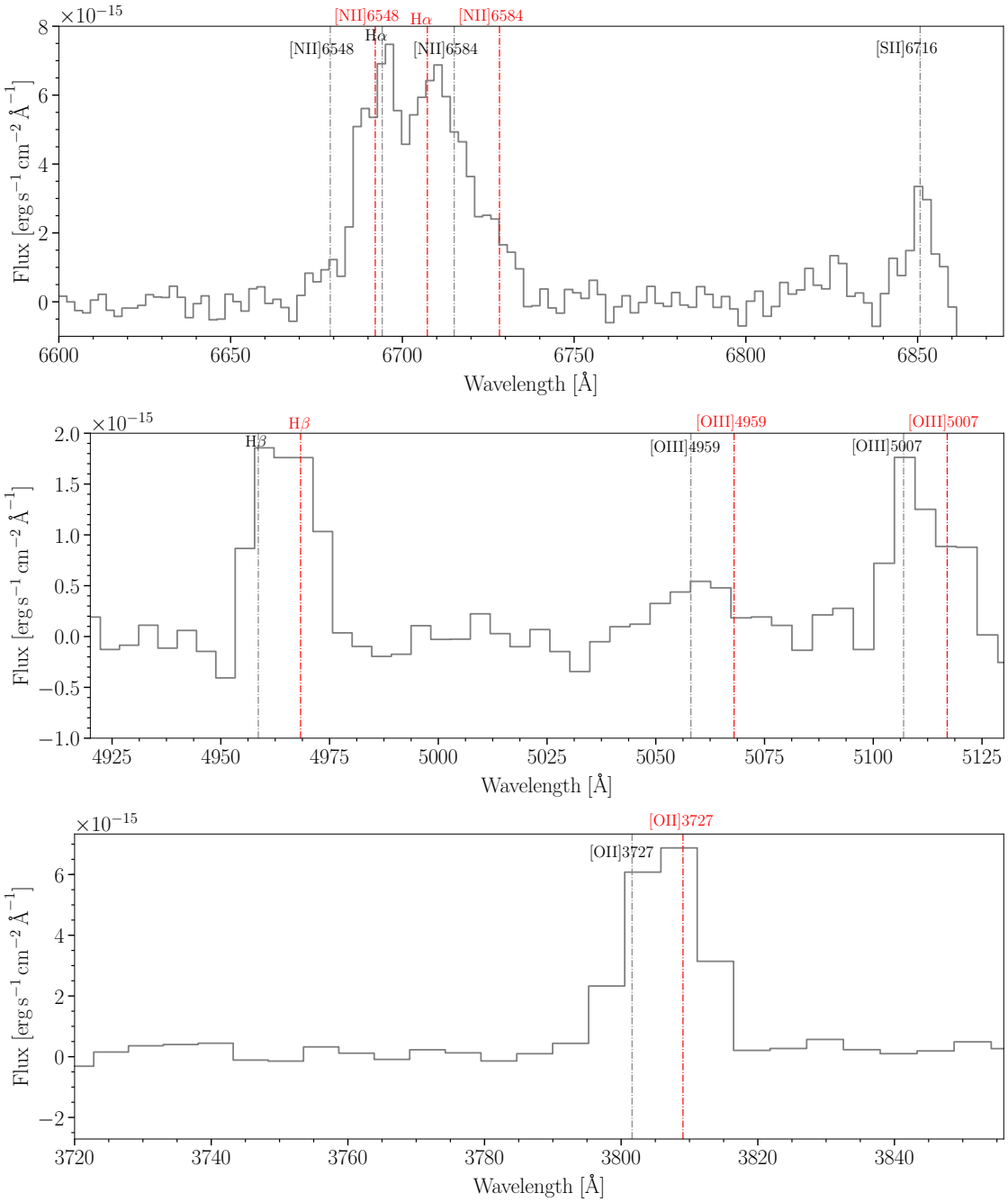

Figure 4.13: Integrated spectra from large scale shock region in SN3, SN2, and SN1 data cubes. The black and red vertical dashed lines show the position of the emission lines studied at Hα radial velocities of 6000 $km\ s^{-1}$ and 6600 $km\ s^{-1}$, respectively.

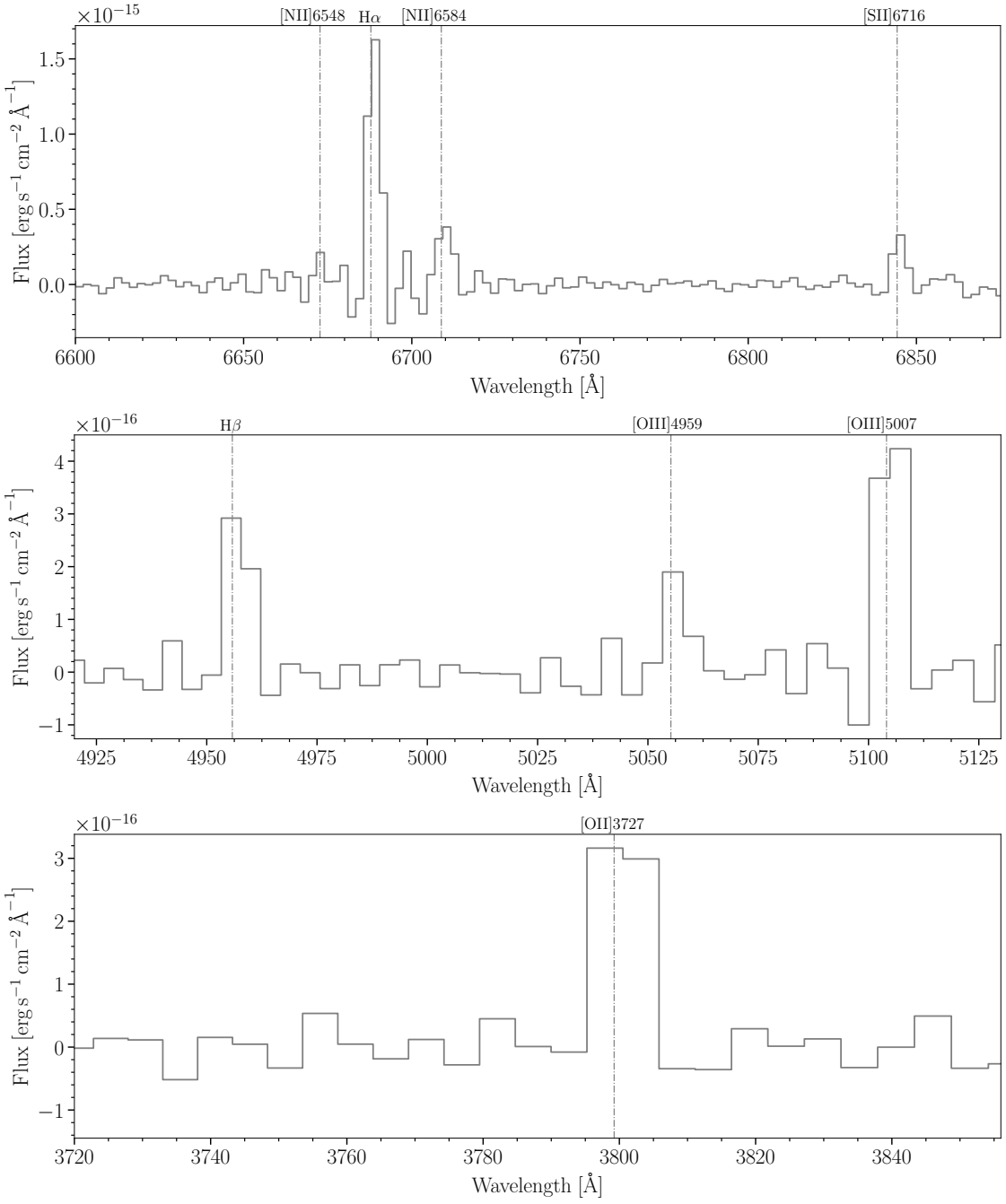

Figure 4.14: Integrated spectra from SQ Hα region 164 in SN3, SN2, and SN1 data cubes.

the NGC7319 'arm' (red squares) emerges up to radial velocities ~6600 $km\ s^{-1}$ westward towards YTT (magenta crosses and squares). The AGN North lobe zone (red circles) covers velocities higher and lower than that of the NGC7319 nucleus (Δv ~200 $km\ s^{-1}$). The right part of the North lobe seems to reach the NGC7319 'arm'. Conversely, in the shock part we see the strands H1 and H2 (yellow circles and triangles). These strands connect Shs with SQA (green stars) in the following ways: i) from Shs (radial velocity ~6660 $km\ s^{-1}$) to the most distant region detected (region 111, radial velocity ~7000 $km\ s^{-1}$) through the strand H2; and ii) from region 111 to SQA (radial velocity ~6670 $km\ s^{-1}$) through strand H1.

We fail to detect ionised gas neither in the old tail, nor in the vicinity of NGC7318A in agreement with Moles et al. (1998), nor in NGC7317 in agreement with Duc et al. (2018). Neither do we find evidence that there is a gas connection between the NGC7319 North lobe and SQA. Finally, we do not detect gas connecting the LSSR and NI5, nor in SDR (salmon stars).

4.3.4 The other galaxies in SQ

In most articles that study SQ, the galaxies that are studied in detail are NGC7317, NGC7318a, NGC7318b, and NGC7319, as well as NGC7320. In this work, thanks to the large SITELLE FoV, we were able to add to the study of the galaxy NGC7320c (the OI) and the NG. In Figs. 4.17 and 4.18 we present the spatially resolved Hα flux and radial velocity maps for NG and NGC7320c, respectively.

We detect Hα emission in NG. This, combined with the fact that NG is extended and presents a galactic rotation of ± 60 $km\ s^{-1}$ as shown in Fig. 4.17 (e.g. Swaters et al. 2002; Westmoquette et al. 2013), indicates that NG is consistent with a dwarf galaxy that will end up interacting with the SQ system in the future, similar to M82 (according to the Tully-Fisher relation). A more detailed study has been made for NG. In Fig. 4.17 we show the Hα flux (left panel) and the radial velocity map (right panel) of NG. The inner panel shows the Hubble Space Telescope optical imaging of NG. The velocity gradient is clearly seen from the South to the North (v~6300 to ~6150 $km\ s^{-1}$). As we can see in Table 4.2, region 176, the average radial velocity for NG is 6246 $km\ s^{-1}$.

In Fig. 4.15 (upper left panel) we show the low surface brightness Hα emission in the strongly stripped galaxy NGC7320c. Past interaction processes have stripped much of the gas in NGC7320c. For a better understanding of this galaxy, we studied the Hα and [NII]λ6584 fluxes for this galaxy. Figure 4.18 shows the Hα flux map (upper left panel), the [NII]λ6584 flux map (upper right panel), the Hα radial velocity map (lower left panel), and the deep image from the SN2 filter (lower right panel) for NGC7320c. In this figure, we see the presence of Hα and [NII]λ6584 emission in the galactic nucleus, and Hα emission in several regions located in the spiral arms. Figure 4.19 shows examples of spectra for several regions with Hα emission found in NGC7320c. Observing the fit for the galactic nucleus emission line (see upper panel in Fig. 4.19), we ascertain that the spectrum has an AGN profile (and found a strong emission of [NII]λ6584). We barely observe [NII]λ6584 emission (or it may be very small) in the rest of the regions located in the NGC7320c spiral arm. The radial velocity map covers a range of radial velocities from ~6540 to ~6640 $km\ s^{-1}$.

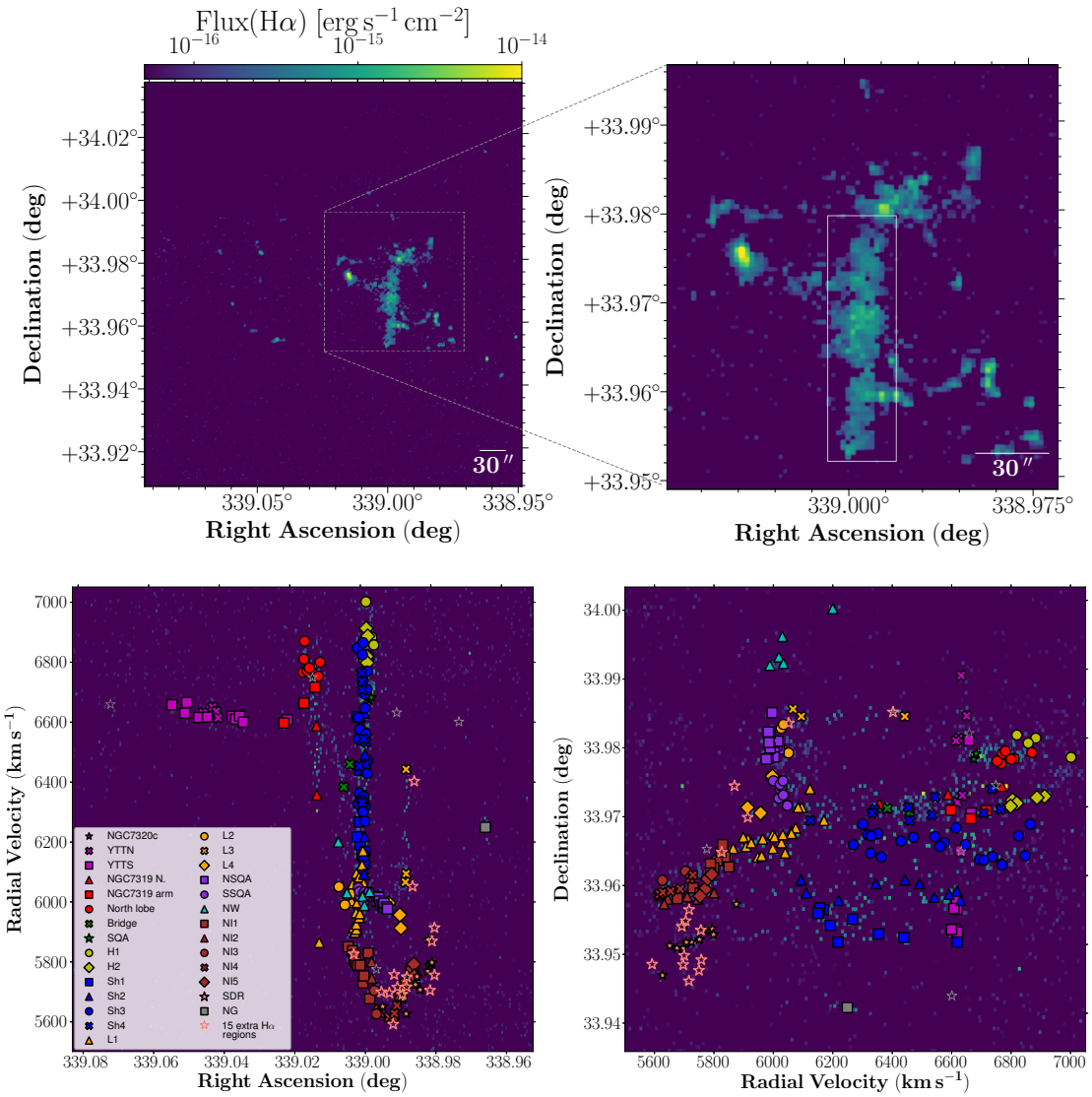

Figure 4.15: Hα flux spatial map of entire SQ (upper left panel), Hα flux spatial map zoomed in to shock region (upper right panel). The lower left panel shows the radial velocity versus RA diagram and the lower right panel shows Dec versus radial velocity diagram. All the points in the lower panels of the figures have the same colours and markers as Fig. 4.8. The white rectangle centred on LSSR is overplotted with a solid line in the upper right panel. This rectangle is centred on the coordinate RA=339 deg and Dec=33.966 deg, with a width of ΔRA=27.786 arcsec and a height of ΔDEC=99.512 arcsec.

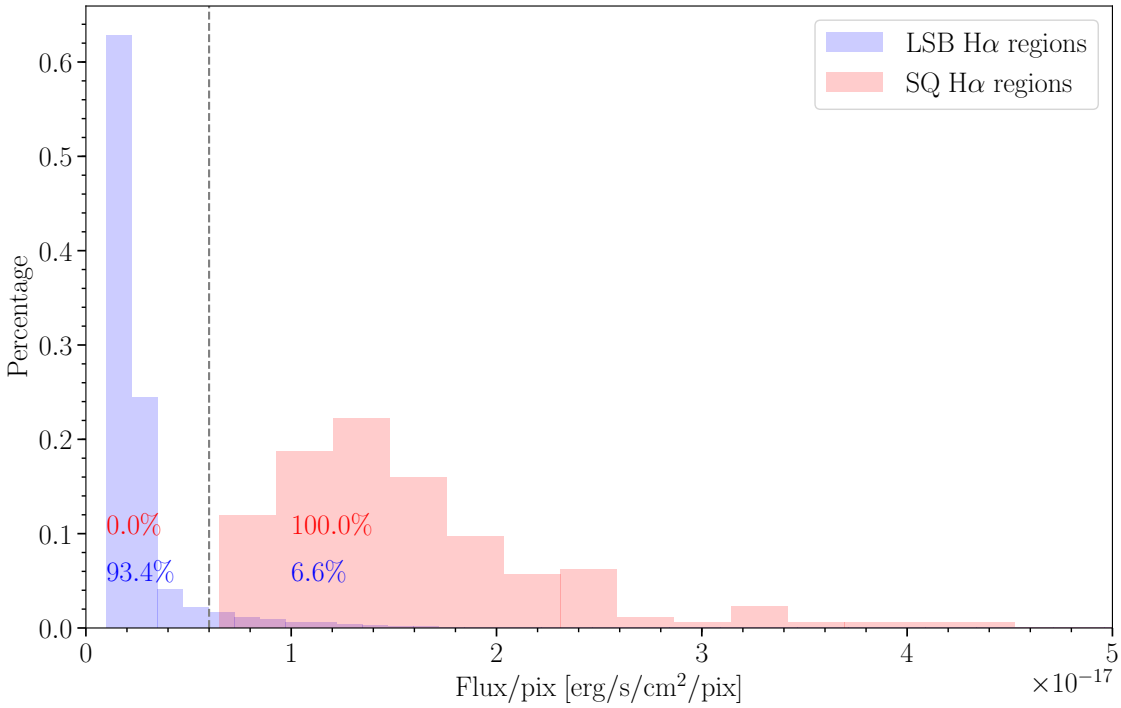

Figure 4.16: Distribution of the flux per pixel of the SQ Hα emission regions and low surface brightness Hα regions (red and blue histograms, respectively). The vertical grey dashed line correspond to the limit value of Hα flux per pixel of $6{\times}10^{-18}$ erg/s/cm^2 which separate the very low surface brightness Hα component besides the SQ Hα emission regions.

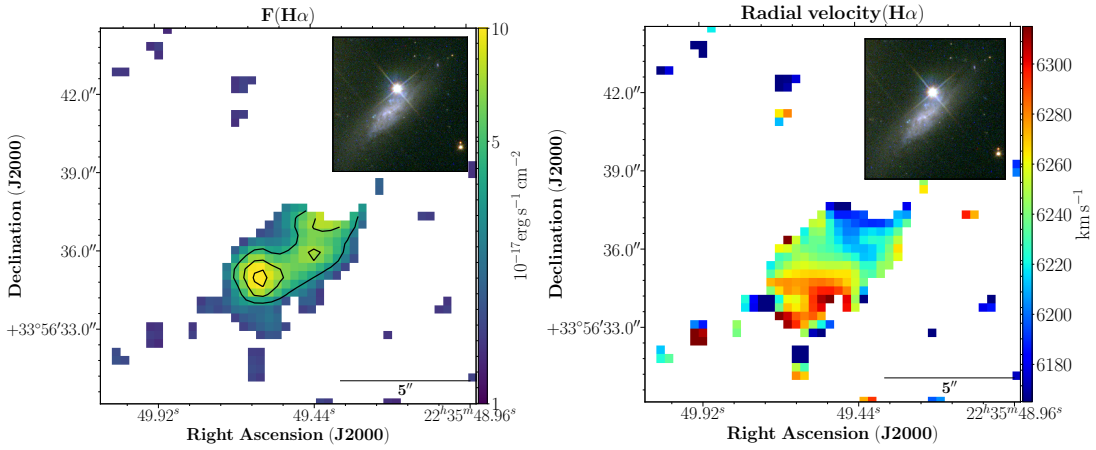

Figure 4.17: NG Hα flux spatial map (left panel) and Hα radial velocity map (right panel). The inner panels show the HST/WFC3 optical imaging for NG. The black contours are 1×10^{-17}, 4×10^{-17}, and 7×10^{-17} $erg\ s^{-1}\ cm^{-2}$.

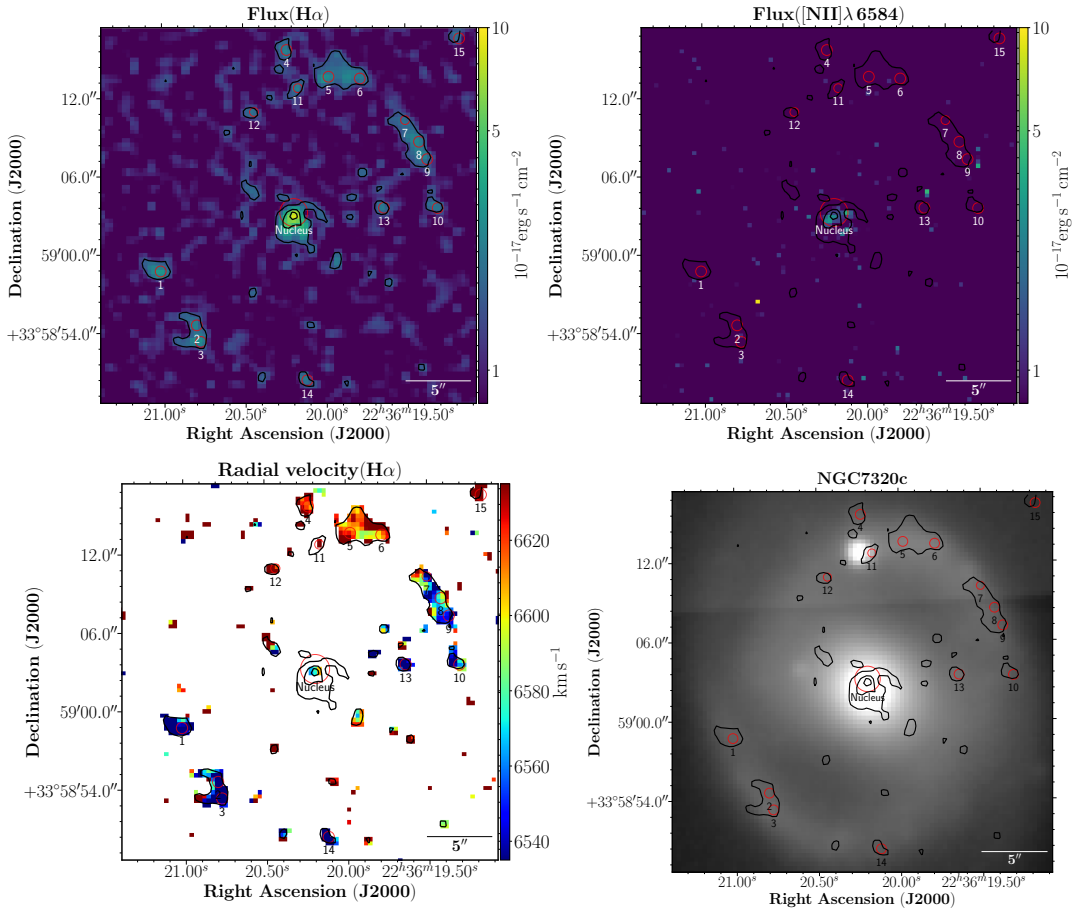

Figure 4.18: NGC7320c Hα flux spatial map (upper left panel), [NII]λ6584 flux spatial map (upper right panel), Hα radial velocity map considering pixels with contrast (Hα) $\geq$ 2.5 (lower left panel), and deep image from SN2 filter (lower right panel). Red circles represent the locations of the NGC7320c nucleus and 15 Hα emission regions from its spiral arms. The black contours are 1.5×10^{-17}, 4×10^{-17}, and 7×10^{-17} $erg\ s^{-1}\ cm^{-2}$.

4.3.5 15 Hα emitters in outer debris regions

A close visual inspection, guided by the HST/WFC3 images (PID 11502, PI Keith S. Noll) of the SQ outskirts of our deep SITELLE images has allowed us to define a set of 15 extra Hα regions (located in SDR, near NI, and West of SQ). In Table 4.3 we show the relevant information for these Hα emitters for the regions from ID 177 to 191.

4.4 Discussion and final remarks

A sample of 175 SQ Hα regions, 22 of them with two velocity components, has been made according to the following criteria: i) the radial velocity of the region is within the range of SQ (between ~5600 and ~7000 $km\ s^{-1}$); ii) the detection of at least one additional emission line besides Hα. Additionally, in Sect. 4.3.5 we add the relevant information of 15 extra Hα emitters that we have found in the southern debris region, close to NI, and to the West of SQ (regions from 177 to 191 in Table 4.3).

Two large groups of radial velocities were found (radial velocities $\leq 6160\ km\ s^{-1}$ and $> 6160\ km\ s^{-1}$). We found five radial velocity components in SQ: i) v=[5600-5900] $km\ s^{-1}$, associated with NI and SDR; ii) v=[5900-6100] $km\ s^{-1}$, associated with the NSQA and SSQA and the strands that are connected to these zones; iii) v=[6100-6600] $km\ s^{-1}$, associated with the strands located in the shock; iv) v=[6600-6800] $km\ s^{-1}$, associated with YTT, SQA, NGC7319, and the North lobe; and v) v=[6800-7000] $km\ s^{-1}$, associated with the strands that connect the shock with SQA.

When considering a contrast (Hα)≥2 and binning 6x6, we do not detect gas in the old tail, in the vicinity of NGC7318A nor in NGC7317. We also do not have evidence that there is any connection between i) the North lobe in NGC7319 and the left side of SQA; or ii) the shock and the right part of NI nor SDR. Conversely, we find a link between the shock and the NGC7319 AGN nucleus (Hα bridge). This bridge was detected in other wavelengths (e.g. Iglesias-Páramo & Vílchez 2001; Sulentic et al. 2001; Trinchieri et al. 2005; Cluver et al. 2010; Guillard et al. 2010, 2012; Appleton et al. 2013, 2017).

A region of remarkable line emission is located between NGC7319 and the NI galaxy (NGC7318B). A rectangular area has been defined (see Sect. 4.3.2, shown in Fig. 4.15) to include this emission which is associated with the LSSR. This has allowed us to investigate the complex kinematical nature of this emitting gas, making use of detailed spatially resolved multi-sincgaussian fitting. The LSSR has revealed a rich knotty substructure, spatially distributed, and also a set of kinematical properties of the Hα emitting knots. These knots show line profiles that have been fitted by two sincgaussian functions, with central velocities clustering around two main radial velocity values (~6000 $km\ s^{-1}$, ~6600 $km\ s^{-1}$), and a different broadness in each case. Overall, taking into account: i) an oblique interaction over a large region, and new and preceding gas (e.g. O'Sullivan et al. 2009; Lesaffre et al. 2013; Appleton et al. 2017); and ii) that the gas is excited by shocks (corresponding to a shock radial velocity ~300 $km\ s^{-1}$ according to Allen et al. 2008, see Chapter 5), we suggest that a variety of interaction processes occurred previous to the intrusion of NI in the main group. We found sub-structures ~400pc or larger in size, typical of giant HII extragalactic regions.

A possible outermost tail of Hα emitting regions is suggested here, which would be in agreement with Renaud et al. (2010). We provide an observational clue of this prediction. We found that this tidal tail connects with NSQA (reg 145). Other strands connected with NSQA have been found: i) the L2 strand that connects NSQA and SSQA; ii) the L3 strand that connects NSQA with region 161 up to radial velocities ~6470 $km\ s^{-1}$; and iii) the L4 strand that connects NSQA with regions 154 and 155. This last connection could be extended up to the NI5 strand according to the diffuse gas show in the low surface brightness gas emission.

From our sample of SQ Hα emission regions we have studied the region 176 (i.e. NG) in detail (see Sect. 4.3.4). This region was previously observed by Torres-Flores et al. (2009) (see their Fig. 14, ID 35) and by Rodríguez-Baras et al. (2014). In this chapter we have made a spatially resolved study of the Hα radial velocity and Hα flux in this region. The data points out that this region is in fact a dwarf galaxy with a velocity gradient across its disc ($\pm 60\ km\ s^{-1}$, see Fig. 4.17), which was not considered by Rodríguez-Baras et al. (2014). These authors found an age of $\sim 10^{10}$ yr for 80% of the stellar mass in this region, assuming that this region is a star cluster separated from a galaxy by some previous interactions. According to the Tully-Fisher relation, we found that NG would be similar to M82. Additionally, we found Hα emission in the NGC7320c galactic disc and a significant presence of broad [NII]λ6584 emission in the NGC7320c nucleus. This leads us to propose that NGC7320c hosts an AGN (see Fig. 4.19).

A panoramic view of the full extent of the low surface brightness emission of the SQ is illustrated in Fig. 4.20, which shows a deep imaging of SQ obtained from the SITELLE SN2 filter. This figure displays the full extension and complexity of the entire system (including the diffuse ionised gas halo around the SQ, the old tail, the halo around NGC7317, and a conspicuously low surface brightness extension to the North-East of the whole system). For details, the reader is referred to the recent work by Duc et al. (2018), which offers an interesting study of the complete system.

Figure 4.21 shows the deep image from the SN2 filter. In this figure, we suggest a possible tidal structure (delineated by an outer rim to the North-West of NGC7318B/A) with diffuse gas emission that could connect the South part of L3 and NSQA with NI4, NI5, and SDR (marked by a green arrow). The detection of the 15 additional low surface brightness Hα emission regions (i.e. IDs from 177 to 191 in Table 4.3, located in: SDR, close to NI, and to the West of SQ) with the expected radial velocities in this zone (~5600 to ~5900 $km\ s^{-1}$) has allowed us to support this possible connection. This outer rim is almost parallel with another inner rim (i.e. strand L4) that shows Hα emitting regions. Conversely, we do not discard the possibility of a connection between NI1 (i.e. region 38) and the left side of SDR going behind NGC7320 (indicated by red arrows). Also this interaction could be supported by the existence of region 31 (v~5860 $km\ s^{-1}$) presenting the same radial velocity as the strand NI1 some 13 kpc away to the East. The interaction suffered, which might explain these rims, appears complex, although we believe that it must have been produced by the interaction between NI and the group. The large-scale outer rim winding the NGC7318B/A system clockwise North-West to South-East has been highlighted in continuum and from Hα. This structure may be reminiscent of a previously proposed scenario for SQ as a sequence of individual interactions (Renaud et al. 2010). Further observations are needed with

higher spectral resolution to distinguish the complex kinematics that is taking place in the LSSR.

Table 4.2: Relevant information of Hα emission regions in Stephan's Quintet.

(1) Region ID	(2) α (h m s)	(2) δ (^{o} $'$ $''$)	(3) Velocity ($km\ s^{-1}$)	(4) Area (kpc^2)	(5) Subzone
1†	22 36 20.3	+33 59 04.4	6657±24	–	NGC7320c
2	22 36 15.3	+33 59 1.9	6644±3	1.0	YTT
3	22 36 15.2	+33 58 59.9	6656±6	0.6	YTT
4	22 36 14.1	+33 58 1.0	6628±2	1.3	YTT
5	22 36 14.0	+33 58 21.4	6664±11	0.2	YTT
6	22 36 13.0	+33 57 36.5	6613±5	0.5	YTT
7	22 36 12.6	+33 59 33.3	6630±15	0.2	YTT
8	22 36 12.4	+33 57 30.2	6614±4	1.3	YTT
9	22 36 11.8	+33 59 11.5	6648±3	1.1	YTT
10	22 36 11.5	+33 58 59.6	6622±1	1.3	YTT
11	22 36 11.5	+33 58 26.0	6618±5	0.5	YTT
12	22 36 11.5	+33 58 30.3	6635±6	0.3	YTT
13	22 36 11.4	+33 58 58.6	6612±1	1.3	YTT
14	22 36 10.2	+33 57 18.5	6618±2	2.3	YTT
15	22 36 10.0	+33 57 20.0	6608±1	1.7	YTT
16	22 36 9.6	+33 57 17.7	6618±5	0.3	YTT
17	22 36 9.4	+33 57 19.2	6598±4	0.8	YTT
18	22 36 6.0	+33 58 20.0	6595±7	0.3	NGC7319 'Arm'
19	22 36 5.7	+33 57 29.9	6606±5	0.5	YTT
20	22 36 4.4	+33 58 44.9	6764±4	1.1	North lobe
21	22 36 4.3	+33 58 46.8	6809±4	1.2	North lobe
22	22 36 4.3	+33 58 16.0	6662±17	0.2	NGC7319 'Arm'
23	22 36 4.3	+33 58 50.4	6868±6	0.7	North lobe
24	22 36 4.0	+33 58 50.0	6769±7	1.3	North lobe
25	22 36 3.8	+33 58 51.3	6779±5	0.9	North lobe
26	22 36 3.4	+33 58 32.3	6768±9	3.8	NGC7319 Nucl.
27	22 36 3.3	+33 58 28.4	6586±20	3.9	NGC7319 Nucl.
28	22 36 3.3	+33 58 20.6	6715±7	0.5	NGC7319 'Arm'
29	22 36 3.3	+33 58 23.5	6355±11	0.3	NGC7319 Nucl.
30	22 36 3.1	+33 58 45.5	6750±8	0.5	North lobe

Continued.

(1)	(2)		(3)	(4)	(5)
Region	α	δ	Velocity	Area	Subzone
ID	(h m s)	(^{o} $'$ $''$)	($km\ s^{-1}$)	(kpc^2)	
31	22 36 3.1	+33 58 0.1	5863±12	0.2	L1
32	22 36 2.9	+33 58 46.8	6799±12	0.2	North lobe
33	22 36 1.4	+33 58 49.0	6049±7	0.5	L2
34	22 36 1.4	+34 0 5.7	6198±14	0.2	NW
35	22 36 1.0	+33 58 21.0	6381±10	1.0	Bridge
36	22 36 0.9	+33 58 36.8	5988±13	0.2	L2
37	22 36 0.7	+33 59 50.7	6028±6	0.6	NW
38	22 36 0.6	+33 57 49.9	5849±9	0.3	NI1
39	22 36 0.5	+33 58 6.3	5996±7	0.6	L1
40	22 36 0.6	+33 58 17.9	6457±14	0.3	Bridge
41	22 36 0.5	+33 59 2.1	6024±8	0.5	L2
42	22 36 0.4	+33 57 55.3	5835±4	0.7	NI1
43	22 36 0.4	+33 58 5.0	6003±11	0.2	L1
44	22 36 0.4	+33 58 8.2	6057±12	0.2	L1
45	22 36 0.3	+33 57 52.7	5809±6	1.0	NI1
46	22 36 0.2	+33 57 57.5	5822±5	0.8	NI1
47	22 36 0.2	+33 58 4.0	5913±9	0.2	L1
48	22 36 0.2	+33 58 5.3	5898±12	0.3	L1
49	22 36 0.2	+33 57 48.8	5797±10	0.6	NI1
50	22 36 0.0	+33 58 4.2	5963±10	0.3	L1
51^a	22 35 60.0	+33 57 11.1	6215±50	1.9	Sh1
51^b	22 35 60.0	+33 57 11.1	6617±20	1.9	Sh1
52	22 35 59.9	+33 57 51.4	5786±3	1.7	NI1
53	22 36 0.0	+33 58 0.4	5907±10	0.2	L1
54	22 36 0.1	+33 58 2.3	5924±10	0.2	L1
55	22 36 0.0	+33 58 20.7	6093±11	0.2	L1
56	22 35 60.0	+33 57 55.5	6846±13	0.2	Sh3
57	22 35 60.0	+33 57 59.1	5997±18	0.2	L1
58^a	22 35 59.9	+33 57 57.5	6037±14	0.6	L1
58^b	22 35 59.9	+33 57 57.5	6325±30	0.6	Sh3

Continued.

(1) Region ID	(2) α (h m s)	(2) δ (^{o} $'$ $''$)	(3) Velocity ($km\ s^{-1}$)	(4) Area (kpc^2)	(5) Subzone
59[a]	22 35 59.9	+33 58 5.2	6165±16	1.6	L1
59[b]	22 35 59.9	+33 58 5.2	6621±32	1.6	Sh3
60[a]	22 35 59.9	+33 58 10.0	6073±14	0.3	L1
60[b]	22 35 59.9	+33 58 10.0	6612±17	0.3	Sh3
61	22 35 59.9	+33 58 21.7	6046±12	0.2	SSQA
62	22 35 59.9	+33 57 13.3	6438±10	0.7	Sh1
63	22 35 59.8	+33 57 22.8	6265±21	0.2	Sh1
64	22 35 59.8	+33 57 36.6	6616±11	0.6	Sh2
65	22 35 59.7	+33 57 45.8	5787±5	1.1	NI1
66[a]	22 35 59.8	+33 57 54.5	5946±12	0.5	L1
66[b]	22 35 59.8	+33 57 54.5	6362±14	0.5	Sh3
67	22 35 59.8	+33 57 55.5	5955±13	0.5	L1
68[a]	22 35 59.7	+33 58 1.0	6025±9	1.6	L1
68[b]	22 35 59.7	+33 58 1.0	6574±37	1.6	Sh3
69[a]	22 35 59.8	+33 58 20.7	6081±20	0.3	L1
69[b]	22 35 59.8	+33 58 20.7	6452±32	0.3	Sh4
70	22 35 59.7	+33 58 25.5	6016±4	0.7	SSQA
71	22 35 59.7	+33 58 27.4	6032±8	0.4	SSQA
72	22 35 59.8	+33 57 18.7	6189±15	0.3	Sh1
73	22 35 59.7	+33 57 13.9	6352±10	0.7	Sh1
74	22 35 59.7	+33 57 35.6	6589±10	0.7	Sh2
75	22 35 59.6	+33 57 38.1	5728±5	1.5	NI1
76[a]	22 35 59.7	+33 58 19.7	6312±27	0.6	Sh4
76[b]	22 35 59.7	+33 58 19.7	6761±35	0.6	Sh4
77	22 35 59.6	+33 57 35.2	6540±12	0.7	Sh2
78	22 35 59.6	+33 57 28.5	6154±13	0.2	Sh1
79[a]	22 35 59.5	+33 58 5.1	6326±31	1.3	Sh3
79[b]	22 35 59.5	+33 58 5.1	6823±10	1.3	Sh3
80[a]	22 35 59.6	+33 58 17.4	6343±19	0.3	Sh4
80[b]	22 35 59.6	+33 58 17.4	6752±23	0.3	Sh4

Continued.

(1) Region ID	(2) α (h m s)	(2) δ (^{o} $'$ $''$)	(3) Velocity ($km\ s^{-1}$)	(4) Area (kpc^2)	(5) Subzone
81[a]	22 35 59.5	+33 58 30.3	6123±17	0.3	L1
81[b]	22 35 59.5	+33 58 30.3	6734±26	0.3	Sh4
82	22 35 59.5	+33 59 39.6	6017±4	1.0	NW
83[a]	22 35 59.4	+33 57 33.3	6211±22	3.0	Sh2
83[b]	22 35 59.4	+33 57 33.3	6626±11	3.0	Sh2
84	22 35 59.5	+33 57 50.6	6767±12	0.3	Sh3
85	22 35 59.5	+33 57 55.4	6735±10	0.3	Sh3
86[a]	22 35 59.4	+33 58 7.0	6059±13	0.8	L1
86[b]	22 35 59.4	+33 58 7.0	6350±25	0.8	Sh3
87[a]	22 35 59.5	+33 58 11.5	6299±21	0.3	Sh3
87[b]	22 35 59.5	+33 58 11.5	6863±16	0.3	Sh3
88	22 35 59.5	+33 58 13.8	6168±18	0.2	L1
89[a]	22 35 59.5	+33 58 26.4	6542±22	0.7	Sh4
89[b]	22 35 59.5	+33 58 26.4	6861±36	0.7	Sh4
90	22 35 59.4	+33 58 29.9	6022±5	0.8	SSQA
91	22 35 59.4	+33 58 31.3	6026±10	0.4	SSQA
92	22 35 59.5	+33 58 34.2	5999±7	0.5	SSQA
93	22 35 59.4	+33 57 25.3	6148±11	0.2	Sh1
94[a]	22 35 59.5	+33 57 35.9	5749±15	0.3	NI1
94[b]	22 35 59.5	+33 57 35.9	6049±28	0.3	Sh2
95[a]	22 35 59.4	+33 57 42.9	6091±57	0.3	Sh2
95[b]	22 35 59.4	+33 57 42.9	6442±27	0.3	Sh2
96	22 35 59.3	+33 58 24.4	6803±11	0.8	H2
97	22 35 59.2	+33 59 34.6	5986±5	0.6	NW
98	22 35 59.3	+33 58 27.0	6031±7	0.4	SSQA
99	22 35 59.4	+33 57 27.5	6166±23	0.2	Sh1
100[a]	22 35 59.4	+33 57 41.0	6233±27	0.3	Sh3
100[b]	22 35 59.4	+33 57 41.0	6490±34	0.3	Sh2
101	22 35 59.4	+33 57 53.2	6692±16	0.2	Sh3
102[a]	22 35 59.3	+33 58 1.2	6267±17	0.3	Sh3

Continued.

(1) Region ID	(2) α (h m s)	(2) δ (^{o} $'$ $''$)	(3) Velocity ($km\ s^{-1}$)	(4) Area (kpc^2)	(5) Subzone
102^b	22 35 59.3	+33 58 1.2	6644±43	0.3	Sh3
103^a	22 35 59.3	+33 58 5.7	6030±13	0.5	L1
103^b	22 35 59.3	+33 58 5.7	6316±42	0.5	Sh3
104^a	22 35 59.4	+33 58 13.4	6124±72	1.6	Sh4
104^b	22 35 59.4	+33 58 13.4	6460±31	1.6	Sh4
105	22 35 59.2	+33 58 25.7	6911±11	0.6	H2
106	22 35 59.2	+33 58 32.2	6021±8	0.7	SSQA
107	22 35 59.2	+33 57 53.1	6707±13	0.8	Sh3
108	22 35 59.2	+33 58 0.2	6558±27	0.2	Sh3
109	22 35 59.2	+33 58 16.3	6532±19	0.2	Sh4
110	22 35 59.2	+33 58 22.1	6817±8	0.8	H2
111	22 35 59.2	+33 58 46.8	7000±6	0.5	H1
112	22 35 59.1	+33 59 4.3	6032±4	1.9	L2
113	22 35 59.1	+33 57 49.9	6768±9	0.3	Sh3
114	22 35 59.1	+33 58 3.1	6427±14	0.3	Sh3
115	22 35 59.1	+33 58 21.1	6797±13	0.4	H2
116	22 35 59.1	+33 58 25.4	6885±8	1.4	H2
117	22 35 59.0	+33 57 33.2	5675±1	2.2	NI1
118	22 35 59.1	+33 58 1.1	5827±9	0.3	NI1
119	22 35 59.1	+33 58 5.0	6469±18	0.2	Sh3
120	22 35 59.0	+33 58 34.1	6031±3	1.5	SSQA
121	22 35 59.0	+33 58 45.7	6672±4	3.0	SQA
122	22 35 58.8	+33 58 48.6	6680±2	4.9	SQA
123	22 35 58.9	+33 58 58.1	6818±10	0.2	H1
124	22 35 58.8	+33 59 35.5	6032±9	0.3	NW
125	22 35 58.8	+33 57 36.0	5799±11	0.7	NI2
126	22 35 58.6	+33 58 56.0	6881±8	1.1	H1
127	22 35 58.8	+33 57 33.2	5744±4	1.4	NI2
128	22 35 58.7	+33 57 34.1	5708±3	0.7	NI2
129	22 35 58.4	+33 58 51.1	6017±2	2.3	NSQA

Continued.

(1) Region ID	(2) α (h m s)	(2) δ (^{o} $'$ $''$)	(3) Velocity ($km\ s^{-1}$)	(4) Area (kpc^2)	(5) Subzone
130	22 35 58.6	+33 57 47.5	5703±3	1.1	NI3
131	22 35 58.6	+33 58 54.4	6856±11	0.6	H1
132	22 35 58.4	+33 58 52.4	6009±2	1.4	NSQA
133	22 35 58.4	+33 57 32.8	5643±1	1.8	NI2
134	22 35 58.4	+33 57 42.4	5624±5	1.0	NI3
135	22 35 58.4	+33 58 48.5	6001±6	1.2	NSQA
136	22 35 58.1	+33 58 54.3	6013±3	1.8	NSQA
137	22 35 58.1	+33 58 46.5	6001±3	2.1	NSQA
138	22 35 58.2	+33 57 29.9	5630±2	1.6	NI2
139	22 35 58.0	+33 58 59.1	5987±2	1.6	NSQA
140	22 35 57.9	+33 58 50.3	5987±5	1.4	NSQA
141	22 35 57.8	+33 58 56.5	5984±2	1.8	NSQA
142	22 35 57.8	+33 58 54.2	5983±3	1.5	NSQA
143	22 35 57.6	+33 58 45.1	5980±3	2.4	NSQA
144	22 35 58.0	+33 57 8.8	5650±13	0.2	SDR
145	22 35 57.7	+33 59 9.8	5994±11	0.2	NSQA
146	22 35 57.5	+33 58 59.6	5981±2	2.2	NSQA
147	22 35 57.4	+33 58 45.3	5974±8	0.3	NSQA
148	22 35 57.4	+33 58 36.6	5994±5	0.6	L4
149	22 35 57.4	+33 57 34.8	5613±7	0.5	NI4
150	22 35 57.0	+33 57 34.8	5615±6	0.4	NI4
151	22 35 57.0	+33 57 35.7	5626±7	0.4	NI4
152	22 35 56.8	+33 57 36.6	5653±5	0.7	NI4
153	22 35 56.6	+33 57 37.6	5684±3	1.4	NI4
154	22 35 56.5	+33 58 17.0	5955±3	1.2	L4
155	22 35 56.4	+33 58 19.9	5911±4	0.7	L4
156	22 35 56.3	+33 57 6.7	5674±5	0.6	SDR
157	22 35 56.3	+33 57 42.9	5717±4	1.0	NI4
158	22 35 56.3	+33 57 19.4	5699±8	0.2	SDR
159	22 35 56.2	+33 57 44.2	5727±5	1.4	NI4

Continued.

(1) Region ID	(2) α (h m s)	(2) δ (^{o} $'$ $''$)	(3) Velocity ($km\ s^{-1}$)	(4) Area (kpc^2)	(5) Subzone
160	22 35 56.1	+33 57 7.0	5695±6	0.3	SDR
161^a	22 35 55.9	+33 59 7.4	6108±26	1.9	L3
161^b	22 35 55.9	+33 59 7.4	6473±68	1.9	L3
162	22 35 56.0	+33 59 11.0	6064±9	0.3	L3
163	22 35 56.1	+33 56 53.1	5625±10	0.2	SDR
164	22 35 55.6	+33 57 37.4	5768±1	2.8	NI5
165	22 35 55.5	+33 57 43.1	5776±1	2.5	NI5
166	22 35 55.4	+33 57 44.7	5790±2	1.4	NI5
167	22 35 55.3	+33 57 33.5	5751±2	1.7	NI5
168	22 35 55.3	+33 57 10.3	5722±2	1.1	SDR
169	22 35 55.2	+33 57 11.6	5750±3	0.7	SDR
170	22 35 54.9	+33 57 9.7	5705±3	1.0	SDR
171	22 35 54.3	+33 57 15.9	5768±3	1.3	SDR
172	22 35 54.2	+33 57 29.5	5873±2	1.1	SDR
173	22 35 54.2	+33 57 15.3	5786±2	1.0	SDR
174	22 35 54.1	+33 57 16.2	5793±2	1.4	SDR
175	22 35 53.9	+33 57 14.3	5797±5	0.7	SDR
176	22 35 49.9	+33 56 36.5	6247±6	1.4	NG

The columns correspond to: (1) Identifier of the Hα emission regions (ID); (2) Right ascension (hours, minutes, and seconds) and declination (degrees, arcminutes, and arcseconds); (3) Hα radial velocity ($km\ s^{-1}$); (4) Area (kpc^2). (5) Subzone. '†' (ID 1) denotes the information about NGC7320c. For regions with two velocity components we use '^{a}' and '^{b}' for low- and high-velocity components, respectively.

Table 4.3: Positional information of 15 extra Hα emitter regions in the southern debris region, close to the NI, and to the West of SQ.

(1)	(2)		(3)
Region	α	δ	Velocity
ID	(h m s)	(^{o} $'$ $''$)	($km\ s^{-1}$)
177	22 35 58.8	+33 56 55.4	5698
178	22 35 58.1	+33 56 50.5	5695
179	22 35 57.8	+33 56 53.0	5756
180	22 35 57.8	+33 56 50.8	5590
181	22 35 57.5	+33 56 42.3	5714
182	22 35 56.7	+33 56 47.5	5748
183	22 35 57.1	+33 57 10.0	5690
184	22 35 56.7	+33 57 18.5	5714
185	22 35 54.8	+33 57 12.5	5703
186	22 35 54.5	+33 57 7.7	5754
187	22 35 54.4	+33 58 5.7	5912
188	22 35 56.0	+33 59 0.9	6401
189	22 35 56.1	+33 58 55.1	6051
190	22 35 54.6	+33 58 22.1	5867
191	22 36 1.0	+33 57 49.0	5824

The columns correspond to: (1) Identifier of the Hα emission regions (ID); (2) Right ascension (hours, minutes, and seconds) and declination (degrees, arcminutes, and arcseconds); (3) Velocity ($km\ s^{-1}$). Information about the 15 extra Hα emitter regions is given in SDR, close to the NI, and to the West of SQ.

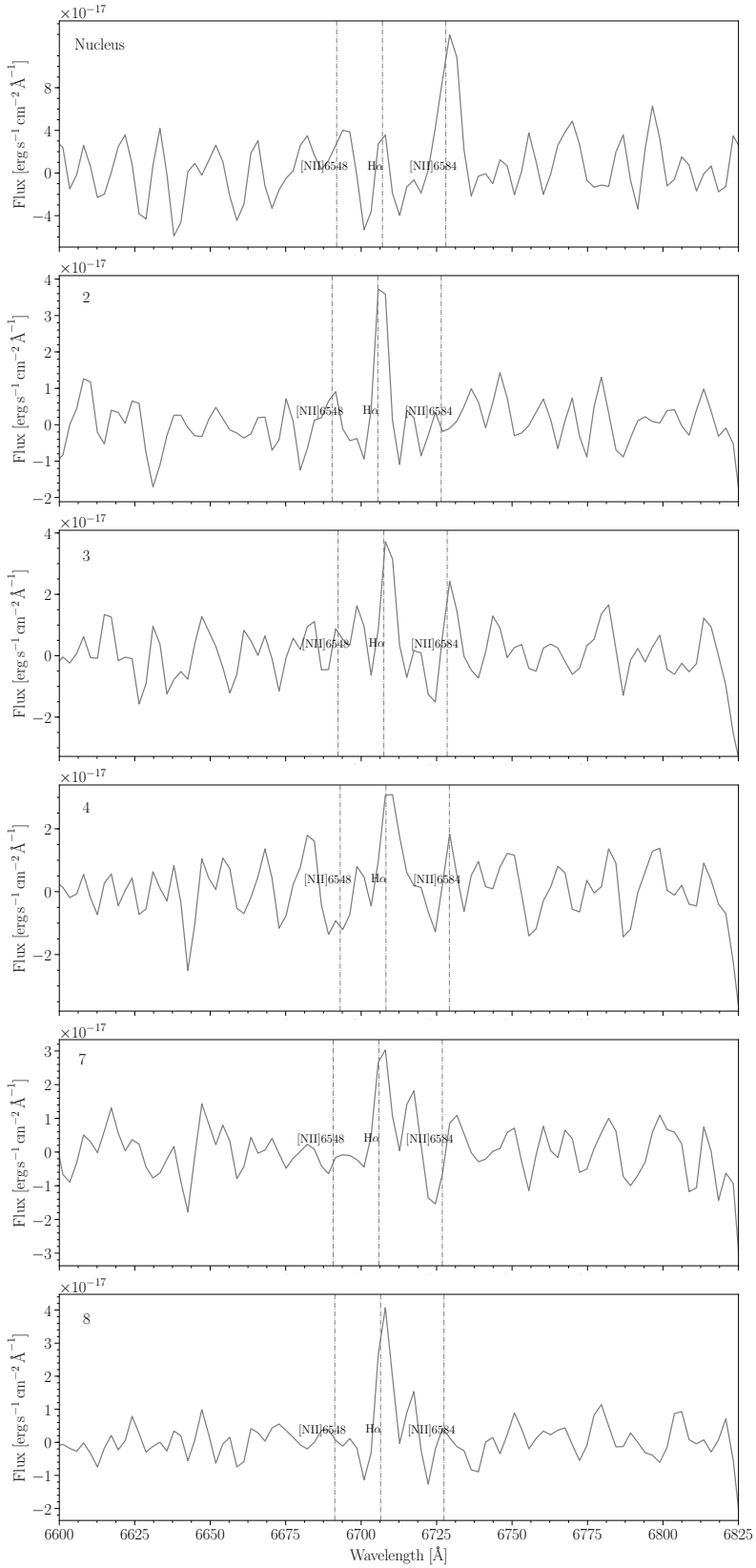

Figure 4.19: Spectra from NGC7320c nucleus, and several Hα regions in its galactic disc. Shown from top to bottom are the NGC7320c galactic nucleus and regions 2, 3, 4, 7, and 8 (see Fig. 4.18). The black vertical dashed lines show the position of the emission lines studied for the SN3 filter at an Hα radial velocity of ~6590 $km\ s^{-1}$.

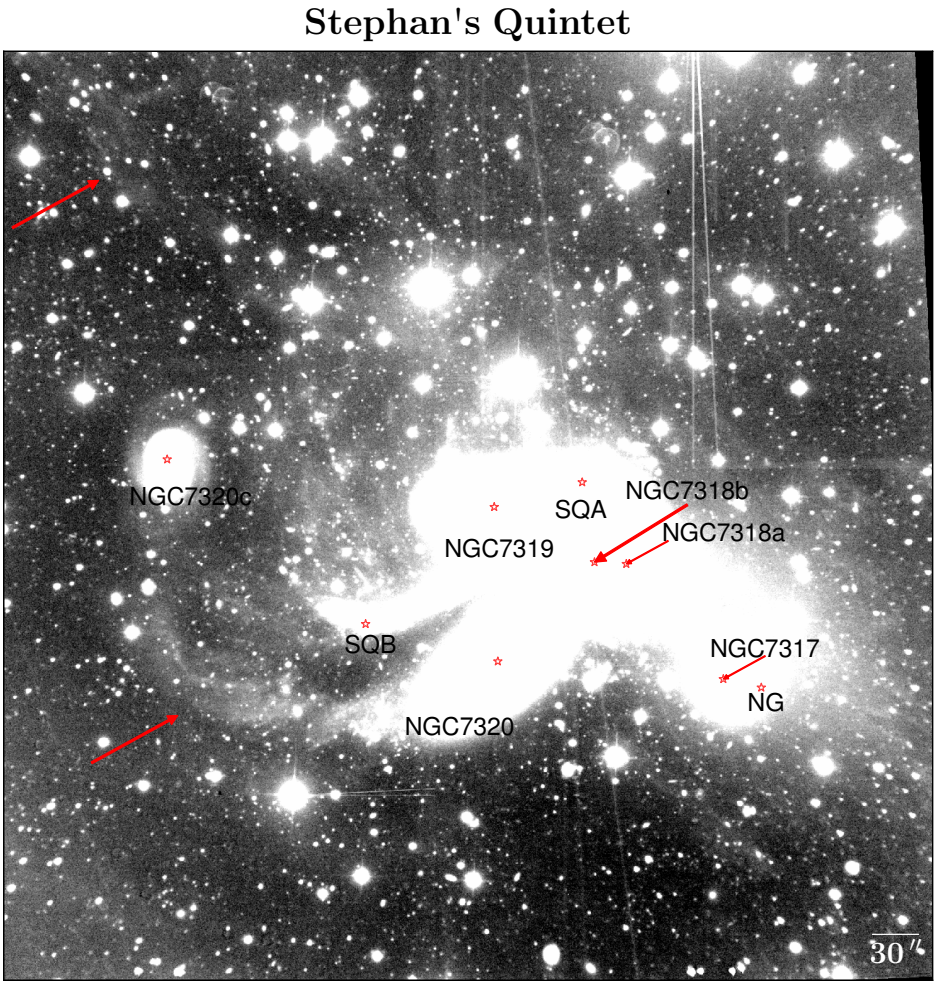

Figure 4.20: Deep imaging from SN2 filter of SQ. This image displays the full extension of the entire system, including the diffuse ionised gas halo around the SQ. The most relevant components are indicated by their labels and red arrows. See the text for details.

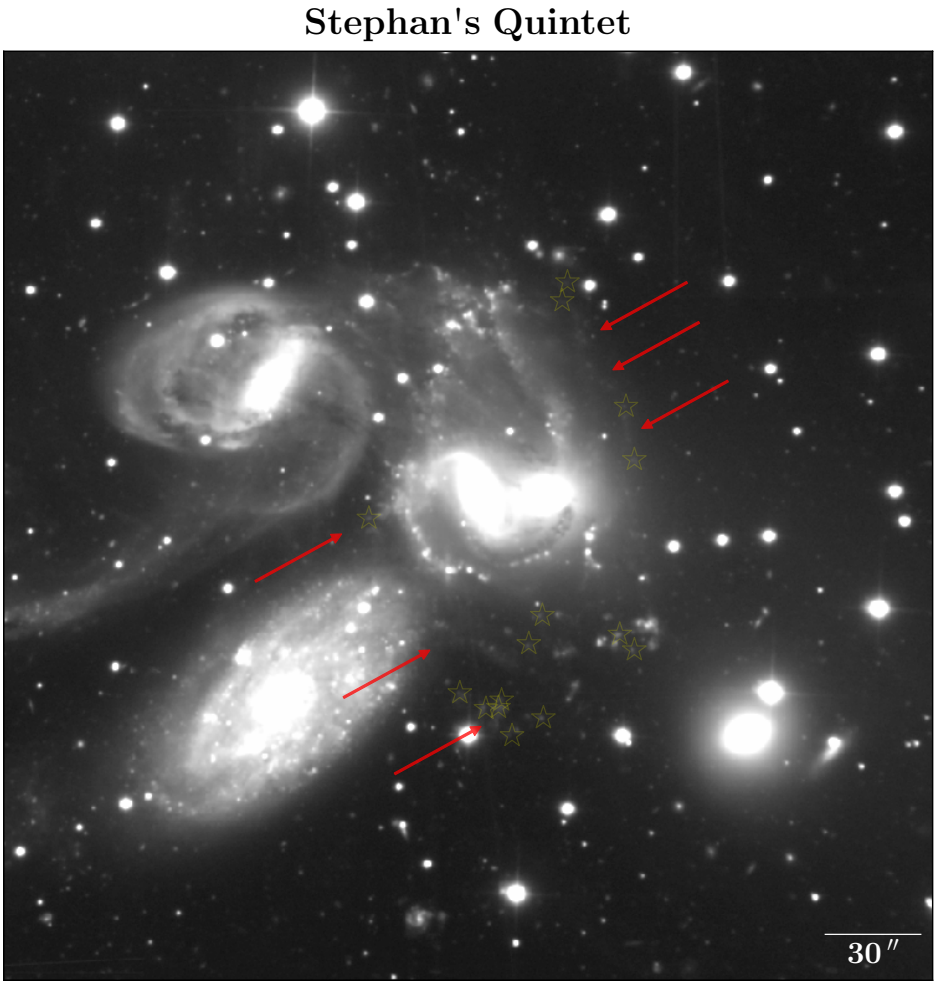

Figure 4.21: Deep imaging from SN2 filter of SQ. Red arrows point out the possible outer structures that can be connected. The yellow stars show the location of the 15 extra Hα emitter regions presented in Table 4.3.

Chapter 5

Searching for intergalactic star forming regions in Stephan's Quintet with SITELLE: II. Physical properties of the ionised gas

Contents

This chapter is based on the paper:
"Searching for intergalactic star forming regions in Stephan's Quintet with SITELLE: II. Physical properties of the ionised gas"
by S. Duarte Puertas, J. M. Vilchez, J. Iglesias-Páramo, L. Drissen, C. Kehrig, T. Martin, and E. Perez-Montero
to be submitted to A&A

5.1 Introduction

SQ is a compact group discovered by Stephan (1877). SQ is formed by two elliptical (NGC7317 and NGC7318A), three spiral (NGC7318B, NGC7319, NGC7320c), and one new dwarf galaxy described recently in Chapter 4. Also, in the FoV of SQ we can see a foreground galaxy (NGC7320) with a discordant distance. In SQ we found diverse structures (e.g. tidal tails), but probably the most remarkable one is the LSSR (e.g. Allen & Hartsuiker 1972; Ohyama et al. 1998; Iglesias-Páramo et al. 2012) produced by the collision between NGC7318B and both NGC7319 and debris material produced from previous interactions. In Chapter 4 we found five velocity systems in SQ: i) v=[5600-5900] $km\ s^{-1}$ associated with NI and SDR; ii) v=[5900-6100] $km\ s^{-1}$, associated with NSQA and SSQA and the strands connected to these zones; iii) v=[6100-6600] $km\ s^{-1}$, associated with the strands from the LSSR; iv) v=[6600-6800] $km\ s^{-1}$, associated with YTT, SQA, NGC7319, and the NGC7319 north lobe; and v) v=[6800-7000] $km\ s^{-1}$, associated with the strands seen connecting LSSR with SQA.

Previous works studied physical and chemical properties of star-forming objects in SQ (e.g. Mendes de Oliveira et al. 2004; Konstantopoulos et al. 2014). The work by Konstantopoulos et al. (2014) studied the properties of 40 Hα emitting regions in the LSSR, NI, and SDR and did not find shocked gas associated with the HII regions or the intrusive galaxy. Massive star formation in regions of the shock zone appears substantially suppressed while SQA appears to be the most active region in star formation of the SQ (Konstantopoulos et al. 2014). The shocked gas presents two velocity components: low velocity ($\leq 6160\ km\ s^{-1}$, and nearly solar metallicities[1]) and high velocity ($> 6160\ km\ s^{-1}$, and low metallicity) (Iglesias-Páramo et al. 2012; Rodríguez-Baras et al. 2014). Again, the SDR presents typical SFR values of nearby galaxies (Konstantopoulos et al. 2014) and its HII regions have subsolar metallicities, presenting a metallicity gradient along the spiral arm of NGC7318B (Iglesias-Páramo et al. 2012).

This work is based on the spectroscopic data from SITELLE (Grandmont et al. 2012), an IFTS, attached to the CFHT. SITELLE has a large FoV (11'x11'), and covers the optical range from 3500 Å to 7500 Å. It allows us to obtain a more complete view of the ionisation structure of the SQ and its physical and chemical properties. Previous comprehensive spectroscopic studies are based on long-slit observations or are made with an Integral Field Units (IFU) with a small FoV and did not cover the whole area of the objects to account for the integrated SFR. However, thanks to SITELLE observations that covers a large FoV we can study the almost the entire SQ with a reasonable spectro and spatial resolution.

The determination of the metallicity in the gas, using oxygen abundance as a proxy, allows us to ascertain its origin helping to distinguish between evolved metal-rich gas from the galaxies and the tidal tails or unevolved metal-poor gas from the intergalactic medium (IGM). It is known that while representative dwarf galaxies present typical values of 12+log(O/H) between 7.1 and 8.4 (van Zee & Haynes 2006; Croxall et al. 2009; Berg et al. 2012; Lee-Waddell et al. 2018), tidal dwarf galaxies present values higher than 8.4 (de Mello et al. 2012; Duc et al. 2014; Lelli et al. 2015). The combination of the results obtained in the 3D study from Chapter 4 with the SQ

[1]Solar metallicity: 12 + log(O/H) = 8.69 (Asplund et al. 2009).

properties derived here (e.g. SFR, O/H, N/O, extinction, and diagnostic line ratios) leaves us in an excellent position to try to answer fundamental questions about the SQ, as for example: Is star formation inhibited for this group of galaxies? Where is located the star formation in SQ? Does the star formation occur outside the galaxies of SQ or not? Does the new intruder chemically enrich the environment? Is extinction associated with the highest star formation zones? Are we seeing different gas components cohabiting in SQ at the same time?

The structure of this chapter is organised as follows: in Sect. 5.2 we detail our main results. Discussion and summary of our work are presented in Sect. 5.3. Throughout the chapter, we assume a Friedman-Robertson-Walker cosmology with $\Omega_{\Lambda 0} = 0.7$, $\Omega_{\rm m0} = 0.3$, and $H_0 = 70\,{\rm km\,s^{-1}\,Mpc^{-1}}$.

5.2 Results

5.2.1 SITELLE spectroscopy. Line fluxes

We considered the sample of 175 SQ Hα emission regions defined in Chapter 4. For each region we fitted the emission lines that we found in the SN1, SN2, and SN3 data cubes: e.g. [OII]λ3727, Hβ, [OIII]$\lambda\lambda$4959,5007, Hα, [NII]$\lambda\lambda$6548,6584, and [SII]$\lambda\lambda$6717,6731. The methodology followed is described in details in Chapter 4. It should be noted that the emission lines were fitted with sincgaussian functions (convolution between sinc and gaussian) using the Python-based package ORCS (Martin et al. 2015). The output parameters are the radial velocity, broadening, intensity peak, total flux, and the corresponding uncertainties. All SQ regions were defined according to the following criteria: the radial velocity of the region is within the radial velocity range of SQ (between ~5600 and ~7000 $km\ s^{-1}$) and at least one additional emission line besides Hα has been detected in the data cubes. From our sample of 175 SQ Hα regions, 127 (73%) fulfil the condition S/N([OII]λ3727) $\geq$ 3, 169 (96%) fulfil the condition S/N(Hβ) $\geq$ 3, 131 (75%) S/N([OIII]λ5007) $\geq$ 3, and 146 (83%) S/N([NII]λ6583) $\geq$ 3. We have defined the S/N as the ratio of the flux to the statistical error flux, calculated with the pipeline ORCS (Martin et al. 2015). [OIII]λ5007 and [OII]λ3727 are not detected in some regions of the North lobe, NGC7319 'arm', and Shs. In Fig. 5.1 we show the emission line maps for [OII]λ3727, Hβ, [OIII]λ5007, Hα, and [NII]λ6583 for SQ. As noted in Chapter 4, we separated the SQ emission regions in two sub-samples: LV for those regions where the radial velocity is lower than or equal to 6160 $km\ s^{-1}$; and HV for all regions with radial velocity higher than 6160 $km\ s^{-1}$.

We correct the emission line fluxes for reddening using the theoretical case B recombination (theoretical Balmer decrement, $I_{H\alpha/H\beta} = 2.86$; electron temperature $T = 10^4\ K$, and low-density limit $n_e \sim 10^2\ cm^{-3}$; Osterbrock 1989; Storey & Hummer 1995) together with the Cardelli et al. (1989) extinction curve with $R_v = A_v/E(B-V) = 3.1$ (O'Donnell 1994; Schlegel et al. 1998), where $A_v = 2.5\,c(H\beta)$. When the reddening coefficient, c(Hβ), is negative we set it as zero. The Galactic extinction is very small in the direction of SQ, E(B - V) = 0.07 according to NED[2], and its contribution to A_v derived for each region is not relevant.

[2] http://ned.ipac.caltech.edu/

In Table 5.1 we present emission line fluxes divided by Hβ and corrected for reddening for the SQ Hα emission regions whenever possible. For the regions where Hβ is not detected, we computed the theoretical flux expected for Hβ when S/N(Hβ)=3, and we corrected each emission line for reddening accordingly. In Col. 1 the region name is presented. Cols. 2, 3, 4, 5, 6, and 7 show the [OII]λ3727, [OIII]λ5007, Hα, [NII]λ6583, [SII]λ6716, and [SII]λ6731 emission line fluxes respectively. Col. 8 shows A_v, and Col. 9 tells us whether the velocity of the region belongs to the LV (0) or HV (1).

In Fig. 5.2 we show the 12 zones and 28 sub-zones defined in Chapter 4 for SQ as follows: i) YTT (e.g. Lisenfeld et al. 2002), so that North and South strands are respectively YTTN and YTTS, and NGC7320c is OI; ii) NGC7319 (NGC7319 nucleus, NGC7319 'arm', North lobe); iii) Hα 'bridge'; iv) Hs (H1 and H2); v) SQA (e.g. Xu et al. 1999); vi) Ls (L1, L2, L3, and L4); vii) Shs (Sh1, Sh2, Sh3, and Sh4); viii) NSQA and SSQA; ix) NW (e.g. Renaud et al. 2010); x) NI (e.g. Moles et al. 1997) strands, NIs (NI1, NI2, NI3, NI4, and NI5); xi) SDR (e.g. Fedotov et al. 2011); and xii) NG.

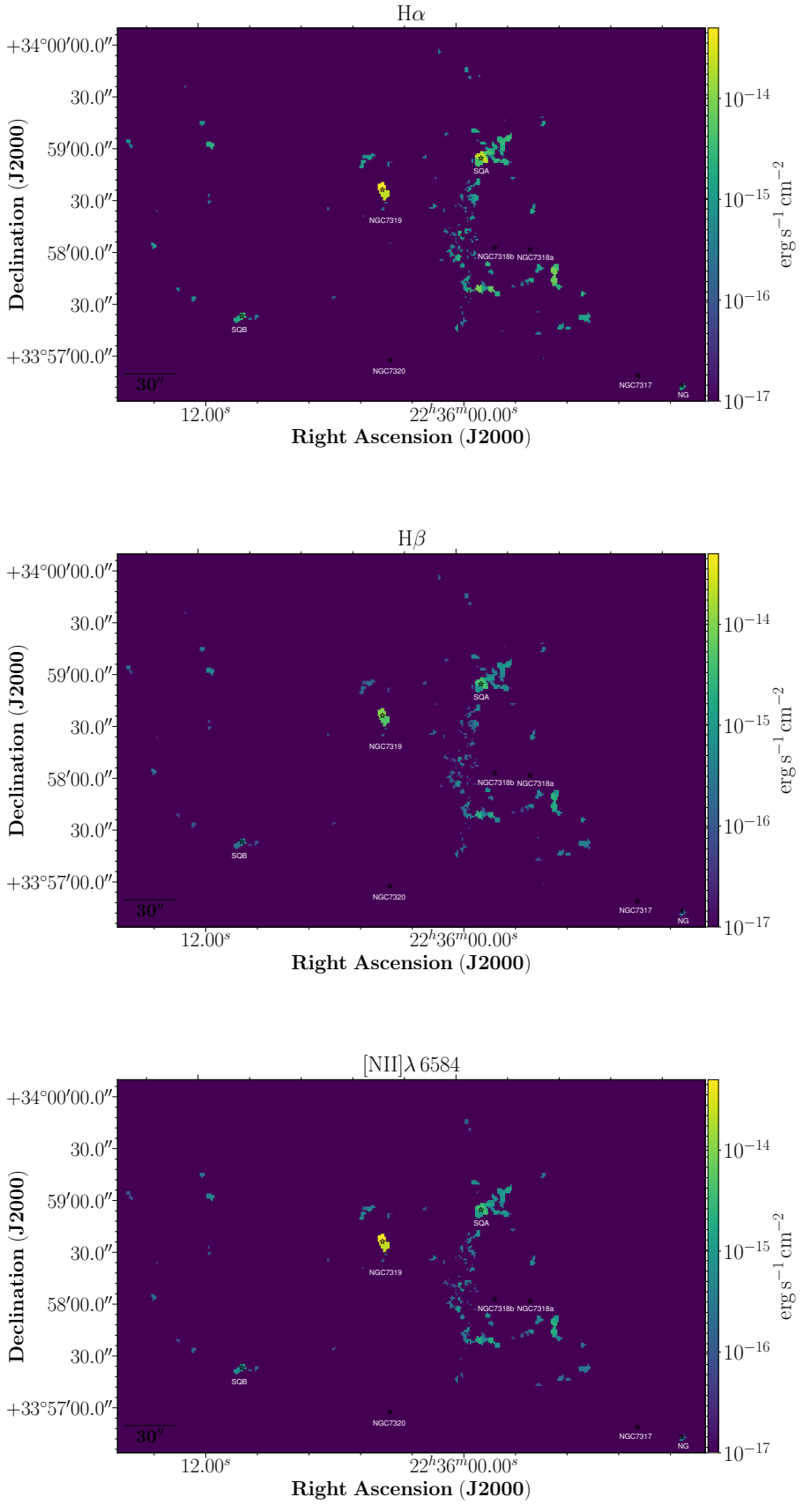

Figure 5.1: Emission-line flux maps of SQ. From top to bottom: Hα, Hβ, [NII], [OIII], and [OII].

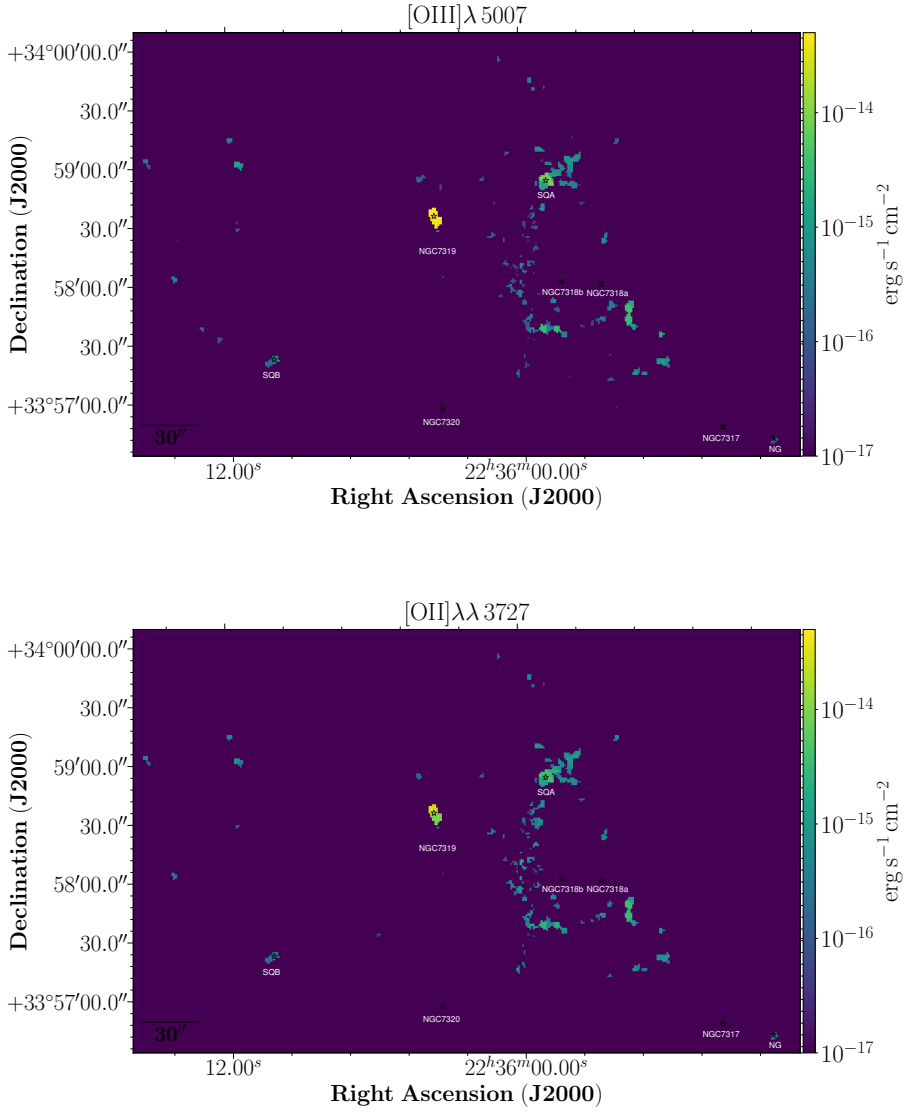

Figure 5.1: (continued)

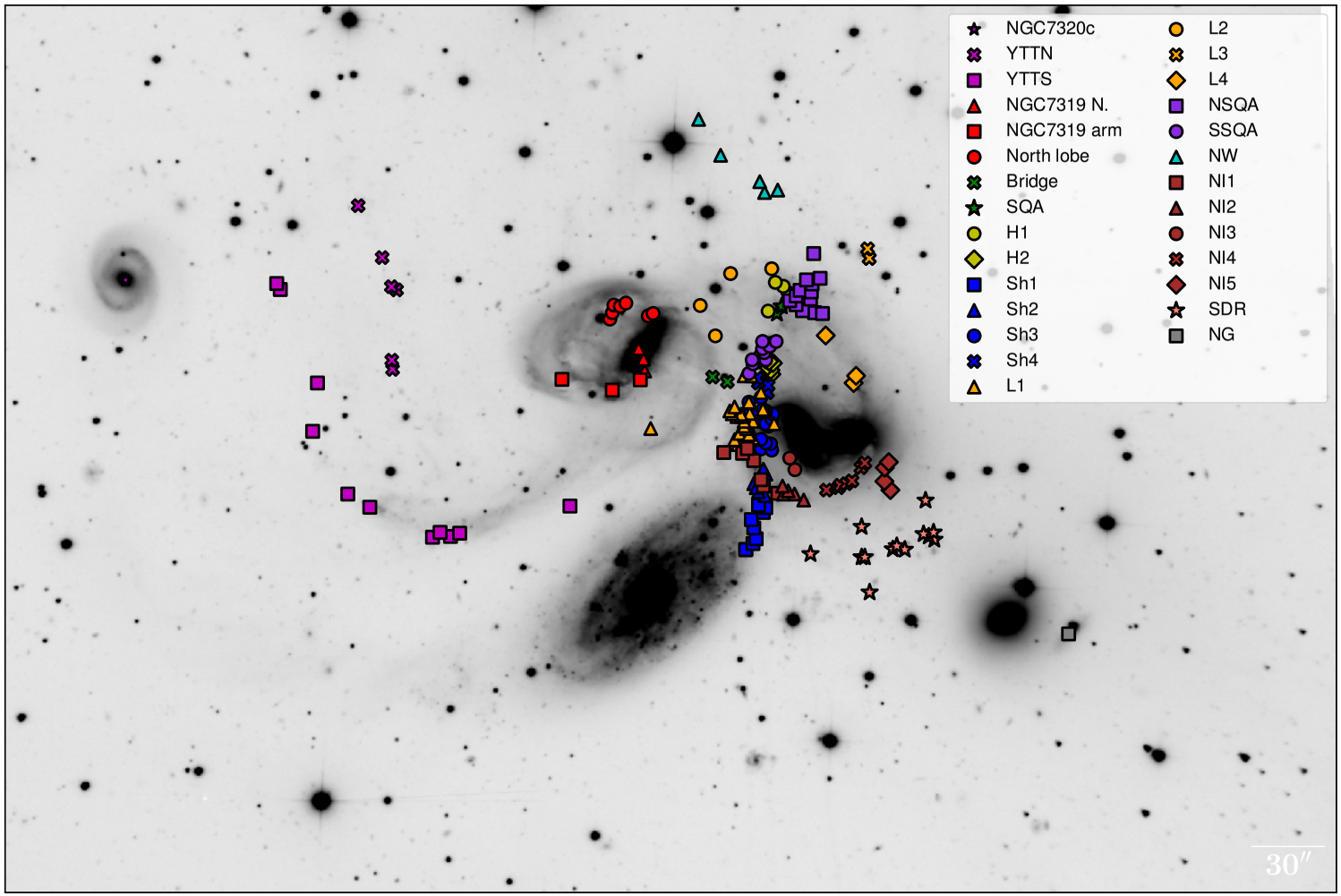

Figure 5.2: Different systems of emission line objects defined here and indicated on SITELLE deep-grayscale image of SQ. Shown are the positions of YTTN and YTTS (magenta crosses and squares, respectively); NGC7319 nucleus, 'arm', and North lobe (red triangles, squares, and circles, respectively); bridge (green crosses); SQA (green stars); Hs (H1: yellow circles; H2: yellow diamonds); Shs (Sh1: blue squares; Sh2: blue triangles; Sh3: blue circles; Sh4: blue crosses); Ls (L1: orange triangles; L2: orange circles; L3: orange crosses; L4: orange diamonds); NSQA and SSQA (violet squares and circles); NW (cyan triangles); NIs (NI1: brown squares; NI2: brown triangles; NI3: brown circles; NI4: brown crosses; NI5: brown diamonds); SDR (salmon stars); and NG (grey squares).

5.2.2 Distribution of emission line ratios

In this section we study the spatial distribution in the SQ of several emission-line ratios considered in the literature as proxies for the oxygen abundance indicators (e.g. [NII]/Hα, R_{23}, O3N2) and of the ionisation degree of the regions (e.g. [OIII]/[OII]). Some of them do not have to be corrected for reddening given the proximity of both emission lines (e.g. [NII]/Hα or [OIII]/Hβ). On the contrary, R_{23}, [OIII]/[OII], and [NII]/[OII] need to be corrected for reddening according to Sect. 5.2.1. We define $R_{23} = \frac{[OII]\lambda3727+[OIII]\lambda\lambda4959,5007}{H\beta}$ (Pagel et al. 1979), [OIII]/[OII]=$\frac{[OIII]\lambda\lambda4959,5007}{[OII]\lambda3727}$ (Díaz et al. 2000), O3N2=$\frac{[OIII]\lambda5007/H\beta}{[NII]\lambda6584/H\alpha}$ (Alloin et al. 1979).

Figure 5.3 shows the line ratio maps in SQ (from left to right and top to bottom: log([NII]/[OII]), log([NII]/Hα), log([OIII]/Hβ), log(O3N2), log([OIII]/[OII]), and log(R_{23})). The values for the line ratios considered here for SDR and NW are compatible with regions detected in the outer discs of galaxies since they have low [NII]/Hα values, and high [OIII]/Hβ, O3N2, and [OIII]/[OII] values. The values derived for SQA are compatible with those of the outer regions of the galaxies, and could also match typical values for a tidal dwarf galaxy. YYTS has an inner-outer gradient presenting lower [NII]/Hα and higher values for [OIII]/Hβ and O3N2 in the West than in the East. The LSSR presents high [NII]/[OII] values, and low [OIII]/Hβ, O3N2, and [OIII]/[OII] values. With these results we can see how the regions from the shock zone are completely different from the rest (see Rodríguez-Baras et al. 2018, for more information about inner and outer HII regions over the discs of spiral galaxies).

Figure 5.4 shows the relation between log([NII]/Hα) and radial velocity for all the regions in SQ. In the figure, the horizontal dashed grey line and the grey band correspond to the reference value at log([NII]/Hα)=-0.2 and the uncertainties for the log([NII]/Hα) ratio, respectively. Above log([NII]/Hα)=-0.2 we assume that the regions are HII, while above we assume that they are either shocked or AGNs (see Sect. 5.2.3). For the LV sub-sample, practically all the regions in NIs, SDR, NSQA, L2, L3, L4, and NW have values lower than -0.2 for log([NII]/Hα). In contrast, L1 and SSQA show values higher than -0.2 for log([NII]/Hα). In the HV sub-sample, most of the regions have values lower than -0.2 for log([NII]/Hα), except the NGC7319 nucleus, Hα 'bridge', and several regions from Shs, North lobe, and the NGC7319 'arm'.

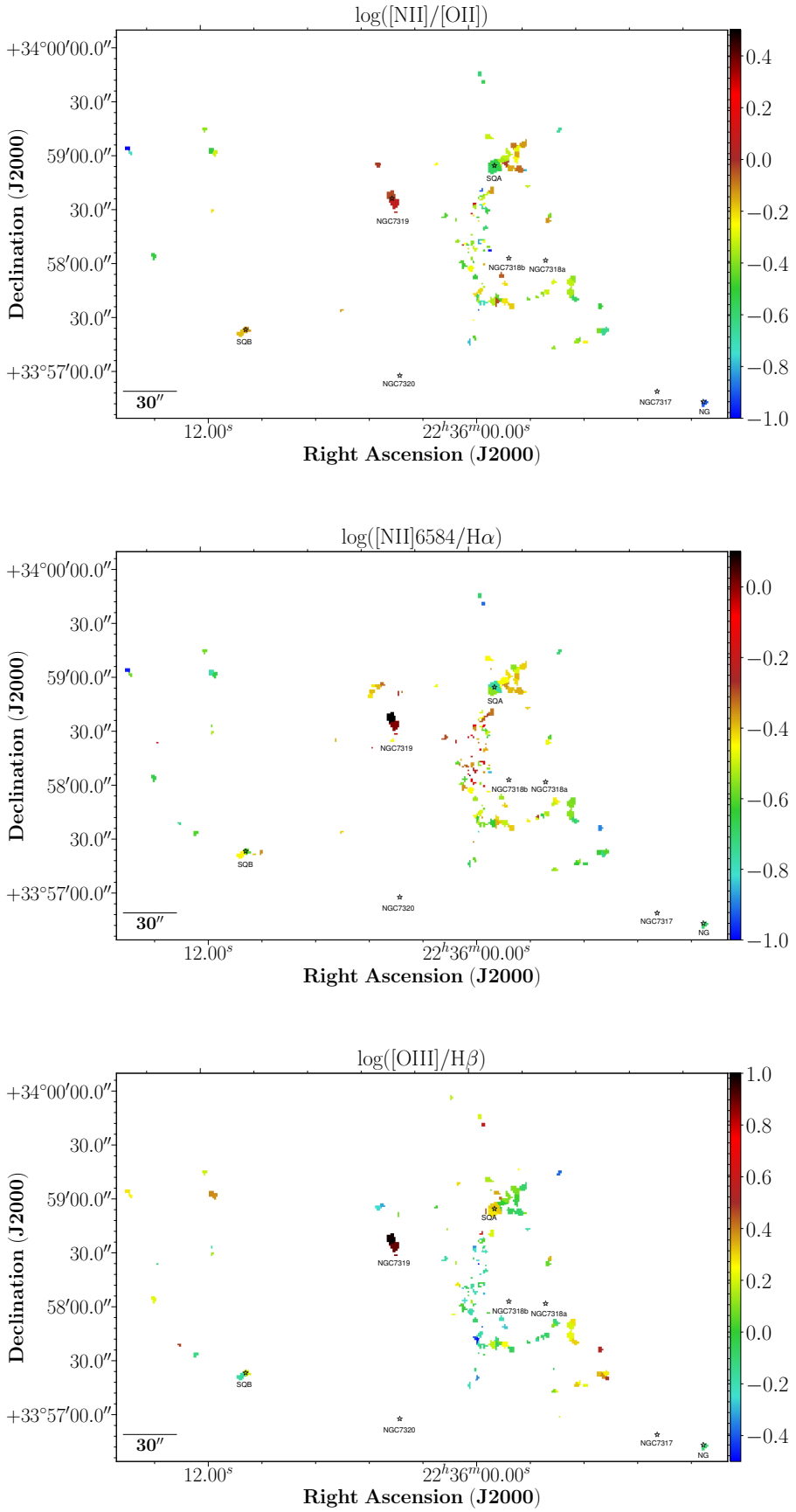

Figure 5.3: Line ratios maps. From top to bottom and left to right: [NII]/[OII], [NII]/Hα, [OIII]/Hβ, O3N2, [OIII]/[OII], R_{23}.

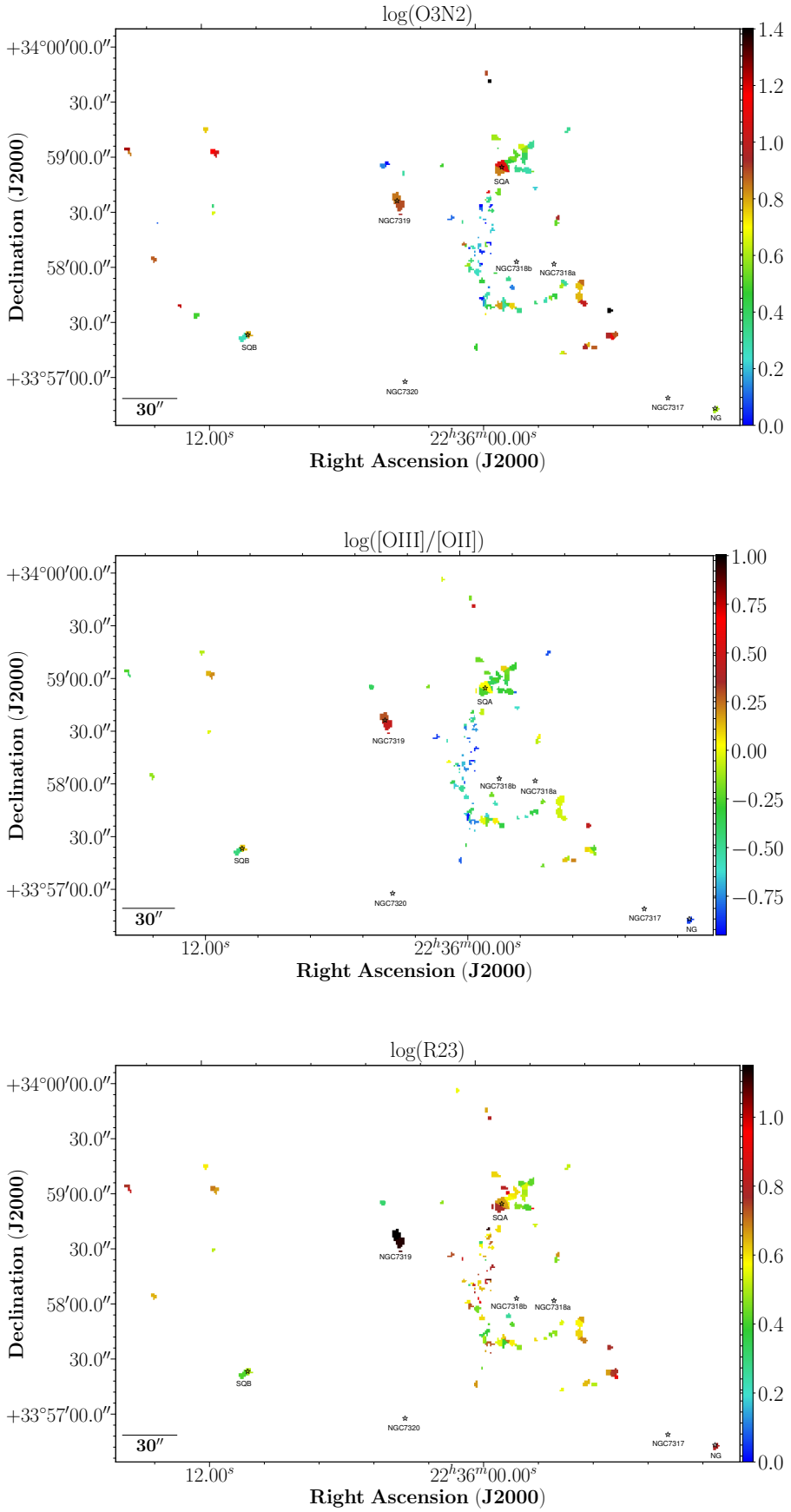

Figure 5.3: (continued)

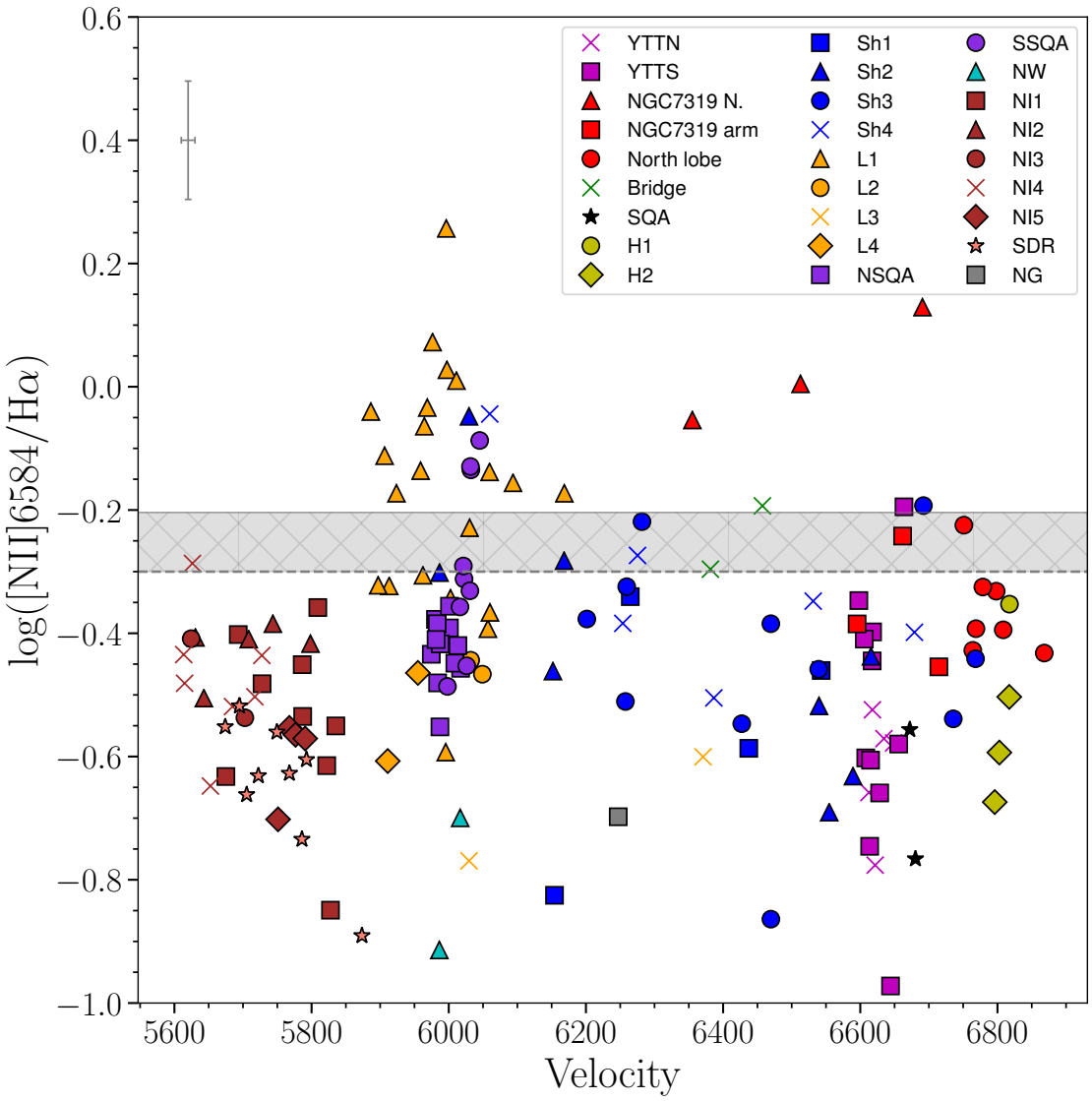

Figure 5.4: log([NII]/Hα) versus radial velocity diagram. All the points in the figure have the same colours and markers as Fig. 5.2. The horizontal dashed grey line and the grey band correspond to the reference value at log([NII]/Hα)=-0.3 and the uncertainties for the log([NII]/Hα) ratio, respectively. The upper left cross indicates the typical error of both parameters.

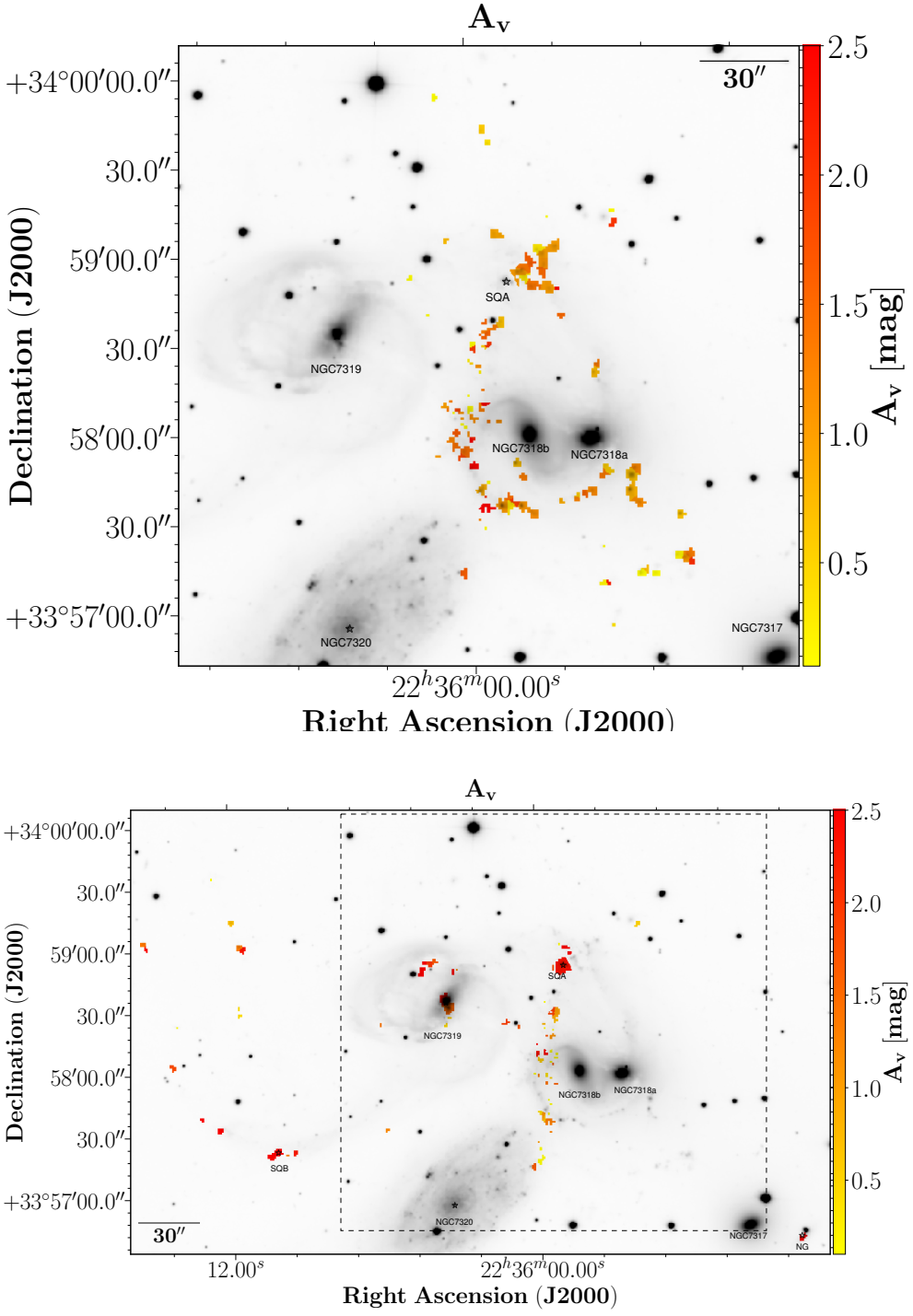

Figure 5.5: SQ spatial map colour coded according to their A_v extinction for the LV sub-sample (upper panel) and the HV sub-sample (lower panel).

5.2.3 Maps of extinction and excitation

In Fig. 5.5 we show the extinction map in magnitudes in the V band, A_v, for the emission regions found in SQ. We separate the maps in LV (upper left panel) and HV (upper right panel) sub-samples according to the definition given in Sect. 5.2.1. The extinction A_v derived in this work goes from 0 to 4 mag. The median is A_v = 1.1 mag, in agreement with the value obtained in Rodríguez-Baras et al. (2018) for a sample of star-forming regions over the discs of spiral galaxies. On average, the regions found in LV show lower values of A_v (∼1 mag) than those located in HV (∼1.3 mag), in line with previous works (e.g. Konstantopoulos et al. 2014). In LV extinction map we can see several interesting distributions. SDR presents A_v values ∼0.5 mag. Moreover, in North and South of the strong HII region SQA (NSQA and SSQA, respectively) a mixture of A_v values are found. Generally, SSQA has higher A_v values than NSQA (SSQA: ∼1.3; NSQA: ∼1). Region 66 has a A_v ∼2.9 (from L1), being the region with the greatest value in the LV map. On the other hand, SQA has an extinction value A_v ∼2.3 mag. In the AGN North lobe we can see A_v >1.2 mag, where the greatest value is seen in the region 20 (A_v ∼4.2 mag, see Table 5.1). NG has also high extinction (with average A_v ∼3.5 mag). YTTS presents higher extinction values, on average, than in the north regions, where the extinction values are lower than 2.5 mag. Conversely, in the LSSR zone, a mixture of extinction values are found (with a median value of A_v ∼1 mag). It is important to note that at the centre of the LSSR zone, several regions with A_v >2 mag (e.g. region 83 and 60) are present in both LV and HV maps.

In order to produce a classification of the emitting regions, we study the BPT diagnostic diagram (Baldwin et al. 1981; Kewley et al. 2001; Kauffmann et al. 2003a). In Fig. 5.6 we show the BPT diagram (log([OIII]5007/Hβ versus log([NII]6583/Hα) for the SQ regions. Overplotted as grey continuous lines the predicted models from Allen et al. (2008) are shown for ionisation of gas considering fast shocks without precursor for solar metallicity and low density (n=0.1), with velocities between 175 and 1000 $km\,s^{-1}$. We added the mean uncertainties found in this work for the HII regions in the line ratios that are considered in the BPT diagram (i.e. [OIII]/Hβ and [NII]/Hα) to the Kauffmann demarcation, shown as a grey band in Fig. 5.6. As expected, the regions from NGC7319 nucleus appear in the AGN zone in the BPT diagram. The remaining SQ regions are displayed within the star-forming and composite (C) zones. We have found 91 star-forming regions, 17 C regions, and 7 AGN-like regions. Rodríguez-Baras et al. (2014) found a fraction of pixels showing emission typical of the composite zone of the BPT diagram and claiming that HII regions can be found in the C zone (see also Sánchez et al. 2014). We believe that these C regions are contaminated by the emission of the shocked regions located in its vicinity.[3] In line with this, HII regions in this work were classified as those regions: i) located in the star-forming (SF) zone according to the Kauffmann demarcation or in the plotted grey band; and ii) where the signal-to-noise ratio for the Hα, Hβ, [OIII]5007, and [NII]6584 emission fluxes are higher than or equal to 3. AGN-like and composite regions are shown in several diagrams and maps. No values of SFR, nitrogen or oxygen abundances have been derived for composite or AGN-like regions.

In Fig. 5.7 (upper panel) we show the BPT map for the HV sub-sample. In the lower left

[3]Notice that [NII]6584 emission line is more sensitive to shocks processes (Sulentic et al. 2001).

panel, we present the BPT map for the LV sub-sample and in the lower right panel we display the three dimensional distribution of BPT class (α, δ, radial velocity) for all the SQ regions. We colour-coded the SQ regions according to their position in the BPT diagram (see Fig. 5.6): i) star-forming regions (BPT colour bar equal to 1, blue regions); ii) C regions (BPT colour bar equal to 2, green regions); iii) AGN-like regions (BPT colour bar equal to 3, red regions). The LV map shows that all regions found in the SDR and NIs are star-forming. It is important to note that LSSR contaminates the NI1 spectra, where [NII] coincides in the same wavelength with Hα from the LSSR, and must be taken into account when fitting the Hα and [NII] emission lines.[4] Also, all regions from NSQA, SSQA, L2, L4, and the northernmost regions (i.e. NW tidal) are star-forming regions. According to Fig. 5.6, most regions from L1 are compatible with the shock models adopted in this work. The HV map shows that all regions in the YTT and in SQA are star-forming regions. NG is a star-forming galaxy. Also, the regions found in the Hα 'bridge' are C and star-forming regions. As expected, NGC7319 presents AGN-like regions, but the North lobe presents star-forming and composite regions.

5.2.4 Derivation of the SFR and chemical abundances

Once we have defined the sample of SQ HII regions, we derive the SFR, as well as the oxygen and nitrogen abundances. In order to derive the SFR, we use the following equation:

$$SFR(M_{\odot}\, yr^{-1}) = 7.9 \times 10^{42} L_{H\alpha}(erg\, s^{-1}) \tag{5.1}$$

where $L_{H\alpha}$=4πD^2 F(Hα) is the Hα luminosity, D is the distance in Mpc (Kennicutt 1998a), and F(Hα) is the Hα flux. We assume that the average distance of SQ is 88.6 Mpc (Hickson 1982; Mould et al. 2000; Fedotov et al. 2015). We only compute the SFR for the 91 HII regions found in SQ according to the classification in Fig. 5.6. In Table 5.2 we present the SFR values for each HII region. The HII regions from SQ span log(SFR/$M_{\odot}yr^{-1}$) values between -3.35 (region 109) and -0.13 (region 122).

To derive the oxygen abundance, we use three empirical calibrators[5]: N2 (eq. 5.2) and O3N2 (eq. 5.3) from Pérez-Montero & Contini (2009), and R calibrator from Pilyugin & Grebel (2016), see eqs. 5.4 and 5.5. The R calibrator uses the line ratios N2, R2, and R3.[6]
Pérez-Montero & Contini (2009) equations are:

$$12 + log(O/H) = 0.79 \times N2 + 9.07 \tag{5.2}$$

$$12 + log(O/H) = 8.74 - 0.31 \times O3N2 \tag{5.3}$$

where N2 = log([NII]λ6584/Hα) and

[4]This fact tell us that care should be exercised when analysing narrow-band photometric observations without spectroscopic information.

[5]These are calibrated against direct derivations of abundances calculated with electron temperature measurements

[6]We are aware that the derivation of oxygen abundance using bright-lines calibrators can be dependent on the precise indicator used. For the sake of the comparison with previous work, and taking into account the typical errors obtained, we have selected these three calibrators for O/H; general consensus shows the situation is better for the N/O abundance ratio, with smaller uncertainty. N/O is a sensitive chemical evolution indicator especially useful for the present work.

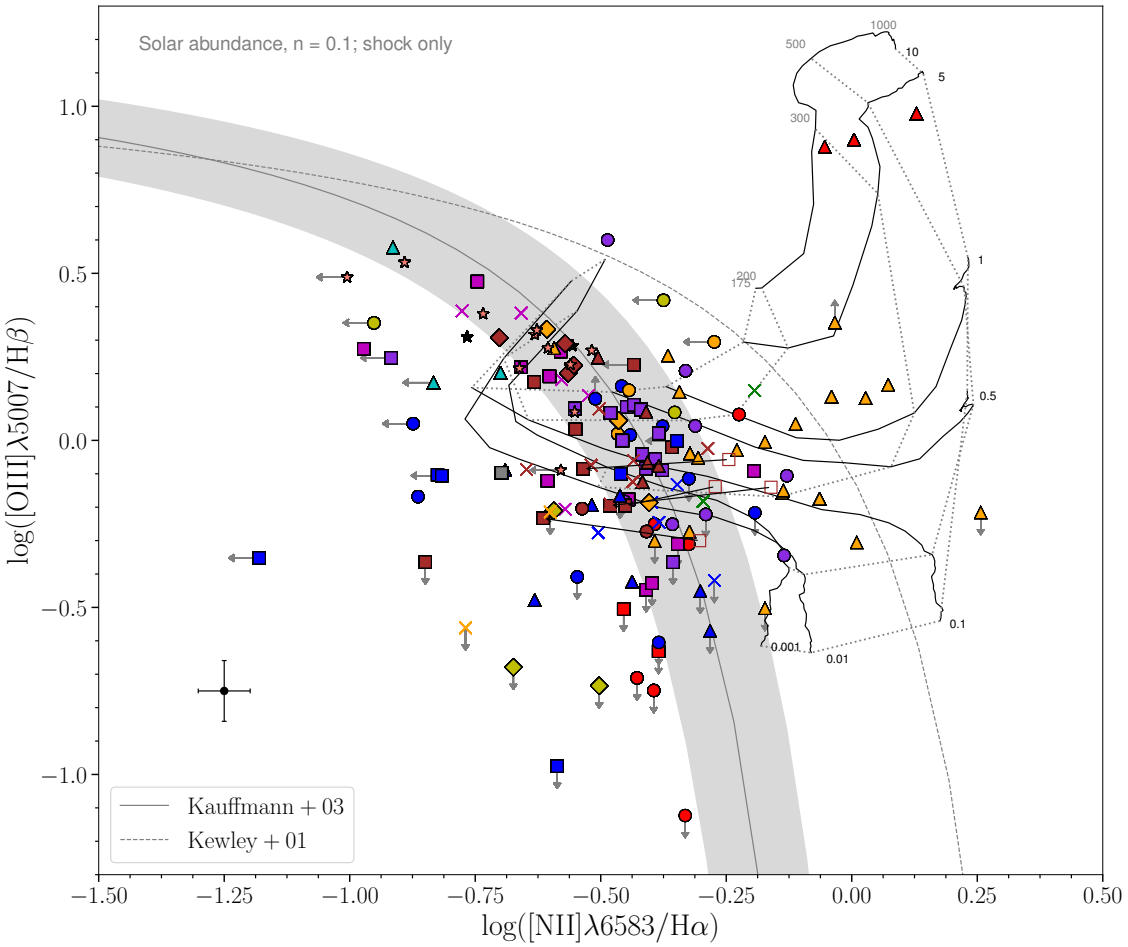

Figure 5.6: [OIII]λ5007/Hβ versus [NII]λ6583/Hα diagnostic diagram (BPT) for the SQ Hα emission regions. Regions without arrow have the S/N higher than 3 for the fluxes in the strong emission lines Hα, Hβ, [OIII]5007, and [NII]6584, the typical error in each axis is represent with the black cross. Regions with ascending grey arrow have S/N(Hβ)<3, regions with decreasing grey arrow have S/N([OIII]5007)<3, while regions with grey arrow pointing left have S/N([NII]6583)<3. All the points in the figure have the same colours and markers as Fig. 5.2. The grey dashed line shows the Kewley et al. (2001) demarcation and the grey continuous line shows the Kauffmann et al. (2003a) curve. The grey band shows the uncertainties for the BPT line ratios (i.e. [OIII]/Hβ and [NII]/Hα) to the Kauffmann demarcation. The black lines correspond to the shock only models of Allen et al. (2008) for solar metallicity and low density (n=0.1), while the dotted lines correspond to the shock velocity.

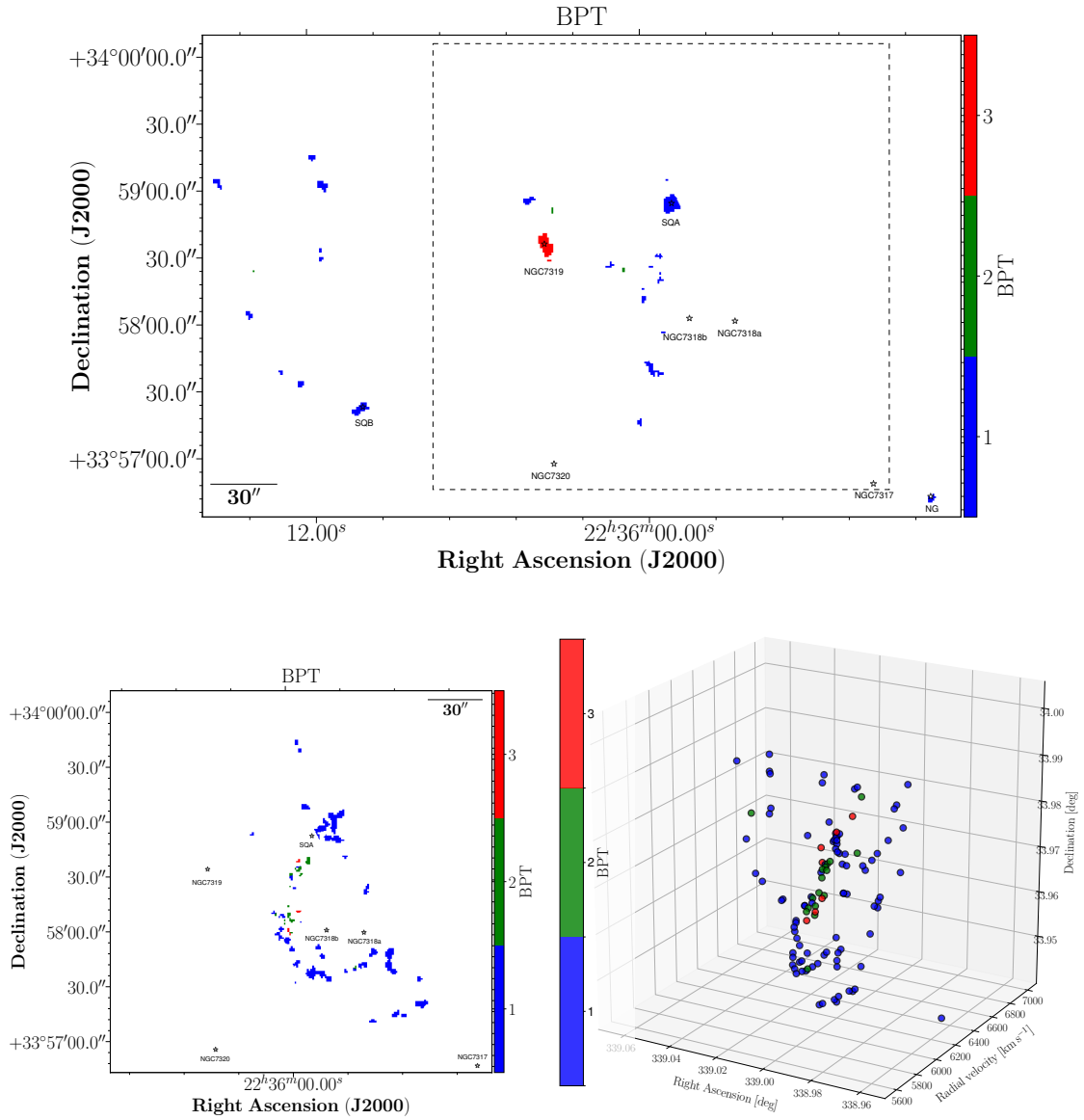

Figure 5.7: SQ spatial map colour coded according to their position in the BPT diagnostic diagram for the HV sub-sample (upper panel), the LV sub-sample (lower left panel), and the three dimensional distribution of BPT class (α, δ, radial velocity; lower right panel). Blue, green, and red pixels represent star-forming (1), composite (2), and AGN-like (3) regions, respectively.

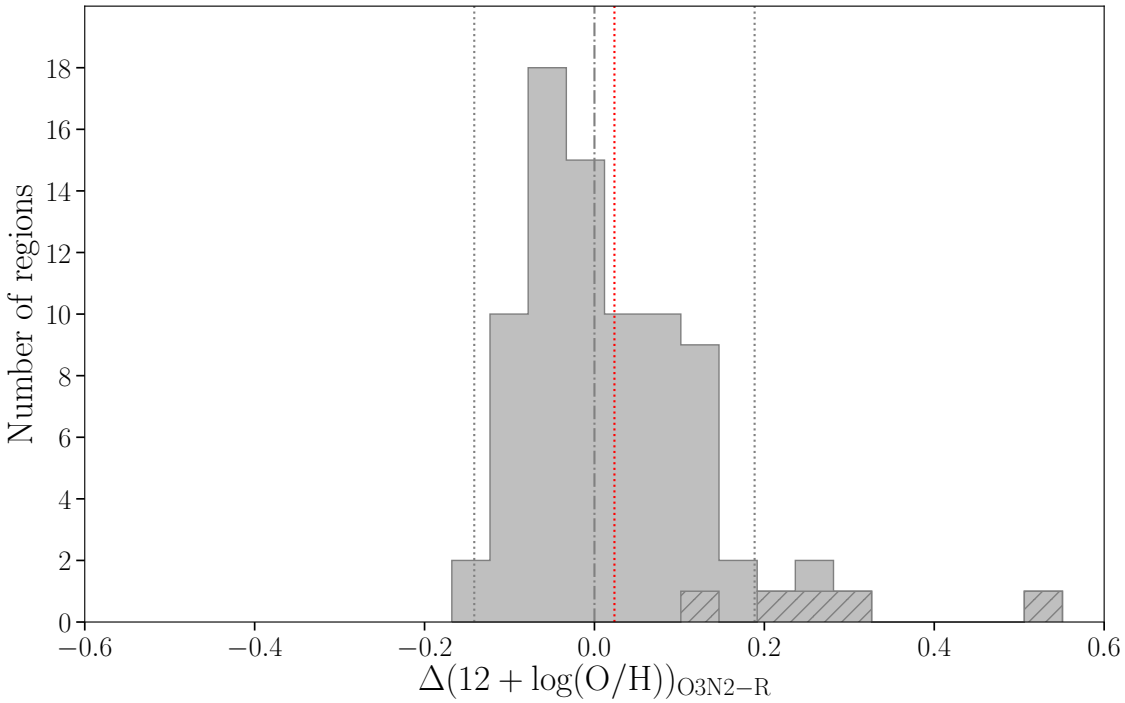

Figure 5.8: Distribution of difference between O3N2 and R calibrators for oxygen abundance for SQ HII regions. The grey and red dashed lines correspond to the value at difference equal to zero and between O3N2 and R calibrators for SQ HII regions (0.02 dex), respectively. The grey dotted lines indicate the 3σ scatter. The dashed histogram represents the sample of SQ HII regions when 12+log(O/H)<8.4, for which the R calibrator has been adopted.

O3N2 = log([OIII]λ5007/Hβ × Hα/[NII]λ6584)
Pilyugin & Grebel (2016) equations are: if log(N2) > -0.6:

$$12 + \log(O/H) = 8.589 + 0.022 \log\left(\frac{R3}{R2}\right) + 0.399 \log(N2) + \left(-0.137 + 0.164 \log\left(\frac{R3}{R2}\right) + 0.589 \log(N2)\right) \times \log(R2) \quad (5.4)$$

on the contrary, if log(N2) ≤ -0.6:

$$12 + \log(O/H) = 7.932 + 0.944 \log\left(\frac{R3}{R2}\right) + 0.695 \log(N2) + \left(0.970 - 0.291 \log\left(\frac{R3}{R2}\right) - 0.019 \log(N2)\right) \times \log(R2) \quad (5.5)$$

Figure 5.8 shows the distribution of difference between the O3N2 and R calibrators used to derive the oxygen abundance for the sample of 91 HII SQ regions. The resulting oxygen abundances derived using both calibrators are consistent within errors when 12+log(O/H)≥8.4, but not when it is <8.4 given the restricted range of validity of these two calibrators. Thus, calibrator can be used for 12+log(O/H)≥8.4. A similar situation holds for N2. When 12+log(O/H)<8.4 we considered the results from the R calibrator. We note that we cannot use the R calibrator for

10 HII regions because they do not have [OII]λ3727. With the intention of having as many regions as possible and knowing that the O3N2 and R calibrators are consistent (within the errors) when 12+log(O/H)≥8.4, we have used the results from O3N2 for 12+log(O/H)≥8.4 and R when 12+log(O/H)<8.4.

To derive N/O, we use the calibrator from Pilyugin & Grebel (2016) (eq. 5.6) as:

$$\log(N/O) = -0.657 - 0.201\log(N2) + (0.742 - 0.075\log(N2)) \times \log\left(\frac{N2}{R2}\right) \tag{5.6}$$

where:

$$R2 = I([OII])\lambda\lambda 3727/I(H\beta),$$

$$\begin{aligned} N2 = I([NII])\lambda 6548 + \lambda 6584/I(H\beta) = \\ 1.333I([NII])\lambda 6548/I(H\beta), \\ R3 = I([OIII])\lambda 4959 + \lambda 5007/I(H\beta) = \\ 1.333I([OIII])\lambda 5007/I(H\beta). \end{aligned} \tag{5.7}$$

In Table 5.2 we show several properties derived in this section. In Col. 1 the region name is presented. Cols. 2 and 3 present the SFR and Hα luminosity. Cols. 4 shows the classification according to the BPT diagram. Col. 5 tells us whether the velocity of the region belongs to the LV (0 in the column) or HV (1 in the column).

In Table 5.3 we show the metallicity and N/O values for the SQ HII regions derived in this section. In Col. 1 the region name is presented. Cols. 2, 3, and 4 show the oxygen abundances using N2, O3N2, and R calibrators, respectively. Col. 5 display the nitrogen to oxygen abundance ratio using Pilyugin & Grebel (2016). Cols. 6 tells us whether the velocity of the region belongs to the LV (0 in the column) or HV (1 in the column) sub-samples.

5.2.5 Spatially resolved analysis of SFR, oxygen and nitrogen abundances

Figure 5.9 shows the SFR map for the SQ. Upper panel presents HII regions belonging to the LV sub-sample, while the lower panel shows regions from the HV sub-sample. The HII regions from SQ, except SQA and SQB, have log(SFR/M$_\odot yr^{-1}$) lower than -1. It can be seen that the regions from Shs, NW tidal tail, L1, L2, and L4 have a quite low SFR (log(SFR/M$_\odot yr^{-1}$)<-2). Moreover, NIs, SDR, Hs, NSQA, SSQA, and the North lobe have a low SFR (log(SFR/M$_\odot yr^{-1}$)<-1). Conversely, SQA has the greatest SFR value found in the SQ (log(SFR/M$_\odot yr^{-1}$)~-0.06). SQB also has a SFR higher than the average SFR found in SQ (region 15, log(SFR/M$_\odot yr^{-1}$)~-0.7). On average, the HII regions from YTTS have higher SFR values than YTTN (log(SFR/M$_\odot yr^{-1}$)=-1.5 versus -2, respectively). NG has a value of log(SFR/M$_\odot yr^{-1}$)=-1 and the North lobe has log(SFR/M$_\odot yr^{-1}$)~-1.5.

In Fig. 5.10 we show the oxygen abundance maps for LV (upper panel) and HV (lower panel) sub-samples using the O3N2 calibrator from Pérez-Montero & Contini (2009). In the Sect. 5.4

we show the oxygen abundance maps using the R calibrator from Pilyugin & Grebel (2016). As we explained in Sect. 5.2.4, the metallicity calibrators (O3N2 and R) are consistent when 12+log(O/H)≥8.4, and either can be selected, we decided to use the O3N2 calibrator because it takes into account 10 more HII regions than the R calibrator. When 12+log(O/H)<8.4, we used the results from the R calibrator. In general, the two metallicity maps for the LV sub-sample show similar trends regardless of the calibrator used. On average, NIs spans metallicity values from solar (12+log(O/H)=8.69) to half-solar (12+log(O/H)=8.4). The regions from the NI1 and NI2 zones, which coincide with the pointings in Iglesias-Páramo et al. (2012), show metallicity values in the range of 8.5 to 8.66, in accordance with Iglesias-Páramo et al. (2012). In Sect. 5.3 we show the relation between metallicity and normalised distance (d/d_{max}) for NIs; also, SDR has an average metallicity of ~8.45 but the minimum value calculated in this zone is 8.3 (region 172); moreover, regions from the tidal tail NW present metallicity values close to 8.45 (regions 97 and 82, respectively), in agreement with de Mello et al. (2012). As we can see in Fig. 5.10 and Table 5.3, NSQA has slightly higher metallicity values than SSQA (8.69 compared to 8.6), on average. The two HII regions from L2 (we recall that this zone connect NSQA with SSQA) present a metallicity of ~8.57, as well as L4 zone. On the other hand, when we focus on the HV sub-sample (lower panel in Fig. 5.10) we can see that SQA, the region 10 (in YTTN), and region 2 (in YTTS) show the lower values of metallicity (12+log(O/H)=8.4 on average), where SQB has 12+log(O/H)=8.5. For NG we found 12+log(O/H)=8.27. The HII regions from Shs, spans metallicity values between 8 < 12+log(O/H) < 8.7. Moreover, the regions from YTT presents metallicity values from 12+log(O/H)=8.2 (region 2) to solar metallicity (region 14), in agreement with Mendes de Oliveira et al. (2004). We have found oversolar metallicity values in the North lobe and in region 35 (Hα 'bridge'). The average metallicity derived in SQ is $\langle 12+log(O/H)\rangle$=8.6, and the minimum value found is 12+log(O/H)=8.0 (region 59).

In Fig. 5.11 we show the nitrogen to oxygen abundance ratio maps for LV (upper panel) and HV (lower panel) sub-samples of SQ HII regions. In this work, we use the calibrator from Pilyugin & Grebel (2016) as the representative nitrogen to oxygen abundance ratio for each HII region. It is important to note that the regions found in HV sub-sample have lower values of nitrogen to oxygen abundance ratio than those located in LV (log(N/O)=-1 and -0.86, respectively). The average value of N/O derived in SQ is -0.88. Except in the North lobe, on average the remaining HII regions in the HV sub-sample have subsolar N/O values.[7] However, in the LV sub-sample, we found two regions with subsolar N/O values (SSQA and NW with mean values of log(N/O)=-0.93 and -0.97, respectively). This may indicate that both parts have different behaviour coming from diverse galaxies. LV could come from NGC7318B, whilst HV could come from NGC7319 and the debris produced in any past interaction between NGC7319 and other galaxies (e.g. NGC7317, NGC7318A, or NGC7320c). Only 6 out of 54 HII regions with N/O in the LV sub-sample have values log(N/O) < -1 (regions 50, 65, 82, 147, 174, and 175). No evidence of a N/O gradient is found in NIs (~solar value, see Sect 5.3). NSQA presents higher values than SSQA on average (log(N/O)=-0.8 and -1, respectively). We can divide NSQA in two parts, East and West. The eastern part has lower N/O values than the western part (log(N/O)=-0.9 versus $\gtrsim$-0.75). The SDR

[7] $log(N/O)_{\odot} = -0.86$ (**?**).

zone on average presents the same N/O as NI5. However, except the North lobe (log(N/O)=-0.64), all zones from the HV sub-sample have log(N/O)$\lesssim$-1. Only 7 out of 33 HII regions with N/O in the HV sub-sample have log(N/O) > -0.86 (regions 11, 13, 14, 15, 24, 64, and 77). Additionally, NG has a low value of log(N/O)=-1.33. The minimum value for N/O in SQ is log(N/O)=-1.6 (region 59).

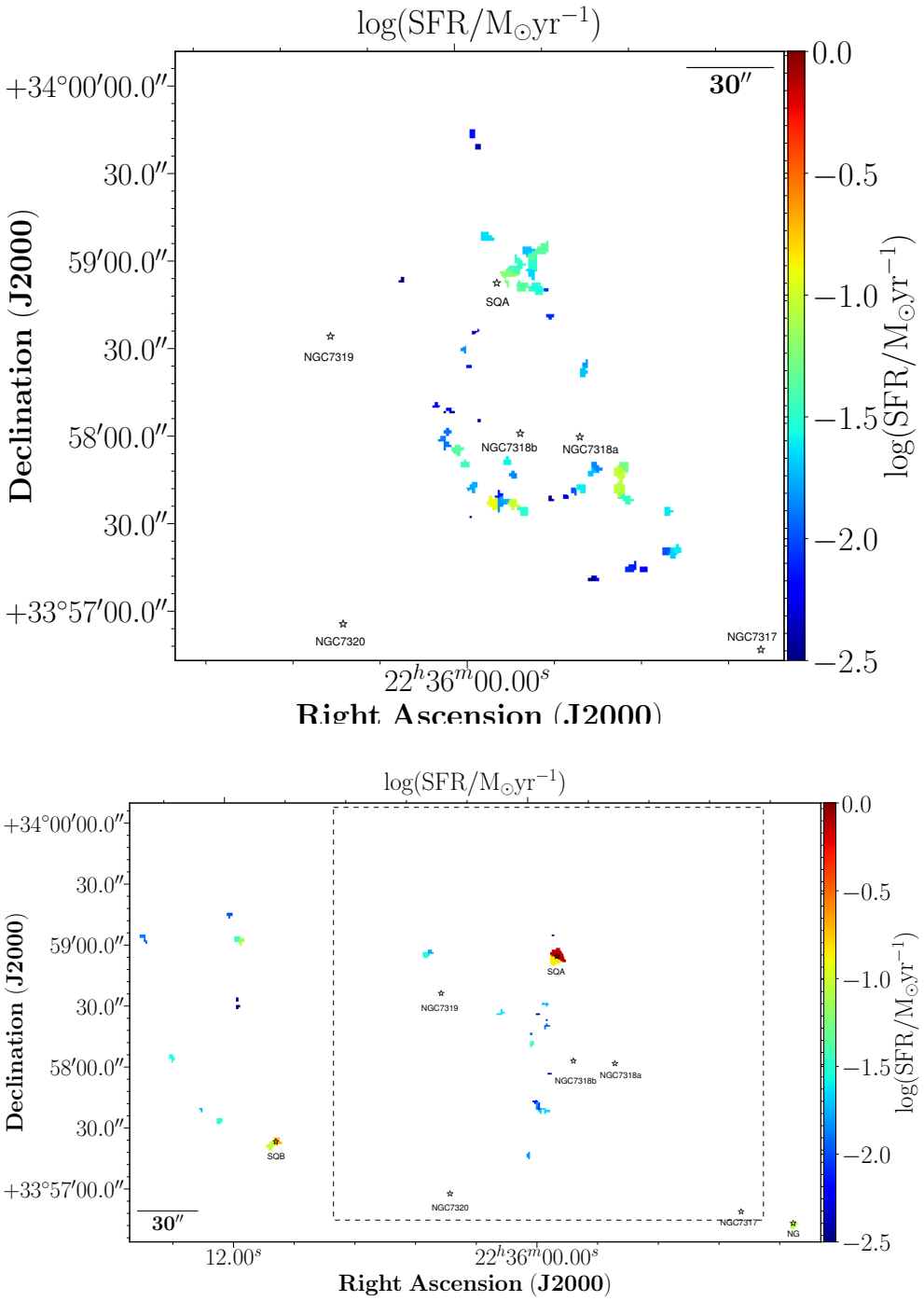

Figure 5.9: SQ spatial map colour coded according to their SFR for the LV sub-sample (upper panel) and the HV sub-sample (lower panel).

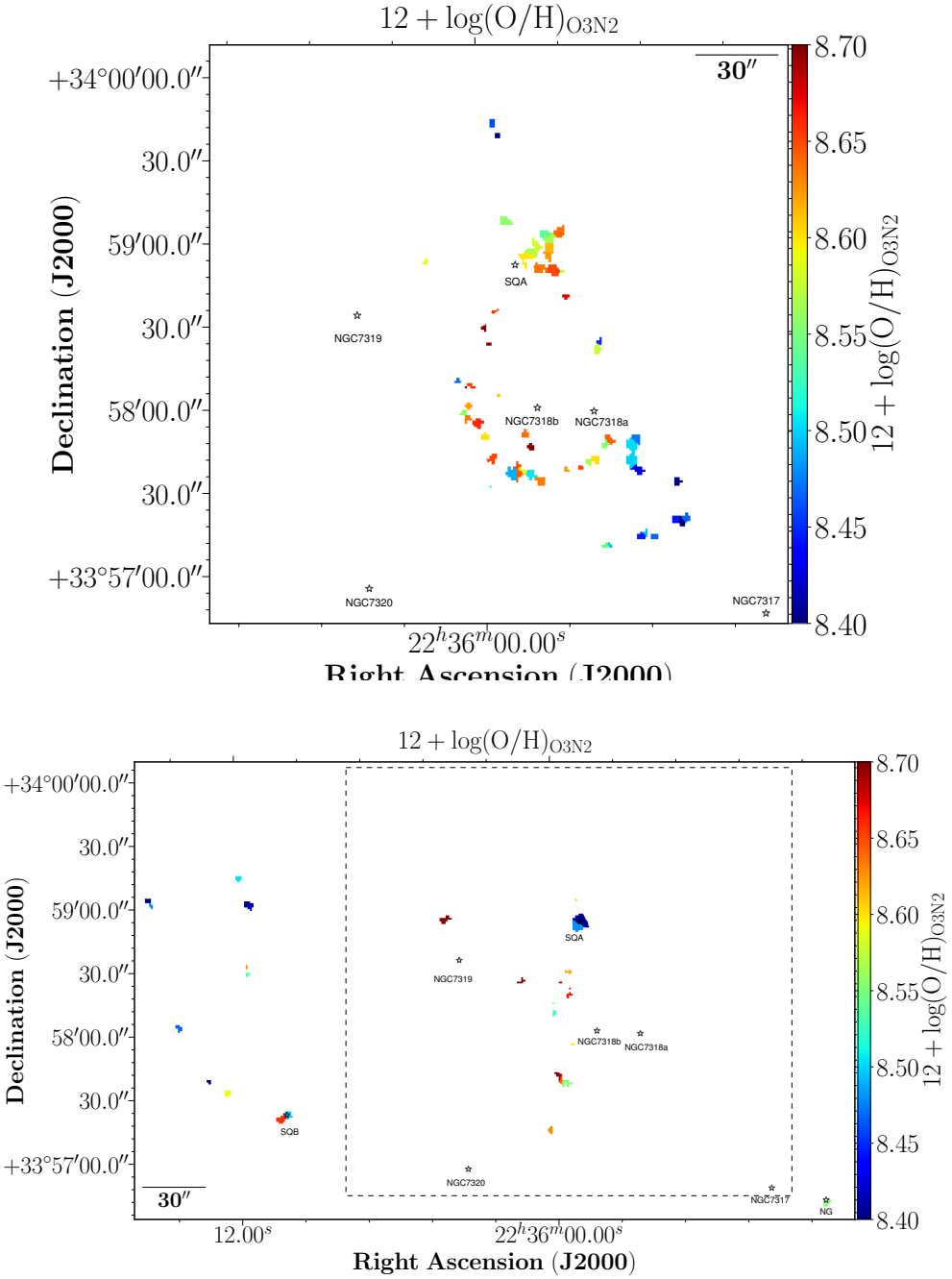

Figure 5.10: SQ spatial map for the LV sub-sample (upper panel) and the HV sub-sample (lower panel) colour coded according to their 12+log(O/H) derived using the O3N2 calibrator from Pérez-Montero & Contini (2009).

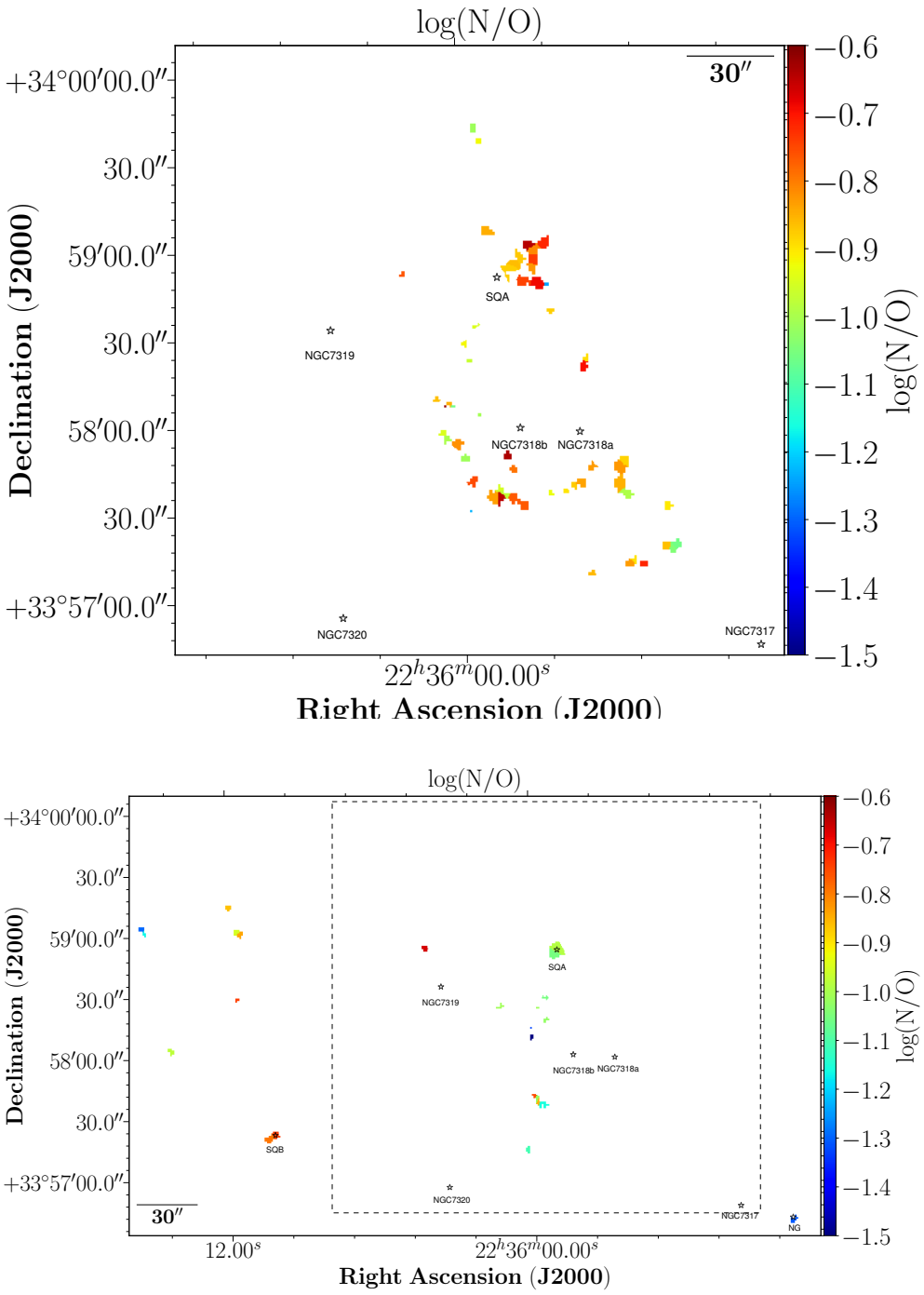

Figure 5.11: SQ spatial map for the LV sub-sample (upper panel) and the HV sub-sample (lower panel) colour coded according to their log(N/O) derived from Pilyugin & Grebel (2016) calibrator.

5.3 Discussion and summary

A sample of 175 SQ Hα emitting regions, 22 of them presenting two velocity components, has been defined according to the following criteria: i) the velocity of the region is within the velocity range of SQ (between ~5500 and ~7000$km\ s^{-1}$); ii) the detection of at least one additional emission line beside Hα. We have selected the SF regions from the BPT diagram. Taking this into account, we have found 91 HII regions, 17 composite, and 7 AGN-like regions. We found all composite and AGN regions in the LV sub-sample, located in the L1, SSQA, Shs, and North lobe zones. This is also confirmed by the log([NII]/Hα) versus radial velocity diagram. We need to keep in mind that the spectra from NI1 are contaminated by the shock zone, since the [NII] from NI1 coincides in wavelength with the Hα from the shock. It is important to correct for this in order not to find HII regions in the composite zone (e.g. Rodríguez-Baras et al. 2014) to avoid misclassifications.

We found three AGN-like spectra in the L1 zone and another one in NSQA. As expected, the NGC7319 nucleus has AGN classification, but the North lobe presents also star-forming and composite regions. The composite and AGN regions are in L1, SSQA, and Shs, being consistent with fast shock ionisation without precursor for solar metallicity and low density (n = 0.1), with velocities between 175 and 300 $km\ s^{-1}$ using the models from Allen et al. (2008). The star-forming regions are located in the North and South zone of the shock (NW-LV, NW-HV, and SW zones in Williams et al. 2002), where there is HI. Conversely, the regions in the YTT, the new intruder (NI, NGC7318B) and SDR are star-forming.

We derived the total SFR for the sample of 91 HII regions in SQ. The total SFR found for SQ is log(SFR/$M_\odot\ yr^{-1}$)=0.496. 55% of the SFR (log(SFR/$M_\odot\ yr^{-1}$)=0.24) comes from the HV sub-sample, while the LV sub-sample is 45% (log(SFR/$M_\odot\ yr^{-1}$) = 0.15). 28% of the total SFR in SQ comes from SQA (log(SFR/$M_\odot\ yr^{-1}$)=-0.06), while 9% (log(SFR/$M_\odot\ yr^{-1}$)=-0.54) is in SQB. So, except for SQA and SQB, the material prior to the collision with NI does not show a high SFR, therefore SQ was apparently quench. There are differences between the SFR derived for SQA from Xu et al. (2005) and the one derived here. The difference is likely due to the fact that Xu et al. (2005, , see region VI) derives the SFR for a larger area which includes SQA, NSQA, L2, and H1. When considering all this zones we obtained log(SFR/$M_\odot\ yr^{-1}$)=0.12, which is in agreement with Xu et al. (2005), that found log(SFR/$M_\odot\ yr^{-1}$)=0.125.

Fig. 5.12 shows the relation between A_v and SFR for the sample of 91 SQ HII regions (upper panel) and for the sample of 209 276 SDSS star-forming galaxies corrected for aperture effects[8] from Duarte Puertas et al. (2017). We show that, in both SQ HII regions and SDSS star-forming galaxies, the extinction is correlated with the SFR, in such a way that the higher the SFR, the higher the extinction (with their dispersion), and spread the same range of A_v values. Therefore, the most massive galaxies and regions present more extinction. It can be expected that the SQ HII regions are shifted in this diagram since they have lower SFR values. In the SDSS star-forming galaxies, each extended galaxy is considered as a single point in the A_v versus SFR diagram. We note that

[8]The total SFR for the SDSS star-forming galaxies was derived using the empirical aperture corrections based on the CALIFA survey defined by Iglesias-Páramo et al. (2016).

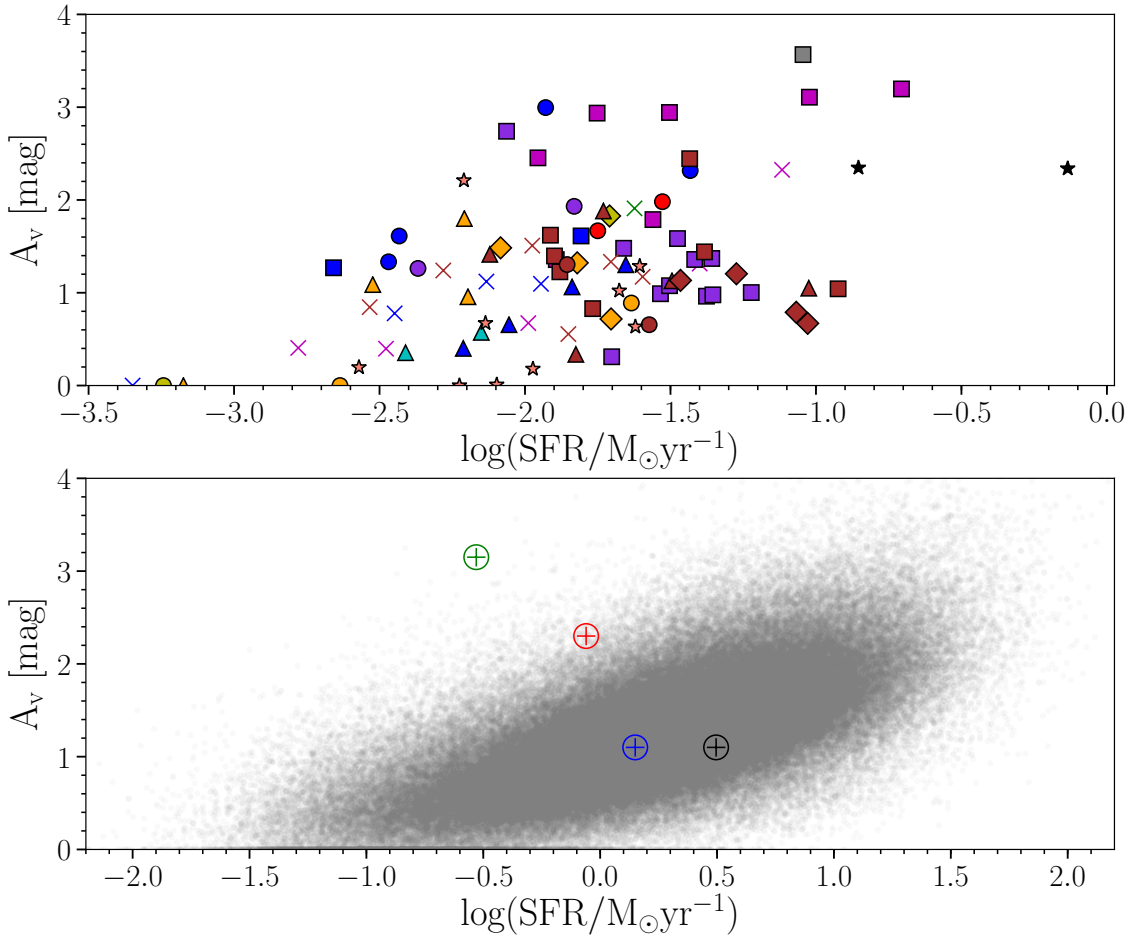

Figure 5.12: Relation between A_v and SFR for: Upper panel) the 91 SQ HII regions, all the points in the figure have the same colours and markers as Fig. 5.2; and Lower panel) a sample of 209 276 SDSS star-forming galaxies corrected for aperture effects found in Duarte Puertas et al. (2017). Black, blue, red, and green ⊕ represent the position of the total SFR and the mean A_v for all the SQ HII regions, NI, SQA, and SQB respectively. Grey points show the values for the sample of 209 276 SDSS star-forming galaxies.

when considering normal galaxies (i.e. not reduced to a single point) the gas is concentrated in the central zones whilst in SQ the gas is not located in the central areas of the galaxies. In our case, when we considered the total SFR and the A_v median for all SQ and NI, both are located in the same part as the footprint of SDSS star-forming galaxy. On the one hand, we can appreciate that both SQA and SQB are outlier in this diagram, since they have more A_v than galaxies with the same SFR. Besides, the SQ HII regions are displaced elsewhere since there is an interaction and, thus, their position depends on whether the HI gas is moving or not. The regions with more extinction and SFR are outside the galaxies because the interactions have dispersed the gas to the peripheral zones. Henceforth, the extinction in the SQ HII regions does not follow the general trend observed in spiral galaxies. Generally, the inner-outer diminishing extinction pattern that occur in spiral galaxies disappears giving rise to a trend dominated by the successive interactions. All above is

in accordance with the interpretation of Verdes-Montenegro et al. (2001) about the distribution of HI in compact groups. SQ is part of Phase 3a according to the evolutionary sequence from the HI distribution of Verdes-Montenegro et al. (2001). They say that the HI has been stripped out entirely, or almost, in this Phase from the disc of the galaxies that belong to the compact groups, suggesting that the HI could be found in the tails produced by the interactions that the galaxies suffered.

The analysis of the chemical abundances of oxygen and nitrogen for our sample of SQ HII regions shows that the range of oxygen and nitrogen to oxygen abundance ratios are between solar and a fourth of solar approximately. The lowest values are found in the region 59b (12+log(O/H)≃8 and log(N/O)≃-1.6). Figure 5.13 shows the relation between metallicity (upper panels) or nitrogen to oxygen abundance ratio (left lower panel) and the radial velocity for the sample of HII SQ regions. Also, in the right lower panel, we show the relation between A_v and the radial velocity for all the SQ emission regions. The presence of an inner-outer radial metallicity gradient along the tail is clearly visible for NIs and it will be commented on below. The YTT presents a median oxygen abundance of ∼8.55 that agrees with Mendes de Oliveira et al. (2004). In the case of the regions in NSQA, a hint for the existence of a radial variation of the oxygen abundance and N/O ratio has been seen, though the complexity of this system prevents us from associating this variation with a spiral arm.

The SQ HII regions are mostly metal-rich (12+log(O/H)$\gtrsim$8.5). All 8 metal-poor regions found here are located in the HV sub-sample and none in the LV sub-sample. In the case of the N/O, we have found 10 regions with log(N/O) lower than half solar value. Ninety percent of the regions with N/O $\leq \frac{1}{2}(\mathrm{N/O})_\odot$ are located in the HV sub-sample. All the regions in the LV sub-sample (except one) have log(N/O) values higher than half solar. This might indicate that at least two chemically different gas components cohabit in SQ, one metal-rich in the LV sub-sample and YTT, and one metal-poor in the shock regions and in several regions in YTT.

The metallicity values obtained from the empirical calibrations for the SQ HII regions have been compared with the theoretical models (HIICHEMISTRY Pérez-Montero 2014). Consistency has been found between the empirical and theoretical oxygen abundances within the errors. A similar comparison carried out for the N/O found less dispersion.

In this work, we have studied the radial gradients for several properties of the spiral arm associated with the NIs (i.e. NI1, NI2, NI4, and NI5 strands) and SDR. As we can see in Fig. 5.14, the oxygen abundance in NI1, NI2, and NI4 appears to be constant. This is compatible with the results found in a spiral arm at a constant distance from the nucleus. Then, the metallicity value decreases as we approach the NI5 and SDR regions. We found a similar result when we studied log([NII]/Hα). We did not find a N/O gradient, because the values are almost constant (solar value). Thus, the metal-rich material could come from the inner part of the galaxy. In the case of the ratio log([OIII]/Hβ), we found lower values in NI1 than in SDR. We obtained an A_v gradient with higher values in NI1 than in SDR. All the properties studied in Fig. 5.14 are consistent with the presence of inner-outer variation along the NI tails in the line of the results obtained by Iglesias-Páramo et al. (2012) and Rodríguez-Baras et al. (2014). Finally, the relation between log(N/O) and 12+log(O/H) for the SQ HII region is presented in Fig. 5.15. A secondary production of nitrogen

can be seen in the behaviour of the relation between log(N/O) and 12+log(O/H) for the HII regions belonging to the arms. In Fig. 5.15 we can see that almost ten HII regions have similar metallicity values to the Large Magellanic Cloud (12+log(O/H)$\lesssim$8.45), and log(N/O) values which belong to the outer part of galactic discs (log(N/O)$\lesssim$-1).

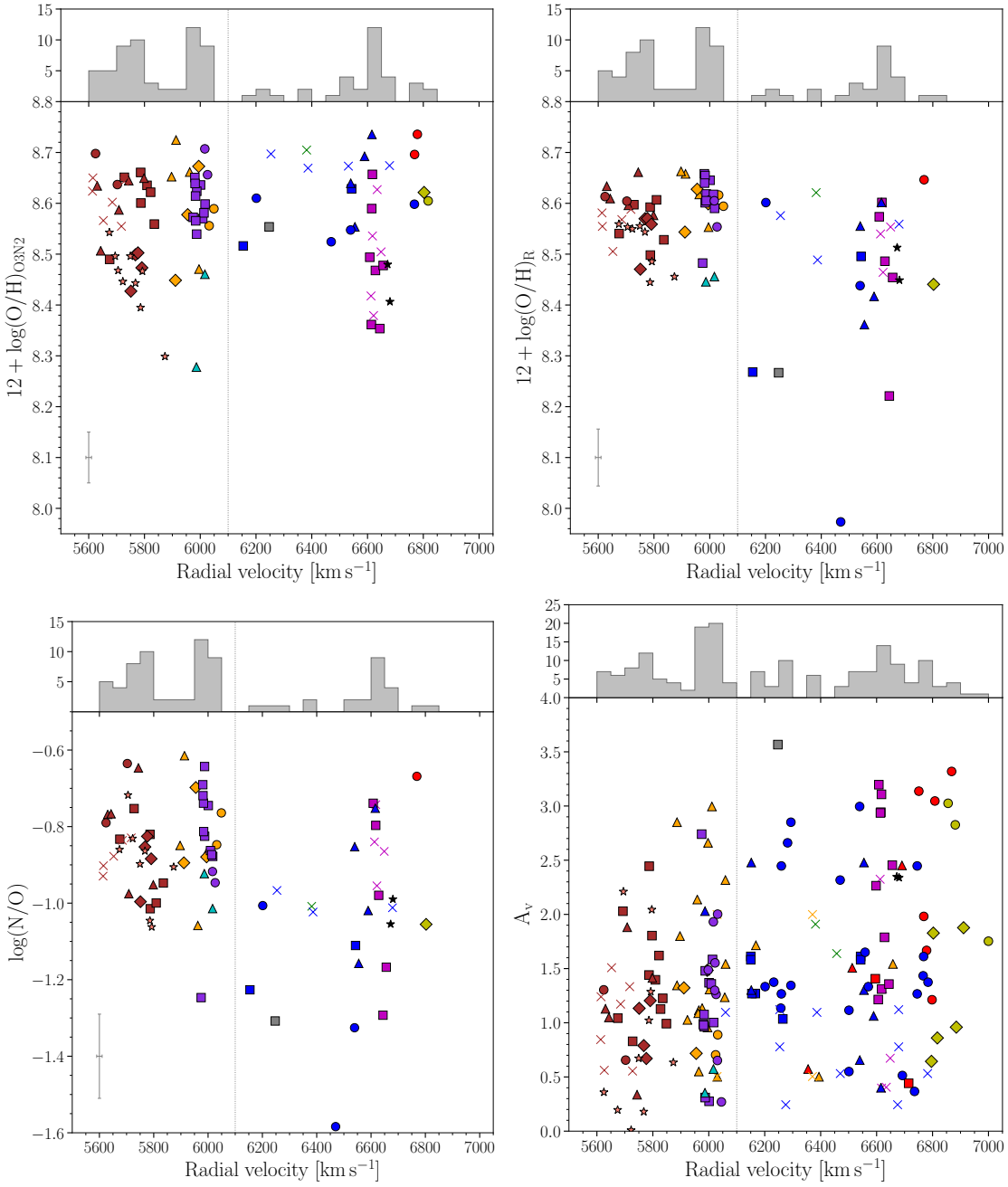

Figure 5.13: i) upper left panel: Relation between 12+log(O/H)$_{O3N2}$ and velocity for the HII regions; ii) upper right panel: Relation between 12+log(O/H)$_R$ and velocity for the HII regions; iii) lower left panel: Relation between log(N/O) and velocity for the HII regions; iv) lower right panel: Relation between A$_v$ and radial velocity for the Hα emission regions. All the points in the figures have the same colours and markers as Fig. 5.2. The vertical black dashed line corresponds to the value at velocity = 6100$km\ s^{-1}$. Above each figure its distribution of the radial velocity for the SQ HII regions is represented. The lower left crosses indicate the typical error of the two parameters.

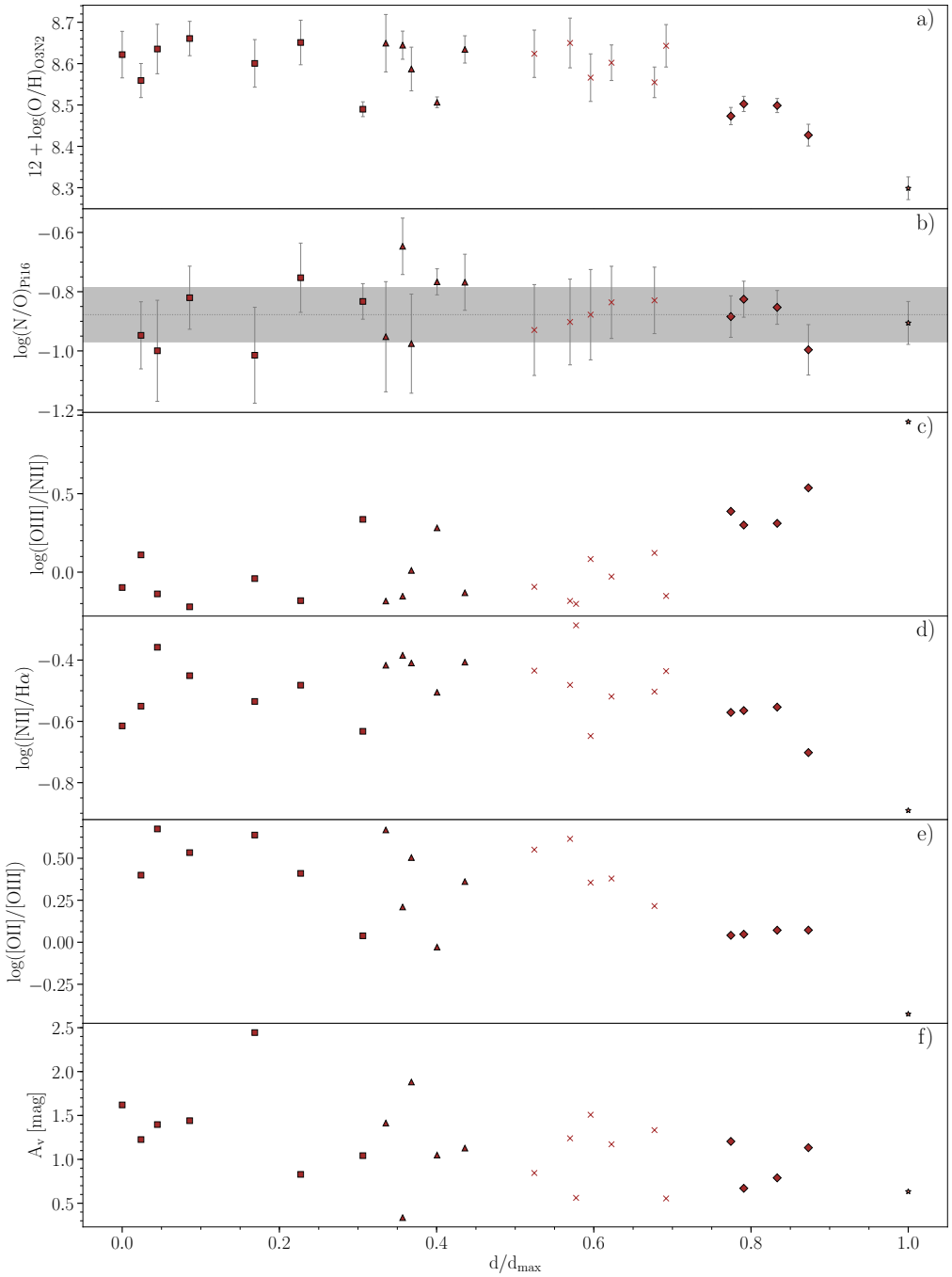

Figure 5.14: From top to bottom: Radial gradients for metallicity, N/O, log([OIII]/[NII]), log([NII]/Hα), log([OII]/[OIII]), and A_v.

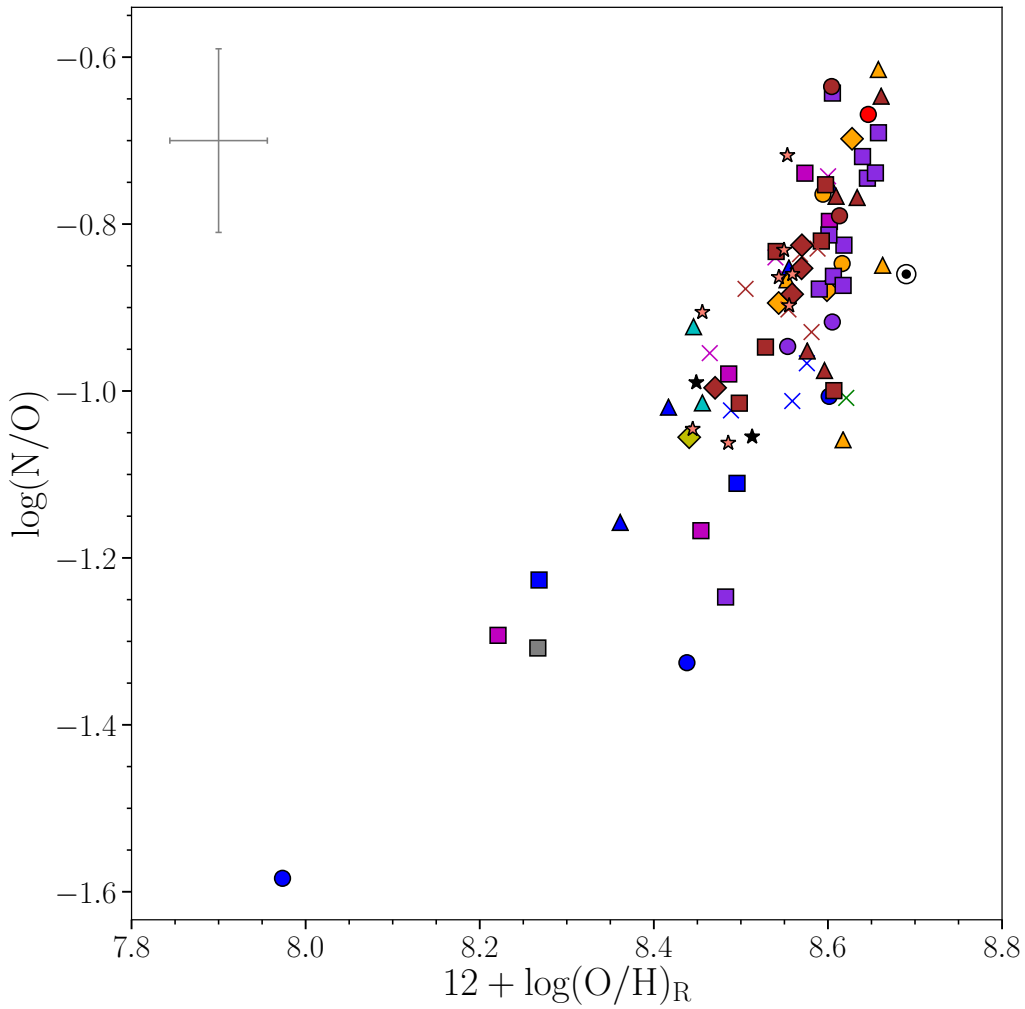

Figure 5.15: Relation between log(N/O) and 12+log(O/H)$_R$. All the points in the figures have the same colours and markers as Fig. 5.2. The upper left cross indicates the typical error of both parameters. The marker ⊙ shows the position of the solar value in this diagram.

5.4 Oxygen abundance using the R calibrator

In Fig. 5.16 we show the oxygen abundance maps for LV (upper panel) and HV (lower panel) subsamples using the R calibrator from Pilyugin & Grebel (2016). See Sect. 5.2.5 for more detail.

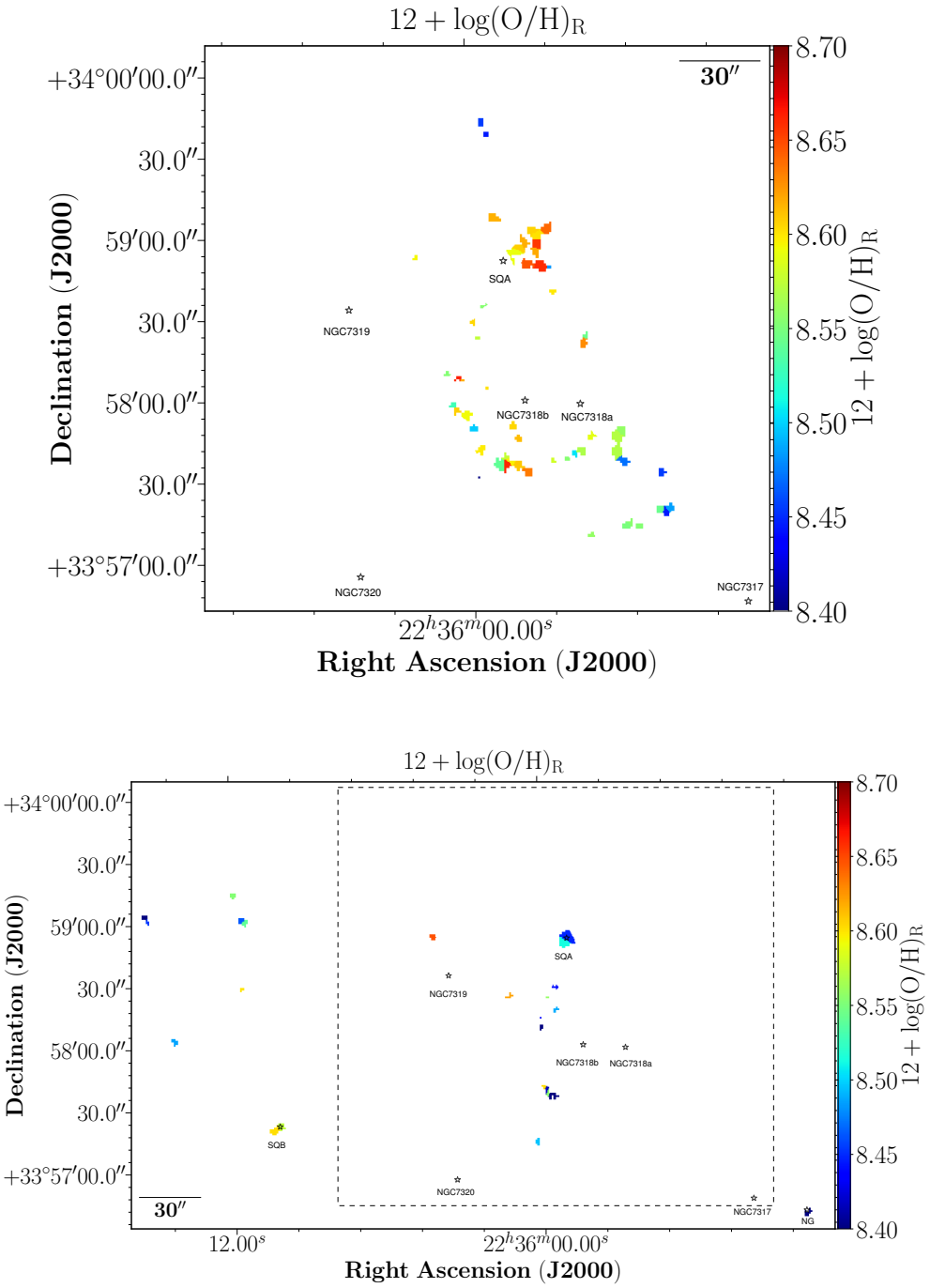

Figure 5.16: SQ spatial map colour coded according to their 12+log(O/H) derived using the R calibrator from Pilyugin & Grebel (2016) calibrator for LV sub-sample (upper left panel) and HV sub-sample (upper right panel).

5.5 Additional table

Table 5.1: Reddening corrected line fluxes relative to Hβ = 100.

(1) Region	(2) [OII]λ3727	(3) [OIII]λ5007	(4) Hα	(5) [NII]λ6583	(6) [SII]λ6716	(7) [SII]λ6731	(8) Av	(9) Vel (mag)	(10) Zone	(11) Subzone
1*	–	–	–	–	–	–	–	–	NGC7320c	NGC7320c
2	341.8±14.0	179.3±5.0	286.0±6.4	30.4±4.1	–	–	1.4	1	YTT	YTT
3	486.2±5.5	169.4±3.3	286.0±4.1	74.8±3.9	–	–	2.5	1	YTT	YTT
4	236.0±6.9	155.4±2.5	286.0±2.3	62.4±1.9	–	–	1.8	1	YTT	YTT
5	–	80.9±27.0	249.2±34.3	159.1±27.3	–	–	0.0	1	YTT	YTT
6	–	269.8±2.5	286.0±3.3	51.0±2.1	–	–	2.9	1	YTT	YTT
7	–	–	276.0±41.9	–	–	–	0.0	1	YTT	YTT
8	–	68.3±1.4	286.0±2.4	70.3±2.0	–	–	2.9	1	YTT	YTT
9	191.4±20.9	148.5±8.0	286.0±8.3	75.5±5.6	–	–	0.7	1	YTT	YTT
10	177.4±5.5	233.2±2.8	286.0±2.7	47.7±1.7	–	–	1.3	1	YTT	YTT
11	143.7±22.9	134.5±12.8	286.0±15.7	85.5±10.7	–	–	0.4	1	YTT	YTT
12	–	61.3±14.1	286.0±21.5	76.7±14.4	–	–	0.4	1	YTT	YTT
13	153.6±2.3	221.8±1.4	286.0±1.3	62.4±0.9	–	–	2.3	1	YTT	YTT
14	193.8±1.3	59.7±0.7	286.0±1.6	101.9±1.1	–	–	3.1	1	YTT	YTT
15	123.7±0.5	139.0±0.6	286.0±1.0	70.9±0.7	–	–	3.2	1	YTT	YTT
16	–	–	286.0±10.4	114.1±7.4	–	–	1.3	1	YTT	YTT
17	–	–	286.0±4.5	127.9±3.3	–	–	2.3	1	YTT	YTT
18	–	–	286.0±12.8	117.5±9.2	–	–	1.4	1	NGC7319	NGC7319 Arm
19	167.0±11.5	–	286.0±7.7	111.1±6.5	–	–	1.2	1	YTT	YTT
20	–	–	286.0±1.1	105.7±0.8	–	–	4.2	1	NGC7319	North lobe
21	–	–	286.0±2.3	114.4±1.6	–	–	3.0	1	NGC7319	North lobe
22†	–	–	286.0±16.1	162.9±12.4	–	–	1.9	1	NGC7319	NGC7319 Arm
23	–	–	286.0±3.3	104.9±2.3	–	–	3.3	1	NGC7319	North lobe

Continued.

(1) Region	(2) [OII]λ3727	(3) [OIII]λ5007	(4) Hα	(5) [NII]λ6583	(6) [SII]λ6716	(7) [SII]λ6731	(8) Av	(9) Vel (mag)	(10) Zone	(11) Subzone
24	141.6±2.4	52.4±2.6	286.0±6.4	115.2±4.4	–	–	2.0	1	NGC7319	North lobe
25	–	46.1±3.2	286.0±8.2	134.8±6.0	–	–	1.7	1	NGC7319	North lobe
26	507.4±1.7	873.6±4.7	286.0±4.2	382.6±4.7	–	–	2.5	1	NGC7319	NGC7319 Nucl.
27	278.0±3.6	753.2±11.3	286.0±10.9	288.0±10.7	–	–	1.5	1	NGC7319	NGC7319 Nucl.
28	–	–	286.0±24.5	100.3±17.0	–	–	0.4	1	NGC7319	NGC7319 Arm
29	259.4±35.1	741.3±38.9	286.0±30.1	252.2±27.7	–	–	0.6	1	NGC7319	NGC7319 Nucl.
30	–	107.1±2.0	286.0±5.3	169.1±4.2	–	–	3.1	1	NGC7319	North lobe
31†	172.9±41.2	298.2±30.1	286.0±32.3	–	–	–	0.3	0	Ls	L1
32	–	–	286.0±21.2	132.8±15.6	–	–	1.2	1	NGC7319	North lobe
33	156.5±38.8	104.6±16.2	256.4±29.6	87.6±20.4	–	–	0.0	0	Ls	L2
34	–	–	283.1±47.1	–	–	–	0.0	1	NW	NW
35	491.4±8.7	61.5±2.8	286.0±8.6	143.9±8.2	–	–	1.9	1	Bridge	Bridge
36	–	136.8±29.4	192.4±35.2	–	–	–	0.0	0	Ls	L2
37	164.2±30.4	148.9±20.6	234.2±23.2	–	–	–	0.0	0	NW	NW
38	–	162.8±12.8	286.0±26.5	–	–	–	1.0	0	NIs	NI1
39	187.5±13.0	182.6±9.2	286.0±14.0	72.8±9.3	–	–	1.0	0	Ls	L1
40	541.6±16.4	133.2±4.1	286.0±10.6	182.5±8.3	–	–	1.6	1	Bridge	Bridge
41	–	192.3±21.4	286.0±24.1	–	–	–	0.7	0	Ls	L2
42	259.4±11.9	103.4±5.5	286.0±8.0	80.3±7.0	39.9±5.8	–	1.2	0	NIs	NI1
43	–	133.4±10.7	286.0±16.2	129.3±11.8	–	–	1.3	0	Ls	L1
44	–	–	286.0±23.1	115.4±10.5	–	–	1.2	0	Ls	L1
45	428.9±14.4	90.8±7.2	286.0±12.1	124.9±9.8	101.4±9.4	–	1.4	0	NIs	NI1
46	–	55.2±3.9	286.0±8.3	69.2±5.3	59.3±5.7	–	1.6	0	NIs	NI1
47	121.7±35.6	53.3±16.7	249.2±36.6	118.4±27.3	–	–	0.0	0	Ls	L1

Continued.

(1) Region	(2) [OII]λ3727	(3) [OIII]λ5007	(4) Hα	(5) [NII]λ6583	(6) [SII]λ6716	(7) [SII]λ6731	(8) Av	(9) Vel (mag)	(10) Zone	(11) Subzone
48	282.9±10.2	85.8±4.8	286.0±13.9	135.6±11.4	–	–	1.8	0	Ls	L1
49	361.7±7.0	–	286.0±10.8	–	117.3±9.5	–	1.8	0	NIs	NI1
50	567.7±35.1	85.3±9.1	286.0±19.8	141.0±14.9	–	–	1.1	0	Ls	L1
51	323.2±14.9	–	286.0±19.2	–	–	–	1.6	0	Shs	Sh1
51	507.3±14.6	75.0±4.5	286.0±15.2	98.7±10.6	–	–	1.6	1	Shs	Sh1
52	207.2±7.1	60.7±3.8	286.0±5.0	100.9±4.2	68.0±3.8	–	1.4	0	NIs	NI1
53	441.0±123.8	112.0±30.5	220.0±41.2	170.0±36.5	117.9±35.4	–	0.0	0	Ls	L1
54	327.7±23.3	95.4±9.5	286.0±21.1	191.6±17.6	–	–	1.0	0	Ls	L1
55[†]	275.4±45.4	–	286.0±37.9	199.4±32.3	–	–	0.6	0	Ls	L1
56	–	–	181.0±37.8	–	–	–	0.0	1	Shs	Sh3
57	–	–	281.5±76.3	508.7±96.0	–	–	0.0	0	Ls	L1
58	488.9±24.3	140.8±7.4	286.0±22.8	336.9±23.9	177.3±15.9	–	1.1	0	Ls	L1
58	–	124.9±7.9	286.0±23.1	87.8±8.6	–	–	1.9	1	Shs	Sh3
59	155.5±28.0	69.6±12.6	253.1±36.7	184.1±34.1	117.9±21.2	–	0.0	0	Ls	L1
59	1009.2±7.3	62.6±2.6	286.0±13.6	38.9±2.6	–	–	2.3	1	Shs	Sh3
60	211.9±70.2	49.5±15.4	270.8±39.8	277.0±62.3	–	–	0.0	0	Ls	L1
60	997.2±6.2	131.0±1.7	286.0±7.3	98.8±2.9	–	–	3.0	1	Shs	Sh3
61	183.9±32.8	–	286.0±40.6	233.8±36.4	128.9±33.4	–	0.3	0	SSQA	SSQA
62	157.8±32.5	–	214.8±15.8	55.6±15.3	–	–	0.0	1	Shs	Sh1
63	256.8±24.2	–	286.0±31.6	130.2±20.1	–	–	1.0	1	Shs	Sh1
64	171.3±20.7	37.2±8.6	286.0±22.6	104.3±26.1	–	–	0.4	1	Shs	Sh2
65	327.9±5.1	75.5±2.5	286.0±3.8	82.9±2.6	45.5±2.6	–	2.4	0	NIs	NI1
66	728.8±7.5	122.3±1.8	286.0±5.9	258.8±7.0	80.7±3.0	–	2.9	0	Ls	L1
66	675.8±42.9	–	286.0±19.1	–	–	–	1.3	1	Shs	Sh3

Continued.

(1) Region	(2) [OII]λ3727	(3) [OIII]λ5007	(4) Hα	(5) [NII]λ6583	(6) [SII]λ6716	(7) [SII]λ6731	(8) Av	(9) Vel (mag)	(10) Zone	(11) Subzone
67	–	65.7±2.9	286.0±10.1	207.8±8.5	117.5±7.7	–	2.1	0	Ls	L1
68	305.2±15.6	64.3±6.6	286.0±14.6	246.1±19.7	83.8±8.8	–	1.1	0	Ls	L1
68	416.7±37.8	–	286.0±49.3	–	–	–	0.6	1	Shs	Sh3
69	–	91.9±15.3	286.0±32.0	168.7±34.4	151.2±31.4	–	0.5	0	Ls	L1
69†	318.9±104.8	–	273.6±60.3	126.9±40.8	–	–	0.0	1	Ls	L1
70	330.5±7.8	52.4±3.1	286.0±5.6	125.0±4.1	79.2±4.2	–	1.9	0	SSQA	SSQA
71	145.2±46.2	45.2±13.8	264.0±29.8	193.6±25.5	83.4±23.0	–	0.0	0	SSQA	SSQA
72	166.5±42.6	78.4±25.1	259.0±35.4	–	–	–	0.0	1	Shs	Sh1
73	–	44.5±14.0	280.0±29.5	–	–	–	0.0	1	Shs	Sh1
74	280.5±14.0	32.1±4.2	286.0±12.6	66.6±9.9	–	–	1.1	1	Shs	Sh2
75	159.2±14.2	62.0±7.7	286.0±10.9	94.1±13.6	91.8±13.9	–	0.8	0	NIs	NI1
76	369.7±21.7	54.7±4.9	286.0±18.7	117.8±12.4	81.3±9.5	–	1.1	0	Shs	Sh4
76	416.1±44.1	63.4±9.7	286.0±32.4	114.0±19.6	–	–	0.8	1	Shs	Sh4
77	204.6±22.1	62.6±8.3	286.0±19.5	86.7±18.0	–	–	0.7	1	Shs	Sh2
78	370.1±18.7	75.5±6.1	286.0±17.8	42.6±5.8	80.3±6.5	–	1.3	0	Shs	Sh1
79	496.8±26.3	–	286.0±29.1	135.1±16.7	–	–	1.3	0	Shs	Sh3
79	703.9±8.3	103.1±2.4	286.0±6.9	–	–	–	2.4	1	Shs	Sh3
80	–	–	286.0±44.4	152.2±32.7	–	–	0.2	0	Shs	Sh4
80	–	–	147.4±35.8	–	–	–	0.0	1	Shs	Sh4
81	–	169.9±7.1	286.0±16.9	122.6±14.1	–	–	1.5	0	Ls	L1
81	–	61.5±20.9	249.2±51.4	–	–	–	0.0	1	Ls	L1
82	244.7±24.5	156.2±9.4	286.0±11.0	57.0±7.2	42.0±7.7	–	0.6	0	NW	NW
83	570.6±7.7	–	286.0±11.9	98.2±6.0	–	–	2.5	0	Shs	Sh2
83	385.5±12.2	77.8±4.4	286.0±17.0	58.1±6.5	–	–	1.3	1	Shs	Sh2

Continued.

(1) Region	(2) [OII]λ3727	(3) [OIII]λ5007	(4) Hα	(5) [NII]λ6583	(6) [SII]λ6716	(7) [SII]λ6731	(8) Av	(9) Vel (mag)	(10) Zone	(11) Subzone
84	452.9±18.8	–	286.0±15.2	–	–	–	1.4	1	Shs	Sh3
85	–	–	286.0±40.2	82.6±19.9	–	–	0.4	1	Shs	Sh3
86	590.7±7.7	121.9±2.8	286.0±9.8	302.6±8.3	105.4±4.4	–	2.7	0	Ls	L1
86†	337.3±96.9	–	260.2±73.8	157.2±52.5	–	–	0.0	1	Shs	Sh3
87	376.4±17.3	–	286.0±25.9	–	–	–	1.4	0	Shs	Sh3
87†	–	67.7±2.1	286.0±7.6	–	–	–	3.1	1	Shs	Sh3
88	–	–	286.0±15.4	191.2±11.1	–	–	1.7	1	Ls	L1
89	265.2±42.3	–	286.0±30.6	–	–	–	0.5	0	Shs	Sh4
89†	–	–	256.9±49.2	128.2±38.4	–	–	0.0	1	Shs	Sh4
90	333.8±12.8	104.6±4.8	286.0±7.6	138.9±5.7	56.1±5.5	–	1.6	0	SSQA	SSQA
91	307.3±15.5	62.8±6.4	286.0±14.8	100.5±10.2	–	–	1.3	0	SSQA	SSQA
92	838.2±40.9	377.7±8.8	286.0±8.5	93.0±8.2	–	–	1.5	0	SSQA	SSQA
93	–	–	128.1±22.7	–	80.8±19.6	–	0.0	0	Shs	Sh1
94	–	–	286.0±9.8	112.7±7.6	–	–	2.0	0	NIs	NI1
94	–	–	231.7±40.9	115.7±35.7	–	–	0.0	1	Shs	Sh2
95†	–	–	148.1±37.3	132.6±40.3	–	–	0.0	0	Shs	Sh2
95	203.1±60.3	–	271.6±45.3	–	–	–	0.0	1	Shs	Sh2
96	335.4±9.4	57.7±3.0	286.0±9.4	72.6±5.5	–	–	1.8	1	Hs	H2
97	126.2±16.6	373.2±15.8	286.0±14.3	34.8±9.3	–	–	0.4	0	NW	NW
98	456.7±10.3	73.1±2.8	286.0±7.0	211.2±6.0	83.1±5.3	–	2.0	0	SSQA	SSQA
99	454.8±31.8	95.3±7.1	286.0±23.7	–	–	–	1.3	1	Shs	Sh1
100	–	–	232.8±49.2	121.6±40.9	–	–	0.0	0	Shs	Sh2
100	–	–	258.0±49.0	–	–	–	0.0	1	Shs	Sh2
101	272.7±34.6	–	286.0±42.5	183.2±43.6	–	–	0.5	1	Shs	Sh3

Continued.

(1) Region	(2) [OII]λ3727	(3) [OIII]λ5007	(4) Hα	(5) [NII]λ6583	(6) [SII]λ6716	(7) [SII]λ6731	(8) Av	(9) Vel (mag)	(10) Zone	(11) Subzone
102	424.2±26.3	105.2±7.3	286.0±22.3	119.7±14.1	59.8±8.8	–	1.3	0	Shs	Sh3
102	–	–	218.3±64.4	–	–	–	0.0	1	Shs	Sh3
103†	–	112.7±5.2	286.0±13.7	263.3±14.3	–	–	1.9	0	Ls	L1
103	253.1±82.9	–	171.7±42.1	–	–	–	0.0	1	Shs	Sh3
104†	–	–	190.0±48.5	171.6±50.4	–	–	0.0	0	Shs	Sh4
104	356.4±21.7	50.9±6.1	286.0±19.7	89.2±9.9	–	–	1.1	1	Shs	Sh4
105	450.5±11.9	–	286.0±9.6	–	–	–	1.9	1	Hs	H2
106	339.7±18.0	–	286.0±12.9	145.9±9.7	–	–	1.3	0	SSQA	SSQA
107	311.8±13.8	–	286.0±16.2	89.2±17.6	–	–	1.3	1	Shs	Sh3
108	335.3±11.3	–	286.0±17.7	–	–	–	1.7	1	Shs	Sh3
109	–	73.8±21.4	174.3±27.4	78.3±26.5	–	–	0.0	1	Shs	Sh4
110	311.1±23.5	–	286.0±14.5	89.6±9.4	–	–	0.9	1	Hs	H2
111	244.1±7.5	254.7±7.7	286.0±8.6	–	–	–	1.8	1	Hs	H1
112	228.6±13.5	137.0±7.2	286.0±8.9	102.7±6.3	61.0±6.5	–	0.9	0	Ls	L2
113	–	98.1±6.0	286.0±15.1	103.1±10.5	–	–	1.6	1	Shs	Sh3
114	190.1±44.4	–	258.1±47.3	73.3±23.5	–	–	0.0	1	Shs	Sh3
115	–	–	286.0±29.5	60.5±12.0	–	–	0.6	1	Hs	H2
116	274.9±15.3	–	286.0±14.1	–	–	–	1.0	1	Hs	H2
117	157.6±4.6	144.2±4.3	286.0±3.3	66.5±1.5	26.4±1.3	26.4±1.3	1.0	0	NIs	NI1
118	425.8±29.1	–	286.0±15.0	40.3±6.5	–	–	1.1	0	NIs	NI1
119	–	–	215.7±47.4	89.0±23.2	–	–	0.0	1	Shs	Sh3
120	190.6±18.7	158.0±9.5	286.0±10.1	133.2±7.5	84.1±7.6	–	0.7	0	SSQA	SSQA
121	357.7±4.5	176.9±2.3	286.0±2.9	79.0±1.9	–	–	2.3	1	SQA	SQA
122	200.7±1.7	188.1±1.2	286.0±1.1	48.7±0.7	–	–	2.3	1	SQA	SQA

Continued.

(1) Region	(2) [OII]λ3727	(3) [OIII]λ5007	(4) Hα	(5) [NII]λ6583	(6) [SII]λ6716	(7) [SII]λ6731	(8) Av	(9) Vel (mag)	(10) Zone	(11) Subzone
123	–	121.3±24.3	242.8±35.1	107.8±32.5	–	–	0.0	1	Hs	H1
124†	305.9±17.0	251.9±13.4	286.0±15.9	–	–	–	1.1	0	NW	NW
125	332.9±14.5	71.4±6.8	286.0±14.8	109.1±10.3	83.5±10.7	–	1.4	0	NIs	NI2
126	381.3±3.9	203.6±2.1	286.0±3.8	–	–	–	2.8	1	Hs	H1
127	134.3±18.1	82.8±10.4	286.0±12.3	117.9±8.9	91.6±9.1	–	0.3	0	NIs	NI2
128	362.7±8.1	113.7±5.3	286.0±4.7	110.9±3.3	70.1±3.4	–	1.9	0	NIs	NI2
129	246.0±13.1	96.5±5.0	286.0±5.2	99.6±3.6	48.9±3.7	–	1.0	0	NSQA	NSQA
130	100.5±10.5	61.1±8.7	286.0±8.8	82.9±6.0	30.2±6.2	–	0.7	0	NIs	NI3
131	679.4±4.2	236.3±2.7	286.0±4.6	–	–	–	3.0	1	Hs	H1
132	237.7±7.6	120.1±3.5	286.0±4.2	101.5±3.0	62.3±3.1	–	1.4	0	NSQA	NSQA
133	159.7±4.0	170.7±3.3	286.0±2.4	89.1±1.6	39.4±1.7	18.8±1.8	1.0	0	NIs	NI2
134	202.5±12.6	51.0±5.5	286.0±10.2	111.2±7.3	67.4±7.4	–	1.3	0	NIs	NI3
135	135.9±28.5	–	286.0±21.2	125.9±15.6	86.1±15.8	–	0.3	0	NSQA	NSQA
136	258.3±9.6	117.0±4.2	286.0±5.2	108.3±3.7	60.2±3.8	–	1.6	0	NSQA	NSQA
137	180.8±8.2	83.8±3.6	286.0±5.5	115.7±3.9	44.7±3.9	–	1.4	0	NSQA	NSQA
138	189.6±8.4	82.6±5.2	286.0±5.1	111.8±3.6	61.2±3.7	35.2±3.8	1.1	0	NIs	NI2
139	100.5±13.1	123.2±7.0	286.0±7.5	80.2±5.1	52.6±5.4	–	0.3	0	NSQA	NSQA
140	222.9±10.0	86.2±3.7	286.0±7.6	109.0±5.4	43.0±5.4	–	1.5	0	NSQA	NSQA
141	192.7±8.7	116.9±5.3	286.0±4.7	94.4±3.2	52.7±3.3	–	1.0	0	NSQA	NSQA
142	179.4±9.0	101.1±5.6	286.0±6.0	117.7±4.4	73.6±4.4	–	1.1	0	NSQA	NSQA
143	155.9±12.1	78.6±5.2	286.0±7.4	119.6±5.4	75.4±5.5	–	1.0	0	NSQA	NSQA
144†	–	146.3±25.3	286.0±49.4	102.9±28.8	–	–	0.4	0	SDR	SDR
145	–	176.5±34.0	254.5±42.1	–	–	–	0.0	0	NSQA	NSQA
146	161.5±10.2	79.6±4.4	286.0±4.8	111.0±3.4	58.3±3.5	–	1.0	0	NSQA	NSQA

Continued.

(1) Region	(2) [OII]λ3727	(3) [OIII]λ5007	(4) Hα	(5) [NII]λ6583	(6) [SII]λ6716	(7) [SII]λ6731	(8) Av	(9) Vel (mag)	(10) Zone	(11) Subzone
147	814.9±8.4	116.1±2.4	286.0±6.1	104.5±4.3	–	–	2.7	0	NSQA	NSQA
148	270.5±14.7	61.8±5.1	286.0±9.9	112.5±6.5	64.9±7.0	–	1.5	0	Ls	L4
149	300.8±33.3	84.6±10.2	286.0±19.0	104.9±13.7	83.8±14.4	–	0.8	0	NIs	NI4
150	254.5±11.3	61.7±6.6	286.0±11.9	94.2±8.3	68.8±8.6	–	1.2	0	NIs	NI4
151	–	92.7±17.2	286.0±17.7	147.6±15.4	88.6±16.3	–	0.6	0	NIs	NI4
152	175.9±5.9	77.7±5.4	286.0±8.2	64.1±5.5	76.9±6.1	–	1.5	0	NIs	NI4
153	193.7±7.0	80.9±6.2	286.0±6.9	86.3±4.7	49.1±4.9	–	1.2	0	NIs	NI4
154	138.0±13.5	111.8±7.6	286.0±7.8	98.0±5.4	40.6±5.5	–	0.7	0	Ls	L4
155	199.1±7.4	205.5±7.3	286.0±6.6	70.4±4.4	–	–	1.3	0	Ls	L4
156	197.6±34.6	120.8±12.8	286.0±21.6	80.2±14.7	–	–	0.2	0	SDR	SDR
157	194.9±8.7	118.6±5.6	286.0±7.2	89.5±5.0	48.1±5.1	–	1.3	0	NIs	NI4
158	–	81.5±20.1	212.1±28.3	–	99.4±32.0	–	0.0	0	SDR	SDR
159	–	73.8±11.9	286.0±14.7	104.7±10.4	67.4±10.7	–	0.6	0	NIs	NI4
160	–	172.1±3.9	286.0±7.3	86.3±5.1	–	–	2.2	0	SDR	SDR
161	–	–	286.0±8.6	48.4±3.5	–	–	2.0	0	Ls	L3
161	353.9±51.4	–	286.0±41.6	71.7±17.7	–	–	0.5	1	Ls	L3
162	–	–	221.4±34.0	80.1±39.2	–	–	0.0	0	Ls	L3
163	–	152.3±22.2	286.0±28.3	–	–	–	0.4	0	SDR	SDR
164	192.5±7.6	163.2±5.4	286.0±3.5	79.8±2.4	55.6±2.5	–	0.8	0	NIs	NI5
165	173.3±7.7	155.2±6.2	286.0±4.1	77.8±2.8	43.6±2.9	–	0.7	0	NIs	NI5
166	205.5±6.8	186.9±4.6	286.0±3.8	76.6±2.5	46.7±2.7	–	1.2	0	NIs	NI5
167	230.3±9.3	195.0±5.8	286.0±4.7	56.6±3.1	45.5±3.3	–	1.1	0	NIs	NI5
168	157.4±30.3	207.4±16.5	286.0±10.8	66.9±7.3	39.0±7.8	39.0±11.1	0.0	0	SDR	SDR
169	218.5±14.0	164.7±8.0	286.0±9.5	78.6±6.5	74.7±7.0	–	0.7	0	SDR	SDR

Continued.

(1) Region	(2) [OII]λ3727	(3) [OIII]λ5007	(4) Hα	(5) [NII]λ6583	(6) [SII]λ6716	(7) [SII]λ6731	(8) Av	(9) Vel (mag)	(10) Zone	(11) Subzone
170	100.6±23.8	164.3±13.2	269.2±14.3	58.6±9.5	38.5±10.2	–	0.0	0	SDR	SDR
171	175.2±25.5	212.5±11.9	286.0±11.3	67.4±7.6	54.7±8.1	–	0.2	0	SDR	SDR
172	124.8±8.8	333.6±6.8	286.0±6.7	36.7±4.3	21.7±4.7	–	0.6	0	SDR	SDR
173	252.7±11.6	231.0±7.4	286.0±5.1	52.6±3.3	40.8±3.6	–	1.0	0	SDR	SDR
174	336.0±10.6	180.9±5.9	286.0±3.8	70.8±3.2	45.4±3.5	–	1.3	0	SDR	SDR
175	443.3±8.1	286.7±6.2	286.0±6.8	–	–	–	2.0	0	SDR	SDR
176	600.4±2.4	70.7±1.0	286.0±2.9	56.8±1.9	–	–	3.6	1	NG	NG

The columns correspond to: (1) Identifier of the SQ Hα emission regions; (2) Integrated [OII]λ3727 flux and its uncertainty; (3) Integrated [OIII]λ5007 flux and its uncertainty; (4) Integrated Hα flux and its uncertainty; (5) Integrated [NII]λ6583 flux and its uncertainty; (6) Integrated [SII]λ6716 flux and its uncertainty; (7) Integrated [SII]λ6731 flux and its uncertainty; (8) A_v extinction (mag); (9) Velocity of the region belongs to the LV (0) or HV (1) sub-sample; (10) Global localisation zone; (11) Local zone. "*" refers to the galaxy NGC7320c. † denotes the information about those regions where Hβ is not detected and we computed the theoretical flux expected for Hβ when S/N(Hβ)=3.

Table 5.2: Star formation rate, Hα luminosity, BPT classification, and radial velocity sub-sample.

(1) Region	(2) SFR (x10^{-3} $M_\odot\, yr^{-1}$)	(3) $L_{H\alpha}$ (x$10^{38} erg\ s^{-1}$)	(4) BPT	(5) Vel
2	12.81±0.29	16.21±0.36	SF	1
3	11.08±0.16	14.02±0.20	SF	1
4	27.53±0.22	34.84±0.28	SF	1
5	–	0.63±0.09	C	1
6	17.70±0.20	22.40±0.26	SF	1
8	31.37±0.27	39.71±0.34	SF	1
9	10.26±0.30	12.99±0.38	SF	1
10	39.85±0.37	50.44±0.47	SF	1
11	3.33±0.18	4.21±0.23	SF	1
12	1.66±0.12	2.10±0.16	SF	1
13	76.48±0.36	96.82±0.45	SF	1
14	94.95±0.54	120.19±0.69	SF	1
15	196.79±0.67	249.10±0.85	SF	1
24	29.67±0.66	37.55±0.83	SF	1
25	17.79±0.51	22.52±0.65	SF	1
26	–	2690.21±39.47	AGN	1
27	–	552.11±21.03	AGN	1
29	–	3.45±0.36	AGN	1
30	–	23.05±0.42	C	1
33	2.31±0.27	2.93±0.34	SF	0
35	23.79±0.71	30.12±0.90	SF	1
39	6.37±0.31	8.06±0.39	SF	0
40	–	11.44±0.42	C	1
42	13.18±0.37	16.68±0.47	SF	0
43	–	3.63±0.21	C	0
45	12.63±0.53	15.99±0.67	SF	0
46	12.23±0.35	15.48±0.45	SF	0
47	0.67±0.10	0.85±0.12	SF	0
48	6.19±0.30	7.83±0.38	SF	0
50	3.00±0.21	3.79±0.26	SF	0

Continued.

(1) Region	(2) SFR ($x10^{-3}\ M_{\odot}\ yr^{-1}$)	(3) $L_{H\alpha}$ ($x10^{38} erg\ s^{-1}$)	(4) BPT	(5) Vel
51	15.59±0.83	19.73±1.05	SF	1
52	41.39±0.73	52.39±0.92	SF	0
53	–	0.82±0.15	C	0
54	–	2.28±0.17	C	0
58	–	7.57±0.60	AGN	0
59	–	10.63±1.54	C	0
59	36.96±1.76	46.78±2.22	SF	1
60	–	1.26±0.19	C	0
60	11.77±0.30	14.90±0.38	SF	1
64	6.14±0.48	7.77±0.61	SF	1
65	36.82±0.49	46.60±0.62	SF	0
66	–	17.69±0.36	AGN	0
67	–	8.74±0.31	C	0
68	–	16.09±0.82	C	0
69	–	1.52±0.17	C	0
70	14.75±0.29	18.68±0.36	SF	0
71	–	2.83±0.32	C	0
74	14.51±0.64	18.37±0.81	SF	1
75	17.09±0.65	21.63±0.82	SF	0
76	7.37±0.48	9.33±0.61	SF	0
76	3.56±0.40	4.51±0.51	SF	1
77	8.81±0.60	11.15±0.76	SF	1
78	2.20±0.14	2.78±0.17	SF	0
81	–	2.45±0.15	C	0
82	7.07±0.27	8.95±0.34	SF	0
83	22.20±1.32	28.10±1.67	SF	1
86	–	15.92±0.55	AGN	0
90	–	19.96±0.53	C	0
91	4.29±0.22	5.43±0.28	SF	0
92	–	6.18±0.18	AGN	0

Continued.

(1) Region	(2) SFR (x10^{-3} $M_\odot\, yr^{-1}$)	(3) $L_{H\alpha}$ (x$10^{38} erg\, s^{-1}$)	(4) BPT	(5) Vel
96	19.53±0.64	24.72±0.82	SF	1
97	3.88±0.19	4.92±0.25	SF	0
98	–	15.75±0.38	C	0
102	3.40±0.27	4.30±0.34	SF	0
104	11.35±0.78	14.36±0.99	SF	1
109	0.45±0.07	0.57±0.09	SF	1
112	23.20±0.72	29.37±0.92	SF	0
113	3.69±0.20	4.68±0.25	SF	1
117	119.16±1.36	150.84±1.72	SF	0
120	–	20.64±0.73	C	0
121	139.98±1.41	177.19±1.79	SF	1
122	733.22±2.90	928.12±3.67	SF	1
123	0.57±0.08	0.72±0.10	SF	1
125	7.57±0.39	9.58±0.50	SF	0
127	14.95±0.64	18.93±0.82	SF	0
128	18.60±0.30	23.54±0.39	SF	0
129	59.93±1.10	75.86±1.39	SF	0
130	26.72±0.82	33.82±1.04	SF	0
132	38.31±0.56	48.49±0.71	SF	0
133	94.48±0.79	119.59±1.00	SF	0
134	13.96±0.50	17.66±0.63	SF	0
136	33.43±0.61	42.32±0.77	SF	0
137	43.84±0.84	55.50±1.06	SF	0
138	32.01±0.57	40.52±0.72	SF	0
139	19.86±0.52	25.14±0.66	SF	0
140	21.83±0.58	27.63±0.73	SF	0
141	42.05±0.69	53.22±0.87	SF	0
142	31.38±0.66	39.73±0.84	SF	0
143	29.21±0.75	36.98±0.95	SF	0

Continued.

(1) Region	(2) SFR (x10^{-3} $M_\odot\, yr^{-1}$)	(3) $L_{H\alpha}$ (x$10^{38} erg\, s^{-1}$)	(4) BPT	(5) Vel
146	44.23±0.74	55.99±0.93	SF	0
147	8.64±0.18	10.94±0.23	SF	0
148	8.24±0.28	10.43±0.36	SF	0
149	2.93±0.19	3.70±0.25	SF	0
150	5.24±0.22	6.63±0.28	SF	0
151	–	2.43±0.15	C	0
152	10.59±0.30	13.41±0.39	SF	0
153	25.37±0.61	32.12±0.77	SF	0
154	19.76±0.54	25.01±0.68	SF	0
155	15.12±0.35	19.14±0.44	SF	0
156	2.69±0.20	3.40±0.26	SF	0
157	19.74±0.50	24.98±0.63	SF	0
159	14.09±0.73	17.84±0.92	SF	0
160	6.16±0.16	7.80±0.20	SF	0
164	85.55±1.04	108.29±1.31	SF	0
165	93.67±1.35	118.57±1.71	SF	0
166	53.28±0.70	67.44±0.89	SF	0
167	34.23±0.56	43.33±0.71	SF	0
168	8.00±0.30	10.12±0.38	SF	0
169	7.31±0.24	9.26±0.31	SF	0
170	5.95±0.32	7.54±0.40	SF	0
171	10.65±0.42	13.48±0.53	SF	0
172	23.95±0.56	30.32±0.71	SF	0
173	21.09±0.38	26.69±0.47	SF	0
174	24.79±0.33	31.38±0.42	SF	0
176	90.27±0.92	114.26±1.16	SF	1

The columns correspond to: (1) Identifier of the HII region; (2) Star formation rate (x10^{-3} $M_\odot\, yr^{-1}$); (3) Hα luminosity (x$10^{38} erg\, s^{-1}$); (4) BPT classification; (5) Velocity of the region belongs to the LV (0) or the HV (1) sub-samples.

Table 5.3: Oxygen abundances for the SQ HII regions using N2 and O3N2 (Pérez-Montero & Contini 2009), and R calibrators (Pilyugin & Grebel 2016), respectively, nitrogen abundances using Pilyugin & Grebel (2016), and radial velocity sub-sample.

(1) #	(2) 12+log(O/H)$_{N2}$	(3) 12+log(O/H)$_{O3N2}$	(4) 12+log(O/H)$_{R}$	(5) log(N/O)$_{Pi16}$	(6) Vel
2	8.30±0.11	8.35±0.05	8.22±0.11	-1.29±0.13	1
3	8.61±0.09	8.48±0.06	8.45±0.10	-1.17±0.20	1
4	8.55±0.03	8.47±0.02	8.49±0.03	-0.98±0.07	1
6	8.48±0.10	8.36±0.06	–	–	1
8	8.59±0.07	8.59±0.05	–	–	1
9	8.61±0.04	8.50±0.03	8.55±0.03	-0.86±0.08	1
10	8.46±0.03	8.38±0.02	8.46±0.02	-0.95±0.05	1
11	8.66±0.06	8.54±0.04	8.60±0.04	-0.74±0.11	1
12	8.62±0.09	8.63±0.06	–	–	1
13	8.55±0.02	8.42±0.02	8.54±0.02	-0.84±0.06	1
14	8.72±0.03	8.66±0.03	8.60±0.02	-0.80±0.07	1
15	8.59±0.03	8.49±0.02	8.57±0.01	-0.74±0.06	1
24	8.76±0.05	8.70±0.05	8.65±0.03	-0.67±0.13	1
25	8.81±0.05	8.74±0.05	–	–	1
33	8.70±0.09	8.59±0.05	8.59±0.06	-0.76±0.06	0
35	8.84±0.08	8.70±0.05	8.62±0.08	-1.01±0.13	1
39	8.60±0.09	8.47±0.04	8.55±0.06	-0.87±0.13	0
42	8.64±0.07	8.56±0.04	8.53±0.06	-0.95±0.11	0
45	8.79±0.08	8.64±0.06	8.61±0.08	-1.00±0.17	0
46	8.58±0.08	8.62±0.06	–	–	0
47	8.81±0.09	8.72±0.06	8.66±0.06	-0.61±0.05	0
48	8.82±0.11	8.65±0.07	8.66±0.09	-0.85±0.17	0
50	8.83±0.09	8.66±0.06	8.62±0.10	-1.06±0.17	0
51	8.71±0.12	8.63±0.07	8.50±0.13	-1.11±0.17	1
52	8.71±0.04	8.66±0.04	8.59±0.03	-0.82±0.11	0
59	8.39±0.13	8.52±0.07	7.97±0.20	-1.58±0.19	1
60	8.71±0.09	8.55±0.06	8.44±0.13	-1.33±0.18	1
64	8.72±0.12	8.74±0.07	8.60±0.08	-0.75±0.12	1
65	8.65±0.06	8.60±0.06	8.50±0.06	-1.01±0.16	0
70	8.79±0.05	8.71±0.05	8.61±0.05	-0.92±0.11	0

Continued.

(1) #	(2) 12+log(O/H)$_{N2}$	(3) 12+log(O/H)$_{O3N2}$	(4) 12+log(O/H)$_{R}$	(5) log(N/O)$_{Pi16}$	(6) Vel
74	8.57±0.11	8.69±0.06	8.42±0.10	-1.02±0.13	1
75	8.69±0.09	8.65±0.05	8.60±0.06	-0.75±0.12	0
76	8.77±0.09	8.70±0.05	8.58±0.09	-0.97±0.12	0
76	8.76±0.12	8.67±0.07	8.56±0.12	-1.01±0.16	1
77	8.66±0.11	8.64±0.06	8.56±0.09	-0.85±0.14	1
78	8.42±0.12	8.52±0.06	8.27±0.14	-1.23±0.18	0
82	8.52±0.07	8.46±0.03	8.46±0.06	-1.01±0.10	0
83	8.52±0.10	8.55±0.05	8.36±0.11	-1.16±0.14	1
91	8.71±0.09	8.66±0.06	8.55±0.08	-0.95±0.14	0
96	8.60±0.09	8.62±0.06	8.44±0.09	-1.06±0.13	1
97	8.35±0.12	8.28±0.05	8.45±0.07	-0.92±0.13	0
102	8.77±0.11	8.61±0.06	8.60±0.12	-1.01±0.18	0
104	8.67±0.09	8.67±0.06	8.49±0.09	-1.02±0.13	1
109	8.80±0.13	8.67±0.07	–	–	1
112	8.72±0.04	8.56±0.03	8.62±0.03	-0.85±0.09	0
113	8.72±0.11	8.60±0.07	–	–	1
117	8.57±0.02	8.49±0.02	8.54±0.02	-0.83±0.06	0
121	8.63±0.04	8.48±0.03	8.51±0.04	-1.05±0.10	1
122	8.46±0.02	8.41±0.02	8.45±0.02	-0.99±0.05	1
123	8.79±0.11	8.60±0.06	–	–	1
125	8.74±0.09	8.65±0.07	8.58±0.09	-0.95±0.19	0
127	8.77±0.04	8.64±0.03	8.66±0.02	-0.65±0.10	0
128	8.75±0.04	8.59±0.05	8.60±0.04	-0.98±0.17	0
129	8.71±0.03	8.60±0.03	8.59±0.02	-0.88±0.08	0
130	8.65±0.04	8.64±0.05	8.60±0.03	-0.64±0.12	0
132	8.72±0.03	8.57±0.02	8.61±0.02	-0.86±0.07	0
133	8.67±0.01	8.51±0.01	8.61±0.01	-0.77±0.04	0
134	8.75±0.06	8.70±0.06	8.61±0.05	-0.79±0.12	0

Continued.

(1) #	(2) 12+log(O/H)$_{N2}$	(3) 12+log(O/H)$_{O3N2}$	(4) 12+log(O/H)$_{R}$	(5) log(N/O)$_{Pi16}$	(6) Vel
136	8.74±0.04	8.58±0.03	8.62±0.03	-0.87±0.10	0
137	8.76±0.03	8.64±0.03	8.65±0.02	-0.75±0.08	0
138	8.75±0.03	8.63±0.03	8.63±0.02	-0.77±0.09	0
139	8.63±0.03	8.54±0.02	8.61±0.02	-0.64±0.06	0
140	8.74±0.05	8.62±0.04	8.62±0.04	-0.83±0.10	0
141	8.69±0.02	8.57±0.02	8.60±0.02	-0.81±0.07	0
142	8.77±0.03	8.61±0.03	8.65±0.02	-0.74±0.09	0
143	8.77±0.03	8.65±0.03	8.66±0.02	-0.69±0.08	0
146	8.75±0.02	8.64±0.03	8.64±0.02	-0.72±0.07	0
147	8.73±0.09	8.57±0.06	8.48±0.12	-1.25±0.19	0
148	8.75±0.06	8.67±0.06	8.60±0.06	-0.88±0.15	0
149	8.73±0.09	8.62±0.06	8.58±0.08	-0.93±0.15	0
150	8.69±0.07	8.65±0.06	8.55±0.07	-0.90±0.14	0
152	8.56±0.08	8.57±0.06	8.51±0.07	-0.88±0.15	0
153	8.66±0.04	8.60±0.04	8.57±0.04	-0.84±0.12	0
154	8.70±0.03	8.58±0.03	8.63±0.02	-0.70±0.09	0
155	8.59±0.05	8.45±0.04	8.54±0.04	-0.89±0.12	0
156	8.63±0.08	8.54±0.04	8.56±0.06	-0.86±0.11	0
157	8.67±0.05	8.55±0.04	8.59±0.04	-0.83±0.11	0
159	8.73±0.05	8.64±0.05	–	–	0
160	8.66±0.09	8.50±0.06	–	–	0
164	8.63±0.02	8.50±0.02	8.57±0.02	-0.85±0.06	0
165	8.62±0.02	8.50±0.02	8.57±0.02	-0.83±0.06	0
166	8.62±0.03	8.47±0.02	8.56±0.02	-0.88±0.07	0
167	8.52±0.04	8.43±0.03	8.47±0.04	-1.00±0.09	0
168	8.57±0.04	8.45±0.03	8.55±0.03	-0.83±0.09	0
169	8.63±0.05	8.50±0.03	8.56±0.04	-0.90±0.08	0
170	8.55±0.06	8.47±0.03	8.55±0.03	-0.72±0.04	0
171	8.57±0.05	8.44±0.02	8.54±0.03	-0.86±0.08	0

Continued.

(1) #	(2) 12+log(O/H)$_{N2}$	(3) 12+log(O/H)$_{O3N2}$	(4) 12+log(O/H)$_{R}$	(5) log(N/O)$_{Pi16}$	(6) Vel
172	8.37±0.06	8.30±0.03	8.46±0.04	-0.91±0.07	0
173	8.49±0.04	8.39±0.03	8.44±0.04	-1.05±0.09	0
174	8.59±0.04	8.47±0.03	8.49±0.04	-1.06±0.10	0
176	8.52±0.12	8.55±0.07	8.27±0.15	-1.31±0.19	1

The columns correspond to: (1) Identifier of the HII region; (2) Oxygen abundances using N2 calibrator (Pérez-Montero & Contini 2009); (3) Oxygen abundances using O3N2 calibrator (Pérez-Montero & Contini 2009); (4) Oxygen abundances using R calibrator (Pilyugin & Grebel 2016); (5) Nitrogen abundances using Pilyugin & Grebel (2016) calibrator; (6) Velocity of the region belongs to the LV (0) or the HV (1) sub-samples.

Chapter 6

Conclusiones

Contents

6.1 Conclusiones

En esta tesis se han estudiado las propiedades de las galaxias con formación estelar (FE) masiva incluyendo los posibles efectos de su entorno. Para ello se ha analizado la FE y la evolución química de las galaxias en distintos entornos: una muestra de galaxias de campo, y el grupo compacto de galaxias Quinteto de Stephan.

Para las galaxias de campo se han aplicado correcciones de apertura obtenidas a partir de la espectroscopía bidimensional del proyecto CALIFA (Iglesias-Páramo et al. 2013, 2016). Estas correcciones han sido utilizadas para determinar el valor total de los flujos de las líneas de emisión predominantes (e.g. [OII]λ3727, Hβ, [OIII]λ5007, Hα y [NII]λ6584) de las galaxias con FE de SDSS. Este estudio se ha basado en el catálogo público de MPA-JHU, que utiliza datos fotométricos y espectroscópicos de galaxias de SDSS. Esta muestra cubre el rango de masa estelar ($M_\star$) desde $10^{8.5}$ $M_\odot$ hasta $10^{11.5}$ $M_\odot$, siendo el parámetro radio Petrosian 50 (R_{50}) menor de 5" y el rango de corrimiento al rojo (z) entre $0.005 \leq z \leq 0.22$. Todas las galaxias están localizadas en la zona de FE en el diagrama BPT y su anchura equivalente de Hα es mayor o igual a 3. Este trabajo proporciona un estudio robusto y empírico de la tasa de formación estelar (SFR) total de las galaxias y su dependencia con la masa estelar, la extinción y el corrimiento al rojo. La muestra de 209.276 galaxias con FE de SDSS ha sido publicada en una base de datos accesible para toda la comunidad científica. Este es el primer estudio que usa el flujo total de Hα, corregido de efectos de apertura a partir de las curvas de crecimiento empíricas de Hα, para analizar el comportamiento de la SFR actual y la SFR específica (sSFR) para todas las galaxias con FE de SDSS. Con esta muestra obtenida, también se ha derivado la metalicidad y la abundancia de nitrógeno a oxígeno (N/O) minimizando los efectos sistemáticos y se examinó en detalle la naturaleza de la relación fundamental existente entre la metalicidad, la masa estelar y la SFR para nuestra muestra de galaxias con FE.

Se ha realizado un estudio de uno de los grupos compactos de galaxias más conocidos, el Quinteto de Stephan (SQ), usando un espectrómetro óptico de transformada de Fourier, SITELLE. Con este instrumento se ha obtenido la muestra más completa hasta la fecha de 175 emisores Hα pertenecientes a SQ, y se han estudiado en detalle sus propiedades físicas y cinemáticas así como las complejas estructuras descubiertas en el gas ionizado extendido; en 22 de las regiones se observa un perfil de línea complejo con dos componentes de velocidad. Posteriormente, se llevó a cabo un estudio de las propiedades físicas (como SFR, O/H, N/O, extinción) de las regiones clasificadas como regiones HII a partir del diagrama BPT (52% de la muestra). El cubo de datos con las posiciones, los flujos de Hα y las velocidades radiales de las 175 regiones Hα emisoras de SQ se ha publicado en una base de datos accesible para toda la comunidad científica.

Las conclusiones generales de esta tesis doctoral aparecen resumidas a continuación:

- Por primera vez se ha podido estudiar la relación SFR–$M_\star$ corregida de efectos de apertura a partir de las correcciones empíricas del flujo de Hα y del cociente Hα/Hβ. La pendiente ($d\log(SFR)/d\log(M_\star)$) que se ha obtenido en esta tesis es 0.935, mayor que la pendiente obtenida por MPA-JHU (0.76).

  - De la comparación de la relación SFR–$M_\star$ con trabajos previos se concluye que existen

claras diferencias entre la relación encontrada en esta tesis y la obtenida a partir de la base de datos de MPA-JHU. Los valores encontrados por MPA-JHU son sistemáticamente mayores (~0.3 dex) para $\log(M_\star/M_\odot) \leq 9$ y menores (hasta 0.3 dex) para $\log(M_\star/M_\odot) \geq 11$, sobrestimando el número de estrellas que se forman por año para las galaxias menos masivas y subestimándolo para las más masivas.

- Además, nuestra relación es consistente con estudios realizados con resolución espacial (e.g. Catalán-Torrecilla et al. 2015; Richards et al. 2016) y presenta una gran correlación con las predicciones de modelos teóricos y semiempíricos (Dutton et al. 2010; Sparre et al. 2015).

- La SFR corregida de efectos de apertura muestra una clara dependencia con la extinción.

- Se ha encontrado una clara correlación de la relación masa estelar – metalicidad (MZR) con la SFR de acuerdo con los trabajos anteriores en la literatura. Del estudio detallado de esta relación, se ha obtenido una novedosa dependencia entre O/H – SFR, y entre N/O – SFR, con la edad de las poblaciones estelares de las galaxias con FE de nuestra muestra de SDSS. Las galaxias con poblaciones estelares más viejas ($D_n(4000) \geq 1.2$) y $\log(M_\star/M_\odot) \geq 10.5$ muestran las relaciones O/H – SFR (N/O – SFR) aplanándose cuando 12+log(O/H) ≥ 8.55 (log(N/O) ≥ -0.9), independientemente de su SFR; esto indica que la metalicidad permanece prácticamente constante sólo dependiente de la masa estelar de estas galaxias masivas.

  - Por el contrario para las galaxias con poblaciones estelares más jóvenes ($D_n(4000) < 1.2$) se ha encontrado una dependencia negativa entre O/H y SFR (también para N/O y SFR) para $\log(M_\star/M_\odot) < 10.5$. Esta dependencia tiene lugar desde valores de metalicidad típicos de galaxias enanas hasta valores solares, cubriendo un amplio rango de masas estelares, y sugiriéndonos que estas galaxias con poblaciones estelares jóvenes no sólo están compuestas por galaxias enanas. Estas galaxias más jóvenes muestran siempre la medida de SFR más alta medida para su masa estelar. Estos objetos con la SFR más alta sólo pueden ser explicados en el escenario de grandes masas de gas en caída libre.

- En el estudio cinemático de SQ se han identificado cinco componentes distintos de velocidad. Se ha detectado una zona con marcada emisión Hα entre NGC7319 y el nuevo intruso (NI), asociado a la región del choque a gran escala (LSSR). El gas emisor en esta zona tiene una naturaleza cinemática compleja evidencia de una estructura enredada y distribuida espacialmente. Se sugiere que una variedad de procesos de interacción tuvieron lugar antes de que NI interaccionara con el grupo principal.

  - También se ha detectado en Hα un puente de gas ionizado entre LSSR y el núcleo de NGC7319.

  - Se ha encontrado una nueva galaxia con emisión extendida en SQ. Según la relación Tully-Fisher se trata de una galaxia enana que presenta un gradiente en el disco de ±60 km s^{-1}.

- A partir del estudio del diagrama BPT de las regiones Hα emisoras se demuestra que las regiones tipo "composite" y AGN de L1, SSQA y Shs son consistentes con la excitación por choques ionizantes rápidos sin precursor con metalicidad solar, baja densidad (n=0.1) y

velocidades entre 175 y 300 km s^{-1}, según los modelos de Allen et al. (2008).

- Las regiones con FE de SQ están localizadas en la parte norte y sur de la zona del choque, en YTT, NI y SDR. No se ha encontrado FE significativa en LSSR.

- La SFR total en SQ es de $\log(SFR/M_{\odot}yr^{-1}) = 0.496$, donde el 55% de la FE tiene lugar en las regiones con velocidad radial menor de o igual que 6160 km s^{-1} y el resto para velocidades radiales mayores de 6160 km s^{-1}. El 28% de toda la FE en SQ se produce en SQA, y el 9% en SQB, por tanto, se sugiere que el material previo a la colisión entre SQ y NI podría estar aparentemente apagado.

- Al igual que en las galaxias con FE de SDSS, se ve una clara correlación entre A_v y SFR para las regiones con FE de SQ. Cuando se ha considerado la SFR integrada y la mediana de A_v para todo SQ y NI se ve que ambas zonas están localizadas en la huella de las galaxias con FE de SDSS.

- Las distintas interacciones sufridas en SQ han dispersado el gas a las zonas periféricas. Se ha medido un gradiente de metalicidad radial dentro - fuera a lo largo de NI. Los rangos de O/H y N/O poseen valores entre solar y $\sim \frac{1}{4}$ solar, aunque la mayoría de las regiones son ricas en metales (12+log(O/H) $\gtrsim$ 8.5) lo que indicaría que este material proviene de los discos de las distintas galaxias espirales que han interaccionado en el grupo. En SQ conviven al menos dos componentes de gas químicamente diferentes: i) uno rico en metales en las regiones con velocidad radial $\leq$ 6160 km s^{-1} y en la mayoría de las de YTT y; ii) uno pobre en metales en las regiones en la zona del choque y en varias regiones de YTT. La relación log(N/O) – 12+log(O/H) que se ha obtenido para SQ indica la producción de nitrógeno secundatio en el sistema.

6.2 Conclusions

In this thesis, the properties of galaxies with massive star formation have been studied from the point of view of their environments and the possible associated effects. For this we analysed star formation and the chemical evolution of galaxies in different environments: a representative sample of galaxies in the field, and the compact group of galaxies Stephan's Quintet.

For field galaxies, we applied aperture corrections obtained from the two-dimensional spectroscopy of the CALIFA project (Iglesias-Páramo et al. 2013, 2016). These empirical aperture corrections were used to determine the total value of the predominant emission line fluxes (e.g. [OII]λ3727, Hβ, [OIII]λ5007, Hα y [NII]λ6584) for SDSS galaxies with star formation. This study is based on the public catalogue of MPA-JHU, which uses photometric and spectroscopic data of SDSS galaxies. The sample covers the stellar mass range from $10^{8.5}$ $M_{\odot}$ to $10^{11.5}$ $M_{\odot}$, the Petrosian radius 50 (R_{50}) parameter of the galaxies is considered to be less than 5", and the considered redshift range (z) is $0.005 \leq z \leq 0.22$. All of the galaxies are located in the star formation area of the BPT diagram and their Hα equivalent width is greater than or equal to 3. This work provides a robust empirical study of the total star formation rate (SFR) of the galaxies and their dependence on stellar mass, extinction and redshift. Our final sample of 209 276 SDSS star-forming

galaxies has been published in a database available to the entire scientific community. This is the first study to use the total Hα flux, corrected for aperture effects from the Hα empirical growth curves, to analyse the behaviour of the current SFR and the specific SFR (sSFR) for all galaxies with star formation from SDSS. Using this sample, we derived the metallicity and nitrogen to oxygen abundance (N/O) minimising the systematic effects, where the nature of the fundamental relation between metallicity, stellar mass, and SFR was analysed in detail.

We conducted a study on one of the best-known compact groups of galaxies, the Stephan's Quintet (SQ), using an optical imaging Fourier transform spectrometer, SITELLE. Using this intrument, the most complete sample to date of 175 Hα emission regions belonging to SQ has been obtained, and their physical and kinematic properties have been studied. In addition, the complex structures discovered in the extended ionised gas have been analysed in detail; twenty-two of the regions have a complex line profile with two velocity components. Subsequently, a study of the physical properties (SFR, O/H, N/O, and extinction) of the star-forming regions (52% of the total sample) was carried out. The data cube with the positions (right ascension and declination), the Hα flux and the radial velocities of the 175 Hα emission regions from SQ has been made public to the entire scientific community.

The general conclusions of this doctoral thesis are summarised below:

- It is the first time that the SFR – $M_\star$ relation corrected for aperture effects based on the empirical corrections of Hα flux and Hα/Hβ ratio has been studied. The slope (d log(SFR)/d log($M_\star$)) derived in this thesis is 0.935, higher than the slope obtained by MPA-JHU (0.76).

  - When comparing our SFR – $M_\star$ relation with previous studies, clear differences between the relation shown in this thesis and that obtained from the data base of MPA-JHU have been found. The values obtained by MPA-JHU are systematically higher (~0.3 dex) for $\log(M_\star/M_\odot) \leq 9$ and lower (by up to 0.3 dex) for $\log(M_\star/M_\odot) \geq 11$, overestimating the number of stars formed per year for the least massive galaxies and underestimating the most massive.

  - In addition, our relation is consistent with selected observational studies based on integral field spectroscopy of individual galaxies (e.g. Catalán-Torrecilla et al. 2015; Richards et al. 2016) and presents an excellent correlation with theoretical predictions and semi-empirical models (Dutton et al. 2010; Sparre et al. 2015).

  - The total SFR values of the entire sample present a clear correlation with extinction.

- A clear correlation of the stellar mass – metallicity (MZR) relation with the SFR has been found, in agreement with previous works. From the detailed study of this relation, a new dependence between O/H – SFR, and between N/O – SFR, has been found with the age of the galaxies' stellar populations. Galaxies with older stellar populations ($D_n(4000) \geq 1.2$) and $\log(M_\star/M_\odot) \geq 10.5$ saturate and flatten in the O/H – SFR (N/O – SFR) relation when 12 + log(O/H) ≥ 8.55 (log(N/O) ≥ -0.9), irrespective of their SFR; which indicates that the metallicity remains constant only depending on the stellar mass of these massive galaxies.

  - On the contrary, for galaxies with younger stellar populations ($D_n(4000) < 1.2$), a negative dependence has been found between O/H and SFR (also for N/O and SFR) for $\log(M_\star/M_\odot)$

< 10.5. This dependence happens between a metallicity range from typical dwarf values to solar values, covering a wide range of stellar masses, suggesting that galaxies with young stellar populations are not only composed of dwarf galaxies. These young galaxies always show the highest SFR measured for their stellar mass and can only be explained by the massive infall scenario.

- Five velocity components have been identified in the kinematic study of SQ. An area with remarkable Hα emission has been detected between NGC7319 and the new intruder (NI), associated with the large-scale shock region (LSSR). The emitting gas in this area has a complex kinematic nature, since it is a knotty and spatially distributed structure. This suggests that a variety of interaction processes occurred before NI interacted with the main group.

  - An ionised gas bridge in Hα has also been detected between LSSR and the NGC7319 nucleus.

  - A new galaxy with extended emission has been found in SQ. According to the Tully-Fisher relation, it is a dwarf galaxy with a velocity gradient across its disc of ± 60 $km\ s^{-1}$.

- By studying the BPT diagram of the Hα emission regions, it has been found that the composite and AGN regions of L1, SSQA and Shs are consistent with fast shock ionisation without precursor for solar metallicity, low density (n=0.1) and velocities between 175 and 300 $km\ s^{-1}$, according to the models of Allen et al. (2008).

  - The star-forming regions of SQ are located in the northern and southern part of the shock zone, YTT, NI, and SDR. No significant star formation was detected in LSSR.

  - The total SFR in SQ is $\log(SFR/M_{\odot}yr^{-1}) = 0.496$, where 55% of the star formation occurs in regions with radial velocity ≤ 6160 $km\ s^{-1}$ while the remaining 45% is in regions with radial velocities > 6160 $km\ s^{-1}$. Around 28% of the total star formation in SQ is produced in SQA, and 9% in SQB. Therefore, it is suggested that the material existing prior to the collision with NI is apparently quench, because it shows a low SFR.

  - As in the SDSS star-forming galaxies, there is a clear correlation between A_v and SFR for SQ regions with star formation. Regarding the integrated SFR and the median of A_v for the entire SQ and for the entire NI, we found that they are located in the footprint of SDSS star-forming galaxies.

  - The different interactions which have occurred in SQ have dispersed the gas to the peripheral areas. There is a gradient of inner-outer radial metallicity along NI. The ranges of O/H and N/O have values between solar and $\sim \frac{1}{4}$ solar value, although most of the regions are metal-rich ($12 + \log(O/H) \gtrsim 8.5$) which would indicate that this material comes from the discs of the different spiral galaxies that have interacted in the group. In SQ, at least two chemically different gas components cohabit: i) a metal-rich material in regions with radial velocity ≤ 6160 $km\ s^{-1}$ and in most of the regions from YTT and; ii) a metal-poor material in the shock regions and in several regions in YTT. Secondary nitrogen production in the relation log(N/O) – 12+log(O/H) was found in the SQ HII regions.

Chapter 7

Future Work

Contents

7.1 Future Work

SIGNALS project

During most of my PhD thesis I had the opportunity to work with a unique data set to date, provided by the new optical imaging Fourier transform spectrometer SITELLE (Mauna Kea Observatory, Hawaii). The experience acquired in the understanding and analysis of these data and the results obtained establish the path to continue my scientific career in the next future: I will focus on the study of star-forming regions in galaxies in the local Universe using the SITELLE data. SITELLE has a wide field-of-view (11'x11') with continuous sampling (0.32"/pixel) and collects 100% of the light entering the instrument, the typical seeing is ~0.8", and very high throughput in the near ultraviolet (40% at 350 nm). The spatial coverage of SITELLE is 100 times greater than that of any competitor. All this makes SITELLE a unique instrument compared with other up to now.

The SIGNALS (Star formation, Ionized Gas, and Nebular Abundances Legacy Survey) project, in which I participate, is a survey devoted to observe ~40 local extended star-forming galaxies within 10 Mpc, with SITELLE. This survey will provide the largest, most complete, and homogeneous database of spectroscopically and spatially resolved extragalactic HII regions ever assembled and will allow the study of small-scale nebular physics and many other phenomena linked to massive star formation and feedback in galaxies at a mean spatial resolution of ~20 pc. In the star-forming galaxies, the interstellar medium is actively modified and recycled. Massive OB stars and their descendants - blue and red supergiants, Luminous Blue Variables and Wolf-Rayet stars - are not only responsible for ionizing their surroundings but also for exercising direct radiative pressure on this gas, as well as for returning enriched material and mechanical energy through their stellar winds and eventual supernovae. The combined study of gas abundances and kinematics on small (10 - 50 pc) and galactic scales holds key information on the chemical evolution of galaxies. SIGNALS' sample will provide a statistically reliable laboratory, with over 50000 resolved HII regions. SIGNALS' legacy will reflect on many topics in astrophysics, from stars to distant galaxies.

The work carried out in my thesis provided me the tools, know-how, and the necessary relevant experience to work with SITELLE data in an optimal way, making the SIGNALS proyect ideal for me. Both cases (my thesis and SIGNALS proyect) focus on the study of star formation regions in galaxies of the local Universe using the properties of ionised gas and the chemical composition of the interstellar medium (e.g. the star formation rate, chemical abundances, extinction, etc) with 3D spectroscopy. Studying star forming regions will help us to understand how galaxies evolve chemically and what their history of star formation was.

Fundamental properties and extinction relations

We want to continue exploiting our selected sample of SDSS star-forming galaxies defined in the second chapter of this thesis. One of the most remarkable objectives is the study of the relations between the fundamental properties (e.g. stellar mass, SFR, sSFR) and extinction. In addition, we

would like to deepen the understanding of the dependence that might exist with other properties (e.g. the relation between FMR and extinction).

One of the most immediate objectives would be to extend this study to the sample of star-forming galaxies in other surveys (e.g. MANGA).

Exploring our sample of star-forming outliers galaxies

In Chapter 3 we found a very interesting population of objects. These objects are outliers galaxies of the relationship between O/H and SFR, where we observed an anticorrelation. We have seen that these galaxies have the youngest stellar populations in our sample of SDSS star-forming galaxies. While the massive infall scenario explains the high SFR that we find for these objects, we cannot explain the anticorrelation observed between N/O and SFR. Therefore, we want to exploit the sample to study the role of the outliers. We have already begun to study these galaxies with the aim of understanding their emitting nature and the presence of HeII. Once they are characterised by their spectra and colors, we want to extend the survey to further objects in the sky. For this, we want to make use of JPAS, both a very low resolution spectrograph and one of the deepest survey to date.

JPAS is also a project of which I am a member. It has 54 narrow filters (width ∼125 Å) and a spectral coverage from ∼ 3500 Å up to *sim* 9000 Å, as well as a large integral field (several square degrees) with a very low spatial resolution. JPAS is a crucial instrument to detect star-forming galaxies with very intense emission lines (e.g. Hα and [OIII]λ5007), which would help us to search for this type of galaxies across the sky thanks to its extensive survey.

Glossary

A

A_v Extinction in magnitude in the V–Band.

AGN Active Galactic Nuclei.

C

C Composite.

c(Hβ) Reddening Coefficient.

CFHT Canada–France–Hawaii Telescope.

D

D_n(4000) Narrow 4000Å Break.

DEC Declination.

E

EW(Hα) Hα Equivalent Width.

F

F(Hα) Hα Flux.

FoV Field-of-View.

FWHM Full-Width Half-Maximum.

G

GMCs Giant Molecular Clouds.

H

Hs High Radial Velocity Strands.

HST Hubble Space Telescope.

HV High Radial Velocity Sub-sample.

I

ICM Intracluster Medium.

IFS Integral Field Spectograph.

IFTS Imaging Fourier Transform Spectrometer.

IFU Integral Field Unit.

IGM Intergalactic Medium.

IMF Initial Mass Function.

IR Infrared.

ISM Interstellar Medium.

K

KS Kolmogorov-Smirnov.

L

L(Hα) Hα Luminosity.

LINERs Low Ionization Nuclear Emission Regions.

Ls Low Radial Velocity Strands.

LSS Large Scale Structure.

LSSR Large Scale Shock Region.

LV Low Radial Velocity Sub-sample.

M

$M_\star$ Stellar Mass.

MPA-JHU Max-Planck-Institut für Astrophysik and Johns Hopkins University.

MS Main Sequence.

MZR Mass–Metallicity Relation.

MZSFR Fundamental Mass–Metallicity SFR Relation.

N

N/O Nitrogen to Oxygen Abundance Ratio.

NED NASA/IPAC Extragalactic Database.

NG New Dwarf Galaxy.

NI New Intruder.

NIs New Intruder Strands.

NSQA North of Starburst A.

NW Tidal Tail at North of NSQA.

O

O/H Oxygen Abundance.

OI Old Intruder.

P

PSF Point Spread Function.

Q

QSO Quasi Stellar Objects.

R

r Petrosian r magnitude.

$\mathbf{R_{50}}$ Petrosian Radius Containing 50% of total galaxy flux in the r-band.

RA Right Ascension.

S

S/N signal-to-noise ratio.

SDR Southern Debris Region.

SDSS Sloan Digital Sky Survey.

SED Spectral Energy Distribution.

SF star-forming.

SFE Star Formation Efficiencies.

SFR Star Formation Rate, $[M_{\odot}\, year^{-1}]$.

Shs Shock Strands.

SITELLE Spectromètre Imageur à Transformée de Fourier pour l'Etude en Long et en Large de raies d'Emission.

SQ Stephan's Quintet.

SQA Starburst A.

SQB Starburst B.

SSFR Specific Star Formation Rate.

sSFR Specific Star Formation Rate.

SSQA South of Starburst A.

T

TDG Tidal Dwarf Galaxy.

U

UV Ultraviolet.

Y

YTT Young Tidal Tail.

Z

z Redshift.

List of Figures

List of Tables

Bibliography

Abazajian, K. N., Adelman-McCarthy, J. K., Agüeros, M. A., et al. 2009, ApJS, 182, 543

Abell, G. O. 1958, ApJS, 3, 211

Alam, S., Albareti, F. D., Allende Prieto, C., et al. 2015, ApJS, 219, 12

Allen, M. G., Groves, B. A., Dopita, M. A., Sutherland, R. S., & Kewley, L. J. 2008, ApJS, 178, 20

Allen, R. J. & Hartsuiker, J. W. 1972, Nature, 239, 324

Alloin, D., Collin-Souffrin, S., Joly, M., & Vigroux, L. 1979, A&A, 78, 200

Andrews, B. H. & Martini, P. 2013, ApJ, 765, 140

Appleton, P. N., Guillard, P., Boulanger, F., et al. 2013, ApJ, 777, 66

Appleton, P. N., Guillard, P., Togi, A., et al. 2017, ApJ, 836, 76

Appleton, P. N., Xu, K. C., Reach, W., et al. 2006, ApJ, 639, L51

Argudo-Fernández, M., Verley, S., Bergond, G., et al. 2015, A&A, 578, A110

Asplund, M., Grevesse, N., Sauval, A. J., & Scott, P. 2009, ARA&A, 47, 481

Bacon, R., Copin, Y., Monnet, G., et al. 2001, MNRAS, 326, 23

Baldwin, J. A., Phillips, M. M., & Terlevich, R. 1981, PASP, 93, 5

Balogh, M., Eke, V., Miller, C., et al. 2004, MNRAS, 348, 1355

Balogh, M. L., Morris, S. L., Yee, H. K. C., Carlberg, R. G., & Ellingson, E. 1999, ApJ, 527, 54

Balogh, M. L., Schade, D., Morris, S. L., et al. 1998, ApJ, 504, L75

Barrera-Ballesteros, J. K., Sánchez, S. F., Heckman, T., Blanc, G. A., & The MaNGA Team. 2017, ApJ, 844, 80

Bekki, K., Couch, W. J., & Shioya, Y. 2002, ApJ, 577, 651

Belfiore, F., Maiolino, R., Maraston, C., et al. 2016, MNRAS, 461, 3111

Berg, D. A., Skillman, E. D., Croxall, K. V., et al. 2015, ApJ, 806, 16

Berg, D. A., Skillman, E. D., Marble, A. R., et al. 2012, ApJ, 754, 98

Blanton, M. R., Lupton, R. H., Schlegel, D. J., et al. 2005, ApJ, 631, 208

Bresolin, F., Kudritzki, R.-P., Urbaneja, M. A., et al. 2016, ApJ, 830, 64

Brinchmann, J., Charlot, S., Heckman, T. M., et al. 2004a, ArXiv Astrophysics e-prints

Brinchmann, J., Charlot, S., White, S. D. M., et al. 2004b, MNRAS, 351, 1151

Brown, J. S., Martini, P., & Andrews, B. H. 2016, MNRAS, 458, 1529

Buat, V., Boselli, A., Gavazzi, G., & Bonfanti, C. 2002, A&A, 383, 801

Bundy, K., Bershady, M. A., Law, D. R., et al. 2015, ApJ, 798, 7

Burbidge, E. M. & Burbidge, G. R. 1961, ApJ, 134, 244

Cardelli, J. A., Clayton, G. C., & Mathis, J. S. 1989, ApJ, 345, 245

Casado, J., Ascasibar, Y., Gavilán, M., et al. 2015, MNRAS, 451, 888

Catalán-Torrecilla, C., Gil de Paz, A., Castillo-Morales, A., et al. 2015, A&A, 584, A87

Chabrier, G. 2003, ApJ, 586, L133

Charlot, S., Kauffmann, G., Longhetti, M., et al. 2002, MNRAS, 330, 876

Cid Fernandes, R., Stasińska, G., Mateus, A., & Vale Asari, N. 2011, MNRAS, 413, 1687

Cluver, M. E., Appleton, P. N., Boulanger, F., et al. 2010, ApJ, 710, 248

Colless, M., Dalton, G., Maddox, S., et al. 2001, MNRAS, 328, 1039

Contini, T., Garilli, B., Le Fèvre, O., et al. 2012, A&A, 539, A91

Cook, D. O., Dale, D. A., Johnson, B. D., et al. 2014, MNRAS, 445, 899

Cooper, M. C., Newman, J. A., Weiner, B. J., et al. 2008, MNRAS, 383, 1058

Cresci, G., Mannucci, F., Sommariva, V., et al. 2012, MNRAS, 421, 262

Croxall, K. V., Pogge, R. W., Berg, D. A., Skillman, E. D., & Moustakas, J. 2016, ApJ, 830, 4

Croxall, K. V., van Zee, L., Lee, H., et al. 2009, ApJ, 705, 723

Curti, M., Cresci, G., Mannucci, F., et al. 2017, MNRAS, 465, 1384

Dahlem, M. 1997, PASP, 109, 1298

Davé, R., Finlator, K., & Oppenheimer, B. D. 2011, MNRAS, 416, 1354

Dayal, P., Ferrara, A., & Dunlop, J. S. 2013, MNRAS, 430, 2891

de Mello, D. F., Urrutia-Viscarra, F., Mendes de Oliveira, C., et al. 2012, MNRAS, 426, 2441

De Rossi, M. E., Bower, R. G., Font, A. S., Schaye, J., & Theuns, T. 2017, MNRAS, 472, 3354

de Vaucouleurs, G. 1959, Handbuch der Physik, 53, 275

Díaz, A. I., Castellanos, M., Terlevich, E., & Luisa García-Vargas, M. 2000, MNRAS, 318, 462

Drake, A. B., Simpson, C., Baldry, I. K., et al. 2015, MNRAS, 454, 2015

Drake, A. B., Simpson, C., Collins, C. A., et al. 2013, MNRAS, 433, 796

Dressler, A. 1980, ApJ, 236, 351

Drissen, L., Martin, T., Rousseau-Nepton, L., et al. 2019, MNRAS, 485, 3930

Driver, S. P., Hill, D. T., Kelvin, L. S., et al. 2011, MNRAS, 413, 971

Duarte Puertas, S., Vilchez, J. M., Iglesias-Páramo, J., et al. 2017, A&A, 599, A71

Duc, P.-A., Cuillandre, J.-C., & Renaud, F. 2018, MNRAS, 475, L40

Duc, P.-A., Paudel, S., McDermid, R. M., et al. 2014, MNRAS, 440, 1458

Dutton, A. A., van den Bosch, F. C., & Dekel, A. 2010, MNRAS, 405, 1690

Edmunds, M. G. & Pagel, B. E. J. 1978, MNRAS, 185, 77P

Elbaz, D., Daddi, E., Le Borgne, D., et al. 2007, A&A, 468, 33

Ellison, S. L., Patton, D. R., Simard, L., & McConnachie, A. W. 2008, ApJ, 672, L107

Ellison, S. L., Simard, L., Cowan, N. B., et al. 2009, MNRAS, 396, 1257

Evans, I. N. & Dopita, M. A. 1985, ApJS, 58, 125

Fedotov, K., Gallagher, S. C., Durrell, P. R., et al. 2015, MNRAS, 449, 2937

Fedotov, K., Gallagher, S. C., Konstantopoulos, I. S., et al. 2011, AJ, 142, 42

Finlator, K. & Davé, R. 2008, MNRAS, 385, 2181

Firpo, V. 2012, PhD thesis, PhD Thesis, 2012

Fisher, D. B. & Drory, N. 2011, ApJ, 733, L47

Gallagher, S. C., Charlton, J. C., Hunsberger, S. D., Zaritsky, D., & Whitmore, B. C. 2001, AJ, 122, 163

Gallazzi, A., Charlot, S., Brinchmann, J., White, S. D. M., & Tremonti, C. A. 2005, MNRAS, 362, 41

García-Benito, R., Zibetti, S., Sánchez, S. F., et al. 2015, A&A, 576, A135

Garnett, D. R. 2002, ApJ, 581, 1019

Gomes, J. M., Papaderos, P., Vílchez, J. M., et al. 2016, A&A, 586, A22

Gómez, P. L., Nichol, R. C., Miller, C. J., et al. 2003, ApJ, 584, 210

Grandmont, F., Drissen, L., Mandar, J., Thibault, S., & Baril, M. 2012, in Society of Photo-Optical Instrumentation Engineers (SPIE) Conference Series, Vol. 8446, Ground-based and Airborne Instrumentation for Astronomy IV, 84460U

Guidi, G., Scannapieco, C., Walcher, J., & Gallazzi, A. 2016, MNRAS, 462, 2046

Guillard, P., Boulanger, F., Cluver, M. E., et al. 2010, A&A, 518, A59

Guillard, P., Boulanger, F., Pineau Des Forêts, G., & Appleton, P. N. 2009, A&A, 502, 515

Guillard, P., Boulanger, F., Pineau des Forêts, G., et al. 2012, ApJ, 749, 158

Gunn, J. E. & Gott, J. Richard, I. 1972, ApJ, 176, 1

Hao, J., McKay, T. A., Koester, B. P., et al. 2010, ApJS, 191, 254

Heida, M., Jonker, P. G., Torres, M. A. P., & Mineo, S. 2012, MNRAS, 424, 1563

Hickson, P. 1982, ApJ, 255, 382

Hickson, P., Mendes de Oliveira, C., Huchra, J. P., & Palumbo, G. G. 1992, ApJ, 399, 353

Hirashita, H., Buat, V., & Inoue, A. K. 2003, A&A, 410, 83

Hopkins, A. M., Driver, S. P., Brough, S., et al. 2013, MNRAS, 430, 2047

Hopkins, A. M., Miller, C. J., Nichol, R. C., et al. 2003, ApJ, 599, 971

Hubble, E. P. 1936, Realm of the Nebulae

Hughes, T. M., Cortese, L., Boselli, A., Gavazzi, G., & Davies, J. I. 2013, A&A, 550, A115

Hunt, L., Dayal, P., Magrini, L., & Ferrara, A. 2016, MNRAS, 463, 2002

Husemann, B., Jahnke, K., Sánchez, S. F., et al. 2013, A&A, 549, A87

Hwang, H. S., Shin, J., & Song, H. 2019, MNRAS, 489, 339

Hwang, J.-S., Struck, C., Renaud, F., & Appleton, P. N. 2012, MNRAS, 419, 1780

Iglesias-Páramo, J., Buat, V., Takeuchi, T. T., et al. 2006, ApJS, 164, 38

Iglesias-Páramo, J., López-Martín, L., Vílchez, J. M., Petropoulou, V., & Sulentic, J. W. 2012, A&A, 539, A127

Iglesias-Páramo, J. & Vílchez, J. M. 2001, ApJ, 550, 204

Iglesias-Páramo, J., Vílchez, J. M., Galbany, L., et al. 2013, A&A, 553, L7

Iglesias-Páramo, J., Vílchez, J. M., Rosales-Ortega, F. F., et al. 2016, ApJ, 826, 71

Kang, X., Zhang, F., Chang, R., Wang, L., & Cheng, L. 2016, A&A, 585, A20

Karachentsev, I. D. 1980, ApJS, 44, 137

Karachentsev, I. D., Karachentseva, V. E., Huchtmeier, W. K., & Makarov, D. I. 2004, AJ, 127, 2031

Karachentsev, I. D., Makarov, D. I., & Kaisina, E. I. 2013, AJ, 145, 101

Karachentseva, V. E. 1973, Soobshcheniya Spetsial'noj Astrofizicheskoj Observatorii, 8, 3

Karim, A., Schinnerer, E., Martínez-Sansigre, A., et al. 2011, ApJ, 730, 61

Kashino, D., Renzini, A., Silverman, J. D., & Daddi, E. 2016, ApJ, 823, L24

Kauffmann, G., Heckman, T. M., Tremonti, C., et al. 2003a, MNRAS, 346, 1055

Kauffmann, G., Heckman, T. M., White, S. D. M., et al. 2003b, MNRAS, 341, 33

Keeler, J. E. 1899, MNRAS, 60, 128

Kehrig, C., Monreal-Ibero, A., Papaderos, P., et al. 2012, A&A, 540, A11

Kehrig, C., Vílchez, J. M., Pérez-Montero, E., et al. 2016, MNRAS, 459, 2992

Kennicutt, R. C., J. & Kent, S. M. 1983, AJ, 88, 1094

Kennicutt, R. C. & Evans, N. J. 2012, ARA&A, 50, 531

Kennicutt, Jr., R. C. 1998a, ARA&A, 36, 189

Kennicutt, Jr., R. C. 1998b, ApJ, 498, 541

Kennicutt, Jr., R. C., Hao, C.-N., Calzetti, D., et al. 2009, ApJ, 703, 1672

Kennicutt, Jr., R. C., Lee, J. C., Funes, José G., S. J., Sakai, S., & Akiyama, S. 2008, ApJS, 178, 247

Kewley, L. J., Dopita, M. A., Sutherland, R. S., Heisler, C. A., & Trevena, J. 2001, ApJ, 556, 121

Kewley, L. J. & Ellison, S. L. 2008, ApJ, 681, 1183

Kewley, L. J., Jansen, R. A., & Geller, M. J. 2005, PASP, 117, 227

Kojima, T., Ouchi, M., Nakajima, K., et al. 2017, PASJ, 69, 44

Konstantopoulos, I. S., Appleton, P. N., Guillard, P., et al. 2014, ApJ, 784, 1

Koyama, Y., Kodama, T., Hayashi, M., et al. 2015, MNRAS, 453, 879

Kroupa, P. 2001, MNRAS, 322, 231

Kudritzki, R.-P., Urbaneja, M. A., Gazak, Z., et al. 2012, ApJ, 747, 15

Lara-López, M. A., Bongiovanni, A., Cepa, J., et al. 2010a, A&A, 519, A31

Lara-López, M. A., Cepa, J., Bongiovanni, A., et al. 2010b, A&A, 521, L53

Larson, R. B. 1975, MNRAS, 173, 671

Larson, R. B., Tinsley, B. M., & Caldwell, C. N. 1980, ApJ, 237, 692

Le Fèvre, O., Vettolani, G., Garilli, B., et al. 2005, A&A, 439, 845

Lee, H., Skillman, E. D., Cannon, J. M., et al. 2006, ApJ, 647, 970

Lee-Waddell, K., Madrid, J. P., Spekkens, K., et al. 2018, MNRAS, 480, 2719

Lelli, F., Duc, P.-A., Brinks, E., et al. 2015, A&A, 584, A113

Lequeux, J., Peimbert, M., Rayo, J. F., Serrano, A., & Torres-Peimbert, S. 1979, A&A, 80, 155

Lesaffre, P., Pineau des Forêts, G., Godard, B., et al. 2013, A&A, 550, A106

Leslie, S. K., Kewley, L. J., Sanders, D. B., & Lee, N. 2016, MNRAS, 455, L82

Lewis, I., Balogh, M., De Propris, R., et al. 2002, MNRAS, 334, 673

Licquia, T. C. & Newman, J. A. 2015, ApJ, 806, 96

Lisenfeld, U., Braine, J., Duc, P.-A., et al. 2004, A&A, 426, 471

Lisenfeld, U., Braine, J., Duc, P.-A., et al. 2002, A&A, 394, 823

Madau, P., Ferguson, H. C., Dickinson, M. E., et al. 1996, MNRAS, 283, 1388

Magrini, L., Gonçalves, D. R., & Vajgel, B. 2017, MNRAS, 464, 739

Maiolino, R. & Mannucci, F. 2019, A&A Rev., 27, 3

Mannucci, F., Cresci, G., Maiolino, R., Marconi, A., & Gnerucci, A. 2010, MNRAS, 408, 2115

Marchesini, D., van Dokkum, P. G., Förster Schreiber, N. M., et al. 2009, ApJ, 701, 1765

Martin, T., Drissen, L., & Joncas, G. 2015, in Astronomical Society of the Pacific Conference Series, Vol. 495, Astronomical Data Analysis Software an Systems XXIV (ADASS XXIV), ed. A. R. Taylor & E. Rosolowsky, 327

Martin, T. B., Drissen, L., & Melchior, A.-L. 2018, MNRAS, 473, 4130

Martin, T. B., Prunet, S., & Drissen, L. 2016, MNRAS, 463, 4223

Mast, D., Rosales-Ortega, F. F., Sánchez, S. F., et al. 2014, A&A, 561, A129

Mateus, A., Sodré, L., Cid Fernandes, R., et al. 2006, MNRAS, 370, 721

McCall, M. L., Rybski, P. M., & Shields, G. A. 1985, ApJS, 57, 1

Mendes de Oliveira, C., Cypriano, E. S., Sodré, Jr., L., & Balkowski, C. 2004, ApJ, 605, L17

Mendes de Oliveira, C., Plana, H., Amram, P., Balkowski, C., & Bolte, M. 2001, AJ, 121, 2524

Moles, M., Marquez, I., & Sulentic, J. W. 1998, A&A, 334, 473

Moles, M., Sulentic, J. W., & Márquez, I. 1997, ApJ, 485, L69

Mollá, M., Vílchez, J. M., Gavilán, M., & Díaz, A. I. 2006, MNRAS, 372, 1069

Møller, P., Fynbo, J. P. U., Ledoux, C., & Nilsson, K. K. 2013, MNRAS, 430, 2680

Momcheva, I. G., Lee, J. C., Ly, C., et al. 2013, AJ, 145, 47

Moore, B., Katz, N., Lake, G., Dressler, A., & Oemler, A. 1996, Nature, 379, 613

Mouhcine, M., Gibson, B. K., Renda, A., & Kawata, D. 2008, A&A, 486, 711

Mould, J. R., Huchra, J. P., Freedman, W. L., et al. 2000, ApJ, 529, 786

Nakamura, O., Fukugita, M., Brinkmann, J., & Schneider, D. P. 2004, AJ, 127, 2511

Nelson, D., Pillepich, A., Genel, S., et al. 2015, Astronomy and Computing, 13, 12

Noeske, K. G., Weiner, B. J., Faber, S. M., et al. 2007, ApJ, 660, L43

O'Donnell, J. E. 1994, ApJ, 422, 158

Ohyama, Y., Nishiura, S., Murayama, T., & Taniguchi, Y. 1998, ApJ, 492, L25

Okamoto, T., Nagashima, M., Lacey, C. G., & Frenk, C. S. 2017, MNRAS, 464, 4866

Osterbrock, D. E. 1989, Astrophysics of gaseous nebulae and active galactic nuclei

O'Sullivan, E., Giacintucci, S., Vrtilek, J. M., Raychaudhury, S., & David, L. P. 2009, ApJ, 701, 1560

Pagel, B. E. J., Edmunds, M. G., Blackwell, D. E., Chun, M. S., & Smith, G. 1979, MNRAS, 189, 95

Payne, C. H. 1925, Stellar Atmospheres; a Contribution to the Observational Study of High Temperature in the Reversing Layers of Stars.

Peng, Y.-j., Lilly, S. J., Kovač, K., et al. 2010, ApJ, 721, 193

Peng, Y.-j. & Maiolino, R. 2014, MNRAS, 438, 262

Pérez-Montero, E. 2014, MNRAS, 441, 2663

Pérez-Montero, E. & Contini, T. 2009, MNRAS, 398, 949

Pérez-Montero, E., Contini, T., Lamareille, F., et al. 2013, A&A, 549, A25

Petropoulou, V., Vílchez, J., & Iglesias-Páramo, J. 2012, ApJ, 749, 133

Petropoulou, V., Vílchez, J., Iglesias-Páramo, J., et al. 2011, ApJ, 734, 32

Pilyugin, L. S. & Grebel, E. K. 2016, MNRAS, 457, 3678

Pilyugin, L. S., Grebel, E. K., Zinchenko, I. A., Nefedyev, Y. A., & Mattsson, L. 2017, MNRAS, 465, 1358

Pilyugin, L. S., Lara-López, M. A., Grebel, E. K., et al. 2013, MNRAS, 432, 1217

Pilyugin, L. S., Thuan, T. X., & Vílchez, J. M. 2003, A&A, 397, 487

Pilyugin, L. S., Thuan, T. X., & Vílchez, J. M. 2007, MNRAS, 376, 353

Pilyugin, L. S., Vílchez, J. M., & Contini, T. 2004, A&A, 425, 849

Pilyugin, L. S., Vílchez, J. M., Mattsson, L., & Thuan, T. X. 2012, MNRAS, 421, 1624

Relaño, M., Lisenfeld, U., Vilchez, J. M., & Battaner, E. 2006, A&A, 452, 413

Renaud, F., Appleton, P. N., & Xu, C. K. 2010, ApJ, 724, 80

Renzini, A. & Peng, Y.-j. 2015, ApJ, 801, L29

Richards, S. N., Bryant, J. J., Croom, S. M., et al. 2016, MNRAS, 455, 2826

Rodighiero, G., Daddi, E., Baronchelli, I., et al. 2011, ApJ, 739, L40

Rodríguez-Baras, M., Díaz, A. I., Rosales-Ortega, F. F., & Sánchez, S. F. 2018, A&A, 609, A102

Rodríguez-Baras, M., Rosales-Ortega, F. F., Díaz, A. I., Sánchez, S. F., & Pasquali, A. 2014, MNRAS, 442, 495

Romeo Velonà, A. D., Sommer-Larsen, J., Napolitano, N. R., et al. 2013, ApJ, 770, 155

Rosales-Ortega, F. F., Kennicutt, R. C., Sánchez, S. F., et al. 2010, MNRAS, 405, 735

Sakstein, J., Pipino, A., Devriendt, J. E. G., & Maiolino, R. 2011, MNRAS, 410, 2203

Salim, S., Lee, J. C., Ly, C., et al. 2014, ApJ, 797, 126

Salim, S., Rich, R. M., Charlot, S., et al. 2007, ApJS, 173, 267

Salpeter, E. E. 1955, ApJ, 121, 161

Sánchez, S. F., Barrera-Ballesteros, J. K., Sánchez-Menguiano, L., et al. 2017, MNRAS, 469, 2121

Sánchez, S. F., Kennicutt, R. C., Gil de Paz, A., et al. 2012, A&A, 538, A8

Sánchez, S. F., Rosales-Ortega, F. F., Iglesias-Páramo, J., et al. 2014, A&A, 563, A49

Sánchez, S. F., Rosales-Ortega, F. F., Jungwiert, B., et al. 2013, A&A, 554, A58

Schlegel, D. J., Finkbeiner, D. P., & Davis, M. 1998, ApJ, 500, 525

Simón-Díaz, S. 2010, A&A, 510, A22

Singh, A., Gulati, M., & Bagla, J. S. 2019, MNRAS, 489, 5582

Skibba, R. A., Engelbracht, C. W., Dale, D., et al. 2011, ApJ, 738, 89

Slipher, V. M. 1917, The Observatory, 40, 304

Sparre, M., Hayward, C. C., Springel, V., et al. 2015, MNRAS, 447, 3548

Speagle, J. S., Steinhardt, C. L., Capak, P. L., & Silverman, J. D. 2014, ApJS, 214, 15

Stasińska, G., Cid Fernandes, R., Mateus, A., Sodré, L., & Asari, N. V. 2006, MNRAS, 371, 972

Stephan, M. 1877, MNRAS, 37, 334

Storey, P. J. & Hummer, D. G. 1995, MNRAS, 272, 41

Strauss, M. A., Weinberg, D. H., Lupton, R. H., et al. 2002, AJ, 124, 1810

Strömgren, B. 1939, ApJ, 89, 526

Sulentic, J. W., Rosado, M., Dultzin-Hacyan, D., et al. 2001, AJ, 122, 2993

Swaters, R. A., van Albada, T. S., van der Hulst, J. M., & Sancisi, R. 2002, A&A, 390, 829

Telford, O. G., Dalcanton, J. J., Skillman, E. D., & Conroy, C. 2016, ApJ, 827, 35

Tissera, P. B., Pedrosa, S. E., Sillero, E., & Vilchez, J. M. 2016, MNRAS, 456, 2982

Toomre, A. & Toomre, J. 1972, ApJ, 178, 623

Torres-Flores, S., Mendes de Oliveira, C., de Mello, D. F., et al. 2009, A&A, 507, 723

Torrey, P., Vogelsberger, M., Hernquist, L., et al. 2018, MNRAS

Trancho, G., Konstantopoulos, I. S., Bastian, N., et al. 2012, ApJ, 748, 102

Tremonti, C. A., Heckman, T. M., Kauffmann, G., et al. 2004, ApJ, 613, 898

Trimble, V. 1995, PASP, 107, 1133

Trinchieri, G., Sulentic, J., Breitschwerdt, D., & Pietsch, W. 2003, A&A, 401, 173

Trinchieri, G., Sulentic, J., Pietsch, W., & Breitschwerdt, D. 2005, A&A, 444, 697

Trujillo, I., Aguerri, J. A. L., Cepa, J., & Gutiérrez, C. M. 2001, MNRAS, 321, 269

van der Wel, A., Chang, Y.-Y., Bell, E. F., et al. 2014, ApJ, 792, L6

van Zee, L. & Haynes, M. P. 2006, ApJ, 636, 214

Veilleux, S. & Osterbrock, D. E. 1987, ApJS, 63, 295

Verdes-Montenegro, L., Yun, M. S., Williams, B. A., et al. 2001, A&A, 377, 812

Vila-Costas, M. B. & Edmunds, M. G. 1992, MNRAS, 259, 121

Walcher, C. J., Wisotzki, L., Bekeraité, S., et al. 2014, A&A, 569, A1

Westmoquette, M. S., Smith, L. J., Gallagher, J. S., & Walter, F. 2013, MNRAS, 428, 1743

Whitaker, K. E., van Dokkum, P. G., Brammer, G., & Franx, M. 2012, ApJ, 754, L29

White, S. D. M. 1978, MNRAS, 184, 185

Williams, B. A., Yun, M. S., & Verdes-Montenegro, L. 2002, AJ, 123, 2417

Xu, C., Sulentic, J. W., & Tuffs, R. 1999, ApJ, 512, 178

Xu, C. K., Iglesias-Páramo, J., Burgarella, D., et al. 2005, ApJ, 619, L95

Yang, X., Mo, H. J., van den Bosch, F. C., et al. 2007, ApJ, 671, 153

York, D. G., Adelman, J., Anderson, Jr., J. E., et al. 2000, AJ, 120, 1579

Zahid, H. J., Dima, G. I., Kewley, L. J., Erb, D. K., & Davé, R. 2012, ApJ, 757, 54

Zahid, H. J., Dima, G. I., Kudritzki, R.-P., et al. 2014, ApJ, 791, 130

Zurita, A. & Bresolin, F. 2012, MNRAS, 427, 1463

Zwicky, F., Herzog, E., Wild, P., Karpowicz, M., & Kowal, C. T. 1961, Catalogue of galaxies and of clusters of galaxies, Vol. I